Beyond the Standard Model physics searches with double-beta decays

Elisabetta Bossio

2022

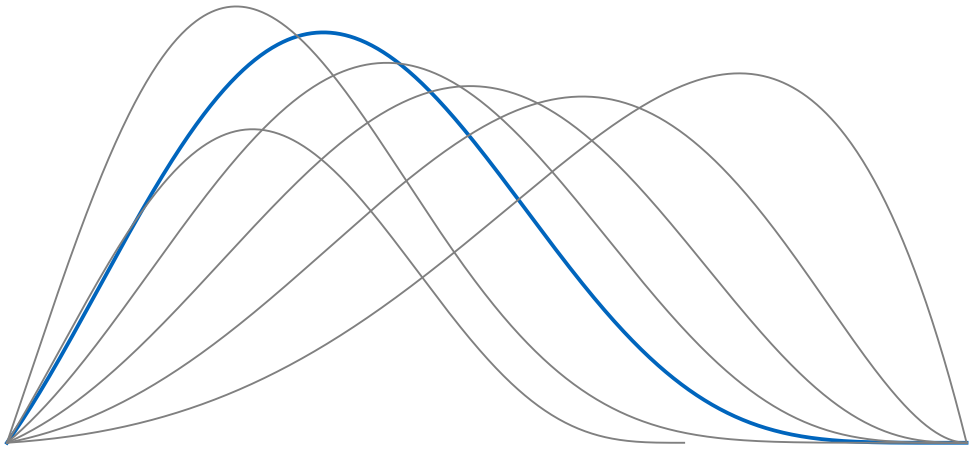

TECHNISCHE UNIVERSITÄT MÜNCHEN

TUM School of Natural Sciences

Beyond the Standard Model physics searches with double-beta decays

Elisabetta Bossio

Vollständiger Abdruck der von der TUM School of Natural Sciences der Technischen Universität München zur Erlangung des akademischen Grades einer

Doktorin der Naturwissenschaften (Dr. rer. nat.)

genehmigten Dissertation.

Vorsitzender:	Prof. Dr. Andreas Weiler
Prüfer der Dissertation:	1. Prof. Dr. Stefan Schönert
	2. Prof. Dr. Susanne Mertens

Die Dissertation wurde am 23.08.2022 bei der Technischen Universität München eingereicht und durch die TUM School of Natural Sciences am 01.11.2022 angenommen.

Abstract

Nuclear double-β decays are powerful probes for new physics beyond the Standard Model (SM). In the SM, the simultaneous decay of two neutrons into two protons is allowed as long as two electrons and two anti-neutrinos are also emitted ($2\nu\beta\beta$ decay), ensuring lepton number conservation. Neutrinoless double-β ($0\nu\beta\beta$) decay, in which only two electrons are emitted, is predicted by many lepton number non-conserving extensions of the SM, and is the only viable experimental test for the Majorana nature of neutrinos. Different extensions of the SM, which predict the existence of new particles, violation of fundamental symmetries, non-standard interactions, or other new physics, can lead to exotic double-β decay modes. This dissertation investigates the emission of light exotic fermions in double-β decay. The sensitivity of current and future double-β decay experiments is estimated. Future experiments will test unexplored regions of the parameter space in the search for sterile neutrinos with masses of hundreds of keV. They will also offer a unique opportunity to test models where only the pair production of light exotic fermions is allowed. Among the current generation of double-β decay experiments, the GERDA experiment stands out for its ultra-low background and excellent performance. The main goal of the GERDA experiment was to search for $0\nu\beta\beta$ decay of ^{76}Ge. This dissertation covers a comprehensive study of the ^{76}Ge $2\nu\beta\beta$ decay spectrum in GERDA Phase II data. The half-life of the ^{76}Ge $2\nu\beta\beta$ decay is determined with unprecedented precision: $T^{2\nu}_{1/2} = (2.022 \pm 0.041)\ 10^{21}$ yr. Exotic double-β decay modes of ^{76}Ge are investigated by searching for distortions of the $2\nu\beta\beta$ decay spectrum compared to the SM prediction. Compared to previous experiments with ^{76}Ge, improved limits on the decays involving Majorons are obtained, with half-life values of the order of 10^{23} yr. For the first time with ^{76}Ge, limits on Lorentz invariance violation are obtained. The isotropic coefficient $\mathring{a}^{(3)}_{\mathrm{of}}$, which embeds Lorentz violation in double-β decay, is constrained at the order of 10^{-6} GeV. The first experimental constraints on light exotic fermions in double-β decay are obtained. In addition, the strongest limit on the lepton-number violating neutrinoless double-electron capture (0νECEC) of ^{36}Ar is achieved in this dissertation work. The interpretation of a future discovery of $0\nu\beta\beta$ decay in terms of effective Majorana neutrino mass relies on nuclear-structure calculations, which to date carry significant uncertainties. Studies of Ordinary Muon Capture (OMC) can provide a robust benchmark for these calculations. The MONUMENT experiment aims to carry out a series of OMC measurements on several isotopes connected to $0\nu\beta\beta$ decay. This dissertation compiles the first steps of the analysis of the data collected during the first measurement campaign with ^{76}Se and ^{136}Ba.

Zusamenfassung

Doppel-Betazerfälle ($\beta\beta$-Zerfälle) sind aussagekräftige Prüfungen von neuer Physik jenseits des Standardmodells (SM). Im SM ist der simultane Zerfall von zwei Neutronen in zwei Protonen erlaubt, solange zwei Elektronen und zwei Anti-Neutrinos emittiert werden ($2\nu\beta\beta$-Zerfall), so dass die Leptonzahl (L) erhalten bleibt. Der Neutrinolose $\beta\beta$-Zerfall ($0\nu\beta\beta$-Zerfall), bei dem nur zwei Elektronen emittiert werden, wird von mehreren, die L nicht erhaltenden Erweiterungen des SMs vorhergesagt und ist der einzige experimentelle Test für die Majorana-Natur des Neutrinos. Weitere Erweiterungen des SMs, die die Existenz neuer Teilchen, die Verletzung fundamentaler Symmetrien, Nicht-Standard-Wechselwirkungen, oder andere neue Physik vorhersagen, können zu exotischeren $\beta\beta$-Zerfällen führen. Diese Dissertation untersucht die Emission von leichten exotischen Fermionen, inklusive steriler Neutrinos, beim $\beta\beta$-Zerfall. Die Empfindlichkeit aktueller und zukünftiger $\beta\beta$-Zerfall Experimente wurde geschätzt. Zukünftige Experimente können unerforschte Bereiche des Parameterraums bei der Suche nach sterilen Neutrinos mit Massen von hunderten von keV testen. Sie bieten auch eine einmalige Chance Modelle zu testen, bei denen nur die paarweise Emission von leichten exotischen Fermionen erlaubt ist. In der aktuellen Generation der $\beta\beta$-Zerfall Experimente ragt das GERDA Experiment mit seinem ultra niedrigen Rauschen und seiner exzellenten Performanz heraus. Das Hauptziel des GERDA Experiments war die Suche nach $0\nu\beta\beta$-Zerfall von ^{76}Ge. Diese Dissertation umfasst eine umfangreiche Untersuchung des Spektrums des $2\nu\beta\beta$-Zerfalls von ^{76}Ge mit den Daten von GERDA Phase II. Die Halbwertszeit des $2\nu\beta\beta$-Zerfalls von ^{76}Ge wurde mit noch nie erreichter Präzision bestimmt: $T^{2\nu}_{1/2} = (2.022 \pm 0.041)\ 10^{21}$ yr. Exotische $\beta\beta$-Zerfälle von ^{76}Ge wurden ebenfalls untersucht, wobei nach Verzerrungen des $2\nu\beta\beta$-Zerfallspektrums im Vergleich zur SM-Vorhersage gesucht wurde. Verbesserte Grenzwerte für die Zerfälle, an denen Majoronen beteiligt sind, wurden mit Halbwertszeiten $\sim 10^{23}$ yr ermittelt. Zum ersten Mal wurden mit ^{76}Ge auch Grenzwerte für die Verletzung der Lorentz-Invarianz und Einschränkungen für leichte exotische Fermionen ermittelt. Der stärkste Grenzwerte bei dem Neutrinolosen doppelten Elektroneneinfang (0νECEC) von ^{36}Ar wurde auch in dieser Dissertation erreicht. Die Interpretation einer zukünftigen Entdeckung des $0\nu\beta\beta$-Zerfalls in Bezug auf die effektive Majorana-Neutrinomasse hängt von Kernstrukturberechnungen ab, die bis heute mit erheblichen Unsicherheiten behaftet sind. Studien zum Ordinary Muon Capture (OMC) können einen robusten Maßstab für diese Berechnungen liefern. MONUMENT zielt darauf ab, eine Reihe von OMC-Messungen an mehreren Isotopen im Zusammenhang mit dem $0\nu\beta\beta$-Zerfall durchzuführen. Diese Dissertation fasst die ersten Schritte der Datenanalyse der ersten Messkampagne mit ^{76}Se und ^{136}Ba zusammen.

A mio padre,
che mi ha insegnato l'entusiasmo e la dedizione

Contents

Part I

Double-β decays

Chapter 1

Double-β decays as probe for new physics

1.1 A brief introduction to neutrinos

In a famous open letter to the participants of the Tubingen conference on radioactivity in 1930 [1], W. Pauli writes: *"Liebe Radioaktive Damen und Herren, ..., bin ich ...auf einen verzweifelten Ausweg verfallen um den Wechselsatz der Statistik und den Energiesatz zu retten. Nämlich die Möglichkeit, es könnten elektrisch neutrale Teilchen, die ich Neutronen nennen will, in den Kernen existieren, ... "*.[1] It was the first time that the concept of the neutrino[2] was introduced to explain the continuous energy spectrum of β decays. A quarter century later, in 1956, the existence of the neutrino was experimentally confirmed using a large anti-neutrino flux from a nuclear reactor: it was the discovery of the electron anti-neutrino by F. Reines and C.L. Cowan [3, 4]. In the same year, in Debrecen, A. Szalay and J. Csikai obtained photographic evidence for the existence of the neutrino [5]. Their photographs of ^{6}He β decays, taken in a cloud chamber filled with hydrogen, demonstrated the presence of an invisible third particle stealing momentum. A few years later, in 1961, the muon neutrino was discovered using the first accelerator neutrino beam [6]. This was the proof that there are two types of neutrinos and that they participate separately in weak interactions with their corresponding charged leptons. In 1989, the measurements of the width of the Z resonance by the LEP experiments established that the total number of neutrino flavors, participating in weak interactions and with masses $\lesssim 91/2\,\text{GeV}$[3], was three [8–11]. The third type of neutrino, the tau neutrino, was finally discovered in 2000 by the DONUT experiment [12].

Once different neutrino families were established, the question of whether there could be mixing between them was open. The first idea of neutrino oscillations goes

[1] Dear radioactive ladies and gentlemen, ..., I have hit upon a desperate remedy to save the exchange theorem of statistics and the law of conservation of energy. Namely, the possibility that in the nuclei, there could exist electrically neutral particles, which I will call neutrinos, ...

[2] Originally Pauli called the new hypothetical particle "neutron". After the discovery of the heavy neutron [2], a new name was needed. It was E. Amaldi who playfully named it "neutrino" in a conversation with E. Fermi, in contrast to the bigger "neutrone". In Italian, the suffix -ino indicates the diminutive, while the suffix -one indicates something big.

[3] The measurement channel $Z \to \nu\nu$ is only sensitive to neutrinos with masses below half the Z boson's mass $m_Z = 91.1876 \pm 0.0021$ [7].

back to B. Pontecorvo in 1957 [13, 14]. In 1962, Z. Maki, M. Nakagawa, and S. Sakata introduced the concept of mixing between mass and flavor eigenstates [15]. The theory was fully developed in the next decade [16–20]. On the experimental side, the first indication of neutrino oscillations emerged in solar neutrino experiments. Around 1969, the Homestake experiment led by R. Davis successfully detected solar neutrinos for the first time [21]. They observed a solar neutrino flux significantly lower than the prediction of the standard solar model [22]. It was the rising of the solar neutrino problem, which was confirmed by the GALLEX experiment [23] and several different experiments in the following years [24–26], and remained unsolved until the neutrino oscillation was established. A similar anomaly was observed with atmospheric neutrinos starting from the 1980s by the Kamiokande and MACRO experiments [27–30]. In 1987, the first neutrinos produced outside the solar system were observed, coming from the supernova 1987A [31–33].

In 1997, the Super-Kamiokande experiment reported the first clear evidence of neutrino oscillation of atmospheric neutrinos [34]. Shortly after, in 2002, the SNO experiment established the flavor conversion of solar neutrinos [35]. The parameters required to explain the solar neutrino flavor conversion were also confirmed soon after in the same year by the reactor neutrino experiment KamLAND [36]. The solar neutrino problem and the atmospheric neutrino anomaly were finally solved. They had indeed a common explanation, which lay in the neutrino oscillations. In the same years, the Borexino experiment was proposed to study solar neutrinos and understand "why and how the Sun and the stars shine" [37]. Since the first R&D efforts in 1990, in more than thirty years of activity, Borexino has obtained real breakthroughs concerning the physics of the Sun and that of the stars [38–44].

Neutrino oscillations have been studied with great precision in solar, atmospheric, accelerator, and reactor neutrino experiments. Today, all the mixing angles and the mass squared splitting Δm^2 have been measured with reasonable accuracy. The sign of $\Delta m^2_{21} = m^2_2 - m^2_1$ is known to be positive, while the sign of Δm^2_{31} is not yet established, leaving open two possibilities, normal ordering (NO) or inverted ordering (IO) [7]. The first hints of CP violation have been reported: there is a preference for large CP violation, although CP conservation is still allowed at 3σ for NO [45]. A global analysis of the latest neutrino oscillation data can be found in [46–48].

Neutrino oscillations are only sensitive to the difference of the mass squared leaving unanswered the question of the absolute neutrino mass scale. The idea that the end-point of the electron spectrum in β decays is affected by the neutrino masses was suggested by E. Fermi and F. Perrin [49–52]. Building on this idea, in the late forties, Curran *et al.* commenced the long history of neutrino mass searches in tritium β decay setting a first upper limit on the neutrino mass to 1 keV [53–55]. This technique was further pursued by the Mainz and Troitsk groups starting in 1994 [56, 57], and still provides the best neutrino-mass sensitivity in the field of direct neutrino-mass measurements. The modern KATRIN experiment reached an unprecedented sub-eV

sensitivity setting a limit on the neutrino mass to $< 0.8\,\text{eV}$ at 90% C.L., and will ultimately reach a sensitivity of 0.2 eV [58]. Other efforts are being explored (ECHo [59], HOLMES [60], and Project 8 [61] experiments) and, although they are not currently competitive with KATRIN, will aim at obtaining sub-eV sensitivities in the future.

Already in 1937, E. Majorana suggested that neutrinos and anti-neutrinos could be indistinguishable [62]. In this case, neutrinos would be Majorana particles, unlike the charged fermions, which are Dirac particles. The Majorana nature of neutrinos turned out to be strictly related to lepton number conservation. Majorana particles cannot carry any $U(1)$ quantum number.[4] Thus, the lepton number is a non-conserved symmetry if neutrinos are of Majorana type. The question of the nature of neutrinos is therefore directly related to the fundamental symmetries of nature. Neutrino oscillations do not distinguish between Majorana and Dirac particles, as they conserve lepton number. To establish the nature of neutrinos, we need a process that breaks the lepton number symmetry. The most sensitive process is neutrinoless double-beta ($0\nu\beta\beta$) decay, which will be introduced in the following.

The discovery of neutrino oscillations conclusively showed that neutrinos have mass, providing the first clear evidence that the Standard Model (SM) of particle physics is incomplete. Thanks to the extensive experimental program developed in the past decades, we now have a quite precise picture of neutrino properties, although some key questions remain unanswered. We can summarize them in the following (incomplete) list:

- What are the absolute values of the neutrino masses? Is the mass ordering normal or inverted?
- Is there CP violation in the leptonic sector? What is the value of the δ_{CP} phase?
- What is the nature of neutrinos? Are neutrinos Dirac or Majorana particles?
- Is the standard 3-neutrino picture correct, or are there other effects, such as sterile neutrinos, non-standard interactions, or even more exotic ones, *e.g.* Lorentz violation?

Direct mass measurements are necessary to access the absolute neutrino mass scale in a model-independent way. In contrast, very sensitive neutrino oscillation experiments are required to shed light on the mass ordering and the question of leptonic CP violation.

We anticipated that $0\nu\beta\beta$ decay might answer the question of the nature of neutrinos. Double-β decay experiments also offer a unique opportunity to test many other exotic physics effects and to try to answer the last question. In section 1.2, we introduce the double-β decay in the SM, and we discuss the lepton number non-conserving $0\nu\beta\beta$ decay in section 1.3. In section 1.4, we present alternative double-β decay channels. From section 1.5 on, we introduce more exotic double-β decay

[4] The definition of Majorana field $\Psi = \Psi^c$ is not invariant under any $U(1)$ transformation of the Lagrangian.

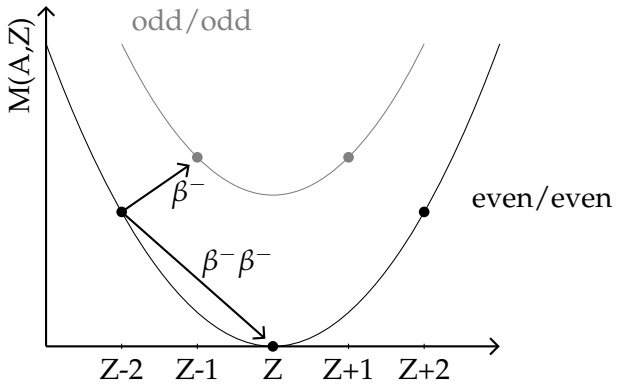

FIGURE 1.1: Mass parabolas of nuclear isobars with even A. Due to the pairing term in the semi-empirical mass formula, β^- transitions of even/even nuclei to their odd/odd isobaric neighbor can be energetically forbidden, whereas in a second-order process, $\beta^-\beta^-$ decay is allowed.

modes, which might involve the emission of new particles (section 1.5), violation of fundamental symmetries (section 1.6), or non-standard interactions (section 1.7).

1.2 Double-β decay in the Standard Model

Double-β decays are nuclear transitions in which the atomic number (Z) increases by two units while the number of nucleons (A) stays constant. This can be the only possible decay channel in those isotopes for which single-β transitions are highly suppressed by energy or spin considerations. Keeping in mind the semi-empirical mass formula of Weizsäcker [63], nuclear isobars with even A can be described by two parabolas in the M(A,Z) versus Z space, as shown in figure 1.1. Because of the pairing energy, even-even nuclei have generally lower masses than the neighboring odd-odd nuclei, and as a result, single-β decay is energetically forbidden. However, in a second-order process, double-β decay is possible.

The SM of particle physics allows for double-β decay as long as two electrons and two anti-neutrinos are also emitted, ensuring the conservation of lepton number:

$$(\beta^-\beta^-): \ (A,Z) \rightarrow (A,Z+2) + 2e^- + 2\overline{\nu}\,. \tag{1.1}$$

The process leading to this final state is called two-neutrino double-beta ($2\nu\beta\beta$) decay. Its Feynman diagram is shown in figure 1.2a.

The existence of $2\nu\beta\beta$ decay was postulated by Maria Goeppert-Maier [64] in 1935, who also estimated that its half-life had to exceed 10^{17} yr. Its discovery came only later, in 1950, in a geochemical experiment with ^{130}Te [65], and almost 40 years passed until its first direct observation with ^{82}Se [66]. To date, the $2\nu\beta\beta$ decay has been observed in 11 isotopes with half-life values in the range of 10^{18}–10^{24} yr [67], making it one of the rarest processes ever observed. The most precise $2\nu\beta\beta$ decay measurements are compiled in table 1.1.

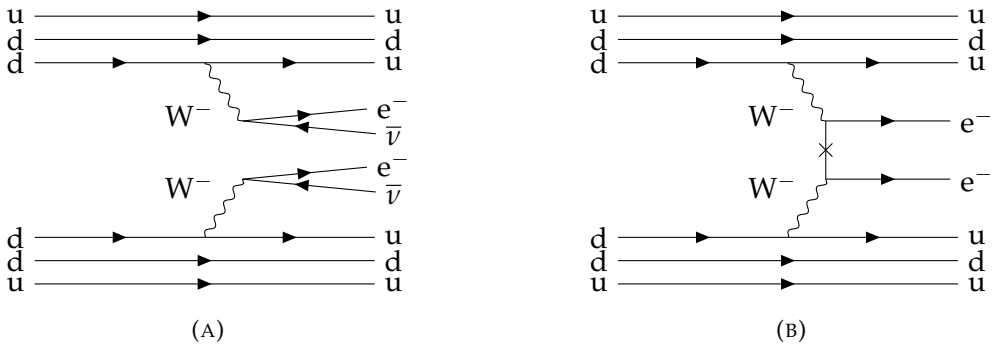

FIGURE 1.2: Feynman diagrams of the (A) SM $2\nu\beta\beta$ decay and (B) the lepton number non-conserving $0\nu\beta\beta$ decay in the light-neutrino exchange scenario.

Among the current double-β decay experiments, one of the most competitive is the Germanium Detector Array (GERDA) experiment, in the scope of which part of this dissertation was conducted. In this work, the most precise determination of the ^{76}Ge $2\nu\beta\beta$ decay half-life is performed with GERDA Phase II data. This is also one of the most precise measurements of a double-β decay process. We refer to chapter 9 for all the details about this result.

Depending on the relative numbers of protons and neutrons in the nucleus, other decay possibilities are also allowed in the SM:

$$(\beta^+\beta^+):\ (A,Z) \rightarrow (A,Z-2) + 2e^+ + 2\nu \tag{1.2a}$$

$$(ECEC):\ (A,Z) + 2e^- \rightarrow (A,Z-2) + 2\nu \tag{1.2b}$$

$$(EC\beta^+):\ (A,Z) + e^- \rightarrow (A,Z-2) + e^+ + 2\nu\,. \tag{1.2c}$$

The energy released in the three processes listed above is smaller compared to the $\beta^-\beta^-$ decay in equation 1.1. Consequently, these processes have lower probabilities compared with $\beta^-\beta^-$ decay due to the smaller phase space, and experimentally they are much more challenging to observe. In the following, we will always refer to the $\beta^-\beta^-$ process as double-β decay.

Double-β transitions can be uniquely identified by the production of the daughter nucleus. With this principle, the first discovery of $2\nu\beta\beta$ decay was made in a geochemical experiment, detecting traces of double-β decay daughters in materials containing the parent isotopes [65]. Nevertheless, a measurement of the two final-state electrons is necessary to distinguish $2\nu\beta\beta$ decay from more exotic double-β decay modes.

Being the electron mass orders of magnitude smaller than the daughter nucleus, the nuclear recoil energy is negligible, and all the available energy in the decay, *i.e.* the $Q_{\beta\beta}$, is shared among the final-state particles:

$$Q_{\beta\beta} = M(A,Z) - M(A,Z+2)\,. \tag{1.3}$$

Isotope	Half-life [yr]	Ref.
^{48}Ca	$(6.4^{+1.4}_{-1.1}) \cdot 10^{19}$	[68]
^{76}Ge	$(2.022 \pm 0.041) \cdot 10^{21}$	*this work*
^{82}Se	$(8.60^{+0.19}_{-0.13}) \cdot 10^{19}$	[69]
^{96}Zr	$(2.35 \pm 0.21) \cdot 10^{19}$	[70]
^{100}Mo	$(7.12^{+0.21}_{-0.17}) \cdot 10^{18}$	[71]
^{116}Cd	$(2.63^{+0.11}_{-0.12}) \cdot 10^{19}$	[72]
^{128}Te (geochem.)	$(2.41 \pm 0.39) \cdot 10^{24}$	[73]
^{130}Te	$(7.71^{+0.14}_{-0.16}) \cdot 10^{20}$	[74]
^{136}Xe	$(2.165 \pm 0.063) \cdot 10^{21}$	[75]
^{150}Nd	$(9.34^{+0.66}_{-0.64}) \cdot 10^{18}$	[76]
^{238}U (radiochem.)	$(2.0 \pm 0.6) \cdot 10^{21}$	[77]

TABLE 1.1: Collection of $2\nu\beta\beta$ decay half-life values. The most precise direct measurements are reported for all the different isotopes, except for ^{128}Te and ^{238}U. Their half-life was determined with geochemical and radiochemical experiments, respectively. The shown uncertainty is the sum in quadrature of the statistical and systematic uncertainties.

In the $2\nu\beta\beta$ decay, two anti-neutrinos are emitted together with the two electrons. They escape undetected and carry away part of the available energy. Consequently, the summed energy of the two electrons is continuously distributed between 0 and $Q_{\beta\beta}$, as shown in figure 1.3.

The rate of $2\nu\beta\beta$ decay can be calculated following Fermi's golden rule for β decay. To a good approximation, the kinematic part (phase space of the leptons emitted in the decay) and the nuclear part (matrix element responsible for the transition

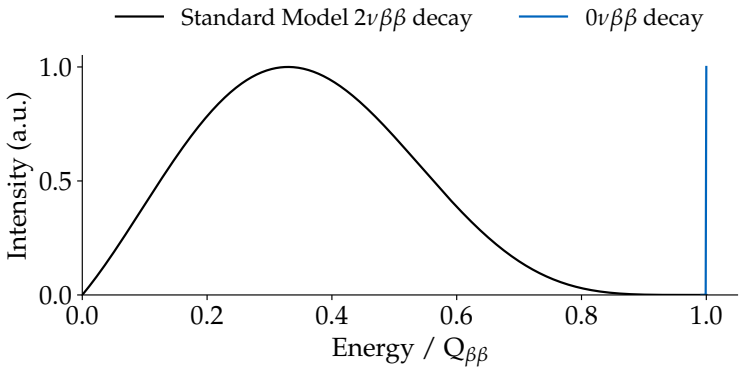

FIGURE 1.3: Summed electron energy distribution for the SM $2\nu\beta\beta$ decay and the lepton number non-conserving $0\nu\beta\beta$ decay. An infinite energy resolution is assumed and an arbitrary normalization is used for illustrative purposes.

probability between the two nuclear states) can be factorized as:

$$\Gamma^{2\nu} = \frac{1}{T^{2\nu}_{1/2}} = \mathcal{G}^{2\nu}(Q_{\beta\beta}, Z)\,|\mathcal{M}^{2\nu}|^2\,, \tag{1.4}$$

where $\mathcal{G}^{2\nu}$ is the phase-space factor and is obtained by integrating over the phase space of the four leptons, and $\mathcal{M}^{2\nu}$ is the nuclear matrix element (NME) and deals with the nuclear structure of the transition. While the phase-space factor can be calculated exactly, the NME is much more difficult to evaluate and relies on nuclear-structure models.

Experiments measure the distribution of the summed kinetic energy of the two electrons (K)

$$\frac{d\Gamma^{2\nu}}{dK} = |\mathcal{M}^{2\nu}|^2\,\frac{d\mathcal{G}^{2\nu}}{dK}\,. \tag{1.5}$$

In the first order, the shape of this distribution (as well as the electron angular distribution) is determined only by the phase space. The contribution of the NME to it is small, and it primarily affects the absolute value of the transition probability.

1.3 Neutrinoless double-β decay

Building on Goeppert Mayer's ideas of double-β decays, and the symmetry between neutrinos and anti-neutrinos postulated by E. Majorana, and further discussed by G. Racah in 1937 [62, 78], W. H. Furry proposed in 1939 the existence of $0\nu\beta\beta$ decay [79]. This process corresponds to the double-β decay transition in which only two electrons are emitted:

$$(A, Z) \rightarrow (A, Z+2) + 2e^-\,. \tag{1.6}$$

The creation of two leptons, not balanced by that of two anti-leptons, violates the lepton number symmetry by two units, implying the existence of new physics beyond the SM. Furthermore, following the Schechter-Valle theorem [80], the observation of $0\nu\beta\beta$ decay would confirm that neutrinos have a Majorana mass component. Given that only two electrons are emitted in $0\nu\beta\beta$ decay, their summed energy is equivalent to $Q_{\beta\beta}$. Hence, the experimental signature of $0\nu\beta\beta$ decay is a monoenergetic peak at $Q_{\beta\beta}$, broadened only by the experimental energy resolution. This is shown in figure 1.3, in comparison with the $2\nu\beta\beta$ decay distribution.

In the simplest and most studied case in which we add to the SM massive neutrinos and assume that they are Majorana particles, the $0\nu\beta\beta$ decay can happen via the exchange of a light Majorana neutrino. This is the so-called *light-neutrino exchange scenario*. The Feynman diagram for the $0\nu\beta\beta$ decay in the light-neutrino exchange scenario is shown in figure 1.2b.

The rate of the $0\nu\beta\beta$ decay in the light-neutrino exchange scenario can be expressed as:

$$\Gamma^{0\nu} = \frac{1}{T^{0\nu}_{1/2}} = \mathcal{G}^{0\nu}(Q_{\beta\beta}, Z)\,|g_A^2\,\mathcal{M}^{0\nu}|^2\,\frac{m^2_{\beta\beta}}{m_e^2}\,, \tag{1.7}$$

where $\mathcal{G}^{0\nu}$ is the phase-space factor and $\mathcal{M}^{0\nu}$ the NME. The axial-vector coupling constant (g_A) is factored out in this expression. The effective Majorana neutrino mass ($m_{\beta\beta}$) is the new physics parameter that embeds all the dependence on neutrino properties:

$$m_{\beta\beta} = \sum_i m_i U_{ei}^2 \,. \tag{1.8}$$

Here, m_i indicates the three light neutrino masses, and the U_{ei} are the elements of the first row of the Pontecorvo-Maki-Nakagawa-Sakata (PMNS) neutrino mixing matrix [7].

Generally, a variety of lepton-number-violating operators can trigger the $0\nu\beta\beta$ decay [81–86]. While the observation of the $0\nu\beta\beta$ decay would unambiguously indicate that neutrinos have a Majorana mass component, it would remain unclear whether the standard mechanism that gives a contribution proportional to the neutrino mass is the dominant one. Some examples of Beyond the Standard Model (BSM) mechanisms, which can induce a non-standard contribution to the $0\nu\beta\beta$ decay rate, are, for instance, the left-right symmetric models [83, 87–91] or sterile neutrinos [92–95]. Considering all possible BSM mechanisms, we can express the decay rate as:

$$\Gamma^{0\nu} = \frac{1}{T^{0\nu}_{1/2}} = \sum_i f_i \, \mathcal{G}_i^{0\nu}(Q_{\beta\beta}, Z) \, |g_A^2 \, \mathcal{M}_i^{0\nu}|^2 \,, \tag{1.9}$$

where f_i is an a-dimensional function which embeds the BSM physics. This expression reduces to equation 1.7 in the light-neutrino exchange scenario with $f_i = m^2_{\beta\beta}/m_e^2$. Once the $0\nu\beta\beta$ is observed, the next challenge would then be the identification of the dominant mechanism [96].

The experimental search of $0\nu\beta\beta$ decay is extremely challenging. From the first direct searches, performed in the 1960s with a sensitivity on the half-life $T^{0\nu}_{1/2}$ of $\sim 10^{19-21}$ yr [97–100], new technologies were developed and tested, leading to experiments with half-life sensitivities $\gtrsim 10^{26}$ years. The next generation of $0\nu\beta\beta$ decay experiments aims to increase the sensitivity by two orders of magnitude, conclusively testing the region $m_{\beta\beta} \gtrsim 10$ meV, where the $0\nu\beta\beta$ decay would occur if neutrinos were Majorana particles and the mass hierarchy was inverted. A discussion about the experimental requirements and an overview of the current and next generation of experiments will be given in chapter 2. Here we report the 90% confidence level (C.L.) (confidence interval (C.I.) in case of Bayesian analysis) limits and the 3σ discovery sensitivities on the half-life of the $0\nu\beta\beta$ decay for a selection of current and future experiments, compiled in table 1.2. Among the current experiments, the GERDA experiment reached the best sensitivity in the search for the $0\nu\beta\beta$ decay of any double-β decay experiment, setting the most stringent limit on the half-life of this process in ^{76}Ge. We refer to chapter 6 for more details on this result.

Isotope	Experiment	Half-life [yr]	$m_{\beta\beta}$ [meV]	Ref.
^{76}Ge	GERDA	$> 1.8 \times 10^{26}$	$< (79 - 180)$	[101]
	Majorana	$> 8.3 \times 10^{25}$	$< (113 - 269)$	[102]
^{82}Se	CUPID-0	$> 4.6 \times 10^{24}$	$< (263 - 545)$	[103]
^{100}Mo	CUPID-Mo	$> 1.8 \times 10^{24}$	$< (280 - 490)$	[104]
	NEMO-3	$> 1.1 \times 10^{24}$	$< (330 - 620)$	[105]
^{130}Te	CUORE	$> 2.2 \times 10^{25}$	$< (90 - 305)$	[106]
^{136}Xe	KamLAND-Zen	$> 2.3 \times 10^{26}$	$< (36 - 156)$	[107]
	EXO-200	$> 3.5 \times 10^{25}$	$< (93 - 286)$	[108]
^{76}Ge	LEGEND-1000	1.3×10^{28}	$(9 - 21)$	[109]
^{100}Mo	CUPID	1.0×10^{27}	$(12 - 20)$	[110]
^{136}Xe	nEXO	0.74×10^{28}	$(6 - 27)$	[111]

TABLE 1.2: Collection of limits and sensitivities on the half-life of $0\nu\beta\beta$ decays. The latest results of a selection of current experiments are reported in the first group. The 90% C.L. (C.I.) lower limit on the $0\nu\beta\beta$ decay half-life and the corresponding upper limit on the $m_{\beta\beta}$ are indicated. In the second group, the 3σ discovery sensitivity after 10 yr of exposure is shown for a selection of future double-β decay experiments.

1.4 Alternative double-β decay channels

1.4.1 Double-electron capture

Double-electron capture (ECEC), corresponding to equation 1.2c, has a lower phase space compared to the $2\nu\beta\beta$ decays. The maximum energy available in ECEC depends on the excitation energy ε of the atomic shell of the daughter nucleus:

$$Q_{ECEC} = M(A, Z) - M(A, Z - 2) - 2\varepsilon\,. \tag{1.10}$$

Consequently, ECEC processes have a smaller probability compared to $2\nu\beta\beta$ decays, and their experimental observation is even more challenging. The first direct observation of ECEC was made only in 2018. The XENON1T experiment claimed the observation of ECEC of ^{124}Xe with a half-life of $(1.8 \pm 0.5) \times 10^{22}$ yr [112]. With geochemical methods, the ECEC of ^{130}Ba and ^{132}Ba was observed with a half-life of $(2.2 \pm 0.5) \times 10^{21}$ yr and $(1.3 \pm 0.9) \times 10^{21}$ yr, respectively [113]. The ECEC of ^{78}Kr was also observed in a large proportional counter filled with the krypton sample, with a half-life of $(1.9^{+1.3}_{-0.8}) \times 10^{22}$ yr [114].

The lepton number violating counterpart of ECEC, namely neutrinoless double-electron capture (0νECEC), was predicted in 1995 by R. Winter [115]:

$$(A, Z) + 2e^- \rightarrow (A, Z - 2)^{**}. \tag{1.11}$$

In the process, all the decay energy is taken by the daughter isotope's excitation. Both the nucleus and the electron shell of the atom are left behind in an excited state.

The consequent de-excitation of the nucleus takes place either through the emission of a γ or a conversion electron. The de-excitation of the electron shell occurs through the release of Auger electrons or a cascade of X-rays [116]. The γ energy is usually sufficiently high for detection and is, therefore, the signature that is commonly used in the search for 0νECEC.

In analogy with the $0\nu\beta\beta$ decay, the 0νECEC violates the lepton number symmetry by two units and implies that neutrinos have a Majorana mass component. Estimates show that the sensitivity of 0νECEC processes to the Majorana neutrino mass is many orders of magnitude lower than that of the $0\nu\beta\beta$ decay. Nevertheless, the interest in 0νECEC is theoretically motivated by the possibility of *resonant enhancement* in this channel when the parent nucleus and an excited state of the daughter nucleus are energetically degenerate. This was already pointed out by Winter [115] and further discussed in the early 80s by several authors [117–119]. In this case, the half-life of 0νECEC processes becomes comparable to the half-life of $0\nu\beta\beta$ decays. A maximum enhancement of $\sim 10^6$ can be achieved, for instance, for a mass difference of the parent and daughter nuclei of the order of 10 keV [116]. A list of nuclei, in which the resonant enhancement is predicted, is provided by several authors [116, 120–123].

Experimental searches for 0νECEC have been performed by double-β decay experiments, even though with less sensitivity compared to the search for $0\nu\beta\beta$ decay. The most sensitive experiments set limits on the half-life of 0νECEC at the level of $10^{21} - 10^{22}$ yr for several isotopes (^{36}Ar, ^{40}Ca, ^{58}Ni, ^{64}Zn, ^{78}Kr, ^{96}Ru, ^{106}Cd, ^{112}Sn, ^{120}Te, ^{124}Xe, ^{126}Xe, ^{130}Ba, ^{132}Ba) [116]. In this dissertation, a search for ^{36}Ar 0νECEC was performed with the whole exposure of GERDA Phase II. The most stringent limit on the half-life of this process was obtained $T_{1/2} > 1.64 \times 10^{22}$ yr at 90% C.L.. We refer to chapter 7 for more details on this result.

1.4.2 Transition to the excited states

Double-β decay can also proceed to the excited states of the daughter nucleus. Here, we consider ^{76}Ge as an example. The $Q_{\beta\beta}$ of the double-β decay of ^{76}Ge into the ground state of ^{76}Se is:

$$Q_{\beta\beta} = 2039.061 \pm 0.007 \text{ keV [125]}. \tag{1.12}$$

This allows the population of the ten lowest nuclear states of ^{76}Se [124]. However, the higher the energy of the nuclear state, the less energy is available for the electrons and the neutrinos emitted in the double-β decay, resulting in lower probabilities due to the smaller phase space. Thus, we restrict our attention to the three lowest excited states of ^{76}Se. Figure 1.4 depicts such transitions. The nuclear spins of mother and daughter nuclei also influence the decay probability. For this reason, for instance, the excited state transition to the 0_1^+ state is favored over the 2_1^+ and 2_2^+ states.

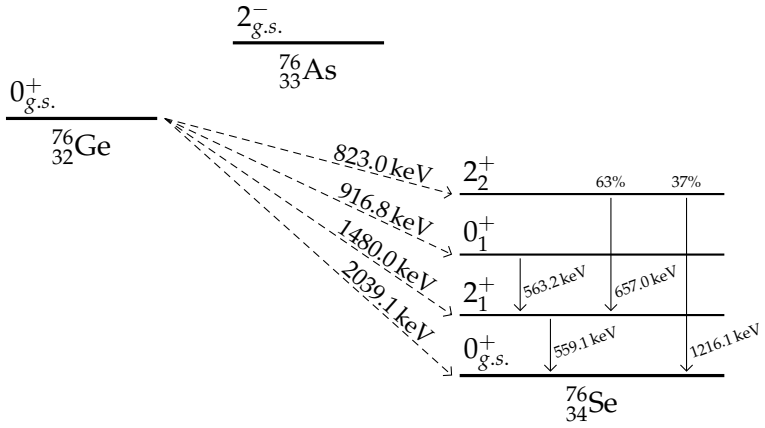

FIGURE 1.4: Decay scheme for the double-β decay of ^{76}Ge into the ^{76}Se ground state and the three lowest excited states. The $Q_{\beta\beta}$ of each transition is indicated on the respective dotted arrow. The energies of the de-excitation γs are also indicated. The de-excitation from the 2^+_2 state can happen with the emission of one or two consecutive γs. The corresponding branching ratios are indicated. Values are taken from [124].

Due to the smaller transition energies, the probability of double-β decay to the excited states is substantially suppressed compared to the ground-state decay, making it more challenging to observe. However, the excited state transitions offer important complementary input to nuclear-structure models [126]. Experimentally, the emission of γs that follows the de-excitation of the daughter nucleus offers a characteristic signature, commonly used in the search for double-β transitions to the excited states.

Only the 0^+_1 transition of the $2\nu\beta\beta$ decay has been observed so far in two isotopes, ^{100}Mo and ^{150}Nd. The latest and most precise measurements of the half-life of these transitions have been performed by the CUPID-Mo [127] and NEMO-3 [128] experiments, respectively. The corresponding half-life values are $(7.5 \pm 0.9) \times 10^{20}$ yr and $(1.11^{+0.25}_{-0.21}) \times 10^{20}$ yr, respectively for ^{100}Mo and ^{150}Nd. For the other double-β decay isotopes, only lower limits on the half-life of the order of $10^{20} - 10^{23}$ yr exist [129].

If the $0\nu\beta\beta$ decay exists, the corresponding transitions to the excited states could also be observed. It was demonstrated that the sensitivities of the $0^+ \rightarrow 2^+$ transitions to the lepton number non-conserving parameters, *e.g.* the $m_{\beta\beta}$, are comparable to those of the $0^+ \rightarrow 0^+$ transitions [130]. Double-β decay experiments set limits on the half-life of these decays as sensitive as $\sim (10^{21} - 10^{25})$ yr [129].

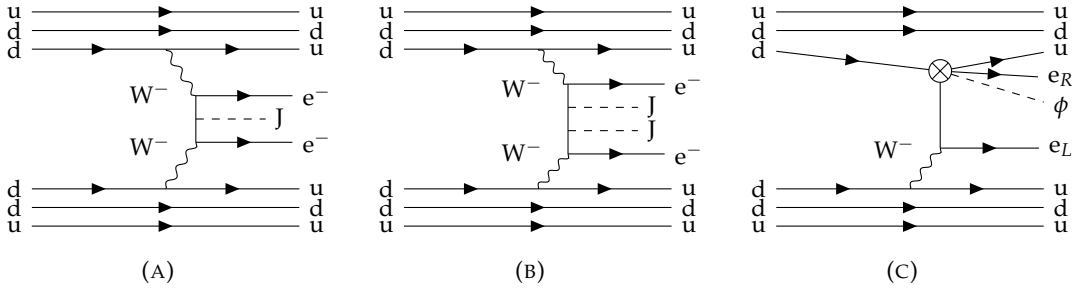

FIGURE 1.5: Feynman diagrams of the double-β decay with the emission of (A) one Majoron and (B) two Majorons in the light-neutrino exchange scenario. The (C) diagram represents the emission of a Majoron-like particle ϕ through an effective dimension-seven operator containing right-handed currents. The latter was adapted from [131].

1.5 Emission of new particles in double-β decay

1.5.1 Majorons

In many extensions of the SM, double-β decays occur with the emission of one or two bosons, the so-called Majorons (J):

$$\begin{aligned}(A, Z) &\rightarrow (A, Z+2) + 2e^- + J, \\ (A, Z) &\rightarrow (A, Z+2) + 2e^- + 2J.\end{aligned} \tag{1.13}$$

The Feynman diagrams of the double-β decay with the emission of one (J$\beta\beta$ decay) or two Majorons (JJ$\beta\beta$ decay) is shown in figure 1.5a and 1.5b, respectively.

In what is typically considered classical models, the Majoron is the Goldstone boson that arises from the spontaneous breakdown of the global B-L symmetry. The first of these models was proposed by Chikashige, Mohapatra, and Peccei in the early 80s [132, 133], who introduced the Majoron through a Higgs singlet and showed that the coupling to light neutrinos would be negligible. Later, Gelmini and Roncadelli proposed a model in which the Majoron arises from a Higgs triplet [134]. In this case, the coupling to light neutrinos could be large, leading to an observable J$\beta\beta$ decay signal in the experiments [117, 135, 136]. Double-β decay with the emission of two Majorons was first investigated in the context of supersymmetric theories [137].

Successively, precision measurements of the width of Z boson decay to invisible channels ruled out the models in which the Majoron arises from a Higgs triplet or doublet [138]. On the other hand, in the first singlet Higgs model, the Majoron is so weakly coupled to neutrinos that it cannot produce detectable effects in double-β decay. At the same time, an excess of events below $Q_{\beta\beta}$ was observed in some double-β decay experiments [139–141]. The sum of these events motivated in the following years the construction of new models able to reconcile the results on the Z decay width with a neutrino-Majoron coupling strong enough to explain the event

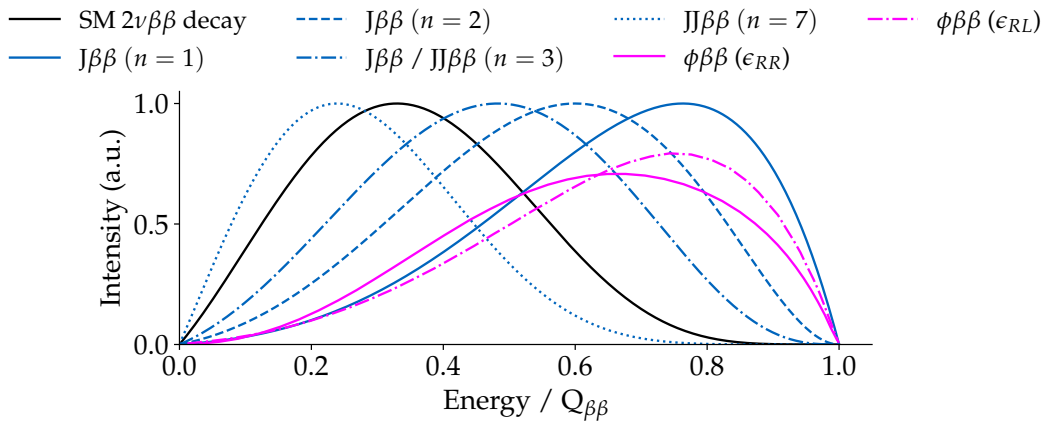

FIGURE 1.6: Summed electron energy distribution for different Majoron models (the spectral index corresponding to each model is indicated) compared to the SM $2\nu\beta\beta$ decay distribution. The decays with the emission of a non-standard Majoron are also shown: they can be triggered by an effective seven-dimension operator, containing right-handed (ϵ_{RR}) and left-handed (ϵ_{RL}) hadronic current. The latter was adapted from [131]. An arbitrary normalization is used for illustrative purposes.

excess [142]. Models in which the Majoron carries a non-zero lepton number were investigated to restore lepton number conservation in double-β decays with the emission of Majorons [143, 144]. Departing from the initial conception of Majorons as Goldstone bosons, new models were proposed in which the Majoron is a component of a massive gauge boson [145] or a bulk field [146]. Also, new models predicting the emission of two Majorons were considered [147].

If one or two Majorons are emitted in the double-β decay, they carry away part of the available energy. In analogy with the SM $2\nu\beta\beta$ decay, the summed energy of the two emitted electrons is continuously distributed between 0 and $Q_{\beta\beta}$. Different Majoron models predict different energy distributions for the two electrons. This can be parameterized to-a-first-approximation with a spectral index n, which appears in the phase space of the emitted particles:

$$\mathcal{G} \sim (Q_{\beta\beta} - T)^n \tag{1.14}$$

Figure 1.6 shows the summed electron energy distribution for different Majoron models compared to the SM $2\nu\beta\beta$ decay distribution.

The spectral index can be used to group models predicting the same experimental signature. These models are not distinguishable by the experiments. Table 1.3 shows a summary of all the Majoron models grouped by the number of emitted Majorons in the second column, the spectral index in the third column, and the Majoron's properties in the last two columns. The fourth column indicates whether the Majoron is a Goldstone boson or not, whereas the last column shows the Majoron's leptonic charge. Models in which the Majoron carries a lepton number different from

	Decay mode	n	Goldstone boson	L
a	J$\beta\beta$	1	yes	0
			no	0
			no	-2
b	J$\beta\beta$	2	Bulk field	0
c	J$\beta\beta$	3	yes	-2
			Gauge boson	-2
d	JJ$\beta\beta$	3	yes	0
			no	0
			no	-1
e	JJ$\beta\beta$	7	yes	-1

TABLE 1.3: Different Majoron models which predict double-β decays with the emission of one or two Majorons. The third column indicates the model's spectral index (n), the fourth column indicates whether the Majoron is a Goldstone boson or not, and the last column indicates the leptonic charge (L) of the Majoron. Models with leptonic charges different from zero preserve the lepton number symmetry.

0 preserve the lepton number symmetry. These models are experimentally indistinguishable from the corresponding lepton number non-conserving processes.

The inverse of the half-life of double-β decay with Majoron emission can be written as:

$$\begin{aligned} [T_{1/2}]^{-1} &= g_J^2 |\mathcal{M}_\alpha|^2 \mathcal{G}_\alpha \quad \text{for the emission of one Majoron,} \\ [T_{1/2}]^{-1} &= g_J^4 |\mathcal{M}_\alpha|^2 \mathcal{G}_\alpha \quad \text{for the emission of two Majorons.} \end{aligned} \tag{1.15}$$

The neutrino-Majoron couping constant (g_J), the NME $\mathcal{M}$, and the phase-space factor $\mathcal{G}$ differ for different models. Phase-space factor calculations for the models listed in table 1.3 are available in [148]. The NME for the $n = 1$ model is the same as for the $0\nu\beta\beta$ decay. The NME for the $n = 3$ and $n = 7$ models have been calculated in [136], and more recently in [149]. No phase-space factor and NME calculations are available for the $n = 2$ model.

All the decay modes discussed so far focus on the emission of one or two Majorons originating from the intermediate neutrino exchanged in the process. Despite the differences among the models, all of them assume the SM V-A structure of the charged currents involving leptons and quarks. Recently a new scenario has been considered, in which a Majoron-like particle (ϕ) is emitted in the double-β decay ($\phi\beta\beta$ decay). The interaction can be described by an effective dimension-seven operator, with right-handed lepton current and right/left-handed quark current [131]. The Feynman diagram of this process is shown in figure 1.5c. The coupling strength between the neutrino and the Majoron-like ϕ is ϵ_{RL} if the effective operator contains left-handed quark current, and ϵ_{RR} when the effective operator contains right-handed quark current. The two cases have been considered separately, with only one of the two operators being present at a time.

The energy distribution predicted for the $\phi\beta\beta$ decay is shown in figure 1.6. The distribution associated with ϵ_{RL} is very similar to the ordinary Majoron emission corresponding to $n = 1$. On the other hand, introducing a hadronic right-handed current in the ϵ_{RR} term changes the shape of the distribution considerably.

Experimental searches for the classical Majoron models (summarized in table 1.3) have been performed by several experiments with different double-β decay isotopes. The excess of events below $Q_{\beta\beta}$ observed by several experiments in the late 80s was interpreted as J$\beta\beta$ decay [139–141]. Half-life limits of the order of $10^{20} - 10^{21}$ yr were obtained by these early experiments. Successively, both the theoretical progress and the results of modern experiments excluded the observation of J$\beta\beta$ decay up to a half-life of the order of $10^{23} - 10^{24}$ yr. A summary of the latest results obtained by different double-β decay experiments is presented in table 1.4. A search for Majoron involving decays in ^{76}Ge was performed as part of this dissertation work with GERDA Phase II data. The results will be discussed in chapter 8.

The EXO-200 experiment recently searched also for the non-standard Majoron decay, which involves right-handed and left-handed hadronic currents [150]. These results are summarized in table 1.4.

In all the previous discussions, we always assumed the Majoron to be massless. However, many of the models already presented do not prevent the Majoron from being a light particle [131, 147, 154]. This possibility becomes extremely popular when considering that the light Majorons could be a dark matter (DM) candidate [155, 156]. If the Majoron mass is below the $Q_{\beta\beta}$, double-β decay with the emission of a Majoron can still happen. In this case, the end-point of the energy distribution is shifted to $Q_{\beta\beta} - m_J$, where m_J is the Majoron mass.

1.5.2 Light exotic fermions

Light exotic fermions (f) coupling with the SM neutrinos can be emitted in double-β decays through the processes:

$$(A, Z) \rightarrow (A, Z+2) + 2e^- + \overline{\nu} + f, \tag{1.16a}$$

$$(A, Z) \rightarrow (A, Z+2) + 2e^- + 2f. \tag{1.16b}$$

The currently most popular exotic fermion is the massive sterile neutrino (N). In analogy with the search for sterile neutrinos in β decays [157–160], if a N with mass below a few MeV exists, the decay channel in equation 1.16a becomes possible because of the mixing between sterile and active neutrinos.

In general, if the production of a single particle is allowed, the production of two exotic particles is suppressed and can be neglected by experiments. However, there are scenarios where the single production is forbidden by additional symmetries. Still, the pair production of exotic fermions via the decay channel in equation 1.16b can be allowed. In these cases, double-β decays offer unique discovery opportunities for laboratory experiments.

Isotope	$T_{1/2}$ (yr)	Ref.	$\mathcal{G}$ (10^{18} yr^{-1})	NME	g_J
	J$\beta\beta$ ($n=1$)				
^{76}Ge	$> 6.4 \times 10^{23}$	*this work*	44.2	(2.66 – 6.34)	$< (1.8 - 4.4) \times 10^{-5}$
^{100}Mo	$> 4.4 \times 10^{22}$	[105]	598	(3.84 – 6.59)	$< (1.8 - 3.1) \times 10^{-5}$
^{116}Cd	$> 8.2 \times 10^{21}$	[72]	569	(3.105 – 5.43)	$< (6.1 - 9.3) \times 10^{-5}$
^{136}Xe	$> 2.6 \times 10^{24}$	[151]	409	(1.11 – 4.77)	$< (0.8 - 1.6) \times 10^{-5}$
	$> 4.3 \times 10^{24}$	[150]			$< (0.4 - 0.9) \times 10^{-5}$
	J$\beta\beta$ ($n=3$)				
^{76}Ge	$> 1.2 \times 10^{23}$	*this work*	0.073	0.381	$< 1.7 \times 10^{-2}$
^{100}Mo	$> 4.4 \times 10^{21}$	[152]	2.42	0.263	$< 2.3 \times 10^{-2}$
^{116}Cd	$> 2.6 \times 10^{21}$	[72]	2.28	0.144	$< 5.6 \times 10^{-2}$
^{136}Xe	$> 4.5 \times 10^{23}$	[151]	1.47	0.160	$< 0.47 \times 10^{-2}$
	$> 6.3 \times 10^{23}$	[150]			$< 0.40 \times 10^{-2}$
	JJ$\beta\beta$ ($n=3$)				
^{76}Ge	$> 1.2 \times 10^{23}$	*this work*	0.22	0.0026	< 1.2
^{100}Mo	$> 4.4 \times 10^{21}$	[152]	6.15	0.0019	< 1.4
^{116}Cd	$> 2.6 \times 10^{21}$	[72]	5.23	0.000945	< 2.4
^{136}Xe	$> 4.5 \times 10^{23}$	[151]	3.05	0.0011	< 0.69
	$> 6.3 \times 10^{23}$	[150]			< 0.64
	JJ$\beta\beta$ ($n=7$)				
^{76}Ge	$> 1.1 \times 10^{23}$	*this work*	0.42	0.0026	< 1.0
^{100}Mo	$> 1.2 \times 10^{21}$	[152]	50.8	0.0019	< 1.15
^{116}Cd	$> 8.9 \times 10^{20}$	[72]	33.9	0.000945	< 1.94
^{136}Xe	$> 1.1 \times 10^{22}$	[151]	12.5	0.0011	< 1.23
	$> 5.1 \times 10^{22}$	[150]			< 0.84
	J$\beta\beta$ ($n=2$)				
^{76}Ge	$> 2.9 \times 10^{23}$	*this work*	–	–	–
^{100}Mo	$> 9.9 \times 10^{21}$	[152]	–	–	–
^{116}Cd	$> 4.1 \times 10^{21}$	[72]	–	–	–
^{136}Xe	$> 1.0 \times 10^{24}$	[151]	–	–	–
	$> 9.8 \times 10^{23}$	[150]	–	–	–
	$\phi\beta\beta$ (ϵ_{RR})				
^{136}Xe	$> 3.7 \times 10^{24}$	[150]	–	–	–
	$\phi\beta\beta$ (ϵ_{RL})				
^{136}Xe	$> 4.1 \times 10^{24}$	[150]	–	–	–

TABLE 1.4: Comparison of the results obtained with different double-β decay isotopes (first column) in the search for Majorons-involving decays. The lower limits on the half-life obtained by the different experiments are reported in the second column. The upper limits on the neutrino-Majoron coupling constant, reported in the last column, have been recalculated in this work. The free-nucleon value of the axial vector coupling constant $g_A = 1.27$ has been assumed, the phase space factors have been taken from [148], the range of NMEs for the spectral index $n = 1$ from [153] and references therein, and the NMEs for the spectral index $n = 3$ and $n = 7$ from [149]. The used values of the phase space factors and NMEs are also reported in the fourth and fifth columns, respectively. The results for ^{76}Ge were obtained in this dissertation. We refer to chapter 8 for more details on these results.

The search for light exotic fermions in double-β decays was one of the subjects of this dissertation work. More details on the considered models, the predicted energy distributions, and the projected sensitivity of double-β decay experiments will be provided in the dedicated chapter 3. A first experimental search of these decays was also performed in the context of this dissertation with GERDA Phase II data. The results will be discussed in chapter 8.

1.6 Violation of fundamental symmetries

1.6.1 Lorentz violation

Lorentz invariance is one of the fundamental symmetries of the SM of particle physics. The breakdown of Lorentz and CPT symmetries at the Plank scale is an interesting feature of many theories of quantum gravity, such as string theory [161]. Despite direct studies of physics at this energy scale remaining inaccessible for current experiments, some suppressed effects could arise at lower energies and be potentially observed with the actual experimental technologies.

The general framework that characterizes Lorentz violation in the SM is the Standard Model Extension (SME) [162, 163]. This is an effective quantum field theory that includes all possible operators that can be constructed with the SM fields and that introduce Lorentz violation but preserve the SM gauge invariance. The development of the SME has led to experimental searches for Lorentz violation in all different sectors of physics, including matter, photon, neutrino, and gravity [164, 165]. A data table of the current constraints is compiled every year in [166].

The behavior of neutrinos in the presence of Lorentz and CPT violation has been extensively studied using the SME framework and the related coefficients have been classified [167–169]. Most of these coefficients can be studied using neutrino oscillations, and the most stringent constraints have been set by oscillation experiments. However, there exist four coefficients that only affect the neutrino phase space and escape detection through the measurement of neutrino oscillations. The corresponding operators are an example of *counter-shaded* Lorentz-violating operators: their effect could be relatively large compared to the suppression given by the Plank scale, and, nonetheless, they could have escaped detection to date [164]. These coefficients can be studied in weak decays, such as single-β decay or double-β decay [170, 171].

Lorentz violation affects the two anti-neutrinos emitted in double-β decay that appear with an effective 4-momentum. Since double-β decay experiments do not measure the two anti-neutrinos, after integration over all possible directions, only the isotropic coefficient ($\mathring{a}^{(3)}_{\mathrm{of}}$) alters the neutrino phase space $d^3q = 4\pi\,\omega^2\,d\omega$, which takes the form:

$$d^3q = 4\pi\,(\omega^2 + 2\omega\mathring{a}^{(3)}_{\mathrm{of}})\,d\omega\ . \tag{1.17}$$

Consequently, the double-β decay rate is affected. If the parameter $\mathring{a}^{(3)}_{\mathrm{of}}$ is very small, the rate of double-β decay in the SME can be written as the sum of the SM decay rate

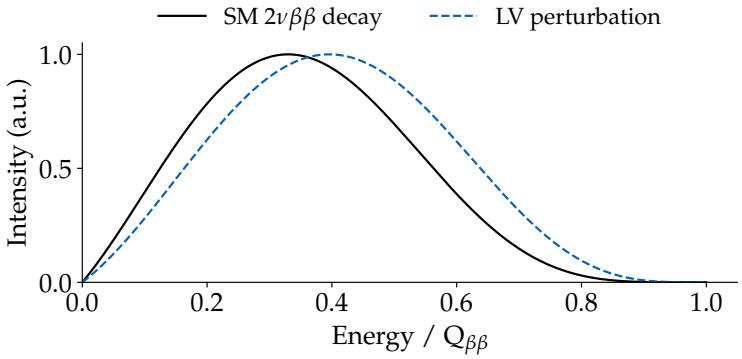

FIGURE 1.7: Summed electron energy distribution of the $2\nu\beta\beta$ decay in the SM and the perturbation term introduced by Lorentz violation (LV). An arbitrary normalization is used for illustrative purposes.

(Γ_{SM}) and a perturbation term ($\delta\Gamma_{LV}$), due to the introduction of Lorentz violation in the phase space of the two anti-neutrinos:

$$\Gamma^{2\nu}_{SME} = \Gamma_{SM} + \delta\Gamma_{LV} \tag{1.18}$$

The perturbation term $\delta\Gamma_{LV}$ contains the coefficient $\mathring{a}^{(3)}_{\text{of}}$, which regulates the strength of Lorentz violation. In fact, the perturbation term only differs from the SM term in the phase space, *i.e.* Lorentz violation only affects the kinematics of the $2\nu\beta\beta$ decay. The energy dependency in the phase space of the perturbation term can be approximated as $\mathcal{G} \sim (Q_{\beta\beta} - E)^4$. Using the same terminology introduced for the Majoron, the spectral index of this perturbation is $n = 4$. On the other hand, the spectral index of the SM term is $n = 5$. Therefore, a non-zero value of the coefficient $\mathring{a}^{(3)}_{\text{of}}$, which implies a non-zero contribution of the perturbation term, produces a distortion of the spectrum of double-β decays compared to the SM expectation. The energy distribution of the Lorentz violating perturbation term is shown in figure 1.7 compared to the SM $2\nu\beta\beta$ decay distribution.

The proposal to search for Lorentz violation in double-β decays came only in 2014 by J. Díaz [171]. Since then, several double-β decay experiments have searched for distortions of the summed electron energy spectrum due to Lorentz violation. The results are summarized in table 1.5. The search for Lorentz violation in the double-β decay of ^{76}Ge was performed for the first time in the context of this dissertation work with GERDA Phase II data. The results will be discussed in chapter 8.

Stringent limits on the counter-shaded Lorentz and CPT violation can be set with β decay experiments. In [170], a constraint on $\mathring{a}^{(3)}_{\text{of}}$ was derived using tritium β decay published data from the Mainz and Troitsk experiments, at the level of 10^{-8} GeV. With the same method, the KATRIN experiment has recently obtained a new limit, using data collected during the first measurement campaign: $|\mathring{a}^{(3)}_{\text{of}}| < 3.0 \cdot 10^{-8}$ GeV at 90% C.L. [172]. This limit is expected to further improve up to a sensitivity of 10^{-9} GeV or more with the full KATRIN exporsure [173].

Isotope	Limits on $\mathring{a}_{\text{of}}^{(3)}$ (GeV) at 90% C.L.	Ref.
^{76}Ge	$(-2.7 < \mathring{a}_{\text{of}}^{(3)} < 6.2) \cdot 10^{-6}$	*this work*
^{136}Xe	$-2.65 \cdot 10^{-5} < \mathring{a}_{\text{of}}^{(3)} < 7.6 \cdot 10^{-6}$	EXO-200 [174]
^{116}Cd	$\mathring{a}_{\text{of}}^{(3)} < 4.0 \cdot 10^{-6}$	AURORA [72]
^{100}Mo	$(-4.2 < \mathring{a}_{\text{of}}^{(3)} < 3.5) \cdot 10^{-7}$	NEMO-3 [152]
^{82}Se	$\mathring{a}_{\text{of}}^{(3)} < 4.1 \cdot 10^{-6}$	CUPID-0 [175]
^{3}H (β decay)	$\lvert\mathring{a}_{\text{of}}^{(3)}\rvert < 2.0 \cdot 10^{-8}$	Díaz *et al.* [170]
	$\lvert\mathring{a}_{\text{of}}^{(3)}\rvert < 3.0 \cdot 10^{-8}$	KATRIN [172]

TABLE 1.5: Summary of the results obtained by different double-β decay experiments in the search for Lorentz violation. In the last two rows, constraints obtained with tritium β decay are reported. The first was derived in [170] using published results from the Mainz and Troitsk experiments. The second is a recent result of the KATRIN experiment [172]. The result for ^{76}Ge has been obtained in this dissertation work. We refer to chapter 8 for more details about this result.

1.6.2 Violation of Pauli exclusion principle

Neutrinos have many peculiarities among all the known particles. They are the only neutral leptons, which leaves the possibility for neutrinos to be a Majorana particle. In addition, the smallness of the neutrino masses points to a different mass mechanism for neutrinos than their charged partners and implies new physics BSM. Therefore, neutrinos might have substantially different properties compared to the charged leptons.

The Pauli exclusion principle, formulated by its homonym for electrons in 1925 and successively extended to all fermions, has been experimentally confirmed for electrons and nucleons with extremely high precision. From the theoretical point of view, the possibility of formulating a local quantum field theory with violation of the Pauli principle has been discussed [176–178], but also some difficulties have been highlighted [179, 180]. However, due to their unique properties, the violation of the Pauli exclusion principle could first appear in neutrinos.

The change of neutrino statistics from fermionic to bosonic would have substantial cosmological and astrophysical consequences investigated in [181–184]. A more recent analysis of available cosmological data showed that only weak bounds could be obtained on neutrino statistics [185]. With two anti-neutrinos with identical quantum numbers in the final state, double-β decay is a good candidate process to test the violation of the Pauli principle [184, 186]. Qualitative conclusions in [184] on double-β decay ruled out a pure bosonic neutrino, but not the possibility that neutrinos obey non-standard statistics, more general than Bose or Fermi ones [187].

If neutrinos obey a mixed statistic, the neutrino state can be written as a combination of one particle's fermionic and bosonic states. As a consequence, the double-β

decay amplitude can be expressed as the sum of two terms, corresponding respectively to the fermionic (anti-symmetric) and bosonic (symmetric) parts of the two anti-neutrino emissions:

$$A_{2\nu\beta\beta} = cos^2\chi\, A_f + sin^2\chi\, A_b \,. \tag{1.19}$$

In the phase-space integration, the interference between the anti-symmetric and symmetric parts of the amplitude vanishes and the double-β decay rate writes:

$$\Gamma_{2\nu\beta\beta} = cos^4\chi\, \Gamma_f + sin^4\chi\, \Gamma_b \,, \tag{1.20}$$

where the decay rates Γ_f and Γ_b are proportional to the squared amplitudes $|A_f|^2$ and $|A_b|^2$, respectively, for pure fermionic and pure bosonic neutrinos. In the decay rates for pure fermionic and pure bosonic neutrinos, both the kinematic terms and the NME are different. Defining the ratio

$$r_0 = \Gamma_b/\Gamma_f \,, \tag{1.21}$$

the normalized differential decay rate can be written as

$$\frac{d\Gamma_{tot}}{\Gamma_{tot}} = \frac{cos^4\chi}{cos^4\chi + sin^4\chi\, r_0}\frac{d\Gamma_f}{\Gamma_f} + \frac{sin^4\chi\, r_0}{cos^4\chi + sin^4\chi\, r_0}\frac{d\Gamma_b}{\Gamma_b} \,. \tag{1.22}$$

The ratio r_0 determines the weight with which the bosonic component enters the total rate and the differential decay distribution. If r_0 is very small, a substantial modification of the energy distribution is expected only for $sin^2\chi$ being very close to 1. In addition, the ratio r_0 needs to be calculated and depends on the values of the NMEs. Thus, it introduces an uncertainty due to the nuclear-structure calculations.

On the other hand, the normalized differential decay rate for pure fermionic $d\Gamma_f/\Gamma_f$ and pure bosonic $d\Gamma_b/\Gamma_b$ neutrinos do not depend on any nuclear model assumption. They are shown in figure 1.8. The spectrum for bosonic neutrinos is softer, with the maximum shifted at lower energy by a factor of about 15%, compared to the pure fermionic spectrum.

The calculations performed in [186] predicted the ratio r_0 for ^{100}Mo and ^{76}Ge to be 0.076 and 0.0014, respectively. The small ratio predicted for ^{76}Ge limits the sensitivity of double-β decay experiments with ^{76}Ge to spectral distortions due to a partly bosonic neutrino. The NEMO-3 experiment searched for an admixture of fermionic and bosonic neutrinos using the $2\nu\beta\beta$ decay spectrum of ^{100}Mo [152]. They obtained an upper limit on the bosonic neutrino contribution $sin^2\chi < 0.27$ at 90% C.L..

Experimental searches for bosonic or partly bosonic neutrinos with double-β decay experiments could use not only the shape of the distributions but also the ratios between the rates of the transitions to the excited states and the ground states if the first were observed [186].

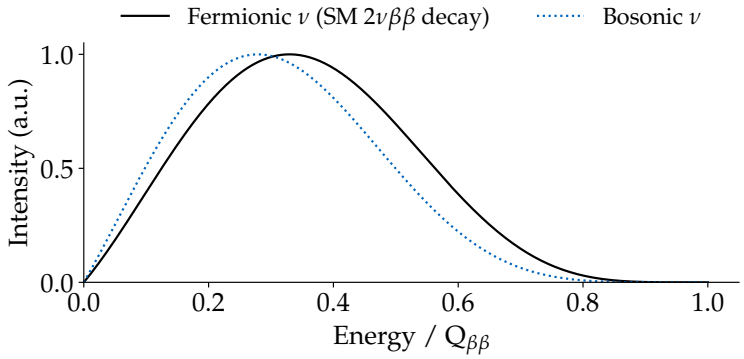

FIGURE 1.8: Summed electron energy distribution of the $2\nu\beta\beta$ decay for pure bosonic neutrinos compared to the case of pure fermionic neutrinos (SM $2\nu\beta\beta$ decay). An arbitrary normalization is used for illustrative purposes.

1.7 Non-standard interaction

1.7.1 Right-handed leptonic currrents

In the SM, the $2\nu\beta\beta$ decay is a second-order transition through the V-A interaction with the strength given by the Fermi constant (G_F). Some BSM theories, such as Left-Right symmetric models with unbroken lepton number [87, 188], predict the existence of V+A lepton current, which could be involved in double-β decays as well [189]. The new physics effects can be modeled through effective charged current operators containing V+A lepton currents. The strength of these exotic interactions is given by $\epsilon_{XR}\, G_F$, where the small dimensionless coupling ϵ_{XR} encapsulates the new physics effects.

Right-handed current interactions are independent of the Majorana or Dirac nature of neutrinos and do not necessarily violate the lepton number. If the neutrino is a Majorana particle, the operators associated with ϵ_{LR} and ϵ_{RR} violate the total lepton number by two units and give rise to extra contributions to the $0\nu\beta\beta$ decay [190]. In this case, $0\nu\beta\beta$ decay searches set stringent limits of the order $\epsilon_{LR} \lesssim 3 \times 10^{-9}$, $\epsilon_{RR} \lesssim 6 \times 10^{-7}$ [83]. On the other hand, if there exists a sterile neutrino state ν_R that combines with ν_L to form a Dirac neutrino, the right-handed current interactions do not necessarily violate lepton number [188]. The strong theoretical interest is therefore supported by the fact that their observation, along with the non-observation of lepton number violation, would indicate that neutrinos are Dirac fermions.

Direct experimental constraints on these operators are set by neutrons and different single-β decays but are rather feeble ($\epsilon_{LR}, \epsilon_{RR} \lesssim 6 \times 10^{-2}$) [191]. Searches at the Large Hadron Collider (LHC) are also possible [192–194] but are generally model dependent and require some caveat on the use of the effective operator analysis at high energies.

In the presence of exotic right-handed leptonic current in the theory, the amplitude of the $2\nu\beta\beta$ decay would be calculated as a coherent sum of the three Feynman

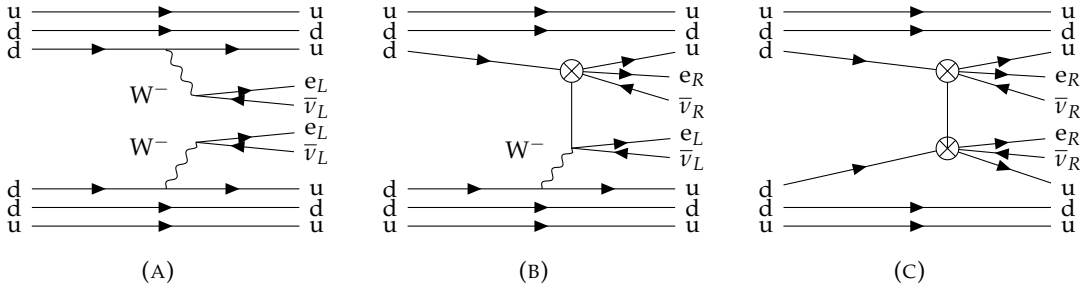

FIGURE 1.9: Feynman diagrams of the double-β decay (A) with two left-handed currents, *i.e.* the SM $2\nu\beta\beta$ decay, (B) with one exotic right-handed current, and (C) with two exotic right-handed currents. Adapted from [189].

diagrams shown in figure 1.9: the SM second-order transition with two left-handed interactions with strength given by G_F^2 (figure 1.9a), a transition involving one exotic right-handed interaction with strength $\epsilon_{XR}\, G_F^2$ (figure 1.9b), and a second-order transition with two exotic right-handed interactions with strength $\epsilon_{XR}^2\, G_F^2$ (figure 1.9c). To the lowest order in the exotic coupling, the dominant contributions to the decay rate are from the first and second diagrams. In contrast, any interference term between the SM contribution and the exotic diagrams is helicity suppressed by the tiny neutrino mass, thus negligible. Contributions to the second-order in the exotic coupling are even more strongly suppressed by the tiny neutrino mass, thus also negligible [189].

The decay rate can be expressed as the incoherent sum:

$$\Gamma^{2\nu} = \Gamma_{SM} + \epsilon_{XR}^2\, \Gamma_\epsilon \ , \tag{1.23}$$

where the first term is the SM decay rate and the second term is the contribution of right-handed current to the decay rate, suppressed by the coupling ϵ_{XR}. Both the phase-space factor and the NME differ in the SM decay rate and the exotic contribution. Thus, the presence of right-handed currents in double-β decay changes both the total decay rate and the shape of the energy spectrum. Nevertheless, given the uncertainties in the NME calculations, the change in the total decay rate is not expected to be measurable. Instead, experiments may be sensitive to the change in the spectral shape. Figure 1.10 shows the $2\nu\beta\beta$ decay distribution in the SM compared to the distribution arising from the presence of right-handed currents. The deviation includes a spectrum shift to smaller energy and a flatter profile near $Q_{\beta\beta}$.

1.7.2 Neutrino self-interaction

The Hubble tension indicates the discrepancy between Cosmic Microwave Background (CMB) and the local measurement of the Hubble constant. This tension has grown to about 4σ, and if confirmed, it would require new physics BSM or a new cosmological model [195, 196].

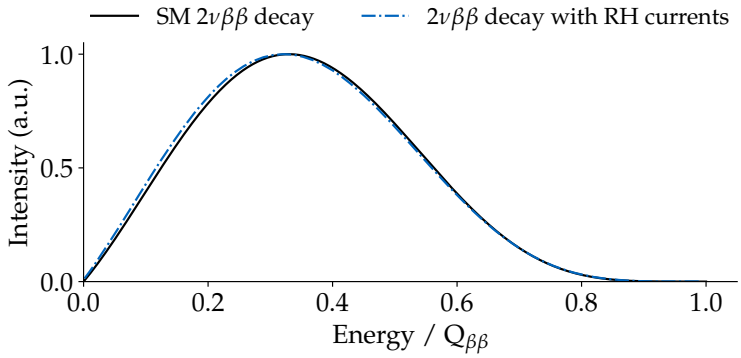

FIGURE 1.10: Summed electron energy distribution of the $2\nu\beta\beta$ decay in the presence of right-handed lepton currents compared to the SM $2\nu\beta\beta$ decay (left-handed lepton currents). An arbitrary normalization is used for illustrative purposes. Adapted from [189].

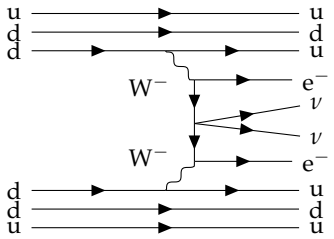

FIGURE 1.11: Feynman diagram of the double-β decay induced by νSI. Adapted from [202].

Introducing a neutrino self-interaction (νSI), *i.e.* a four-neutrino contact interaction, could resolve the Hubble tension. Such a νSI interaction can be written as $G_S(\nu\nu)(\nu\nu)$, and it would inhibit neutrino free-streaming in the early Universe if its strength is much larger than the Fermi effective interaction predicted by the SM, $G_S \sim 10^9\, G_F$ [197, 198]. This new strong interaction would indicate the presence of new physics at a scale $1/\sqrt{G_S} \sim 10\,\text{MeV} - 1\,\text{GeV}$. In general, such strong νSI interactions are difficult to probe in laboratory experiments due to the absence of electrons or quarks involved. With some assumptions on the origin of the νSI operator, constraints can be obtained from different physics observations [199, 200], while no model-independent constraint is currently available. The study of νSI in single-β decays has been considered [201]. More recently, the search for νSI in double-β decays has also been proposed [202].

In the presence of νSI, independently of the Dirac/Majorana nature of neutrinos, the two neutrinos in double-β decay can be emitted via the corresponding effective operator, resulting in a νSI-induced $2\nu\beta\beta$ ($2\nu\text{SI}\beta\beta$) decay. The Feynman diagram of this process is shown in figure 1.11. The final state of the $2\nu\text{SI}\beta\beta$ decay is identical to that of the SM $2\nu\beta\beta$ decay. The contribution from νSI to the decay rate can be written as:

$$\Gamma_{\nu SI} = \frac{G_S^2 m_e^2}{4R^2}\, \mathcal{G}_{\nu SI}\, |\mathcal{M}_{0\nu}|^2 \,, \tag{1.24}$$

where m_e denotes the electron mass and R the radius of the nucleus. For an exact

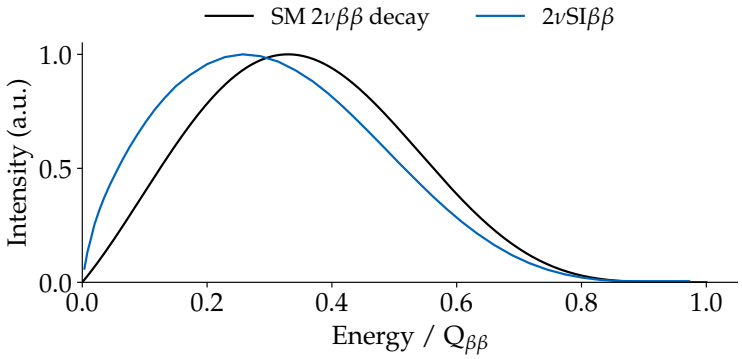

FIGURE 1.12: Summed electron energy distribution of 2νSI$\beta\beta$ decay where the νSI operator is generated by an s-channel mediator with a mass of $M = Q_{\beta\beta} + 0.1m_e$, compared to the SM $2\nu\beta\beta$ decay. An arbitrary normalization is used for illustrative purposes. Adapted from [202].

contact interaction of four neutrinos and neglecting the final state lepton momenta, the phase-space factor for the 2νSI$\beta\beta$ decay is related to the phase-space factor of the $2\nu\beta\beta$ decay as $\mathcal{G}_{\nu SI} = \mathcal{G}_{2\nu}/(4\pi)^2$. The NME of 2νSI$\beta\beta$ is the same as of $0\nu\beta\beta$. In this scenario, no difference is expected in the summed electron energy distribution of the 2νSI$\beta\beta$ decay compared to the SM $2\nu\beta\beta$ decay. Therefore, only the experimental measurements of the $2\nu\beta\beta$ decay rate can be used to constrain the contribution of νSI.

This approach was used in [202] to determine upper limits on the coupling G_S from the measured $2\nu\beta\beta$ decay rates of several double-β decay isotopes. Limits in the range $G_S/G_F \lesssim (0.32 - 2.50) \times 10^9$ were obtained. The sensitivity on G_S is limited by the uncertainty of the NME ratio $|\mathcal{M}_{0\nu}|/|\mathcal{M}_{2\nu}|$. Cosmological data favoured a strong interactive regime with $G_S = 3.83 \times 10^9 G_F$. Even including the theoretical NME uncertainties, all the considered isotopes can fully exclude the strongly interacting cosmologically favored regime [202]. However, one should note that this bound applies only under the assumption that two electron neutrinos are involved in the νSI. This might not be the case if only muon neutrinos and tau neutrinos participate in νSI.

Possible distortions of the electron energy distribution could arise from the νSI contribution if the νSI operator were generated by light mediators. In this scenario, the energy dependence of the coupling G_S could cause observable spectral distortions. In [202], the simplest case of an s-channel scalar mediator with a mass just above the kinematic threshold ($M = Q_{\beta\beta} + 0.1m_e$) was discussed. The coupling G_S acquires the following energy dependence

$$G_S = \frac{-M^2}{s - M^2} G_S^0 \,, \tag{1.25}$$

where M is the mediator mass and $s \equiv p^2$, with p being the momentum of the mediator (in the context of the 2νSI$\beta\beta$, this is of the order $s \lesssim Q_{\beta\beta}^2$). The value

of G_S at zero momentum transferred (G_S^0) is denoted as $G_S^0 = g^2/M^2$, with g the coupling between the mediator and the neutrino. Using G_S in equation 1.25, the differential decay rate of the $2\nu\text{SI}\beta\beta$ decay can be calculated. The corresponding summed electron energy distribution is shown in figure 1.12, for a mass of the mediator $M = Q_{\beta\beta} + 0.1m_e$. The energy spectrum of the $2\nu\text{SI}\beta\beta$ decay is shifted at lower energy compared to the $2\nu\beta\beta$ decay spectrum. This shift can be understood qualitatively: with the summed energy of the two electrons increasing, the energy available for the neutrinos is smaller, leading to a smaller value of s and hence a smaller value of G_S.

References

[1] W. Pauli. "Pauli letter collection: letter to Lise Meitner". 1930. URL: http://cds.cern.ch/record/83282.

[2] J. Chadwick. "Possible Existence of a Neutron". In: *Nature* 129 (1932), p. 312. DOI: 10.1038/129312a0.

[3] C. L. Cowan et al. "Detection of the free neutrino: A Confirmation". In: *Science* 124 (1956), pp. 103–104. DOI: 10.1126/science.124.3212.103.

[4] F. Reines and C. L. Cowan. "The neutrino". In: *Nature* 178 (1956), pp. 446–449. DOI: 10.1038/178446a0.

[5] J. Csikai. "Photographic evidence for the existence of the neutrino". In: *Il Nuovo Cimento (1955-1965)* 5.4 (1957). DOI: 10.1007/BF02903226.

[6] G. Danby et al. "Observation of High-Energy Neutrino Reactions and the Existence of Two Kinds of Neutrinos". In: *Phys. Rev. Lett.* 9 (1962), pp. 36–44. DOI: 10.1103/PhysRevLett.9.36.

[7] Particle Data Group, R.L. Workman, et al. "Review of Particle Physics". In: *PTEP* 2022 (2022), p. 083C01. DOI: 10.1093/ptep/ptac097.

[8] ALEPH Collaboration, D. Decamp, et al. "A Precise Determination of the Number of Families With Light Neutrinos and of the Z Boson Partial Widths". In: *Phys. Lett. B* 235 (1990), pp. 399–411. DOI: 10.1016/0370-2693(90)91984-J.

[9] DELPHI Collaboration, P. Aarnio, et al. "Measurement of the Mass and Width of the Z^0 Particle from Multi - Hadronic Final States Produced in e^+e^- Annihilations". In: *Phys. Lett. B* 231 (1989), pp. 539–547. DOI: 10.1016/0370-2693(89)90706-5.

[10] L3 Collaboration, B. Adeva, et al. "A Determination of the Properties of the Neutral Intermediate Vector Boson Z^0". In: *Phys. Lett. B* 231 (1989), p. 509. DOI: 10.1016/0370-2693(89)90703-X.

[11] OPAL Collaboration, M. Z. Akrawy, et al. "Measurement of the Z^0 Mass and Width with the OPAL Detector at LEP". In: *Phys. Lett. B* 231 (1989), pp. 530–538. DOI: 10.1016/0370-2693(89)90705-3.

[12] DONUT Collaboration, K. Kodama, et al. "Observation of tau neutrino interactions". In: *Phys. Lett. B* 504 (2001), pp. 218–224. DOI: 10.1016/S0370-2693(01)00307-0. arXiv: hep-ex/0012035.

[13] B. Pontecorvo. "Mesonium and anti-mesonium". In: *Sov. Phys. JETP* 6 (1957), p. 429.

[14] B. Pontecorvo. "Inverse beta processes and nonconservation of lepton charge". In: *Zh. Eksp. Teor. Fiz.* 34 (1957), p. 247.

[15] Z. Maki, M. Nakagawa, and S. Sakata. "Remarks on the unified model of elementary particles". In: *Prog. Theor. Phys.* 28 (1962), pp. 870–880. DOI: 10.1143/PTP.28.870.

[16] B. Pontecorvo. "Neutrino Experiments and the Problem of Conservation of Leptonic Charge". In: *Zh. Eksp. Teor. Fiz.* 53 (1967), pp. 1717–1725.

[17] V. N. Gribov and B. Pontecorvo. "Neutrino astronomy and lepton charge". In: *Phys. Lett. B* 28 (1969), p. 493. DOI: 10.1016/0370-2693(69)90525-5.

[18] S. Eliezer and A. R. Swift. "Experimental Consequences of electron Neutrino-Muon-neutrino Mixing in Neutrino Beams". In: *Nucl. Phys. B* 105 (1976), pp. 45–51. DOI: 10.1016/0550-3213(76)90059-6.

[19] H. Fritzsch and P. Minkowski. "Vector-Like Weak Currents, Massive Neutrinos, and Neutrino Beam Oscillations". In: *Phys. Lett. B* 62 (1976), pp. 72–76. DOI: 10.1016/0370-2693(76)90051-4.

[20] S. M. Bilenky and B. Pontecorvo. "Again on Neutrino Oscillations". In: *Lett. Nuovo Cim.* 17 (1976), p. 569. DOI: 10.1007/BF02746567.

[21] R. Davis. "Nobel Lecture: A half-century with solar neutrinos". In: *Rev. Mod. Phys.* 75 (2003), pp. 985–994. DOI: 10.1103/RevModPhys.75.985.

[22] J. N. Bahcall, M. H. Pinsonneault, and S. Basu. "Solar models: Current epoch and time dependences, neutrinos, and helioseismological properties". In: *Astrophys. J.* 555 (2001), pp. 990–1012. DOI: 10.1086/321493. arXiv: astro-ph/0010346.

[23] GALLEX Collaboration, W. Hampel, et al. "GALLEX solar neutrino observations: Results for GALLEX IV". In: *Phys. Lett. B* 447 (1999), pp. 127–133. DOI: 10.1016/S0370-2693(98)01579-2.

[24] B. T. Cleveland et al. "Measurement of the solar electron neutrino flux with the Homestake chlorine detector". In: *Astrophys. J.* 496 (1998), pp. 505–526. DOI: 10.1086/305343.

[25] SAGE Collaboration, J. N. Abdurashitov, et al. "Solar neutrino flux measurements by the Soviet-American Gallium Experiment (SAGE) for half the 22 year solar cycle". In: *J. Exp. Theor. Phys.* 95 (2002), pp. 181–193. DOI: 10.1134/1.1506424. arXiv: astro-ph/0204245.

[26] Super-Kamiokande Collaboration, Y. Fukuda, et al. "Measurement of the solar neutrino energy spectrum using neutrino electron scattering". In: *Phys. Rev. Lett.* 82 (1999), pp. 2430–2434. DOI: 10.1103/PhysRevLett.82.2430. arXiv: hep-ex/9812011.

[27] Kamiokande-II Collaboration, K. S. Hirata, et al. "Experimental Study of the Atmospheric Neutrino Flux". In: *Phys. Lett. B* 205 (1988), p. 416. DOI: 10.1016/0370-2693(88)91690-5.

[28] Kamiokande Collaboration, Y. Fukuda, et al. "Atmospheric ν_μ / ν_e ratio in the multi-GeV energy range". In: *Phys. Lett. B* 335 (1994), pp. 237–245. DOI: 10.1016/0370-2693(94)91420-6.

[29] MACRO Collaboration, S. Ahlen, et al. "Atmospheric neutrino flux measurement using upgoing muons". In: *Phys. Lett. B* 357 (1995), pp. 481–486. DOI: 10.1016/0370-2693(95)00958-N.

[30] MACRO Collaboration, M. Ambrosio, et al. "Measurement of the atmospheric neutrino induced upgoing muon flux using MACRO". In: *Phys. Lett. B* 434 (1998), pp. 451–457. DOI: 10.1016/S0370-2693(98)00885-5. arXiv: hep-ex/9807005.

[31] K. S. Hirata et al. "Observation in the Kamiokande-II Detector of the Neutrino Burst from Supernova SN 1987a". In: *Phys. Rev. D* 38 (1988), pp. 448–458. DOI: 10.1103/PhysRevD.38.448.

[32] IMB Collaboration, T. Haines, et al. "Neutrinos From SN1987a in the IMB Detector". In: *Nucl. Instrum. Meth. A* 264 (1988), pp. 28–31. DOI: 10.1016/0168-9002(88)91097-2.

[33] E. N. Alekseev et al. "Detection of the Neutrino Signal From SN1987A in the LMC Using the INR Baksan Underground Scintillation Telescope". In: *Phys. Lett. B* 205 (1988), pp. 209–214. DOI: 10.1016/0370-2693(88)91651-6.

[34] Super-Kamiokande Collaboration, Y. Fukuda, et al. "Evidence for oscillation of atmospheric neutrinos". In: *Phys. Rev. Lett.* 81 (1998), pp. 1562–1567. DOI: 10.1103/PhysRevLett.81.1562. arXiv: hep-ex/9807003.

[35] SNO Collaboration, B. Aharmim, et al. "Combined Analysis of all Three Phases of Solar Neutrino Data from the Sudbury Neutrino Observatory". In: *Phys. Rev. C* 88 (2013), p. 025501. DOI: 10.1103/PhysRevC.88.025501. arXiv: 1109.0763.

[36] KamLAND Collaboration, A. Gando, et al. "Reactor On-Off Antineutrino Measurement with KamLAND". In: *Phys. Rev. D* 88.3 (2013), p. 033001. DOI: 10.1103/PhysRevD.88.033001. arXiv: 1303.4667.

[37] G. Bellini. "Why and how the Sun and the stars shine". In: *Il Nuovo Saggiatore* 36.5–6 (2020).

[38] Borexino Collaboration, C. Arpesella, et al. "First real time detection of Be-7 solar neutrinos by Borexino". In: *Phys. Lett. B* 658 (2008), pp. 101–108. DOI: 10.1016/j.physletb.2007.09.054. arXiv: 0708.2251.

[39] Borexino Collaboration, G. Bellini, et al. "Precision measurement of the 7Be solar neutrino interaction rate in Borexino". In: *Phys. Rev. Lett.* 107 (2011), p. 141302. DOI: 10.1103/PhysRevLett.107.141302. arXiv: 1104.1816.

[40] Borexino Collaboration, G. Bellini, et al. "First evidence of pep solar neutrinos by direct detection in Borexino". In: *Phys. Rev. Lett.* 108 (2012), p. 051302. DOI: 10.1103/PhysRevLett.108.051302. arXiv: 1110.3230.

[41] Borexino Collaboration, G. Bellini, et al. "Neutrinos from the primary proton–proton fusion process in the Sun". In: *Nature* 512.7515 (2014), pp. 383–386. DOI: 10.1038/nature13702.

[42] Borexino Collaboration, M. Agostini, et al. "First Simultaneous Precision Spectroscopy of *pp*, ^{7}Be, and *pep* Solar Neutrinos with Borexino Phase-II". In: *Phys. Rev. D* 100.8 (2019), p. 082004. DOI: 10.1103/PhysRevD.100.082004. arXiv: 1707.09279.

[43] Borexino Collaboration, M. Agostini, et al. "Comprehensive measurement of *pp*-chain solar neutrinos". In: *Nature* 562.7728 (2018), pp. 505–510. DOI: 10.1038/s41586-018-0624-y.

[44] Borexino Collaboration, M. Agostini, et al. "Experimental evidence of neutrinos produced in the CNO fusion cycle in the Sun". In: *Nature* 587 (2020), pp. 577–582. DOI: 10.1038/s41586-020-2934-0. arXiv: 2006.15115.

[45] T2K Collaboration, K. Abe, et al. "Constraint on the matter-antimatter symmetry-violating phase in neutrino oscillations". In: *Nature* 580.7803 (2020). [Erratum: Nature 583, E16 (2020)], pp. 339–344. DOI: 10.1038/s41586-020-2177-0. arXiv: 1910.03887.

[46] F. Capozzi et al. "Current unknowns in the three neutrino framework". In: *Prog. Part. Nucl. Phys.* 102 (2018), pp. 48–72. DOI: 10.1016/j.ppnp.2018.05.005. arXiv: 1804.09678.

[47] I. Esteban et al. "The fate of hints: updated global analysis of three-flavor neutrino oscillations". In: *JHEP* 09 (2020), p. 178. DOI: 10.1007/JHEP09(2020)178. arXiv: 2007.14792.

[48] P. F. de Salas et al. "2020 global reassessment of the neutrino oscillation picture". In: *JHEP* 02 (2021), p. 071. DOI: 10.1007/JHEP02(2021)071. arXiv: 2006.11237.

[49] E. Fermi. "Versuch einer Theorie der β-Strahlen. I". In: *Z. Phys.* 88 (1934), pp. 161–177. DOI: 10.1007/BF01351864.

[50] E. Fermi. "Tentativo di una Teoria Dei Raggi β". In: *Nuovo Cim.* 11 (1934), pp. 1–19. DOI: 10.1007/BF02959820.

[51] F. Perrin. "Possibilité démission de particules neutres de masse intrinsèque nulle dans les radioactivités beta". In: *Comptes-Rendus* 197 (1933).

[52] F. Perrin. "La dissymétrie des spectres beta positifs et négatifs et la masse intrinsèque du neutrino ou ergon". In: *Comptes-Rendus* 198 (1934).

[53] S. C. Curran, J. Angus, and A. L. Cockroft. "Beta Spectrum of Tritium". In: *Nature* 162.4112 (1948).

[54] S. C. Curran, J. Angus, and A. L. Cockroft. "The Beta-Spectrum of Tritium". In: *Phys. Rev.* 76 (1949), pp. 853–854. DOI: 10.1103/PhysRev.76.853.

[55] G. C. Hanna and B. Pontecorvo. "The β-Spectrum of H^3". In: *Phys. Rev.* 75 (6 1949), pp. 983–984. DOI: 10.1103/PhysRev.75.983.3.

[56] Ch. Kraus et al. "Final results from phase II of the Mainz neutrino mass search in tritium beta decay". In: *Eur. Phys. J. C* 40 (2005), pp. 447–468. DOI: 10.1140/epjc/s2005-02139-7. arXiv: hep-ex/0412056.

[57] Troitsk Collaboration, V. N. Aseev, et al. "An upper limit on electron antineutrino mass from Troitsk experiment". In: *Phys. Rev. D* 84 (2011), p. 112003. DOI: 10.1103/PhysRevD.84.112003. arXiv: 1108.5034.

[58] KATRIN Collaboration, M. Aker, et al. "Direct neutrino-mass measurement with sub-electronvolt sensitivity". In: *Nature Phys.* 18.2 (2022), pp. 160–166. DOI: 10.1038/s41567-021-01463-1. arXiv: 2105.08533.

[59] C. Hassel et al. "Recent Results for the ECHo Experiment". In: *J. Low Temp. Phys.* 184.3-4 (2016), pp. 910–921. DOI: 10.1007/s10909-016-1541-9.

[60] M. Faverzani et al. "Status of the HOLMES Experiment". In: *J. Low Temp. Phys.* 199.3-4 (2020), pp. 1098–1106. DOI: 10.1007/s10909-020-02385-7.

[61] Project 8 Collaboration, A. A. Esfahani, et al. "The Project 8 Neutrino Mass Experiment". Contribution to Snowmass Summer Study. 2022. arXiv: 2203.07349.

[62] E. Majorana. "Teoria simmetrica dell'elettrone e del positrone". In: *Nuovo Cim.* 14 (1937), pp. 171–184. DOI: 10.1007/BF02961314.

[63] C. F. V. Weizsacker. "Zur Theorie der Kernmassen". In: *Z. Phys.* 96 (1935), pp. 431–458. DOI: 10.1007/BF01337700.

[64] M. Goeppert-Mayer. "Double beta-disintegration". In: *Phys. Rev.* 48 (1935), pp. 512–516. DOI: 10.1103/PhysRev.48.512.

[65] M. G. Inghram and J. H. Reynolds. "Double beta-decay of ^{130}Te". In: *Phys. Rev.* 78 (1950), pp. 822–823. DOI: 10.1103/PhysRev.78.822.2.

[66] S. R. Elliott, A. A. Hahn, and M. K. Moe. "Direct Evidence for Two Neutrino Double Beta Decay in ^{82}Se". In: *Phys. Rev. Lett.* 59 (1987), pp. 2020–2023. DOI: 10.1103/PhysRevLett.59.2020.

[67] A. S. Barabash. "Precise Half-Life Values for Two-Neutrino Double-β Decay: 2020 Review". In: *Universe* 6.10 (2020), p. 159. DOI: 10.3390/universe6100159. arXiv: 2009.14451.

[68] NEMO-3 Collaboration, R. Arnold, et al. "Measurement of the double-beta decay half-life and search for the neutrinoless double-beta decay of ^{48}Ca with the NEMO-3 detector". In: *Phys. Rev. D* 93.11 (2016), p. 112008. DOI: 10.1103/PhysRevD.93.112008. arXiv: 1604.01710.

[69] O. Azzolini et al. "Evidence of Single State Dominance in the Two-Neutrino Double-β Decay of ^{82}Se with CUPID-0". In: *Phys. Rev. Lett.* 123.26 (2019), p. 262501. DOI: 10.1103/PhysRevLett.123.262501. arXiv: 1909.03397.

[70] NEMO-3 Collaboration, J. Argyriades, et al. "Measurement of the two neutrino double beta decay half-life of Zr-96 with the NEMO-3 detector". In: *Nucl. Phys. A* 847 (2010), pp. 168–179. DOI: 10.1016/j.nuclphysa.2010.07.009. arXiv: 0906.2694.

[71] E. Armengaud et al. "Precise measurement of $2\nu\beta\beta$ decay of ^{100}Mo with the CUPID-Mo detection technology". In: *Eur. Phys. J. C* 80.7 (2020), p. 674. DOI: 10.1140/epjc/s10052-020-8203-4. arXiv: 1912.07272.

[72] A. S. Barabash et al. "Final results of the Aurora experiment to study 2β decay of ^{116}Cd with enriched $^{116}CdWO_4$ crystal scintillators". In: *Phys. Rev. D* 98.9 (2018), p. 092007. DOI: 10.1103/PhysRevD.98.092007. arXiv: 1811.06398.

[73] A. P. Meshik et al. "^{130}Te and ^{128}Te double beta decay half-lives". In: *Nucl. Phys. A* 809 (2008), pp. 275–289. DOI: 10.1016/j.nuclphysa.2008.06.010.

[74] CUORE Collaboration, D. Q. Adams, et al. "Measurement of the $2\nu\beta\beta$ Decay Half-Life of ^{130}Te with CUORE". In: *Phys. Rev. Lett.* 126.17 (2021), p. 171801. DOI: 10.1103/PhysRevLett.126.171801. arXiv: 2012.11749.

[75] EXO-200 Collaboration, J. B. Albert, et al. "Improved measurement of the $2\nu\beta\beta$ half-life of ^{136}Xe with the EXO-200 detector". In: *Phys. Rev. C* 89.1 (2014), p. 015502. DOI: 10.1103/PhysRevC.89.015502. arXiv: 1306.6106.

[76] NEMO-3 Collaboration, R. Arnold, et al. "Measurement of the $2\nu\beta\beta$ decay half-life of ^{150}Nd and a search for $0\nu\beta\beta$ decay processes with the full exposure from the NEMO-3 detector". In: *Phys. Rev. D* 94.7 (2016), p. 072003. DOI: 10.1103/PhysRevD.94.072003. arXiv: 1606.08494.

[77] A. L. Turkevich, T. E. Economou, and G. A. Cowan. "Double beta decay of ^{238}U". In: *Phys. Rev. Lett.* 67 (1991), pp. 3211–3214. DOI: 10.1103/PhysRevLett.67.3211.

[78] G. Racah. "Sulla Simmetria Tra Particelle e Antiparticelle". In: *Nuovo Cim.* 14 (1937), pp. 322–328. DOI: 10.1007/BF02961321.

[79] W. H. Furry. "On transition probabilities in double beta-disintegration". In: *Phys. Rev.* 56 (1939), pp. 1184–1193. DOI: 10.1103/PhysRev.56.1184.

[80] J. Schechter and J. W. F. Valle. "Neutrinoless Double beta Decay in SU(2) x U(1) Theories". In: *Phys. Rev. D* 25 (1982), p. 2951. DOI: 10.1103/PhysRevD.25.2951.

[81] H. Pas et al. "Towards a superformula for neutrinoless double beta decay". In: *Phys. Lett. B* 453 (1999), pp. 194–198. DOI: 10.1016/S0370-2693(99)00330-5.

[82] H. Pas et al. "A Superformula for neutrinoless double beta decay II: the short range part". In: *Phys. Lett. B* 498 (2001), pp. 35–39. DOI: 10.1016/S0370-2693(00)01359-9. arXiv: hep-ph/0008182.

[83] F. F. Deppisch, M. Hirsch, and H. Pas. "Neutrinoless Double Beta Decay and Physics Beyond the Standard Model". In: *J. Phys. G* 39 (2012), p. 124007. DOI: 10.1088/0954-3899/39/12/124007. arXiv: 1208.0727.

[84] V. Cirigliano et al. "Neutrinoless double beta decay in chiral effective field theory: lepton number violation at dimension seven". In: *JHEP* 12 (2017), p. 082. DOI: 10.1007/JHEP12(2017)082. arXiv: 1708.09390.

[85] L. Gráf et al. "Short-Range Neutrinoless Double Beta Decay Mechanisms". In: *Phys. Rev. D* 98.9 (2018), p. 095023. DOI: 10.1103/PhysRevD.98.095023. arXiv: 1806.06058.

[86] F. F. Deppisch et al. "Analysis of light neutrino exchange and short-range mechanisms in $0\nu\beta\beta$ decay". In: *Phys. Rev. D* 102.9 (2020), p. 095016. DOI: 10.1103/PhysRevD.102.095016. arXiv: 2009.10119.

[87] J. C. Pati and A. Salam. "Lepton Number as the Fourth Color". In: *Phys. Rev. D* 10 (1974). [Erratum: Phys.Rev.D 11, 703–703 (1975)], pp. 275–289. DOI: 10.1103/PhysRevD.10.275.

[88] R. N. Mohapatra and J. C. Pati. "Left-Right Gauge Symmetry and an Isoconjugate Model of CP Violation". In: *Phys. Rev. D* 11 (1975), pp. 566–571. DOI: 10.1103/PhysRevD.11.566.

[89] R. N. Mohapatra and J. C. Pati. "A Natural Left-Right Symmetry". In: *Phys. Rev. D* 11 (1975), p. 2558. DOI: 10.1103/PhysRevD.11.2558.

[90] G. Senjanovic and R. N. Mohapatra. "Exact Left-Right Symmetry and Spontaneous Violation of Parity". In: *Phys. Rev. D* 12 (1975), p. 1502. DOI: 10.1103/PhysRevD.12.1502.

[91] W. Huang and J. Lopez-Pavon. "On neutrinoless double beta decay in the minimal left-right symmetric model". In: *Eur. Phys. J. C* 74 (2014), p. 2853. DOI: 10.1140/epjc/s10052-014-2853-z. arXiv: 1310.0265.

[92] J. Barea, J. Kotila, and F. Iachello. "Limits on sterile neutrino contributions to neutrinoless double beta decay". In: *Phys. Rev. D* 92 (2015), p. 093001. DOI: 10.1103/PhysRevD.92.093001. arXiv: 1509.01925.

[93] W. Dekens et al. "Sterile neutrinos and neutrinoless double beta decay in effective field theory". In: *JHEP* 06 (2020), p. 097. DOI: 10.1007/JHEP06(2020)097. arXiv: 2002.07182.

[94] G. Li, M. Ramsey-Musolf, and J. C. Vasquez. "Left-Right Symmetry and Leading Contributions to Neutrinoless Double Beta Decay". In: *Phys. Rev. Lett.* 126.15 (2021), p. 151801. DOI: 10.1103/PhysRevLett.126.151801. arXiv: 2009.01257.

[95] P. D. Bolton, F. F. Deppisch, and P. S. Bhupal Dev. "Neutrinoless double beta decay versus other probes of heavy sterile neutrinos". In: *JHEP* 03 (2020), p. 170. DOI: 10.1007/JHEP03(2020)170. arXiv: 1912.03058.

[96] L. Gráf, M. Lindner, and O. Scholer. "Unraveling the $0\nu\beta\beta$ Decay Mechanisms". In: *Phys. Rev. D* 106.3 (2022), p. 035022. DOI: 10.1103/PhysRevD.106.035022. eprint: 2204.10845.

[97] E. der Mateosian and M. Goldhaber. "Limits for lepton-conserving and lepton-nonconserving double beta decay in ^{48}Ca". In: *Phys. Rev.* 146 (1966), pp. 810–815. DOI: 10.1103/PhysRev.146.810.

[98] E. Fiorini et al. "A Search for Lepton Nonconservation in Double Beta Decay With a Germanium Detector". In: *Phys. Lett. B* 25 (1967), pp. 602–603. DOI: 10.1016/0370-2693(67)90127-X.

[99] R. K. Bardin et al. "Double beta decay in ^{48}Ca and the conservation of leptons". In: *Phys. Lett. B* 26 (1967), pp. 112–116. DOI: 10.1016/0370-2693(67)90563-1.

[100] B. T. Cleveland et al. "Lepton Conservation in the Double β Decay of ^{82}Se ". In: *Phys. Rev. Lett.* 35 (1975), pp. 757–760. DOI: 10.1103/PhysRevLett.35.757.

[101] GERDA Collaboration, M. Agostini, et al. "Final Results of GERDA on the Search for Neutrinoless Double-β Decay". In: *Phys. Rev. Lett.* 125.25 (2020), p. 252502. DOI: 10.1103/PhysRevLett.125.252502. arXiv: 2009.06079.

[102] J. Gruszko. "0nbb search in Ge Detectors". Contribution to NEUTRINO2022. URL: https://indico.kps.or.kr/event/30/contributions/866/.

[103] O. Azzolini et al. "Final Result on the Neutrinoless Double Beta Decay of ^{82}Se with CUPID-0". In: *Phys. Rev. Lett.* 129.11 (2022), p. 111801. DOI: 10.1103/PhysRevLett.129.111801. arXiv: 2206.05130.

[104] C. Augier et al. "Final results on the $0\nu\beta\beta$ decay half-life limit of ^{100}Mo from the CUPID-Mo experiment". In: *Eur. Phys. J. C* 82.11 (2022), p. 1033. DOI: 10.1140/epjc/s10052-022-10942-5. arXiv: 2202.08716.

[105] NEMO-3 Collaboration, R. Arnold, et al. "Results of the search for neutrinoless double-β decay in ^{100}Mo with the NEMO-3 experiment". In: *Phys. Rev. D* 92.7 (2015), p. 072011. DOI: 10.1103/PhysRevD.92.072011. arXiv: 1506.05825.

[106] CUORE Collaboration, D. Q. Adams, et al. "Search for Majorana neutrinos exploiting millikelvin cryogenics with CUORE". In: *Nature* 604.7904 (2022), pp. 53–58. DOI: 10.1038/s41586-022-04497-4. arXiv: 2104.06906.

[107] KamLAND-Zen Collaboration, S. Abe, et al. "First Search for the Majorana Nature of Neutrinos in the Inverted Mass Ordering Region with KamLAND-Zen". 2022. arXiv: 2203.02139.

[108] EXO-200 Collaboration, G. Anton, et al. "Search for Neutrinoless Double-β Decay with the Complete EXO-200 Dataset". In: *Phys. Rev. Lett.* 123.16 (2019), p. 161802. DOI: 10.1103/PhysRevLett.123.161802. arXiv: 1906.02723.

[109] LEGEND Collaboration, N. Abgrall, et al. "The Large Enriched Germanium Experiment for Neutrinoless $\beta\beta$ Decay: LEGEND-1000 Preconceptual Design Report". 2021. arXiv: 2107.11462.

[110] A. Zolotarova. "CUPID, CUPID-0, CUPID-Mo". Contribution to NEUTRINO2022. URL: https://indico.kps.or.kr/event/30/contributions/863/.

[111] nEXO Collaboration, G. Adhikari, et al. "nEXO: neutrinoless double beta decay search beyond 10^{28} year half-life sensitivity". In: *J. Phys. G* 49.1 (2022), p. 015104. DOI: 10.1088/1361-6471/ac3631. arXiv: 2106.16243.

[112] XENON Collaboration, E. Aprile, et al. "Observation of two-neutrino double electron capture in ^{124}Xe with XENON1T". In: *Nature* 568.7753 (2019), pp. 532–535. DOI: 10.1038/s41586-019-1124-4. arXiv: 1904.11002.

[113] A. P. Meshik et al. "Weak decay of ^{130}Ba and ^{132}Ba: Geochemical measurements". In: *Phys. Rev. C* 64 (2001), p. 035205. DOI: 10.1103/PhysRevC.64.035205.

[114] S. S. Ratkevich et al. "Comparative study of the double K-shell-vacancy production in single- and double-electron capture decay". In: *Phys. Rev. C* 96.6 (2017), p. 065502. DOI: 10.1103/PhysRevC.96.065502. arXiv: 1707.07171.

[115] R. G. Winter. "Double $\mathcal{K}$ Capture and Single $\mathcal{K}$ Capture with Positron Emission". In: *Phys. Rev.* 100 (1955), pp. 142–144. DOI: 10.1103/PhysRev.100.142.

[116] K. Blaum et al. "Neutrinoless Double-Electron Capture". In: *Rev. Mod. Phys.* 92 (2020), p. 045007. DOI: 10.1103/RevModPhys.92.045007. arXiv: 2007.14908.

[117] H. M. Georgi, S. L. Glashow, and S. Nussinov. "Unconventional Model of Neutrino Masses". In: *Nucl. Phys. B* 193 (1981), pp. 297–316. DOI: 10.1016/0550-3213(81)90336-9.

[118] R. A. Eramzhian, G. Mitselmakher, and M. B. Voloshin. "Conversion of an Atomic Electron Into a Positron and Double β^+ Decay". In: *JETP Lett.* 35 (1982), p. 656.

[119] J. Bernabeu, A. De Rujula, and C. Jarlskog. "Neutrinoless Double Electron Capture as a Tool to Measure the ν_e Mass". In: *Nucl. Phys. B* 223 (1983), pp. 15–28. DOI: 10.1016/0550-3213(83)90089-5.

[120] Z. Sujkowski and S. Wycech. "Neutrinoless double electron capture: A Tool to search for Majorana neutrinos". In: *Phys. Rev. C* 70 (2004), p. 052501. DOI: 10.1103/PhysRevC.70.052501. arXiv: hep-ph/0312040.

[121] F. F. Karpeshin. "On neutrinoless double e capture problem". In: *Phys. Part. Nucl. Lett.* 5 (2008), pp. 379–382. DOI: 10.1134/S1547477108040080.

[122] M. I. Krivoruchenko et al. "Resonance enhancement of neutrinoless double electron capture". In: *Nucl. Phys. A* 859 (2011), pp. 140–171. DOI: 10.1016/j.nuclphysa.2011.04.009. arXiv: 1012.1204.

[123] J. Maalampi and J. T. Suhonen. "Neutrinoless Double β^+/ EC Decays". In: *Adv. High Energy Phys.* 2013 (2013), p. 505874. DOI: 10.1155/2013/505874.

[124] "Live Chart of Nuclides". URL: https://www-nds.iaea.org/relnsd/vcharthtml/VChartHTML.html.

[125] B. J. Mount, M. Redshaw, and E. G. Myers. "Double-β-decay Q values of ^{74}Se and ^{76}Ge". In: *Phys. Rev. C* 81 (2010), p. 032501. DOI: 10.1103/PhysRevC.81.032501.

[126] J. Engel and J. Menéndez. "Status and Future of Nuclear Matrix Elements for Neutrinoless Double-Beta Decay: A Review". In: *Rept. Prog. Phys.* 80.4 (2017), p. 046301. DOI: 10.1088/1361-6633/aa5bc5. arXiv: 1610.06548.

[127] L. Imbert. "The CUPID-Mo experiment". Contribution to MEDEX22. URL: https://indico.utef.cvut.cz/event/32/contributions/553/.

[128] NEMO-3 Collaboration, R. Arnold, et al. "Measurement of double beta decay of ^{150}Nd to the 0^+_1 excited state of ^{150}Sm in NEMO-3". 2022. arXiv: 2203.03356.

[129] A. S. Barabash. "Double beta decay to the excited states: Review". In: *AIP Conf. Proc.* 1894.1 (2017), p. 020002. DOI: 10.1063/1.5007627. arXiv: 1709.06890.

[130] T. Tomoda. "$0^+ \to 2^+$ $0\nu\beta\beta$ decay triggered directly by the Majorana neutrino mass". In: *Phys. Lett. B* 474 (2000), pp. 245–250. DOI: 10.1016/S0370-2693(00)00025-3. arXiv: hep-ph/9909330.

[131] R. Cepedello et al. "Neutrinoless Double-β Decay with Nonstandard Majoron Emission". In: *Phys. Rev. Lett.* 122.18 (2019), p. 181801. DOI: 10.1103/PhysRevLett.122.181801. arXiv: 1811.00031.

[132] Y. Chikashige, R. N. Mohapatra, and R. D. Peccei. "Are There Real Goldstone Bosons Associated with Broken Lepton Number?" In: *Phys. Lett. B* 98 (1981), pp. 265–268. DOI: 10.1016/0370-2693(81)90011-3.

[133] Y. Chikashige, R. N. Mohapatra, and R. D. Peccei. "Spontaneously Broken Lepton Number and Cosmological Constraints on the Neutrino Mass Spectrum". In: *Phys. Rev. Lett.* 45 (1980), p. 1926. DOI: 10.1103/PhysRevLett.45.1926.

[134] G. B. Gelmini and M. Roncadelli. "Left-Handed Neutrino Mass Scale and Spontaneously Broken Lepton Number". In: *Phys. Lett. B* 99 (1981), pp. 411–415. DOI: 10.1016/0370-2693(81)90559-1.

[135] M. Doi, T. Kotani, and E. Takasugi. "The Neutrinoless Double Beta Decay With Majoron Emission". In: *Phys. Rev. D* 37 (1988), p. 2575. DOI: 10.1103/PhysRevD.37.2575.

[136] M. Hirsch et al. "On the observability of majoron emitting double beta decays". In: *Phys. Lett. B* 372 (1996), pp. 8–14. DOI: 10.1016/0370-2693(96)00038-X. arXiv: hep-ph/9511227.

[137] R. N. Mohapatra and E. Takasugi. "Neutrinoless Double Beta Decay With Double Majoron Emission". In: *Phys. Lett. B* 211 (1988), pp. 192–196. DOI: 10.1016/0370-2693(88)90832-5.

[138] S. Schael et al. "Precision electroweak measurements on the Z resonance". In: *Phys. Rept.* 427 (2006), pp. 257–454. DOI: 10.1016/j.physrep.2005.12.006. arXiv: hep-ex/0509008.

[139] S. R. Elliott, A. A. Hahn, and M. K. Moe. "Limit on Neutrinoless Double Beta Decay With Majoron Emission in ^{82}Se". In: *Phys. Rev. Lett.* 59 (1987), pp. 1649–1651. DOI: 10.1103/PhysRevLett.59.1649.

[140] F. T. Avignone et al. "Confirmation of the observation of $2\nu\beta\beta$ decay of ^{76}Ge". In: *Phys. Lett. B* 256 (1991), pp. 559–561. DOI: 10.1016/0370-2693(91)91810-I.

[141] P. Fisher et al. "Limit on Double Beta Decay With Majoron Emission". In: *Phys. Lett. B* 192 (1987), pp. 460–462. DOI: 10.1016/0370-2693(87)90138-9.

[142] Z. G. Berezhiani, A. Yu. Smirnov, and J. W. F. Valle. "Observable Majoron emission in neutrinoless double beta decay". In: *Phys. Lett. B* 291 (1992), pp. 99–105. DOI: 10.1016/0370-2693(92)90126-O. arXiv: hep-ph/9207209.

[143] C. P. Burgess and J. M. Cline. "Majorons without Majorana masses and neutrinoless double beta decay". In: *Phys. Lett. B* 298 (1993), pp. 141–148. DOI: 10.1016/0370-2693(93)91720-8. arXiv: hep-ph/9209299.

[144] C. P. Burgess and J. M. Cline. "A New class of Majoron emitting double beta decays". In: *Phys. Rev. D* 49 (1994), pp. 5925–5944. DOI: 10.1103/PhysRevD.49.5925. arXiv: hep-ph/9307316.

[145] C. D. Carone. "Double beta decay with vector majorons". In: *Phys. Lett. B* 308 (1993), pp. 85–88. DOI: 10.1016/0370-2693(93)90605-H. arXiv: hep-ph/9302290.

[146] R. N. Mohapatra, A. Perez-Lorenzana, and C. A. de S. Pires. "Neutrino mass, bulk Majoron and neutrinoless double beta decay". In: *Phys. Lett. B* 491 (2000), pp. 143–147. DOI: 10.1016/S0370-2693(00)01031-5. arXiv: hep-ph/0008158.

[147] P. Bamert, C. P. Burgess, and R. N. Mohapatra. "Multi-Majoron modes for neutrinoless double beta decay". In: *Nucl. Phys. B* 449 (1995), pp. 25–48. DOI: 10.1016/0550-3213(95)00273-U. arXiv: hep-ph/9412365.

[148] J. Kotila, J. Barea, and F. Iachello. "Phase-space factors and half-life predictions for Majoron-emitting decay". In: *Phys. Rev. C* 91.6 (2015). [Erratum: Phys.Rev.C 92, 029903 (2015)], p. 064310. DOI: 10.1103/PhysRevC.91.064310. arXiv: 1509.05154.

[149] J. Kotila and F. Iachello. "Nuclear matrix elements for Majoron-emitting double-β decay". In: *Phys. Rev. C* 103.4 (2021), p. 044302. DOI: 10.1103/PhysRevC.103.044302. arXiv: 2104.02327.

[150] EXO-200 Collaboration, S. Al Kharusi, et al. "Search for Majoron-emitting modes of ^{136}Xe double beta decay with the complete EXO-200 dataset". In: *Phys. Rev. D* 104.11 (2021), p. 112002. DOI: 10.1103/PhysRevD.104.112002. arXiv: 2109.01327.

[151] KamLAND-Zen Collaboration, A. Gando, et al. "Limits on Majoron-emitting double-β decays of ^{136}Xe in the KamLAND-Zen experiment". In: *Phys. Rev. C* 86 (2012), p. 021601. DOI: 10.1103/PhysRevC.86.021601. arXiv: 1205.6372.

[152] NEMO-3 Collaboration, R. Arnold, et al. "Detailed studies of ^{100}Mo two-neutrino double beta decay in NEMO-3". In: *Eur. Phys. J. C* 79.5 (2019), p. 440. DOI: 10.1140/epjc/s10052-019-6948-4. arXiv: 1903.08084.

[153] M. Agostini et al. "Toward the discovery of matter creation with neutrinoless double-beta decay". 2022. arXiv: 2202.01787.

[154] K. Blum, Y. Nir, and M. Shavit. "Neutrinoless double-beta decay with massive scalar emission". In: *Phys. Lett. B* 785 (2018), pp. 354–361. DOI: 10.1016/j.physletb.2018.08.022. arXiv: 1802.08019.

[155] V. Berezinsky and J. W. F. Valle. "The KeV majoron as a dark matter particle". In: *Phys. Lett. B* 318 (1993), pp. 360–366. DOI: 10.1016/0370-2693(93)90140-D. arXiv: hep-ph/9309214.

[156] T. Brune and H. Päs. "Massive Majorons and constraints on the Majoron-neutrino coupling". In: *Phys. Rev. D* 99.9 (2019), p. 096005. DOI: 10.1103/PhysRevD.99.096005. arXiv: 1808.08158.

[157] R. E. Shrock. "New Tests For, and Bounds On, Neutrino Masses and Lepton Mixing". In: *Phys. Lett. B* 96 (1980), pp. 159–164. DOI: 10.1016/0370-2693(80)90235-X.

[158] A. S. Riis and S. Hannestad. "Detecting sterile neutrinos with KATRIN like experiments". In: *JCAP* 02 (2011), p. 011. DOI: 10.1088/1475-7516/2011/02/011. arXiv: 1008.1495.

[159] S. Mertens et al. "Sensitivity of Next-Generation Tritium Beta-Decay Experiments for keV-Scale Sterile Neutrinos". In: *JCAP* 02 (2015), p. 020. DOI: 10.1088/1475-7516/2015/02/020. arXiv: 1409.0920.

[160] A. Abada, A. Hernández-Cabezudo, and X. Marcano. "Beta and Neutrinoless Double Beta Decays with KeV Sterile Fermions". In: *JHEP* 01 (2019), p. 041. DOI: 10.1007/JHEP01(2019)041. arXiv: 1807.01331.

[161] V. A. Kostelecky and S. Samuel. "Spontaneous Breaking of Lorentz Symmetry in String Theory". In: *Phys. Rev. D* 39 (1989), p. 683. DOI: 10.1103/PhysRevD.39.683.

[162] D. Colladay and V. A. Kostelecky. "CPT violation and the standard model". In: *Phys. Rev. D* 55 (1997), pp. 6760–6774. DOI: 10.1103/PhysRevD.55.6760. arXiv: hep-ph/9703464.

[163] D. Colladay and V. A. Kostelecky. "Lorentz violating extension of the Standard Model". In: *Phys. Rev. D* 58 (1998), p. 116002. DOI: 10.1103/PhysRevD.58.116002. arXiv: hep-ph/9809521.

[164] V. A. Kostelecky and J. D. Tasson. "Prospects for Large Relativity Violations in Matter-Gravity Couplings". In: *Phys. Rev. Lett.* 102 (2009), p. 010402. DOI: 10.1103/PhysRevLett.102.010402. arXiv: 0810.1459.

[165] A. V. Kostelecky and J. D. Tasson. "Matter-gravity couplings and Lorentz violation". In: *Phys. Rev. D* 83 (2011), p. 016013. DOI: 10.1103/PhysRevD.83.016013. arXiv: 1006.4106.

[166] V. A. Kostelecky and N. Russell. "Data Tables for Lorentz and CPT Violation". In: *Rev. Mod. Phys.* 83 (2011), pp. 11–31. DOI: 10.1103/RevModPhys.83.11.

[167] V. A. Kostelecky and M. Mewes. "Lorentz and CPT violation in the neutrino sector". In: *Phys. Rev. D* 70 (2004), p. 031902. DOI: 10.1103/PhysRevD.70.031902. arXiv: hep-ph/0308300.

[168] V. A. Kostelecky and M. Mewes. "Lorentz and CPT violation in neutrinos". In: *Phys. Rev. D* 69 (2004), p. 016005. DOI: 10.1103/PhysRevD.69.016005. arXiv: hep-ph/0309025.

[169] A. Kostelecky and M. Mewes. "Neutrinos with Lorentz-violating operators of arbitrary dimension". In: *Phys. Rev. D* 85 (2012), p. 096005. DOI: 10.1103/PhysRevD.85.096005. arXiv: 1112.6395.

[170] J. S. Díaz, A. Kostelecký, and R. Lehnert. "Relativity violations and beta decay". In: *Phys. Rev. D* 88.7 (2013), p. 071902. DOI: 10.1103/PhysRevD.88.071902. arXiv: 1305.4636.

[171] J. S. Díaz. "Limits on Lorentz and CPT violation from double beta decay". In: *Phys. Rev. D* 89 (2014), p. 036002. DOI: 10.1103/PhysRevD.89.036002. arXiv: 1311.0930.

[172] M. Aker et al. "Search for Lorentz-Invariance Violation with the first KATRIN data". 2022. arXiv: 2207.06326.

[173] Ralf Lehnert. "Beta-decay spectrum and Lorentz violation". In: *Phys. Lett. B* 828 (2022), p. 137017. DOI: 10.1016/j.physletb.2022.137017. arXiv: 2112.13803.

[174] EXO-200 Collaboration, J. B. Albert, et al. "First Search for Lorentz and CPT Violation in Double Beta Decay with EXO-200". In: *Phys. Rev. D* 93.7 (2016), p. 072001. DOI: 10.1103/PhysRevD.93.072001. arXiv: 1601.07266.

[175] CUPID Collaboration, O. Azzolini, et al. "First search for Lorentz violation in double beta decay with scintillating calorimeters". In: *Phys. Rev. D* 100.9 (2019), p. 092002. DOI: 10.1103/PhysRevD.100.092002. arXiv: 1911.02446.

[176] A. Yu. Ignatiev and V. A. Kuzmin. "Is small violation of the Pauli principle possible?" 1987. URL: https://lib-extopc.kek.jp/preprints/PDF/2000/0031/0031952.pdf.

[177] O. W. Greenberg and R. N. Mohapatra. "Local Quantum Field Theory of Violation of the Pauli Principle". In: *Phys. Rev. Lett.* 59 (1987). [Erratum: Phys.Rev.Lett. 61, 1432 (1988)], p. 2507. DOI: 10.1103/PhysRevLett.59.2507.

[178] L. B. Okun. "On the Possibility of Pauli Principle Violation in Atoms". In: *JETP Lett.* 46 (1987), pp. 529–532.

[179] O. W. Greenberg and R. N. Mohapatra. "Difficulties With a Local Quantum Field Theory of Possible Violation of the Pauli Principle". In: *Phys. Rev. Lett.* 62 (1989). [Erratum: Phys.Rev.Lett. 62, 1927 (1989)], p. 712. DOI: 10.1103/PhysRevLett.62.712.

[180] A. B. Govorkov. "Can the Pauli Principle Be Deduced With Local Quantum Field Theory?" In: *Phys. Lett. A* 137 (1989), pp. 7–10. DOI: 10.1016/0375-9601(89)90959-6.

[181] L. Cucurull, J. A. Grifols, and R. Toldra. "Spin statistics theorem, neutrinos, and big bang nucleosynthesis". In: *Astropart. Phys.* 4 (1996), pp. 391–396. DOI: 10.1016/0927-6505(95)00053-4. arXiv: astro-ph/9506040.

[182] S. Choubey and K. Kar. "Possible violation of the spin-statistics relation for neutrinos: Checking through future galactic supernova". In: *Phys. Lett. B* 634 (2006), pp. 14–22. DOI: 10.1016/j.physletb.2006.01.041. arXiv: hep-ph/0510261.

[183] A. D. Dolgov and A. Yu. Smirnov. "Possible violation of the spin-statistics relation for neutrinos: Cosmological and astrophysical consequences". In: *Phys. Lett. B* 621 (2005), pp. 1–10. DOI: 10.1016/j.physletb.2005.06.035. arXiv: hep-ph/0501066.

[184] A. D. Dolgov, Steen H. Hansen, and A. Yu. Smirnov. "Neutrino statistics and Big Bang nucleosynthesis". In: *JCAP* 06 (2005), p. 004. DOI: 10.1088/1475-7516/2005/06/004. arXiv: astro-ph/0503612.

[185] P. F. de Salas et al. "Cosmological bounds on neutrino statistics". In: *JCAP* 03 (2018), p. 050. DOI: 10.1088/1475-7516/2018/03/050. arXiv: 1802.04639.

[186] A. S. Barabash et al. "Statistics of neutrinos and the double beta decay". In: *Nucl. Phys. B* 783 (2007), pp. 90–111. DOI: 10.1016/j.nuclphysb.2007.05.033. arXiv: 0704.2944.

[187] A. Yu. Ignatiev and V. A. Kuzmin. "Neutrino statistics and non-standard commutation relations". In: *Phys. Lett. A* 359 (2006), pp. 26–30. DOI: 10.1016/j.physleta.2006.05.083. arXiv: hep-ph/0510209.

[188] Patrick D. Bolton et al. "Alternative formulation of left-right symmetry with $B - L$ conservation and purely Dirac neutrinos". In: *Phys. Rev. D* 100.3 (2019), p. 035013. DOI: 10.1103/PhysRevD.100.035013. arXiv: 1902.05802.

[189] F. F. Deppisch, L. Gráf, and F. Šimkovic. "Searching for New Physics in Two-Neutrino Double Beta Decay". In: *Phys. Rev. Lett.* 125.17 (2020), p. 171801. DOI: 10.1103/PhysRevLett.125.171801. arXiv: 2003.11836.

[190] M. Doi et al. "DOUBLE BETA DECAY". In: *Prog. Theor. Phys.* 69 (1983), p. 602. DOI: 10.1143/PTP.69.602.

[191] M. González-Alonso, O. Naviliat-Cuncic, and N. Severijns. "New physics searches in nuclear and neutron β decay". In: *Prog. Part. Nucl. Phys.* 104 (2019), pp. 165–223. DOI: 10.1016/j.ppnp.2018.08.002. arXiv: 1803.08732.

[192] A. Greljo and D. Marzocca. "High-p_T dilepton tails and flavor physics". In: *Eur. Phys. J. C* 77.8 (2017), p. 548. DOI: 10.1140/epjc/s10052-017-5119-8. arXiv: 1704.09015.

[193] CMS Collaboration, V. Khachatryan, et al. "Search for physics beyond the standard model in final states with a lepton and missing transverse energy in proton-proton collisions at $\sqrt{s} = 8$ TeV". In: *Phys. Rev. D* 91.9 (2015), p. 092005. DOI: 10.1103/PhysRevD.91.092005. arXiv: 1408.2745.

[194] ATLAS Collaboration, M. Aaboud, et al. "Search for heavy Majorana or Dirac neutrinos and right-handed W gauge bosons in final states with two charged leptons and two jets at $\sqrt{s} = 13$ TeV with the ATLAS detector". In: *JHEP* 01 (2019), p. 016. DOI: 10.1007/JHEP01(2019)016. arXiv: 1809.11105.

[195] A. G. Riess et al. "Large Magellanic Cloud Cepheid Standards Provide a 1% Foundation for the Determination of the Hubble Constant and Stronger Evidence for Physics beyond ΛCDM". In: *Astrophys. J.* 876.1 (2019), p. 85. DOI: 10.3847/1538-4357/ab1422. arXiv: 1903.07603.

[196] Planck Collaboration, N. Aghanim, et al. "Planck 2018 results. VI. Cosmological parameters". In: *Astron. Astrophys.* 641 (2020). [Erratum: Astron.Astrophys. 652, C4 (2021)], A6. DOI: 10.1051/0004-6361/201833910. arXiv: 1807.06209.

[197] I. M. Oldengott et al. "Interacting neutrinos in cosmology: exact description and constraints". In: *JCAP* 11 (2017), p. 027. DOI: 10.1088/1475-7516/2017/11/027. arXiv: 1706.02123.

[198] C. D. Kreisch, F. Cyr-Racine, and O. Doré. "Neutrino puzzle: Anomalies, interactions, and cosmological tensions". In: *Phys. Rev. D* 101.12 (2020), p. 123505. DOI: 10.1103/PhysRevD.101.123505. arXiv: 1902.00534.

[199] N. Blinov et al. "Constraining the Self-Interacting Neutrino Interpretation of the Hubble Tension". In: *Phys. Rev. Lett.* 123.19 (2019), p. 191102. DOI: 10.1103/PhysRevLett.123.191102. arXiv: 1905.02727.

[200] Kun-Feng Lyu, Emmanuel Stamou, and Lian-Tao Wang. "Self-interacting neutrinos: Solution to Hubble tension versus experimental constraints". In: *Phys. Rev. D* 103.1 (2021), p. 015004. DOI: 10.1103/PhysRevD.103.015004. arXiv: 2004.10868.

[201] G. Arcadi et al. "Tritium beta decay with additional emission of new light bosons". In: *JHEP* 01 (2019), p. 206. DOI: 10.1007/JHEP01(2019)206. arXiv: 1811.03530.

[202] F. F. Deppisch et al. "Neutrino Self-Interactions and Double Beta Decay". In: *Phys. Rev. D* 102.5 (2020), p. 051701. DOI: 10.1103/PhysRevD.102.051701. arXiv: 2004.11919.

Chapter 2

Double-β decay experiments

The hunt for $0\nu\beta\beta$ decay has led, in the past, to a vast experimental program using different isotopes and diverse detection techniques, which converged, today, on a few future ton-scale experiments. The challenge of identifying a single $0\nu\beta\beta$ decay signal in thousands of moles of material defines the main experimental requirements.

2.1 Experimental requirements

2.1.1 Double-β isotopes

Double-β decay can appear in nature in 35 different isotopes. However, not all of them are suitable for experimental searches. The criteria that drive the isotope choice are a high $Q_{\beta\beta}$, the isotopic abundance (together with the feasibility of enrichment), and compatibility with an appropriate detection technique. Nine isotopes have been used in double-β decay experiments, all with a $Q_{\beta\beta}$ above 2 MeV, listed in table 2.1.

A high $Q_{\beta\beta}$ is essential because it influences the phase space and background level. The phase space, which determines the $0\nu\beta\beta$ decay rate, scales approximately as $Q^5_{\beta\beta}$ for light neutrino exchange [11].[1] On the other hand, at high energy, the background induced by natural radioactivity, *i.e.* the decays of primordial elements

[1] The phase space scales as $Q^7_{\beta\beta}$ for exchange mechanisms other than light neutrino exchange. [11]

Isotope	Natural abundance (%)	$Q_{\beta\beta}$ (keV)
^{48}Ca	0.187	4267.98 [1]
^{76}Ge	7.8	2039.061 [2]
^{82}Se	8.7	2997.9 [3]
^{96}Zr	2.8	3355.9 [4]
^{100}Mo	9.8	3034.36 [5]
^{116}Cd	7.5	2813.49 [6]
^{130}Te	34.08	2527.52 [7]
^{136}Xe	8.9	2457.8 [8]
^{150}Nd	5.6	3371.38 [9]

TABLE 2.1: Key features of double-β decay isotopes used in experiments. The natural isotopic abundances are taken from [10].

in the ^{238}U and ^{232}Th decay chains which are unavoidably present in all materials, is strongly reduced. β radiation mostly concentrates below 2 MeV, except for ^{214}Bi, whose β-decay endpoint lies at 3.3 MeV. γ radiation extends up to the highest ^{208}Tl line at 2.6 MeV. α radiation extends to higher energies, up to 7 – 8 MeV.

The isotopic abundance of all the elements listed in table 2.1 lies in the few percent range, with the positive exception of ^{130}Te ($\sim$ 34%) and the negative exception of ^{48}Ca ($\sim$ 0.2%). While it was demonstrated that a ton-scale experiment is possible with the natural abundance of ^{130}Te [12], isotopic enrichment is necessary for all the other elements to reach the desired isotope masses with reasonable size detectors. Current experiments use isotope masses of the order of 10 – 100 kg, while future experiments need masses in the 100 – 1000 kg scale to be able to cover the inverted order region.

2.1.2 Energy resolution

The experimental signature of $0\nu\beta\beta$ decay, a monoenergetic peak at $Q_{\beta\beta}$, requires the experiment to have an optimal energy resolution. Since the $Q_{\beta\beta}$ is well measured, usually in high-precision atomic traps, the search for a $0\nu\beta\beta$ decay signal can be performed over a narrow energy window around $Q_{\beta\beta}$. The width of this energy window, the so-called region of interest (ROI), is defined based on the energy resolution. The number of background events that limit the sensitivity is proportional to the size of the ROI.

Unlike most potential background sources, which can be mitigated by exploiting the event topology, the $2\nu\beta\beta$ decay is an irreducible background to future $0\nu\beta\beta$ decay search. The ratio of the $0\nu\beta\beta$ decay signal to the $2\nu\beta\beta$ decay background can be approximated as [13, 14]:

$$\frac{S}{B} \propto \left(\frac{Q_{\beta\beta}}{\Delta E}\right)^6 \frac{T_{1/2}^{2\nu}}{T_{1/2}^{0\nu}}, \tag{2.1}$$

which highlights the slight $2\nu\beta\beta$ decay half-life dependence and the strongest dependence on the energy resolution ΔE. The energy resolution is given in Full Width Half Maximum (FWHM): $\Delta E = \text{FWHM} \simeq 2.355\,\sigma$, where σ is the expected width of the $0\nu\beta\beta$ decay peak. An educative illustration of the importance of the energy resolution to separate $0\nu\beta\beta$ decay from $2\nu\beta\beta$ decay is presented in figure 2.1.

2.1.3 Background level

In future experiments using tons of material for a decade, the observation of $0\nu\beta\beta$ decay with half-life values of 10^{27} – 10^{28} yr will occur at most with a handful of signal events. The requirement for discovery is that the number of background events is less than the number of expected signal events, which poses extremely stringent requirements on the level of the background of these experiments. This need to be at the level of 10^{-4} – 10^{-5} events per mole of material per year [15].

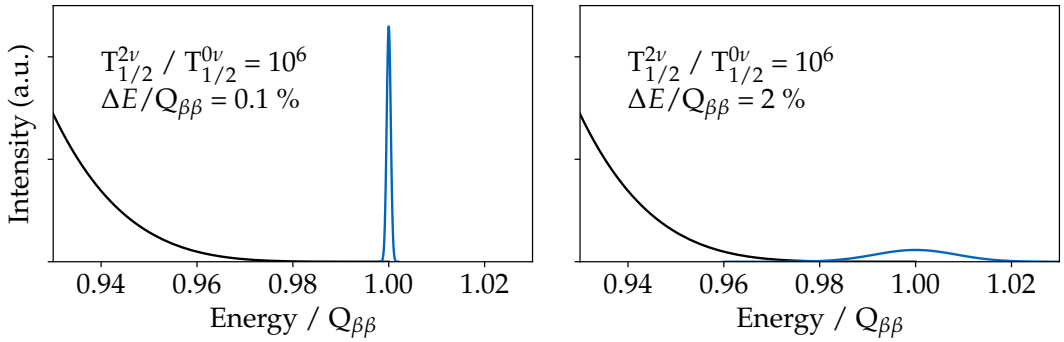

FIGURE 2.1: $2\nu\beta\beta$ decay contamination in the region of interest of $0\nu\beta\beta$ decay depending on the energy resolution (FWHM) at $Q_{\beta\beta}$.

Numerous physics processes can mimic $0\nu\beta\beta$ decay events if their energy is around $Q_{\beta\beta}$ and must be eliminated or at least minimized. Double-β decay experiments must be conducted in deep underground laboratories where they are shielded from the cosmic ray background. Additional precautions need to be taken by experiments to reduce the cosmic ray background to negligible levels [16]. Natural radioactivity can also constitute a source of background, as anticipated above. The use of very radiopure materials around the detectors is of primary importance. Additionally, a well-designed passive and active shielding against local environmental radioactivity is required. The study of the event topology or particle identification techniques must be utilized to identify and suppress the remaining background.

Experiments aim to meet the *background-free* regime, that is when the number of background events in the ROI over the whole experiment exposure is smaller than 1. The advantage of being background-free clearly emerges in the sensitivity to the $0\nu\beta\beta$ decay half-life, which depends on the total number of counts in the ROI, some of which may be background events:

$$T^{0\nu}_{1/2} \propto \begin{cases} \sqrt{\frac{M \cdot t}{BI \cdot \Delta E}} & \text{with background,} \\ M \cdot t & \text{background-free,} \end{cases} \tag{2.2}$$

where M is the detector mass, t the measurement time (their product defines the exposure of the experiment $\mathcal{E} = M \cdot t$), ΔE is the detector energy resolution, and BI is the background index, normalized to the width of the ROI and exposure, *e.g.* in units of (keV kg yr)$^{-1}$. The sensitivity to $T^{0\nu}_{1/2}$ scales linearly with $\mathcal{E}$ in the case of a background-free experiment, as opposed to $\sqrt{\mathcal{E}}$ in the presence of background.

2.1.4 Detection efficiency

High detection efficiency is demanded to maximize the use of costly double-β materials. Using source material as a detector significantly enhances the detection efficiency of double-β decay. With few exceptions, this strategy is pursued by all existing and future double-β decay experiments, based on solid-state detectors with

an embedded source or monolithic liquid or gas detectors with an embedded o dissolved source.

Solid state detectors consist of crystals grown from material containing a double-β isotope. Electrons of a few MeV emitted at the center of the detector are typically fully contained. Only a small fraction of those emitted near the borders can be missed. This results in high containment efficiencies for solid detectors, in the range of 70–95%.

Monolithic liquid and gas-based detectors have the double-β isotope which coincides with or is dissolved in the active material. The range of electrons of a few MeV is typically shorter than the detector size guaranteeing a containment efficiency close to 100%. Nevertheless, these detectors usually require *fiducialization* of the volume, that is the definition of a fraction of the full volume, *i.e.* the fiducial volume, to be used for the analysis. This fiducial volume ranges between 20–80% and reduces the effective detection efficiency.

Composite experiments, in which the double-β decay isotope is separated from the detector, have also been carried out, but they proved to be the most challenging to achieve the half-life goal of 10^{27}–10^{28} yr. The composite detector system, typically thin foils with an embedded double-β source surrounded by tracking and calorimetric detectors, yields a low detection efficiency of the order of 10%.

2.2 Experimental landscape

Various detector technologies have been developed and are being pursued for the discovery of $0\nu\beta\beta$ decay. These include high-purity germanium (HPGe) semiconductor detectors, cryogenic calorimeters, time projection chambers (TPCs), large liquid scintillators, and tracking calorimeters. In the following, we review these technologies focusing on the most sensitive double-β decay experiments of the current and future generations.

HPGe semiconductor detectors HPGe detectors have been used since the very first $0\nu\beta\beta$ decay searches [17]. Experiments using HPGe detectors have always had leading half-life sensitivities given the several advantages that this detector technology offers. HPGe detectors are intrinsically radio-pure, as impurities are removed in the crystal-growing process and they can be fabricated with materials enriched up to 90% in ^{76}Ge. The detector size is currently limited to 1 – 3 kg, requiring the simultaneous operation of multiple detectors. HPGe detectors have superior energy resolution, the best of any double-β decay experiment, while also providing information on the event topology. Nearly all ^{76}Ge double-β decays occur in the active detector region and no volume fiducialization is required to eliminate background leading to very high detector efficiency. They have undetectably low ^{232}Th- and ^{238}U-chain internal contaminations, no known background source produces a peak in the vicinity of $Q_{\beta\beta}$, and no contaminations are expected from the $2\nu\beta\beta$ decay in

the ROI. Therefore, a $0\nu\beta\beta$ decay signal would be a sharp peak in the ROI, whose identification does not rely on the background modeling with consequently negligible systematic uncertainties.

Among the current generation of double-β decay experiments, the Germanium Detector Array (GERDA) experiment [18] and the MAJORANA DEMONSTRATOR (MJD) experiment [19] have utilized HPGe detectors. The GERDA experiment was located at the Laboratori Nazionali del Gran Sasso (LNGS) in central Italy and operated about 40 kg of HPGe detectors in a liquid argon (LAr) cryostat.[2] An excellent energy resolution of 2.6 keV FWHM at $Q_{\beta\beta}$ was achieved, and, the lowest background level of any double-β decay experiment, when normalizes to the energy resolution, was reached 5.2×10^{-4} counts/keV kg yr, allowing a background-free search for $0\nu\beta\beta$ decay [20]. The MJD experiment was located in the Sanford Underground Research Facility (SURF) in South Dakota, and operated about 30 kg of HPGe detectors in two vacuum cryostats. It reached a superior energy resolution of 2.5 keV FWHM at $Q_{\beta\beta}$, and a background index of 41.8×10^{-3} counts/keV kg yr, the second-lowest in the double-β decay field [21]. The results of the GERDA and MJD experiments have demonstrated the feasibility of building a background-free ton-scale ^{76}Ge-based $0\nu\beta\beta$ decay experiment with superior energy resolution.

With the GERDA and MJD experiments now completed, the next generation experiment will be realized in the framework of the Large Enriched Germanium Experiment for Neutrinoless $\beta\beta$ decay (LEGEND) project in two stages: LEGEND-200 and LEGEND-1000 [22]. In the first stage, 200 kg of HPGe detectors will be operated in the GERDA setup after upgrading part of the infrastructure. With an energy resolution equal to or better than the one achieved by the GERDA and MJD experiments and a background level of 2×10^{-4} counts/keV kg yr (just a factor of 3 lower than what was achieved in GERDA), LEGEND-200 will reach a discovery sensitivity of 10^{27} yr after 5 years of data taking. LEGEND-1000 will be realized in a new infrastructure able to host 1 ton of target mass. With further reduction of the background to 4.9×10^{-5} counts/keV kg yr, a discovery sensitivity of 1.3×10^{28} yr will be achieved after 10 years of data taking.

Cryogenic calorimeters Cryogenic calorimeters also referred to as bolometers, have been employed for $0\nu\beta\beta$ decay and dark-matter searches since the 80s [23]. Bolometers can be grown from various materials, including multiple double-β decay isotopes. Advantages of the bolometric technique include good energy resolution and very high detection efficiency. On the other hand, the small masses of the crystals (typically between 0.2 and 0.8 kg) and the necessity of operating them at extremely low temperatures (10 – 20 mK) constitute challenges for building large detectors.

At present, the largest bolometric experiment is the Cryogenic Underground Observatory for Rare Events (CUORE) experiment at LNGS, which utilizes about

[2] The GERDA experiment will be the focus of the second part of this dissertation. A complete description of the experiment will be provided in chapter 4.

750 kg of TeO_2 crystals with natural isotopic composition (containing 206 kg of ^{130}Te) in a large custom cryogen-free cryostat [24]. The CUORE experiment successfully demonstrated the feasibility of a ton-scale bolometric experiment [25]. Despite the good energy resolution achieved with the CUORE detectors (7.8 keV FWHM at $Q_{\beta\beta}$), the experiment is limited by poor background discrimination capabilities of the surface α's background, which led to a background level of 1.5×10^{-2} counts/keV kg yr.

The next generation bolometric experiment, the CUORE Upgrade with Particle Identification (CUPID) experiment, will be realized in the CUORE's cryogenic facility [26]. Two major improvements compared to CUORE will be implemented: the use of scintillating bolometers with particle identification capabilities and the choice of an isotope with higher $Q_{\beta\beta}$, above most of the natural β/γ radiation. Two independent experiments have investigated the potential of this approach: the CUPID-0 experiment at LNGS, which utilized ZnSe crystals enriched in ^{82}Se [27], and the CUPID-Mo experiment at Laboratoire Souterrain de Modane (LSM) in France, which utilized Li_2MoO_4 crystals enriched in ^{100}Mo [28]. They both demonstrated a background level of the order of 10^{-3} counts/keV kg yr [29, 30]. Finally, the Li_2MoO_4 crystals enriched in ^{100}Mo were chosen for the CUPID experiment because of the superior energy resolution (7.4 keV FWHM at $Q_{\beta\beta}$ [30]) compared to the ZnSe crystals (20 keV FWHM at $Q_{\beta\beta}$ [29]). The CUPID experiment will deploy about 250 kg of ^{100}Mo. With a background index of 10^{-4} counts/keV kg yr, it will reach a discovery sensitivity of 1.1×10^{27} yr after 10 years of data taking. A ton-scale bolometric experiment is also foreseen by the CUPID Collaboration, with 1 ton of ^{100}Mo, a background index goal of 5×10^{-6} counts/keV kg yr, and a projected discovery sensitivity of 8×10^{27} yr after 10 years of data taking [31].

In parallel, the bolometric technique has been investigated by the Advanced Molybdenum based Rare process Experiment (AMoRE) at the Yangyang Underground Laboratory (Y2L) in South Korea, which utilizes $CaMoO_4$ and Li_2MoO_4 scintillating crystals, enriched in ^{100}Mo. The goal of the AMoRE experiment is to reach a discovery sensitivity of 5×10^{26} yr after 5 years of data taking with 100 kg of ^{100}Mo and a background index below 10^{-4} counts/keV kg yr [32].

Time projection chambers The first direct observation of $2\nu\beta\beta$ decay was made using a TPC [33]. Since then, this technology has been at the forefront of $0\nu\beta\beta$ decay searches because of the combination of mass scalability and optimal background discrimination capabilities using the reconstructed event topology, position, and energy. TPCs are particularly well-suited to search for $0\nu\beta\beta$ decay of ^{136}Xe: Xe is a noble element that can be used directly in TPCs as a liquid or gas. On the other hand, TPC detectors have a limited energy resolution and require a multi-variate analysis to constrain background features close to the $Q_{\beta\beta}$, which are often not resolved (*e.g.* ^{214}Bi γ line at 2447.7 keV, just below the ^{136}Xe $Q_{\beta\beta}$).

The most sensitive Xe TPC among the current generation of double-β decay experiments was EXO-200, a prototype of the Enriched Xenon Observatory (EXO)

project at Waste Isolation Pilot Plant (WIPP) near Carlsbad New Mexico. It consisted of a single-phase liquid-Xe TPC, filled with 161 kg of ^{136}Xe [34]. EXO-200 demonstrated the capabilities of a monolithic liquid-Xe TPC, which includes good energy resolution (67 keV FWHM at $Q_{\beta\beta}$ [35]), near maximal signal detection efficiency, and solid topological discrimination of backgrounds.

Based on the success of EXO-200, the next generation ton-scale ^{136}Xe-based $0\nu\beta\beta$ decay experiment is planned [36]. The next-generation Enriched Xenon Observatory (nEXO) experiment will utilize 5 tons of Xe enriched to 90% in ^{136}Xe and, provided an energy resolution of 46 keV FWHM at $Q_{\beta\beta}$, will reach a discovery potential of 0.74×10^{28} yr after 10 years of data taking.

The Neutrino Experiment with a Xenon TPC (NEXT) implements a electroluminescent high-pressure gas-phase Xe TPC at Laboratorio Subterráneo de Canfranc (LSC) in Spain. The advantages of this detector technology are a good energy resolution (< 1% FWHM at $Q_{\beta\beta}$) and charged-particle tracking for the active suppression of background [37]. Both were demonstrated by the NEXT-White detector, a proof-of-principle detector with 4.3 kg of Xe [38], whose main goals were the validation of the reconstruction algorithms, the background modeling, and the measurement of the $2\nu\beta\beta$ decay of ^{136}Xe [39–41]. A second stage of the NEXT project is currently under construction: the NEXT-100 detector will contain 91 kg of ^{136}Xe and aims to demonstrate a background index of 4×10^{-4} counts/kg yr [42].

A concept for a ton-scale phase of NEXT is under investigation: the NEXT-HD detector should accommodate a full ton of ^{136}Xe in the form of enriched Xe gas [43]. The NEXT-BOLD detector aims to take this concept further by instrumenting the NEXT-HD TPC with Ba tagging capability, reaching a discovery potential of 10^{28} yr [44].

The high-pressure gas-phase Xe TPC technique is also being pursued by the Particle and Astrophysical Xenon III (PandaX-III) experiment at China Jin-Ping underground Laboratory II (CJPL-II) [45]. The first phase of the PandaX-III experiment will feature one 200 kg TPC module, whereas the second phase will consist of five upgraded modules for a ton-scale experiment. The projected sensitivity for the ton-scale PandaX-III experiment is 10^{27} yr after 3 years of data taking [45].

Among the future generation of Xe TPC experiments, we should also mention the Dark matter Wimp search with liquid xenon (DARWIN) project, which will employ a dual-phase TPC containing 40 tons of liquid Xe with natural abundance (containing about 3.6 tons of ^{136}Xe) [46]. Even if the primary physics goal of the DARWIN experiment is the direct dark matter search, it might have the capability to search for $0\nu\beta\beta$ decay of ^{136}Xe, with a projected discovery sensitivity of 1.1×10^{27} yr after 10 years of data taking [47].

Large liquid scintillators Large liquid scintillators may not have the best energy resolution, but they still represent an attractive detector technology in searching for $0\nu\beta\beta$ decay because of the mass scalability.

The KamLAND - Zero Neutrino double beta decay search (KamLAND-Zen) experiment successfully demonstrated the potential of this technology, with the first exploration of the inverted mass order region [48]. The KamLAND infrastructure, located in the Kamioka Mine in Japan, was upgraded with a nylon balloon in the active detector volume filled with a liquid scintillator. Enriched Xe has been dissolved in the liquid scintillator such that the KamLAND-Zen experiment could search for $0\nu\beta\beta$ decay of ^{136}Xe [49]. After the first phase with loading up to 340 kg of ^{136}Xe, the KamLAND-Zen experiment is now running with 680 kg of ^{136}Xe, loaded in a larger and cleaner inner balloon [48].

A ton-scale phase of the experiment is in preparation by the KamLAND-Zen Collaboration. About 1 ton of ^{136}Xe will be deployed, with significant improvement in the energy resolution at $Q_{\beta\beta}$, and a consequent reduction of the background in the region of interest [50].

The SNO experiment, located at SNOLAB in Canada, is a multi-purpose neutrino experiment consisting of an acrylic sphere filled with 780 tons of organic liquid scintillator [51]. Currently, the experiment is taking data with the unloaded scintillator for low-energy neutrino analysis, such as ^{8}B solar neutrinos, reactor and geo anti-neutrinos, and supernova neutrinos. The SNO liquid scintillator is planned to be loaded with natural Te from 2024. Initially, a 0.5% loading is planned (corresponding to 1.3 tons of ^{130}Te), with a projected sensitivity of 2×10^{26} yr after 5 years of data taking [51], which will be comparable to what the CUORE experiment will achieve by that time. This phase of the SNO experiment is primarily conceived to assess the experiment's performance and background in the search for $0\nu\beta\beta$ decay. At the same time, several R&D projects are ongoing to increase the loading of Te up to 2.5% (6.6 tons of ^{130}Te) in a subsequent phase of the experiment with a sensitivity goal of 10^{27} yr [51].

Among future-generation of double-β decay experiments, we should also mention the Jiangmen Underground Neutrino Observatory (JUNO) project, which is currently under construction and will contain 20 kton of unloaded liquid scintillator [52]. The primary goal of the JUNO experiment is the investigation of the neutrino mass ordering, which will be determined with a $3-4\,\sigma$ significance after 6 years of data taking [52]. After the completion of this physics goal, an upgrade of the experiment is conceived, roughly for 2030, in which the scintillator might be loaded with a double-β decay isotope, still under investigation [53–55].

Tracking calorimeters Tracking calorimeters are the only technology in which the double-β decay isotope is decoupled from the detector. The source is in the form of thin foils placed in the center of a sandwich configuration, surrounded by tracking and calorimetric layers. This configuration allows a precise measurement of the decay kinematics, such as single electron spectra and angular distributions. The reconstruction of the entire event kinematics allows suppressing most of the backgrounds at the price of limited detection efficiency. As another drawback, the requirement

of using very thin foils to minimize energy losses makes it extremely challenging to scale up the isotope mass.

The Neutrino Ettore Majorana Observatory 3 (NEMO-3) experiment utilized this technology to search for $0\nu\beta\beta$ decay of several isotopes [56–59] at the LSM.

SuperNEMO is a next-generation detector based on the technology demonstrated by NEMO-3 [60]. In its first phase, the SuperNEMO Demonstrator will deploy one module with 7 kg of ^{82}Se. A successive full-scale experiment would consist of multiple modules for a total ^{82}Se mass of 100 kg and a projected sensitivity of 1.2×10^{26} yr [61], though not yet defined.

References

[1] A. A. Kwiatkowski et al. "New determination of double-β-decay properties in ^{48}Ca : High-precision $Q_{\beta\beta}$-value measurement and improved nuclear matrix element calculations". In: *Phys. Rev. C* 89.4 (2014), p. 045502. DOI: 10.1103/PhysRevC.89.045502. arXiv: 1308.3815.

[2] B. J. Mount, M. Redshaw, and E. G. Myers. "Double-β-decay Q values of ^{74}Se and ^{76}Ge". In: *Phys. Rev. C* 81 (2010), p. 032501. DOI: 10.1103/PhysRevC.81.032501.

[3] David L. Lincoln et al. "First direct double-β decay Q-Value measurement of ^{82}Se in support of understanding the nature of the Neutrino". In: *Phys. Rev. Lett.* 110.1 (2013), p. 012501. DOI: 10.1103/PhysRevLett.110.012501. arXiv: 1211.5659.

[4] K. Gulyuz et al. "Determination of the direct double-β-decay Q value of ^{96}Zr and atomic masses of $^{90-92,94,96}$Zr and $^{92,94-98,100}$Mo". In: *Phys. Rev. C* 91.5 (2015), p. 055501. DOI: 10.1103/PhysRevC.91.055501.

[5] S. Rahaman et al. "Q values of the ^{76}Ge and ^{100}Mo double-beta decays". In: *Phys. Lett. B* 662 (2008), pp. 111–116. DOI: 10.1016/j.physletb.2008.02.047. arXiv: 0712.3337.

[6] S. Rahaman et al. "Double-beta decay Q values of ^{116}Cd and ^{130}Te". In: *Phys. Lett. B* 703 (2011), pp. 412–416. DOI: 10.1016/j.physletb.2011.07.078.

[7] M. Redshaw et al. "Masses of ^{130}Te and ^{130}Xe and Double-β-Decay Q Value of ^{130}Te". In: *Phys. Rev. Lett.* 102 (2009), p. 212502. DOI: 10.1103/PhysRevLett.102.212502. arXiv: 0902.2139.

[8] M. Redshaw et al. "Mass and double-beta-decay Q value of ^{136}Xe". In: *Phys. Rev. Lett.* 98 (2007), p. 053003. DOI: 10.1103/PhysRevLett.98.053003.

[9] V. S. Kolhinen et al. "Double-β decay Q value of ^{150}Nd". In: *Phys. Rev. C* 82 (2010), p. 022501. DOI: 10.1103/PhysRevC.82.022501.

[10] Juris Meija et al. "Isotopic compositions of the elements 2013 (IUPAC Technical Report)". In: *Pure and Applied Chemistry* 88.3 (2016), pp. 293–306. DOI: doi:10.1515/pac-2015-0503.

[11] W. C. Haxton and G. J. Stephenson. "Double beta Decay". In: *Prog. Part. Nucl. Phys.* 12 (1984), pp. 409–479. DOI: 10.1016/0146-6410(84)90006-1.

[12] CUORE Collaboration, D. Q. Adams, et al. "Search for Majorana neutrinos exploiting millikelvin cryogenics with CUORE". In: *Nature* 604.7904 (2022), pp. 53–58. DOI: 10.1038/s41586-022-04497-4. arXiv: 2104.06906.

[13] S. R. Elliott and P. Vogel. "Double beta decay". In: *Ann. Rev. Nucl. Part. Sci.* 52 (2002), pp. 115–151. DOI: 10.1146/annurev.nucl.52.050102.090641. arXiv: hep-ph/0202264.

[14] M. J. Dolinski, A. W. P. Poon, and W. Rodejohann. "Neutrinoless Double-Beta Decay: Status and Prospects". In: *Ann. Rev. Nucl. Part. Sci.* 69 (2019), pp. 219–251. DOI: 10.1146/annurev-nucl-101918-023407. arXiv: 1902.04097.

[15] M. Agostini et al. "Toward the discovery of matter creation with neutrinoless double-beta decay". 2022. arXiv: 2202.01787.

[16] K. Freund et al. "The Performance of the Muon Veto of the GERDA Experiment". In: *Eur. Phys. J. C* 76.5 (2016), p. 298. DOI: 10.1140/epjc/s10052-016-4140-7. arXiv: 1601.05935.

[17] F. T. Avignone and S. R. Elliott. "The Search for Double Beta Decay With Germanium Detectors: Past, Present, and Future". In: *Front. in Phys.* 7 (2019), p. 6. DOI: 10.3389/fphy.2019.00006. arXiv: 1901.02805.

[18] GERDA Collaboration, M. Agostini, et al. "Upgrade for Phase II of the GERDA experiment". In: *Eur. Phys. J. C* 78.5 (2018), p. 388. DOI: 10.1140/epjc/s10052-018-5812-2. arXiv: 1711.01452.

[19] Majorana Collaboration, N. Abgrall, et al. "The Majorana Demonstrator Neutrinoless Double-Beta Decay Experiment". In: *Adv. High Energy Phys.* 2014 (2014), p. 365432. DOI: 10.1155/2014/365432. arXiv: 1308.1633.

[20] GERDA Collaboration, M. Agostini, et al. "Final Results of GERDA on the Search for Neutrinoless Double-β Decay". In: *Phys. Rev. Lett.* 125.25 (2020), p. 252502. DOI: 10.1103/PhysRevLett.125.252502. arXiv: 2009.06079.

[21] Majorana Collaboration, I. J. Arnquist, et al. "Final Result of the MAJORANA DEMONSTRATOR's Search for Neutrinoless Double-β Decay in ^{76}Ge". 2022. arXiv: 2207.07638.

[22] LEGEND Collaboration, N. Abgrall, et al. "The Large Enriched Germanium Experiment for Neutrinoless $\beta\beta$ Decay: LEGEND-1000 Preconceptual Design Report". 2021. arXiv: 2107.11462.

[23] C. Brofferio and S. Dell'Oro. "Contributed Review: The saga of neutrinoless double beta decay search with TeO_2 thermal detectors". In: *Rev. Sci. Instrum.* 89.12 (2018), p. 121502. DOI: 10.1063/1.5031485. arXiv: 1801.03580.

[24] C. Alduino et al. "The CUORE cryostat: An infrastructure for rare event searches at millikelvin temperatures". In: *Cryogenics* 102 (2019), pp. 9–21. DOI: 10.1016/j.cryogenics.2019.06.011. arXiv: 1904.05745.

[25] CUORE Collaboration, D. Q. Adams, et al. "CUORE opens the door to tonne-scale cryogenics experiments". In: *Prog. Part. Nucl. Phys.* 122 (2022), p. 103902. DOI: 10.1016/j.ppnp.2021.103902. arXiv: 2108.07883.

[26] CUPID Collaboration, W. R. Armstrong, et al. "CUPID pre-CDR". 2019. arXiv: 1907.09376.

[27] CUPID Collaboration, O. Azzolini, et al. "CUPID-0: the first array of enriched scintillating bolometers for $0\nu\beta\beta$ decay investigations". In: *Eur. Phys. J. C* 78.5 (2018), p. 428. DOI: 10.1140/epjc/s10052-018-5896-8. arXiv: 1802.06562.

[28] E. Armengaud et al. "The CUPID-Mo experiment for neutrinoless double-beta decay: performance and prospects". In: *Eur. Phys. J. C* 80.1 (2020), p. 44. DOI: 10.1140/epjc/s10052-019-7578-6. arXiv: 1909.02994.

[29] O. Azzolini et al. "Final Result on the Neutrinoless Double Beta Decay of ^{82}Se with CUPID-0". In: *Phys. Rev. Lett.* 129.11 (2022), p. 111801. DOI: 10.1103/PhysRevLett.129.111801. arXiv: 2206.05130.

[30] C. Augier et al. "Final results on the $0\nu\beta\beta$ decay half-life limit of ^{100}Mo from the CUPID-Mo experiment". In: *Eur. Phys. J. C* 82.11 (2022), p. 1033. DOI: 10.1140/epjc/s10052-022-10942-5. arXiv: 2202.08716.

[31] CUPID Collaboration, A. Armatol, et al. "Toward CUPID-1T". Contribution to Snowmass Summer Study. 2022. arXiv: 2203.08386.

[32] Y. Oh. "AMoRE new results". Contribution to NEUTRINO2022. URL: https://indico.kps.or.kr/event/30/contributions/864/.

[33] S. R. Elliott, A. A. Hahn, and M. K. Moe. "Direct Evidence for Two Neutrino Double Beta Decay in ^{82}Se". In: *Phys. Rev. Lett.* 59 (1987), pp. 2020–2023. DOI: 10.1103/PhysRevLett.59.2020.

[34] M. Auger et al. "The EXO-200 detector, part I: Detector design and construction". In: *JINST* 7 (2012), P05010. DOI: 10.1088/1748-0221/7/05/P05010. arXiv: 1202.2192.

[35] EXO-200 Collaboration, G. Anton, et al. "Search for Neutrinoless Double-β Decay with the Complete EXO-200 Dataset". In: *Phys. Rev. Lett.* 123.16 (2019), p. 161802. DOI: 10.1103/PhysRevLett.123.161802. arXiv: 1906.02723.

[36] nEXO Collaboration, G. Adhikari, et al. "nEXO: neutrinoless double beta decay search beyond 10^{28} year half-life sensitivity". In: *J. Phys. G* 49.1 (2022), p. 015104. DOI: 10.1088/1361-6471/ac3631. arXiv: 2106.16243.

[37] J. J. Gomez-Cadenas, F. Monrabal Capilla, and P. Ferrario. "High Pressure Gas Xenon TPCs for Double Beta Decay Searches". In: *Front. in Phys.* 7 (2019), p. 51. DOI: 10.3389/fphy.2019.00051. arXiv: 1903.02435.

[38] NEXT Collaboration, F. Monrabal, et al. "The Next White (NEW) Detector". In: *JINST* 13.12 (2018), P12010. DOI: 10.1088/1748-0221/13/12/P12010. arXiv: 1804.02409.

[39] NEXT Collaboration, J. Renner, et al. "Energy calibration of the NEXT-White detector with 1% resolution near $Q_{\beta\beta}$ of ^{136}Xe". In: *JHEP* 10 (2019), p. 230. DOI: 10.1007/JHEP10(2019)230. arXiv: 1905.13110.

[40] NEXT Collaboration, P. Novella, et al. "Measurement of the Xe136 two-neutrino double-β-decay half-life via direct background subtraction in NEXT". In: *Phys. Rev. C* 105.5 (2022), p. 055501. DOI: 10.1103/PhysRevC.105.055501. arXiv: 2111.11091.

[41] NEXT Collaboration, A. Simón, et al. "Boosting background suppression in the NEXT experiment through Richardson-Lucy deconvolution". In: *JHEP* 07 (2021), p. 146. DOI: 10.1007/JHEP07(2021)146. arXiv: 2102.11931.

[42] NEXT Collaboration, J. Martín-Albo, et al. "Sensitivity of NEXT-100 to Neutrinoless Double Beta Decay". In: *JHEP* 05 (2016), p. 159. DOI: 10.1007/JHEP05(2016)159. arXiv: 1511.09246.

[43] NEXT Collaboration, C. Adams, et al. "Sensitivity of a tonne-scale NEXT detector for neutrinoless double beta decay searches". In: *JHEP* 2021.08 (2021), p. 164. DOI: 10.1007/JHEP08(2021)164. arXiv: 2005.06467.

[44] Iván Rivilla et al. "Fluorescent bicolour sensor for low-background neutrinoless double β decay experiments". In: *Nature* 583.7814 (2020), pp. 48–54. DOI: 10.1038/s41586-020-2431-5.

[45] PandaX-III Collaboration and Ke Han. "PandaX-III: Searching for Neutrinoless Double Beta Decay with High Pressure Gaseous Time Projection Chambers". In: *J. Phys. Conf. Ser.* 1342.1 (2020), p. 012095. DOI: 10.1088/1742-6596/1342/1/012095. arXiv: 1710.08908.

[46] DARWIN Collaboration, J. Aalbers, et al. "DARWIN: towards the ultimate dark matter detector". In: *JCAP* 11 (2016), p. 017. DOI: 10.1088/1475-7516/2016/11/017. arXiv: 1606.07001.

[47] DARWIN Collaboration, F. Agostini, et al. "Sensitivity of the DARWIN observatory to the neutrinoless double beta decay of ^{136}Xe". In: *Eur. Phys. J. C* 80.9 (2020), p. 808. DOI: 10.1140/epjc/s10052-020-8196-z. arXiv: 2003.13407.

[48] KamLAND-Zen Collaboration, S. Abe, et al. "First Search for the Majorana Nature of Neutrinos in the Inverted Mass Ordering Region with KamLAND-Zen". 2022. arXiv: 2203.02139.

[49] KamLAND-Zen Collaboration, A. Gando, et al. "Search for Majorana Neutrinos near the Inverted Mass Hierarchy Region with KamLAND-Zen". In: *Phys. Rev. Lett.* 117.8 (2016). [Addendum: Phys.Rev.Lett. 117, 109903 (2016)], p. 082503. DOI: 10.1103/PhysRevLett.117.082503. arXiv: 1605.02889.

[50] KamLAND-Zen Collaboration and J. Shirai. "Results and future plans for the KamLAND-Zen experiment". In: *J. Phys. Conf. Ser.* 888.1 (2017), p. 012031. DOI: 10.1088/1742-6596/888/1/012031.

[51] SNO+ Collaboration, V. Albanese, et al. "The SNO+ experiment". In: *JINST* 16.08 (2021), P08059. DOI: 10.1088/1748-0221/16/08/P08059. arXiv: 2104.11687.

[52] JUNO Collaboration, A. Abusleme, et al. "JUNO physics and detector". In: *Prog. Part. Nucl. Phys.* 123 (2022), p. 103927. DOI: 10.1016/j.ppnp.2021.103927.

[53] JUNO Collaboration et al. "The JUNO Experiment". Snowmass2021 - Letter of Interest. URL: https://www.snowmass21.org/docs/files/summaries/NF/SNOWMASS21-NF1_NF4_Pedro_Ochoa-034.pdf.

[54] J. Zhao et al. "Physics potential of searching for $0\nu\beta\beta$ decays in JUNO". In: *Chin. Phys. C* 41.5 (2017), p. 053001. DOI: 10.1088/1674-1137/41/5/053001. arXiv: 1610.07143.

[55] J. Cao et al. "Towards the meV limit of the effective neutrino mass in neutrinoless double-beta decays". In: *Chin. Phys. C* 44.3 (2020), p. 031001. DOI: 10.1088/1674-1137/44/3/031001. arXiv: 1908.08355.

[56] NEMO-3 Collaboration, R. Arnold, et al. "Results of the search for neutrinoless double-β decay in ^{100}Mo with the NEMO-3 experiment". In: *Phys. Rev. D* 92.7 (2015), p. 072011. DOI: 10.1103/PhysRevD.92.072011. arXiv: 1506.05825.

[57] NEMO-3 Collaboration, R. Arnold, et al. "Measurement of the double-beta decay half-life and search for the neutrinoless double-beta decay of ^{48}Ca with the NEMO-3 detector". In: *Phys. Rev. D* 93.11 (2016), p. 112008. DOI: 10.1103/PhysRevD.93.112008. arXiv: 1604.01710.

[58] NEMO-3 Collaboration, J. Argyriades, et al. "Measurement of the two neutrino double beta decay half-life of Zr-96 with the NEMO-3 detector". In: *Nucl. Phys. A* 847 (2010), pp. 168–179. DOI: 10.1016/j.nuclphysa.2010.07.009. arXiv: 0906.2694.

[59] NEMO-3 Collaboration, R. Arnold, et al. "Measurement of the $2\nu\beta\beta$ decay half-life of ^{150}Nd and a search for $0\nu\beta\beta$ decay processes with the full exposure from the NEMO-3 detector". In: *Phys. Rev. D* 94.7 (2016), p. 072003. DOI: 10.1103/PhysRevD.94.072003. arXiv: 1606.08494.

[60] NEMO Collaboration and F. Piquemal. "The SuperNEMO project". In: *Phys. Atom. Nucl.* 69 (2006), pp. 2096–2100. DOI: 10.1134/S1063778806120131.

[61] SuperNEMO Collaboration, R. Arnold, et al. "Probing New Physics Models of Neutrinoless Double Beta Decay with SuperNEMO". In: *Eur. Phys. J. C* 70 (2010), pp. 927–943. DOI: 10.1140/epjc/s10052-010-1481-5. arXiv: 1005.1241.

Chapter 3

Search for light exotic fermions in double-β decays

Many Beyond the Standard Model (BSM) theories contain new particles, possibly related to the mechanism of neutrino mass generation or the dark matter (DM) of the Universe. If these particles couple with neutrinos and their masses are small enough, they can also be produced in double-β decay. Double-β decay with the emission of massless or light bosons, the Majorons, have been extensively studied, and experimental searches have been performed since pioneer experiments, as discussed in chapter 1. On the other hand, the emission of light exotic fermions in double-β decay has only recently been considered.

As part of this dissertation work, as a result of the author's collaboration with *M. Agostini*, *A. Ibarra*, and *X. Marcano*, the emission of light exotic fermions in double-β decays was investigated. Two scenarios were considered. In the first, the existence of a massive sterile neutrino (N) that mixes with the electron neutrino is assumed. The second scenario is characterized by the presence of an additional Z_2 symmetry that only allows the exotic fermion to be produced in pairs. Both scenarios lead to exotic double-β decay modes that are discussed in this chapter. The work has been published in [1].

3.1 Introduction

Many models of new physics contain new spin 1/2 particles, singlets under the Standard Model (SM) gauge group, possibly related to the mechanism of neutrino mass generation or to the DM of the Universe. An archetype of such fermions is the sterile neutrino, also called the right-handed neutrino. In a variant of this scenario, the singlet fermion is furnished with a Z_2 symmetry, so it can only be produced in pairs. Unfortunately, in either of these scenarios, the mass of the light exotic fermion and the coupling strength to the SM particles are free parameters of the model, leaving a vast parameter space that must be probed in laboratory experiments or astrophysical and cosmological observations.

From the phenomenological standpoint, sub-GeV sterile neutrinos are particularly attractive since they could be produced in charged lepton or in hadron decays and possibly be discovered in a laboratory experiment. In fact, there is an intense experimental program aiming to detect signals of sterile neutrinos in the sub-GeV range, either in dedicated experiments or as a by-product of an experiment initially designed for a different purpose. The current limits are fairly stringent below $\sim$ 100 keV and above $\sim$ 100 MeV [2]. However, the intermediate-mass region remains relatively unexplored, and some of the current constraints date back to the 1990s [3, 4]. The scenario with Z_2-odd singlet fermions has been even less studied, and, to the best of our knowledge, there is no laboratory constraint for the mass range $\sim$ 100 keV $-$100 MeV.

If light exotic fermions exist, they will also be produced in double-β decays, replacing one or both neutrinos in the final state. The fermion mass range accessible with this kind of search extends from a few hundred keV to a few MeV, *i.e.*, from the energy threshold of the experiments till the $Q_{\beta\beta}$ of the decay.

The existence of a massive sterile neutrino (N) that mixes with the electron neutrino opens the possibility of observing a double-β decay final state in which a standard neutrino is replaced by N (νN$\beta\beta$ decay):

$$(A, Z) \rightarrow (A, Z+2) + 2e + \nu + N \,, \tag{3.1}$$

with a modified spectrum due to the sterile neutrino mass. This is indeed the same principle as the one used in kink searches with single-β decays [5–9], which currently provide the strongest laboratory bounds in our mass range of interest [3, 4, 10, 11]. As we will see, the presence of light exotic fermions does not create a kink in the total double-β energy spectrum but still creates a continuous distortion that is detectable by experiments.

The presence of a new symmetry that forbids the production of a single exotic fermion in double-β decays is a typical scenario for models adding new exotic fermions χ as DM candidates, which are charged under a Z_2 symmetry to make them stable. This kind of model cannot be tested through single-β decays but would result in a new final state in double-β decays ($\chi\chi\beta\beta$ decay):

$$(A, Z) \rightarrow (A, Z+2) + 2e + 2\chi \,. \tag{3.2}$$

Thus, double-β decay experiments can provide the first laboratory-based constraints on several models.

3.2 Double-β decay into sterile neutrinos

One of the simplest extensions of the SM consists in adding to the particle content one spin 1/2 particle, singlet under the gauge group, N. The gauge symmetry allows a Yukawa coupling of N to the SM Higgs doublet and lepton doublets, which

leads upon electroweak symmetry breaking to a Dirac mass term which couples N to ν, $m_D \overline{\nu} N$. For this reason, N is commonly denominated as right-handed neutrino or sterile neutrino. Furthermore, the gauge symmetry also allows a Majorana mass term for N, $M\overline{N^c}N$, which we assume to be in the range 0.1-2 MeV. The two parameters of the model, m_D and M_N are usually recast in terms of the misalignment angle between the interaction and mass eigenstates, $\sin\theta \simeq m_D/M$, and the mass of the heaviest eigenstate $m_N \simeq M$.

If kinematically possible, sterile neutrinos could be produced in any decay process involving SM neutrinos due to the active-sterile mixing angle. The new decay channels lead to distortions in the energy distribution for the visible particles compared to the SM expectations, which constitute a test for the sterile neutrino scenario.

In the presence of sterile neutrinos, and provided their mass is below the $Q_{\beta\beta}$ of the decay, the decay channels $\nu\mathrm{N}\beta\beta$ and $\mathrm{NN}\beta\beta$ become kinematically possible. The differential energy spectrum Γ is given by the incoherent superposition of three channels and can be expressed as:

$$\begin{aligned}\frac{d\Gamma}{dT} = \cos^4\theta\,\frac{d\Gamma_{\nu\nu}}{dT}\,\theta(T_0 - T) + 2\cos^2\theta\sin^2\theta\,\frac{d\Gamma_{\nu N}}{dT}\,\theta(T_0 - T - x_N) \\ + \sin^4\theta\,\frac{d\Gamma_{NN}}{dT}\,\theta(T_0 - T - 2x_N)\,,\end{aligned} \tag{3.3}$$

where $T = (E_{e_1} + E_{e_2} - 2m_e)/m_e$ is the sum of the kinetic energies of the two electrons (normalized to the electron mass). This variable is kinematically restricted to be $0 \leq T \leq T_0$, $T_0 - x_N$ and $T_0 - 2x_N$, for $2\nu\beta\beta$, $\nu\mathrm{N}\beta\beta$ and $\mathrm{NN}\beta\beta$ decays respectively, with $x_N = m_N/m_e$ and $T_0 = Q_{\beta\beta}/m_e$. $Q_{\beta\beta}$ is the end-point energy assuming massless neutrinos and depends on the particular nucleus. The $2\nu\beta\beta$ decay has been studied in several works [12–18], always assuming vanishing neutrino masses. In this work we extend this analysis, leaving the masses of the invisible fermions as free parameters. To this end, we follow and generalize [16], and express the differential rate for a generic decay $(A, Z) \to (A, Z+2) + 2e + a + b$, with a and b being either ν or N, as:

$$\frac{d\Gamma_{ab}}{dT} = |\mathcal{M}^{\mathrm{eff}}_{2\nu}|^2\,\frac{d\mathcal{G}^{(0)}_{ab}}{dT}\,, \tag{3.4}$$

with $M^{\mathrm{eff}}_{2\nu}$ is the dimensionless NME. The phase-space factor is given by

$$\begin{aligned}\mathcal{G}^{(0)}_{ab} = \frac{1}{g_A^4 m_e^2}\frac{2\widetilde{A}^2}{3\log 2}\int_{m_e}^{E^{\max}_{e_1}} dE_{e_1}\int_{m_e}^{E^{\max}_{e_2}} dE_{e_2}\int_{m_a}^{E^{\max}_{a}} dE_a \Big(\langle K_{\mathcal{N}}\rangle^2 \\ + \langle L_{\mathcal{N}}\rangle^2 + \langle K_{\mathcal{N}}\rangle\langle L_{\mathcal{N}}\rangle\Big)\, f^{(0)}_{11}\,\omega_{ab}\,,\end{aligned} \tag{3.5}$$

where

$$\widetilde{A} = \frac{1}{2}(Q_{\beta\beta} + 2m_e) + \langle E_{\mathcal{N}} \rangle - E_I \,, \tag{3.6a}$$

$$\langle K_{\mathcal{N}} \rangle = \frac{1}{E_{e_1} + E_a + \langle E_{\mathcal{N}} \rangle - E_I} + \frac{1}{E_{e_2} + E_b + \langle E_{\mathcal{N}} \rangle - E_I} \,, \tag{3.6b}$$

$$\langle L_{\mathcal{N}} \rangle = \frac{1}{E_{e_1} + E_b + \langle E_{\mathcal{N}} \rangle - E_I} + \frac{1}{E_{e_2} + E_a + \langle E_{\mathcal{N}} \rangle - E_I} \,, \tag{3.6c}$$

with E_I the energy of the initial nucleus, $\langle E_{\mathcal{N}} \rangle$ a suitable excitation energy in the intermediate nucleus and

$$\omega_{ab} = \frac{g_A^4 G_F^4}{64\pi^7} \, p_a E_a p_b E_b p_{e_1} E_{e_1} p_{e_2} E_{e_2} \,. \tag{3.7}$$

Here, E_X and $p_X = \sqrt{E_X^2 - m_X^2}$ denote the energy and the modulus of the 3-momentum of the particle $X = e_1, e_2, a, b$ with mass m_X, and subject to the condition $E_b = Q_{\beta\beta} + 2m_e - E_{e_1} - E_{e_2} - E_a$ from energy conservation. The integration limits read $E_{e_1}^{\max} = Q_{\beta\beta} + m_e - m_a - m_b$, $E_{e_2}^{\max} = Q_{\beta\beta} + 2m_e - E_{e_1} - m_a - m_b$ and $E_a^{\max} = Q_{\beta\beta} + 2m_e - E_{e_1} - E_{e_2} - m_b$, which for $m_a, m_b \neq 0$ shifts the end-point of the spectrum to lower values. Finally, the factor $f_{11}^{(0)}$ originates from the Coulomb interaction of the electrons with the daughter nucleus, which we parametrize using the Fermi function [13]

$$f_{11}^{(0)} \simeq F_0(Z+2, E_{e_1}) \, F_0(Z+2, E_{e_2}) \,. \tag{3.8}$$

In the limit $a, b = \nu$ and $m_\nu = 0$ we recover the results of [16].

The complete analysis of the spectrum requires a numerical evaluation of equation 3.4. However, we also identified accurate analytical approximations for the dominant $2\nu\beta\beta$ and $\nu\mathrm{N}\beta\beta$ decay channels (the $\mathrm{NN}\beta\beta$ decay channel is negligible for small $\sin\theta$), which assumes the Primakoff-Rosen approximation [19] for the Fermi function and neglects the lepton energies in

$$\langle K_{\mathcal{N}} \rangle \simeq \langle L_{\mathcal{N}} \rangle \simeq \frac{4}{2\widetilde{A} - Q_{\beta\beta} - 2m_e} \approx \frac{2}{\widetilde{A}} \,. \tag{3.9}$$

Then, neglecting also the active neutrino mass but keeping the sterile neutrino one, we obtain:

$$\frac{d\mathcal{G}_{ab}}{dT} \approx \frac{G_F^4 m_e^8}{7200\pi^7 \log 2} \left[\frac{2\pi\alpha(Z+2)}{1 - \exp\big(-2\pi\alpha(Z+2)\big)} \right]^2 F_{ab}(T) \,, \tag{3.10}$$

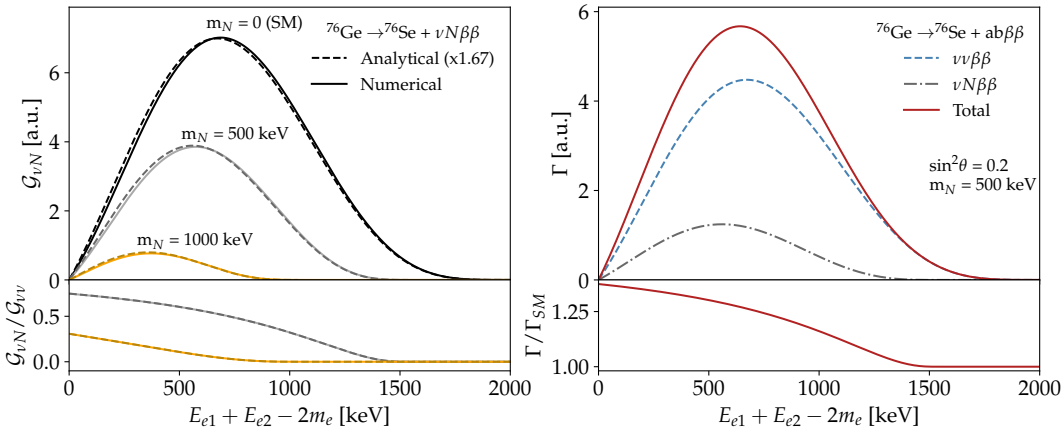

FIGURE 3.1: Left: Phase space for different sterile neutrino mass hypotheses computed using a numerical evaluation of equation 3.4 and the analytical approximation of equation 3.10. Right: $2\nu\beta\beta$ decay, νN$\beta\beta$ decay and summed energy spectra for $m_N = 500\,\text{keV}$ and an illustrative large mixing $\sin^2\theta = 0.2$.

where we have introduced the form factors

$$F_{\nu\nu}(T) = T\,(T^4 + 10T^3 + 40T^2 + 60T + 30)\,(T_0 - T)^5\,, \tag{3.11a}$$

$$\begin{aligned} F_{\nu N}(T) = \frac{T}{2}(T^4 + 10T^3 + 40T^2 + 60T + 30)\Bigg\{ & \\ \left(2(T_0 - T)^4 - 9x_N^2(T_0 - T)^2 - 8x_N^4\right)\sqrt{(T_0 - T)^2 - x_N^2} & \\ + 15x_N^4(T_0 - T)\left[\log\left(T_0 - T + \sqrt{(T_0 - T)^2 - x_N^2}\right) - \log x_N\right]\Bigg\}\,. & \end{aligned} \tag{3.11b}$$

The left panel of figure 3.1 displays the phase space resulting from our numerical calculation applied to ^{76}Ge ($Q_{\beta\beta} \simeq 2039\,\text{keV}$), showing how the presence of a final massive invisible fermion modifies the energy spectrum, shifting the end-point as well as the peak to lower values as m_N increases. We can also see that the analytical expression reproduces the full result to a good approximation, up to a global factor of 1.67. This factor is due to the approximation we considered, but it does not affect the analysis, which is sensitive to the $\mathcal{G}_{\nu N}/\mathcal{G}_{\nu\nu}$ ratio. We stress that, contrary to the single-β decay spectrum, the end-point of the νN$\beta\beta$ decay spectrum is smooth, and, therefore, the total spectrum does not manifest a kink at $Q_{\beta\beta} - m_N$. Nevertheless, the spectrum differs from the standard one, allowing double-β decay experiments to probe this hypothesis by measuring the $2\nu\beta\beta$ decay spectrum very accurately.

3.3 Double-β decay into Z_2-odd singlet fermions

In general, the production of a pair of exotic particles is strongly suppressed compared to the production of a single one and can be neglected. However, there are scenarios in which single production is forbidden, and only double production can

take place. These scenarios cannot be tested by single-β decay experiments, whereas double-β decay experiments are still sensitive to double production and have the unique opportunity to explore these channels.

In this section, we consider a variant of the previous model, in which the symmetry group is extended by a discrete Z_2 symmetry, possibly related to the DM sector, which is exact or mildly broken in the electroweak vacuum. We assume that all SM particles are even under the Z_2 symmetry, while the neutral singlet fermion is odd. We will denote the Z_2-odd neutral singlet fermion as χ to differentiate it from the sterile neutrino since the Z_2 symmetry forbids the mass term $m_D\bar{\nu}N$ characteristic of the latter. Correspondingly, the Z_2 symmetry forbids the single-β decay $(A, Z) \to (A, Z+1) + e + \chi$, as well as the double-$\beta$ decay $(A, Z) \to (A, Z+2) + 2e + \nu + \chi$. However, the $\chi\chi\beta\beta$ decay introduced in equation 3.2 is possible. The search for spectral distortions in the double-β decay spectrum can therefore probe scenarios with light Z_2-odd singlet fermions.

The total differential decay rate receives in this scenario two contributions:

$$\frac{d\Gamma}{dT} = \frac{d\Gamma_{\nu\nu}}{dT}\,\theta(T_0 - T) + \frac{d\Gamma_{\chi\chi}}{dT}\,\theta(T_0 - T - 2x_\chi)\,, \tag{3.12}$$

where $d\Gamma_{\nu\nu}/dT$ is the SM contribution, defined in equation 3.4, and $d\Gamma_{\chi\chi}/dT$ is the exotic contribution. Here, T and T_0 are defined as in equation (3.3), with $x_\chi = m_\chi/m_e$.

The exotic contribution is very model dependent. For definiteness, we will consider the following effective interaction between the active neutrinos and χ:

$$\mathcal{L} = g_\chi \nu\nu\chi\chi\,, \tag{3.13}$$

with a constant coupling g_χ. We use the results of [20], which considered a similar four-fermion scalar interaction as in equation 3.13 but for neutrino self-interactions, to relate the decay rate for the $\chi\chi\beta\beta$ decay to that of the NN$\beta\beta$ decay. We obtain

$$\frac{d\Gamma_{\chi\chi}}{dT} = \frac{g_\chi^2 m_e^2}{8\pi^2 R^2}|\mathcal{M}_{0\nu}|^2 \frac{d\mathcal{G}^{(0)}_{\chi\chi}}{dT}\,, \tag{3.14}$$

where $\mathcal{M}_{0\nu}$ is the NME of the $0\nu\beta\beta$ decay, R is the nuclear radius and the phase factor $\mathcal{G}^{(0)}_{\chi\chi}$ is given in equation 3.5 (replacing m_N by m_χ). The translation of experimental measurements into constraints on g_χ will hence need to rely on NME calculations.

3.4 Discovery potential of future double-β decay experiment

A large experimental program has been mounted to search for the $0\nu\beta\beta$ decay of different isotopes using different detection techniques, as discussed in chapter 2. Among the experiments proposed for the next decade, we will focus on LEGEND [21], nEXO [22] and CUPID [23]. We selected these experiments because their efficiencies

Isotope	Experiment	$T_{1/2}^{2\nu\beta\beta}$ [yr]	Efficiency	Exposure [mol yr]
^{76}Ge	GERDA	$2.0 \cdot 10^{21}$ [27]	75% [24]	$1.4 \cdot 10^{3}$ [28]
	LEGEND-200			$1.4 \cdot 10^{4}$ [21]
	LEGEND-1000			$1.4 \cdot 10^{5}$ [21]
^{136}Xe	EXO-200	$2.2 \cdot 10^{21}$ [25]	85% [25]	$1.7 \cdot 10^{3}$ [29]
	nEXO			$3.7 \cdot 10^{5}$ [22]
^{100}Mo	CUPID-Mo	$7.1 \cdot 10^{18}$ [26]	91% [26]	$6.5 \cdot 10^{-1}$ [26]
	CUPID			$2.7 \cdot 10^{4}$ [23]

TABLE 3.1: Parameters used for the sensitivity projections of each experiment. $T_{1/2}^{2\nu}$ is the double-β decay half-life, *i.e.* the inverse of the decay rate $R_{2\nu}$. The detection efficiency refers to the fraction of $2\nu\beta\beta$ decay events that populate the energy window of interest after all analysis cuts. The exposure is given in numbers of moles of detector material per year of live time.

and uncertainties in the search for massive fermions can be inferred from the $2\nu\beta\beta$ decay analysis published by their predecessors, *i.e.*, GERDA [24], EXO-200 [25] and CUPID-Mo [26]. The parameters assumed for each experiment are listed in table 3.1.

3.4.1 Statistical analysis

While the target isotope and the backgrounds vary across these experiments, the analysis to search for light exotic fermions is always conceptually the same. The energy window of interest goes from the detector threshold to the $Q_{\beta\beta}$ of the decay. In this window, the majority of the events are due to $2\nu\beta\beta$ decays ($> 95\%$ in the current-generation experiments). The other events can be due to a multitude of processes, for instance, natural radioactivity and cosmic rays. The most important parameters affecting the sensitivity of an experiment to light exotic fermions are the exposure, the background rate, and the systematic uncertainties due to the energy reconstruction. The exposure is given by the product of the number of observed nuclei and the observation time. The background rate is primarily given by the $2\nu\beta\beta$ decay rate with a subdominant contribution due to the other sources. The systematic uncertainties related to the event energy reconstruction can largely differ between experiments, but in general, their impact can be parametrized through an energy-dependent shape factor.

To accurately quantify the sensitivity of the experiments, we have implemented a comprehensive frequentist analysis framework. Distortions of the double-β decay energy distribution due to light exotic fermions are searched through a binned maximum-likelihood fit based on a profile-likelihood test statistic [30]. Each process possibly contributing to the count rate in the energy window of interest should be added to the fit through a probability distribution function (PDF) that describes its expected event energy distribution. For this work, we use a PDF for the sought-after signal and one for the dominant $2\nu\beta\beta$ decay. Both these PDFs are based on the

calculations described in the previous sections. We use a third uniform probability distribution to account for other generic sub-dominant background sources. The actual shape of this third PDF affects only marginally our results. The parameters of the fit are the scaling factors of each PDF, *i.e.* the number of events attributed to each process.

The probability distributions of the test statistic are computed from large ensembles of pseudo-data generated under different hypotheses on the signal rate. This approach provides the right coverage by construction, including when the signal rate is close to the physical border.

3.4.2 Impact of systematic uncertainties

Systematic uncertainties can bias the event energy reconstruction. Many detector-specific sources of bias should be considered. However, their overall impact can be parameterized through a shape factor with the form

$$f(E) = 1 + a \cdot E + b \cdot E^2 + c/E \,, \tag{3.15}$$

where a, b and c are parameters that are considered to be known with limited accuracy (*i.e.* σ_a, σ_b and σ_c). Current-generation experiments are typically able to control the energy reconstruction bias at the percent level. To incorporate this systematic uncertainty in our analysis, we randomize a, b, and c during the generation of the pseudo-data and run the fit using not-deformed PDFs [31]. The parameters are sampled from normal distributions centred at 0 and with a sigma of $10^{-3}\,\mathrm{keV}^{-1}$, $10^{-6}\,\mathrm{keV}^{-2}$ and $10^{-3}\,\mathrm{keV}$, respectively. We tested that this parameterization covers the maximal distortions estimated by the experiments. The result of this procedure is a broadening of the test statistic distribution and a reduction of the power of the statistical analysis.

Figure 3.2 shows our projected sensitivity for a generic ^{76}Ge experiment and a sterile neutrino with a mass of 500 keV. The sensitivity for different background rates and exposure values is given as the median 90% C.L. upper limit on $\sin^2\theta$ [30].

The upper limit scales approximately as the sum in quadrature of the statistical and systematic uncertainties. As long as the statistical uncertainty is dominant, the upper limit improves by increasing the exposure. The sensitivity saturates when the statistical uncertainty becomes comparable with the systematic one. The vertical lines in the figure mark the exposure that has been collected by GERDA, as well as the exposure planned for the two phases of LEGEND. LEGEND has the potential to improve the sensitivity by one order of magnitude compared to GERDA, assuming that the systematic uncertainties can be kept below the statistical uncertainty. A significant improvement is expected even in the conservative scenario in which the systematic uncertainties are not reduced compared to the current level.

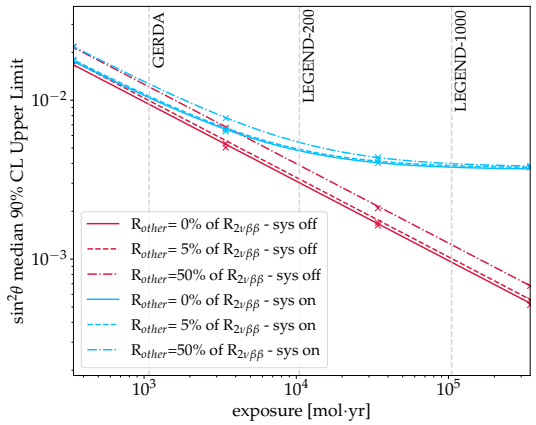

FIGURE 3.2: Sensitivity of a ^{76}Ge double-β decay experiment searching for massive sterile neutrinos with a mass of 500 keV, given as a function of exposure and background level. The sensitivity is expressed in terms of the median 90% C.L. upper limit on the squared of the mixing angle ($\sin^2\theta$), computed assuming no signal. The markers indicate the value computed using a full frequentist analysis, while the lines show their best fit with a function $f(\mathcal{E}) = \sqrt{\sigma^2_{\text{stat}}(\mathcal{E}) + \sigma^2_{\text{sys}}} = \sqrt{\alpha/\mathcal{E} + \beta}$ where α and β are free parameters and $\mathcal{E}$ is the exposure. The plot shows the impact of additional backgrounds with a rate R_{other} which is expressed w.r.t. the irreducible $2\nu\beta\beta$ decay rate $R_{2\nu\beta\beta}$.

3.4.3 Sensitivity projections

The parameter of interest for sterile neutrino searches is the mixing angle, *i.e.*, the ratio between the number of reconstructed νN$\beta\beta$ and $2\nu\beta\beta$ decay events. If we express the statistical uncertainty on the number of decays in terms of the $2\nu\beta\beta$ decay rate ($R_{2\nu\beta\beta}$) and exposure ($\mathcal{E}$) and propagate these uncertainties to the mixing angle, we find that the sensitivity scales as $\sin^2\theta \propto \sqrt{1/(\mathcal{E}\cdot R_{2\nu\beta\beta})}$. The parameter of interest for the search of Z_2-odd fermions is instead the number of $\chi\chi\beta\beta$ decay events, and its conversion into a coupling constant also requires the NME $\mathcal{M}$ and phase space factor $\mathcal{G}$. By propagating the uncertainties, we obtain that the sensitivity scales as $g^2_\chi \propto \mathcal{G}^{-1}\mathcal{M}^{-2}\sqrt{R_{2\nu\beta\beta}/\mathcal{E}}$. In both cases the sensitivity is proportional to $1/\sqrt{\mathcal{E}}$, but the functional dependence from $R_{2\nu\beta\beta}$ is inverted. The complete derivation of the analytical expression of the sensitivity for the two considered cases is given in appendix A. In sterile neutrino searches, the larger $2\nu\beta\beta$ decay rate, the larger the number of νN$\beta\beta$ decays. An increase of $R_{2\nu\beta\beta}$ will hence lead to a reduction of the statistical uncertainty. In the search for $\chi\chi\beta\beta$ decays, the $2\nu\beta\beta$ decay constitutes a background. The higher the background, the lower the sensitivity is. Because of this difference, isotopes favorable for one search might not be optimal for the other.

Our sensitivity projections for the search for sterile neutrinos and Z_2-odd fermions are shown in figure 3.3. The sensitivities are shown using bands in which the upper edge corresponds to the conservative scenario in which the systematic uncertainties will not be improved compared to the current-generation experiments. In contrast,

the lower edge corresponds to the optimistic scenario in which they will be subdominant. These two scenarios define the ballpark for the sensitivity of future experiments, and the results for intermediate scenarios can be interpolated from these two cases. The sensitivity evolution as a function of the fermion mass has a parabolic shape. Its minimum depends on the $Q_{\beta\beta}$ of the decay and corresponds to the fermion mass for which the experiment is most sensitive. The experiments quickly lose sensitivity towards vanishing masses. This is because the smaller the fermion mass, the smaller the spectral distortion. A similar loss of sensitivity occurs at larger masses, where the fermion mass approaches the maximum energy available in the decay and the phase space shrinks[1]. The exposure, isotope properties, and experimental parameters define the offset of the curves. These projections assume that each experiment can extend its analysis window to arbitrarily small energies. If this is not the case, the upper edge of the curve will be lowered by the value of the energy threshold, and the offset will slightly increase because of the reduction in detection efficiency. The sensitivity on the coupling constant g_χ is computed from the decay rate of the $\chi\chi\beta\beta$ decay, using equation 3.14. In addition to the systematic uncertainty considered for the sterile neutrino search, the width of the bands also accounts for the uncertainties due to the NME calculations.

3.5 Results and outlook

The main results of our analysis are displayed in figure 3.3. The left panel shows the projected upper limits on the active-sterile mixing, parametrized as $\sin^2\theta$, as a function of the sterile neutrino mass. We also show in the plot the current limits from single-β decay experiments [3, 4, 10, 11] and from solar neutrinos [32]. As can be seen from the plot, the sensitivity of current double-β decay experiments is weaker than the existing limits, but only by a factor of a few. The larger exposure of future double-β decay experiments encourages a dedicated search for these exotic decay channels.

Indeed, our sensitivity study demonstrates the potential of future double-β decay experiments to improve the current limits on the active-sterile mixing angle in this mass range. Figure 3.3 shows our projected sensitivities for LEGEND-1000, nEXO, and CUPID, assuming no improvement in the systematic uncertainties compared to the current-generation experiments (upper side of the bands) or assuming that the systematic uncertainties will be reduced below the statistical ones (lower side of the bands). In the most conservative scenario, the sensitivity of future searches will be comparable to the current limits. However, even with a modest reduction of the systematic uncertainties, next-generation experiments will explore uncharted

[1] Fermions with masses up to the $Q_{\beta\beta}$ of the decay could be produced, although with significantly suppressed phase space. When the simultaneous production of two fermions is considered, the maximum mass is equal to half of the $Q_{\beta\beta}$.

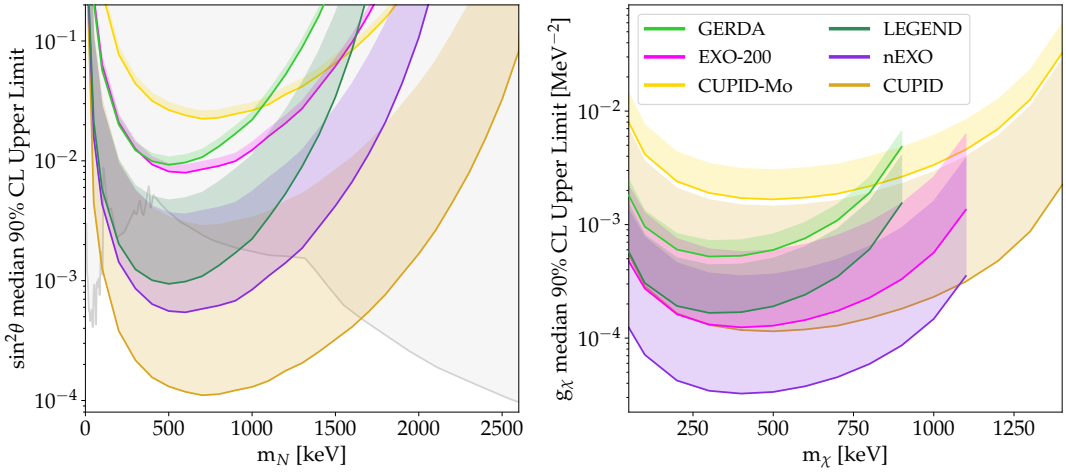

FIGURE 3.3: Sensitivity to light exotic fermions for a selection of double-β decay experiments. The left panel shows the median 90% C.L. upper limit on the squared of the sterile neutrino mixing angle as a function of its mass. The experimental constraints are displayed through a band covering a range of sensitivities from the most optimistic scenario (systematic uncertainty smaller than statistical uncertainty) to a conservative scenario (systematic uncertainty at the level of past analyses). Existing sterile neutrino constraints from single-β decay experiments [3, 4, 10, 11] and solar neutrinos [32] are shown in the background. The right panel shows the median upper limit on the coupling constant between Z_2-odd fermion and the neutrinos assuming the effective interaction in equation 3.13. The spread of the bands account for the systematic uncertainties as in the case of the sterile neutrinos, but additionally it covers also the full range of possible NME values found in literature [18, 33–42].

regions of the sterile neutrino parameter space, even reaching $\sin^2\theta \sim 10^{-3} - 10^{-4}$ for $m_N \sim (100 - 1600)$ keV.

Double-β decay experiments also have the capability of probing models in which only the double production of light exotic fermions is allowed. This previously overlooked opportunity can lead to the first constraints on this kind of model. This is shown in the right panel of figure 3.3 for the Z_2-odd singlet χ introduced in section 3.3. The sensitivities of current experiments for the effective coupling g_χ lie between 10^{-2} and 10^{-3} MeV^{-2}, which could be improved up to 10^{-4} MeV^{-2} with a favorable NME value and negligible systematic uncertainties.

Assuming that this effective interaction originates at some scale Λ with $\mathcal{O}(1)$ dimensionless Wilson coefficient, this would imply that $\Lambda \sim 100$ MeV. This is comparable to the typical momentum transfer in double-β decay experiments, and therefore the effective field theory approach employed in this work to recast the limits on the decay rate into limits on the coupling strength should be taken with a grain of salt. Yet, the search for distortions in the double-β decay spectrum due to the emission of two light exotic particles (fermions or scalars) is well motivated theoretically and deserves further investigation.

Cosmological observations offer complementary constraints on the existence of long-lived light exotic fermions. For the values of the mixing angles that can be probed by future and planned double-β decay experiments, the light exotic fermion would thermalize with the primeval plasma and thereby alter the successful predictions of the standard Big Bang nucleosynthesis scenario [43, 44]. One should note that the strong constraints from cosmology can be circumvented if the light exotic fermion decays before the onset of the nucleosynthesis reactions, for instance, if the Z_2 symmetry is only approximate, so that χ is still produced in pairs and stable within the detectors, but is not cosmologically long-lived, or if N decays promptly into invisible particles. Therefore, it is of utmost importance to perform searches for exotic light fermions in laboratory experiments, as their implications for cosmology depend on additional parameters (most notably their lifetime).

Note added During the final stages of this project, a preprint by Bolton *et al.* [45] appeared, also exploring the possibility of searching for sterile neutrinos with double-β decay experiments. While they focus exclusively on sterile neutrinos (left and right-handed models) we considered generic single and double production of light exotic fermions. Their procedure to derive the sensitivity projections and their treatment of the systematic uncertainties differ from ours. Nevertheless, in the aspects where our analysis overlap, the results are qualitatively similar.

References

[1] M. Agostini, E. Bossio, A. Ibarra, and X. Marcano. "Search for Light Exotic Fermions in Double-Beta Decays". In: *Phys. Lett. B* 815 (2021), p. 136127. DOI: 10.1016/j.physletb.2021.136127. arXiv: 2012.09281.

[2] P. D. Bolton, F. F. Deppisch, and P. S. Bhupal Dev. "Neutrinoless double beta decay versus other probes of heavy sterile neutrinos". In: *JHEP* 03 (2020), p. 170. DOI: 10.1007/JHEP03(2020)170. arXiv: 1912.03058.

[3] J. Deutsch, M. Lebrun, and R. Prieels. "Searches for admixture of massive neutrinos into the electron flavor". In: *Nucl. Phys. A* 518 (1990), pp. 149–155. DOI: 10.1016/0375-9474(90)90541-S.

[4] K. Schreckenbach, G. Colvin, and F. Von Feilitzsch. "Search for mixing of heavy neutrinos in the β^+ and β^- spectra of the ^{64}Cu decay". In: *Phys. Lett. B* 129 (1983), pp. 265–268. DOI: 10.1016/0370-2693(83)90858-4.

[5] R. E. Shrock. "New Tests For, and Bounds On, Neutrino Masses and Lepton Mixing". In: *Phys. Lett. B* 96 (1980), pp. 159–164. DOI: 10.1016/0370-2693(80)90235-X.

[6] A. S. Riis and S. Hannestad. "Detecting sterile neutrinos with KATRIN like experiments". In: *JCAP* 02 (2011), p. 011. DOI: 10.1088/1475-7516/2011/02/011. arXiv: 1008.1495.

[7] S. Mertens et al. "Sensitivity of Next-Generation Tritium Beta-Decay Experiments for keV-Scale Sterile Neutrinos". In: *JCAP* 02 (2015), p. 020. DOI: 10.1088/1475-7516/2015/02/020. arXiv: 1409.0920.

[8] A. Abada, A. Hernández-Cabezudo, and X. Marcano. "Beta and Neutrinoless Double Beta Decays with KeV Sterile Fermions". In: *JHEP* 01 (2019), p. 041. DOI: 10.1007/JHEP01(2019)041. arXiv: 1807.01331.

[9] KATRIN Collaboration, M. Aker, et al. "Bound on 3+1 Active-Sterile Neutrino Mixing from the First Four-Week Science Run of KATRIN". In: *Phys. Rev. Lett.* 126.9 (2021), p. 091803. DOI: 10.1103/PhysRevLett.126.091803. arXiv: 2011.05087.

[10] E. Holzschuh et al. "The β-spectrum of ^{35}S and search for the admixture of heavy neutrinos". In: *Phys. Lett. B* 482 (2000), pp. 1–9. DOI: 10.1016/S0370-2693(00)00476-7.

[11] A. V. Derbin et al. "Search for a Neutrino with a Mass of 0.01 - 1.0 MeV in Beta Decays of ^{144}Ce and ^{144}Pr Nuclei". In: *JETP Lett.* 108.8 (2018), pp. 499–503. DOI: 10.1134/S0021364018200067.

[12] M. Doi et al. "Neutrino Mass, the Right-handed Interaction and the Double Beta Decay.II: General Properties and Data Analysis". In: *Prog. Theor. Phys.* 66 (1981). [Erratum: Prog.Theor.Phys. 68, 348 (1982)], p. 1765. DOI: 10.1143/PTP.66.1765.

[13] M. Doi, T. Kotani, and E. Takasugi. "Double beta Decay and Majorana Neutrino". In: *Prog. Theor. Phys. Suppl.* 83 (1985), p. 1. DOI: 10.1143/PTPS.83.1.

[14] W. C. Haxton and G. J. Stephenson. "Double beta Decay". In: *Prog. Part. Nucl. Phys.* 12 (1984), pp. 409–479. DOI: 10.1016/0146-6410(84)90006-1.

[15] T. Tomoda. "Double beta decay". In: *Rept. Prog. Phys.* 54 (1991), pp. 53–126. DOI: 10.1088/0034-4885/54/1/002.

[16] J. Kotila and F. Iachello. "Phase space factors for $\beta^+\beta^+$ decay and competing modes of double-β decay". In: *Phys. Rev. C* 87.2 (2013), p. 024313. DOI: 10.1103/PhysRevC.87.024313. arXiv: 1303.4124.

[17] D. Stefanik, F. Šimkovic, and A. Faessler. "Structure of the two-neutrino double-β decay matrix elements within perturbation theory". In: *Phys. Rev. C* 91.6 (2015), p. 064311. DOI: 10.1103/PhysRevC.91.064311. arXiv: 1506.00835.

[18] F. Šimkovic, A. Smetana, and P. Vogel. "$0\nu\beta\beta$ nuclear matrix elements, neutrino potentials and SU(4) symmetry". In: *Phys. Rev. C* 98.6 (2018), p. 064325. DOI: 10.1103/PhysRevC.98.064325. arXiv: 1808.05016.

[19] H. Primakoff and S. P. Rosen. "Double beta decay". In: *Rept. Prog. Phys.* 22.1 (1959), pp. 121–166. DOI: 10.1088/0034-4885/22/1/305.

[20] F. F. Deppisch et al. "Neutrino Self-Interactions and Double Beta Decay". In: *Phys. Rev. D* 102.5 (2020), p. 051701. DOI: 10.1103/PhysRevD.102.051701. arXiv: 2004.11919.

[21] LEGEND Collaboration, N. Abgrall, et al. "The Large Enriched Germanium Experiment for Neutrinoless Double Beta Decay (LEGEND)". In: *AIP Conf. Proc.* 1894.1 (2017), p. 020027. DOI: 10.1063/1.5007652. arXiv: 1709.01980.

[22] nEXO Collaboration, S. Al Kharusi, et al. "nEXO Pre-Conceptual Design Report". 2018. arXiv: 1805.11142.

[23] CUPID Collaboration, W. R. Armstrong, et al. "CUPID pre-CDR". 2019. arXiv: 1907.09376.

[24] GERDA Collaboration, M. Agostini, et al. "Results on $\beta\beta$ decay with emission of two neutrinos or Majorons in ^{76}Ge from GERDA Phase I". In: *Eur. Phys. J. C* 75.9 (2015), p. 416. DOI: 10.1140/epjc/s10052-015-3627-y. arXiv: 1501.02345.

[25] EXO-200 Collaboration, J. B. Albert, et al. "Improved measurement of the $2\nu\beta\beta$ half-life of ^{136}Xe with the EXO-200 detector". In: *Phys. Rev. C* 89.1 (2014), p. 015502. DOI: 10.1103/PhysRevC.89.015502. arXiv: 1306.6106.

[26] E. Armengaud et al. "Precise measurement of $2\nu\beta\beta$ decay of ^{100}Mo with the CUPID-Mo detection technology". In: *Eur. Phys. J. C* 80.7 (2020), p. 674. DOI: 10.1140/epjc/s10052-020-8203-4. arXiv: 1912.07272.

[27] GERDA Collaboration, M. Agostini, et al. "Modeling of GERDA Phase II data". In: *JHEP* 03 (2020), p. 139. DOI: 10.1007/JHEP03(2020)139. arXiv: 1909.02522.

[28] GERDA Collaboration, M. Agostini, et al. "Final Results of GERDA on the Search for Neutrinoless Double-β Decay". In: *Phys. Rev. Lett.* 125.25 (2020), p. 252502. DOI: 10.1103/PhysRevLett.125.252502. arXiv: 2009.06079.

[29] EXO-200 Collaboration, G. Anton, et al. "Search for Neutrinoless Double-β Decay with the Complete EXO-200 Dataset". In: *Phys. Rev. Lett.* 123.16 (2019), p. 161802. DOI: 10.1103/PhysRevLett.123.161802. arXiv: 1906.02723.

[30] G. Cowan et al. "Asymptotic formulae for likelihood-based tests of new physics". In: *Eur. Phys. J. C* 71 (2011). [Erratum: Eur.Phys.J.C 73, 2501 (2013)], p. 1554. DOI: 10.1140/epjc/s10052-011-1554-0. arXiv: 1007.1727.

[31] R. D. Cousins and V. L. Highland. "Incorporating systematic uncertainties into an upper limit". In: *Nucl. Instrum. Meth. A* 320 (1992), pp. 331–335. DOI: 10.1016/0168-9002(92)90794-5.

[32] Borexino Collaboration, G. Bellini, et al. "New limits on heavy sterile neutrino mixing in ^{8}B decay obtained with the Borexino detector". In: *Phys. Rev. D* 88.7 (2013), p. 072010. DOI: 10.1103/PhysRevD.88.072010. arXiv: 1311.5347.

[33] J. Barea, J. Kotila, and F. Iachello. "$0\nu\beta\beta$ and $2\nu\beta\beta$ nuclear matrix elements in the interacting boson model with isospin restoration". In: *Phys. Rev. C* 91.3 (2015), p. 034304. DOI: 10.1103/PhysRevC.91.034304. arXiv: 1506.08530.

[34] J. Menéndez. "Neutrinoless $\beta\beta$ decay mediated by the exchange of light and heavy neutrinos: The role of nuclear structure correlations". In: *J. Phys. G* 45.1 (2018), p. 014003. DOI: 10.1088/1361-6471/aa9bd4. arXiv: 1804.02105.

[35] M. Horoi and A. Neacsu. "Shell model predictions for ^{124}Sn double-β decay". In: *Phys. Rev. C* 93.2 (2016), p. 024308. DOI: 10.1103/PhysRevC.93.024308. arXiv: 1511.03711.

[36] N. López Vaquero, T. R. Rodríguez, and J. L. Egido. "Shape and pairing fluctuations effects on neutrinoless double beta decay nuclear matrix elements". In: *Phys. Rev. Lett.* 111.14 (2013), p. 142501. DOI: 10.1103/PhysRevLett.111.142501. arXiv: 1401.0650.

[37] T. R. Rodriguez and G. Martinez-Pinedo. "Energy density functional study of nuclear matrix elements for neutrinoless $\beta\beta$ decay". In: *Phys. Rev. Lett.* 105 (2010), p. 252503. DOI: 10.1103/PhysRevLett.105.252503. arXiv: 1008.5260.

[38] L. S. Song et al. "Nuclear matrix element of neutrinoless double-β decay: Relativity and short-range correlations". In: *Phys. Rev. C* 95.2 (2017), p. 024305. DOI: 10.1103/PhysRevC.95.024305. arXiv: 1702.02448.

[39] J. Hyvärinen and J. T. Suhonen. "Nuclear matrix elements for $0\nu\beta\beta$ decays with light or heavy Majorana-neutrino exchange". In: *Phys. Rev. C* 91.2 (2015), p. 024613. DOI: 10.1103/PhysRevC.91.024613.

[40] M. T. Mustonen and J. Engel. "Large-scale calculations of the double-β decay of ^{76}Ge,^{130}Te,^{136}Xe, and ^{150}Nd in the deformed self-consistent Skyrme quasiparticle random-phase approximation". In: *Phys. Rev. C* 87.6 (2013), p. 064302. DOI: 10.1103/PhysRevC.87.064302. arXiv: 1301.6997.

[41] D. Fang, A. Faessler, and F. Šimkovic. "$0\nu\beta\beta$-decay nuclear matrix element for light and heavy neutrino mass mechanisms from deformed quasiparticle random-phase approximation calculations for ^{76}Ge, ^{82}Se, ^{130}Te, ^{136}Xe , and ^{150}Nd with isospin restoration". In: *Phys. Rev. C* 97.4 (2018), p. 045503. DOI: 10.1103/PhysRevC.97.045503. arXiv: 1803.09195.

[42] L. Coraggio et al. "Calculation of the neutrinoless double-β decay matrix element within the realistic shell model". In: *Phys. Rev. C* 101.4 (2020), p. 044315. DOI: 10.1103/PhysRevC.101.044315. arXiv: 2001.00890.

[43] Aaron C. Vincent et al. "Revisiting cosmological bounds on sterile neutrinos". In: *JCAP* 04 (2015), p. 006. DOI: 10.1088/1475-7516/2015/04/006. arXiv: 1408.1956.

[44] N. Sabti et al. "Refined Bounds on MeV-scale Thermal Dark Sectors from BBN and the CMB". In: *JCAP* 01 (2020), p. 004. DOI: 10.1088/1475-7516/2020/01/004. arXiv: 1910.01649.

[45] P. D. Bolton et al. "Two-Neutrino Double Beta Decay with Sterile Neutrinos". In: *Phys. Rev. D* 103.5 (2021), p. 055019. DOI: 10.1103/PhysRevD.103.055019. arXiv: 2011.13387.

Part II

Search for new physics with GERDA Phase II

Chapter 4

The GERDA experiment

The GERDA experiment searched for $0\nu\beta\beta$ decay of ^{76}Ge with enriched HPGe detectors in liquid argon (LAr) at the LNGS in central Italy. GERDA Phase II has been taking data from December 2015 to November 2019, with only one short interruption for an upgrade in Summer 2018.

During the full Phase II, the GERDA experiment was operated in *background-free* regime[1], combining low-radioactive materials, passive shielding, germanium detectors with superior energy resolution, and active discrimination of signal and background events by their different topology.

In this chapter, the GERDA Phase II experiment is introduced. The data-taking scheme, data selection procedure, and data structure are discussed. Finally, the final GERDA Phase II exposure is given. The analysis techniques utilized for active background suppression will be discussed in the next chapter. As part of this dissertation work, the data selection of the last year of GERDA data, as described in section 4.4 of this chapter, was carried out together with other members of the Collaboration.

4.1 High-purity germanium detectors

The GERDA experiment utilized HPGe detectors enriched in ^{76}Ge. HPGe detectors are operated under reverse bias to achieve fully depleted detectors: a positive voltage is applied to the n^+ electrode with respect to the p^+ contact. In the depleted volume, an electric field is established by both the applied bias voltage and the charge density due to the impurity concentration [1]. Energy deposition in the depleted volume creates several electron-hole pairs proportional to the deposited energy. The charge carriers drift according to the electric field; electrons are collected at the n^+ contact and holes at the p^+ contact, which is used for read-out.

The n^+ layer covers most of the crystal surface of HPGe detectors. In this layer, a reduced electric field exists such that charges created there move only by thermal diffusion and can either recombine or reach the depleted volume. Consequently, the charge collection efficiency (CCE) in this region is reduced. For each HPGe detector, we can identify an active volume (AV), where all charges are collected (CCE = 1), a

[1] Here we speak about *background free* regime when the number of expected background events in the ROI, over the full experiment exposure, is smaller than 1.

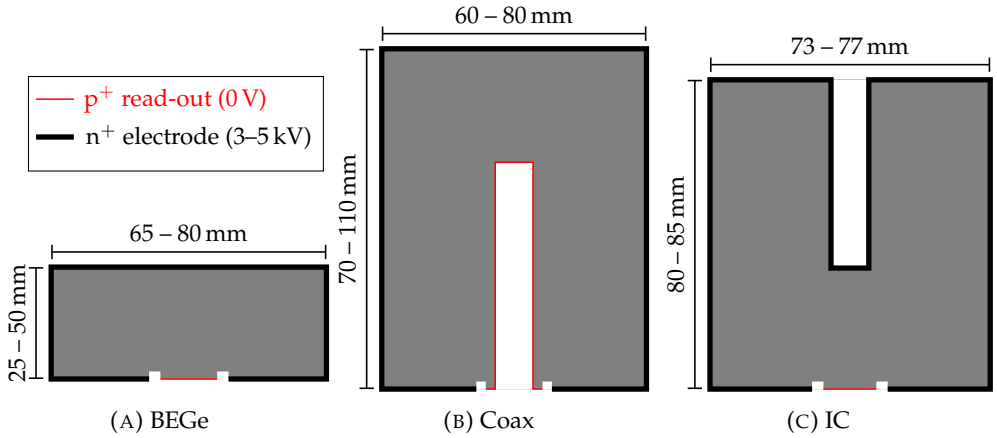

FIGURE 4.1: Cross-section of the different HPGe detector geometries used in GERDA Phase II. The boron implanted p^+ read-out electrode and the lithium diffused n^+ electrode are indicated. Their average thickness is about 100 nm and 1 mm, respectively. The typical dimensions of each geometry are also indicated.

dead layer (DL), where no charges are collected (CCE = 0), and an intermediate semi-active layer, the transition layer (TL), with incomplete charge collection (0 < CCE < 1) [2].

All the GERDA HPGe detectors were made from p-type germanium material and featured lithium diffused n^+ and boron implanted p^+ electrode separated by a groove with a non-conducting surface. The n^+ layer has a thickness of about 1 mm, while the p^+ layer is only about 100 nm thick.

During the entire Phase II, three different types of HPGe detectors were used, namely coaxial (Coax) detectors, Broad Energy Germanium (BEGe) detectors, and inverted coaxial (IC) detectors. The different geometries and performances of each type are described in the following. Their cross-sections are shown in figure 4.1.

Coax detectors The Coax detectors used in GERDA Phase II were already deployed in Phase I [3] and in the predecessors Heidelberg-Moscow [4] and IGEX [5] experiments.

HPGe detectors with a coaxial geometry have one electrode at the outer cylindrical surface, the n^+ contact, in the case of the GERDA Coax detectors, and the second electrode over a concentric borehole, the p^+ contact, where the GERDA Coax detectors are read out. This configuration allows large masses to be depleted, but on the other hand, the energy resolution is limited by the relatively high capacitance of the large read-out electrode. The response of the Coax detectors shows a considerable variation inside the detector volume. This results in a limited discrimination power between single-site and multi-site energy depositions using pulse shape analysis.

At the beginning of Phase II, seven enriched Coax detectors were deployed (after the upgrade, only six), with enrichment fractions ranging from 85.5% to 88.3%. The mass of the GERDA Coax detectors ranges from 2.1 kg to 3.0 kg, with only one exception of a smaller detector with a mass of 0.96 kg, removed during the upgrade.

Successively removed during the upgrade, three natural detectors, coaxial detectors with natural isotopic abundance (7.8%), were also deployed before the upgrade.

BEGe detectors The BEGe detectors were introduced in Phase II of the experiment to increase the exposure via an increase of the total detector mass and improve the background suppression via an enhanced pulse shape performance.

The BEGe detectors have cylindrical (conical in a few cases) shapes with a wrap-around n^+ electrode and a small p^+ read-out electrode, separated by a small insulating groove. The small read-out electrode has a very low detector capacitance and an excellent energy resolution [6]. The advantage of the BEGe geometry is also to have a uniform detector response that results in a high discrimination power between single-site and multi-site energy depositions using pulse shape analysis [7]. On the other hand, this configuration restricts the detector mass, which can be depleted.

During the entire Phase II, 30 BEGe detectors were deployed, with an enrichment fraction of about 88%. Their average mass is 667 g.

IC detectors The IC detectors have similar geometry to the Coax detectors but substantially different electrode configurations. In the IC design, the p^+ read-out contact is reduced to a small electrode on the closed face of the detector crystal. The n^+ contact extends over the rest of the cylindrical surface and throughout the surface of the borehole. The presence of the borehole allows depletion of a large volume, comparable to that of the Coax detectors. On the other hand, the reduced dimensions of the p^+ contact allow for smaller detector capacitance and an excellent energy resolution, comparable to that of BEGe detectors [8]. In addition, the IC detectors provide similar pulse shape analysis performance to the smaller BEGe detectors [9]. However, collective effects in the charge carriers' clusters on the signal formation become important due to longer drift paths [10].

During the upgrade, five enriched IC detectors were deployed in GERDA, with an average mass of 1.6 kg and a mean enrichment fraction of 87.8%.

Due to their main characteristics, namely large mass, excellent energy resolution, and good pulse shape analysis performance, the IC detectors represent the baseline detector geometry to be used in LEGEND [11].

4.2 The GERDA Phase II setup

The GERDA experiment was located underground at the LNGS of INFN, in central Italy. A rock overburden of 3500 m water equivalent reduces the flux of cosmic muons at the experimental site by six orders of magnitude, to 1.2 muons /(m^2 h) [12].

The HPGe detectors were operated inside a 4 m-diameter cryostat made from stainless steel and an internal copper shield [13]. The cryostat was filled with 64 m^3 of radiopure LAr, which cools the detectors at their operating temperature of about 90 K and shields them from external radiation. Further, the cryostat was surrounded

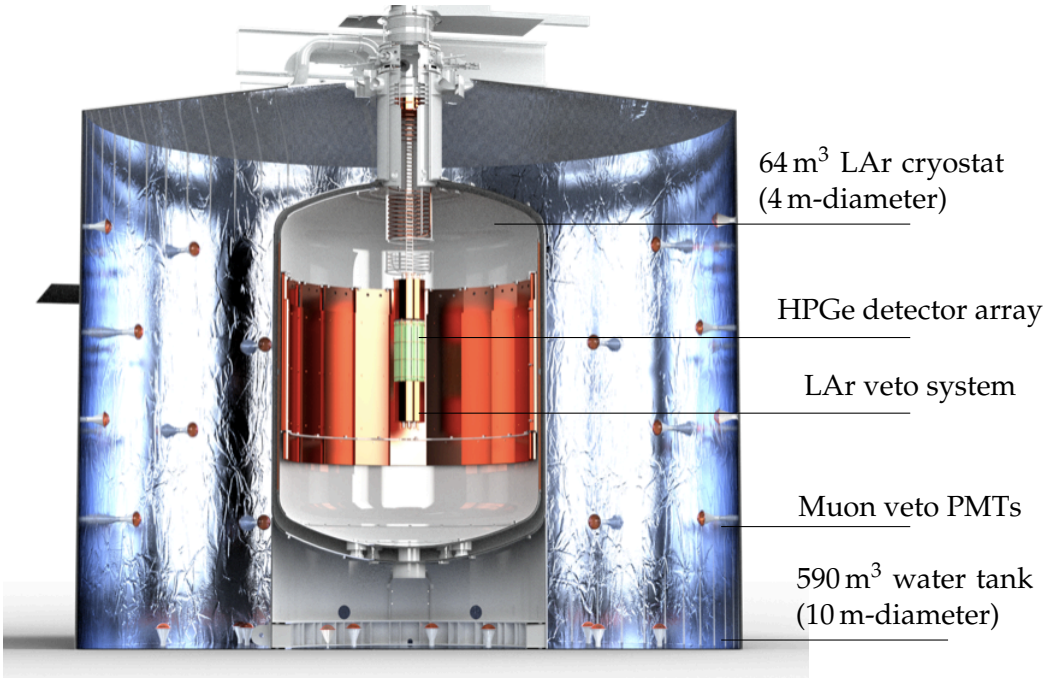

FIGURE 4.2: Artistic view of the GERDA Phase II setup. The main components are indicated. Image credit to *P. Krause*.

by a 10 m-diameter water tank containing 590 m^3 of pure water, which completes the passive shield [14].

The array of HPGe detectors was lowered into the LAr cryostat through a lock system situated inside a clean room on top of the experiment. The clean room was instrumented with a glove box for clean handling and deployment of the detectors [14].

The unique feature of the GERDA Phase II setup is the instrumentation of the LAr volume, which allows rejecting events in which energy is deposited in the LAr surrounding the germanium detectors [14]. This is described in detail in 4.2.2.

Figure 4.2 represents the GERDA Phase II setup.

4.2.1 The detector array

The HPGe detectors were assembled into a compact 7-strings array configuration. Each string was placed inside a transparent nylon cylinder (mini-shroud), to limit the accumulation of radioactive ions like ^{42}K on the detector surfaces [15]. The inside and the outside of the mini-shroud were covered with tetraphenyl butadiene (TPB) to shift the LAr scintillation light to >400 nm, where the nylon is transparent.

Before the upgrade, the enriched detectors were arranged in six strings, with BEGe and Coax detectors kept in separated strings. The natural detectors were mounted in the center of the array. The total mass of HPGe detectors was 43.2 kg, with 35.6 kg of enriched material.

During the upgrade, in the spring of 2018, the natural detectors in the central string were replaced by four IC detectors. In addition, one of the Coax detectors,

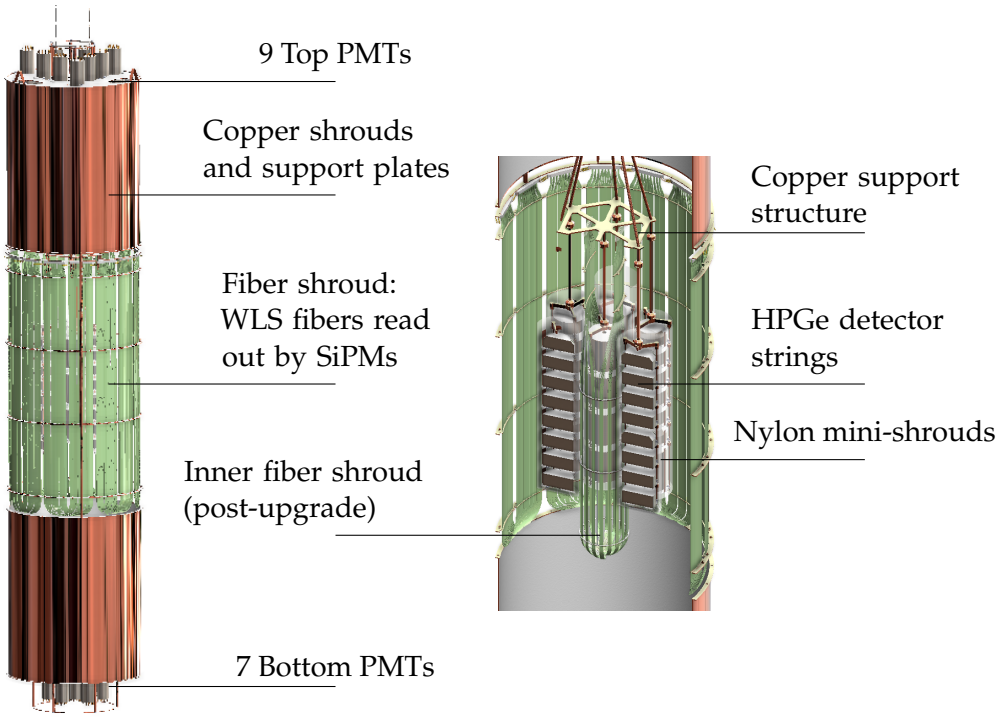

FIGURE 4.3: Artistic view of the GERDA Phase II setup. Zoom on the LAr instrumentation and the HPGe detector array. The main components are indicated. The inner fiber shroud was introduced during the upgrade in the Summer 2018. Image credit to *P. Krause*.

the smallest one, was replaced by one IC detector. The total mass of HPGe detectors increased to 44.2 kg, all made of enriched material.

A representation of the HPGe detector array is shown in figure 4.3.

4.2.2 The LAr instrumentation

Some energy can be deposited in the argon in background events, producing scintillation light. A cylindrical volume of 0.5 m diameter and 2.2 m height around the detector array was instrumented with light sensors to detect this scintillation light [14].

The LAr instrumentation consists of a curtain of wavelength-shifting (WLS) fibers, read out at both ends with 90 silicon photomultipliersss (SiPMs) grouped in 15 readout channels. In addition, 16 3-inch low-background cryogenic photomultiplier tubess (PMTs) were mounted at the top (9 PMTs) and bottom (7 PMTs) of the cylindrical volume on two copper support plates. Due to the high intrinsic Th/U radioactivity of the PMT components, they were placed at $>$1 m from the germanium detectors. The surfaces of the copper shrouds and support plates were lined with TetraTex to enhance the reflection of visible light into the instrumented LAr volume.

The fibers, the PMTs, and the TetraTex-covered surfaces were coated with TPB to shift the LAr scintillation light from 128 nm to about 400 nm, to match the peak quantum efficiency of the PMTs and the absorption maximum of the fibers. The efficiency of the complete wavelength shifting chain was estimated to be about 60% [16].

During the upgrade, the LAr instrumentation underwent major design improvements [17]. The most noticeable change affected the geometry of the fiber shroud. The number of fibers increased by 50%. Consequently, the number of SiPMs increased by the same amount, but they were grouped such that the number of read-out channels was still 15. The new design resulted in a denser fiber curtain, thus in higher coverage and higher light yield. A central fiber shroud was also introduced, with 81 additional fibers and 18 additional SiPMs grouped in 2 read-out channels. It surrounded the central detector string to improve the background suppression in the array's center.

A representation of the LAr instrumentation is shown in figure 4.3.

4.2.3 The water Cherenkov detector

The remaining muon flux at the experimental site is low but sufficient to cause a non-negligible background in searching for $0\nu\beta\beta$ decay and other BSM physics. Muons can contribute to the energy spectrum through direct energy deposition or decay radiation of spallation products.

The GERDA experiment was equipped with a muon veto system to detect the residual cosmic muons reaching the detector site. The muon veto system consisted of two independent parts. The main part was a water Cherenkov veto to detect Cherenkov light of muons passing through the water tank, with 66 PMTs mounted in the water tank. The second part of the muon veto was obtained with three layers of plastic scintillator panels, 36 panels in total, mounted on top of the clean room and covering the central $4\times3\,\mathrm{m}^2$, where the Cherenkov veto offered reduced tagging capability. The detection efficiency for muons with potential energy depositions in the vicinity of the detector array was $99.2^{+0.3}_{-0.4}$ % [12].

4.3 Data taking

GERDA Phase II data taking started in December 2015; it was shortly interrupted in Summer 2018 for the upgrade of the setup and lasted until November 2019.

The data taking was organized in runs. Each run should contain data taken under the same hardware configuration without any change to the setup.

During physics data taking, all waveforms from the HPGe detectors and LAr instrumentation (PMTs and SiPM) were recorded once the signal in one of the HPGe detectors exceeded a certain threshold. Given the very low event rate of the order of 10 mHz in physics data taking, all the waveforms were fully digitized and stored for offline analysis. Each HPGe detector waveform was recorded at a sampling frequency of 25 MHz for a total trace length of 160 μs. We will refer to it as low frequency (LF) trace. In addition, the central $\pm5\,\mu$s around the signal trigger were recorded with the maximum sampling frequency of 100 MHz. We will refer to it as high frequency (HF) trace. While the LF trace was utilized for most Digital Signal

Processing (DSP) tasks, the HF trace allowed high precision analysis of the pulse formation. The PMTs waveforms were recorded at a sampling frequency of 100 MHz. The traces covered a time window between -5 and 7 μs around the HPGe detector trigger. The SiPM waveforms were recorded at a reduced sampling frequency of 12.5 MHz, with a longer trace covering a time window between -40 and 80 μs around the trigger.

Each physics run was preceded and followed by a calibration run to monitor the energy scale and pulse shape parameters over time. Calibration data was taken with radioactive sources inserted into the detector array, with an activity of the order of 10 kBq. The relatively high event rate in calibration runs would permanently saturate the SiPMs and ultimately damage them. Consequently, in calibration runs, PMTs and SiPMs were turned off and only the HPGe detector waveforms were recorded.

Special calibration runs were also performed in GERDA Phase II. During these *photon calibration* runs, low activity calibration sources of the order of 1 kBq were inserted into the detector array allowing the data-taking configuration of the physics run, with all the HPGe detector, PMTs, and SiPM waveforms being recorded. These special calibration runs were performed twice during the whole GERDA Phase II period. The corresponding data was used to study the performance of the LAr veto [16].

In addition to the HPGe detector, PMT, and SiPM waveforms, artificial waveforms were recorded regularly during the whole data taking. Test Pulses (TPs) were injected into the preamplifier of each HPGe detector at a constant rate of 50 mHz and 500 mHz during physics and calibration data takings, respectively. Empty traces, characterized by a flat baseline (BL), were also recorded every 47 s (after the upgrade 40 s). These artificial waveforms were used to monitor the stability of the data taking and to estimate the efficiency of the quality cuts (QC), which will be discussed in the following.

A GERDA Phase II event consists of 40 (after the upgrade 41) HPGe detector waveforms, 16 PMT waveforms, and 15 (after the upgrade 17) SiPM waveforms. All of them were utilized to evaluate the event. The muon veto featured an independent data acquisition system providing a muon veto flag stored for each event as auxiliary information.

4.4 Data selection

A careful data validation process was performed manually at the end of each run. Parameters like the waveform baseline, baseline RMS, and the calibrated and uncalibrated TP amplitude were inspected for each detector.

If unstable behaviors were observed in an individual detector, it was set to be used only for detector anti-coincidence (AC) in the corresponding run. A detector in AC mode was used to define the multiplicity of the event, *i.e.* the number of

coincident signals in the HPGe detectors, but its energy scale was considered unreliable. Problematic detectors which did not produce proper signals were set to be OFF, and they were completely ignored in the analysis. The rest of the detectors, stable and properly calibrated, were considered ON, and they contributed to the analysis exposure.

Periods in which the stability of the entire system could not be guaranteed were not considered at all for analysis. Files containing such instabilities were removed from the list of files to be used for analysis (analysis key lists). The typical file length was about 3 h, corresponding to approximately 0.01 kg yr of exposure.

The criteria used to determine the analysis key lists and the status of each detector in each run are described in the following.

- Hardware/environment changes: these included instabilities at the beginning of data taking (both before and after the upgrade) due to ^{222}Rn decay, operations in the clean room, power losses, and temperature changes in the electric cabinet. If the bias voltage of a detector was changed during the data-taking run without consecutive calibration, the detector was set to AC mode for the whole run.

- Stability of the energy scale: the TP events were used to monitor the stability of each detector. Periods in which no TPs were available for any of the HPGe channels were completely removed from the analysis key lists. If the TPs were missing in one specific detector, this was set to AC mode. Instabilities in the TP amplitude were observed in detectors developing high leakage currents. They were set to AC mode. A detector was considered stable if the fluctuations of the TP amplitude (normalized to the input amplitude) were below 0.1%.[2]

- Non-Poissonian rate distribution: individual files in which the event rate was anomalously high were removed from the analysis key lists. The average rate of physics events above 200 keV was 0.0093 events/s^{-1} for the full Phase II exposure. The time distribution of these events was built with a very fine binning, such that the average number of counts in each bin was 1. The distribution of the bin populations was then compared to a Poisson distribution. Given the expectation value of one count per bin, bins containing more than 12 counts, expected with a probability of $\sim 10^{-3}$, were considered anomalous and removed from the analysis key.

- Stability of the LAr veto system: periods in which the full capabilities of the LAr veto system could not be guaranteed were removed from the analysis list, *e.g.* high rate in PMT/SiPM channels, not operable PMTs/SiPMs.

[2] Excpections were made for groups of channels connected to the same electronics which showed coherent fluctuations in the TP amplitude, if the position of the 2.6 MeV γ line in the previous and following calibrations was stable within 3 keV.

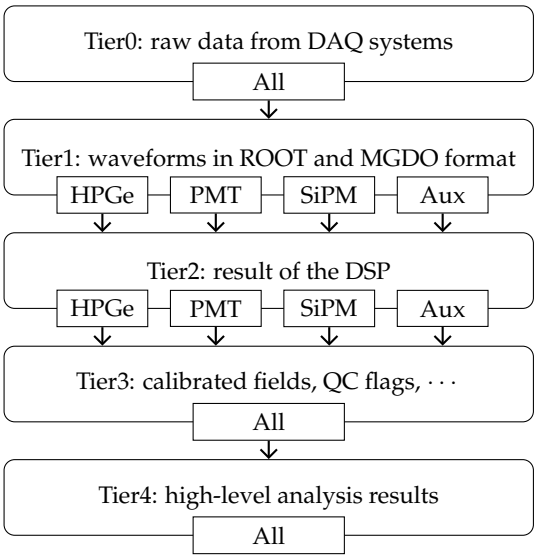

FIGURE 4.4: Multi-level structure of GERDA data.

4.5 Data processing

The event information at successive analysis steps was stored in a multi-tier hierarchical structure, which is sketched in figure 4.4.

In the first step, the raw data is converted into a new standardized format based on ROOT [18] and the MGDO libraries [19]. The amount of information contained in the lowest level (Tier0) and the successive level (Tier1) is precisely the same. They only differ in the data format: the native DAQ format in Tier0 and the standardized MGDO format in Tier1. In the conversion step, a *blinding* procedure was applied. Events having energies between $Q_{\beta\beta}$ $\pm$25 keV were excluded from Tier1, using the online energy reconstruction of the FADC. The *blind* data was used to define the analysis steps, which were applied to the full *unblind* data only after being finalized.

The following level (Tier2) contains the results of DSP. The DSP algorithms were implemented in the software framework GELATIO [20]. The data processing followed the procedure described in [21]. An essential task of the DSP is reconstructing the energy of the event. The energy was reconstructed using a Zero Area Cusp (ZAC) signal shaping filter, developed for the GERDA experiment, with superior performance than standard filters [22]. The ZAC filter parameters were optimized for each detector periodically using calibration data.

Until the Tier2 level, data from the different detectors (HPGe/PMT/SiPM) are analyzed along separated chains. In the successive level (Tier3), the different streams are integrated together. Tier3 contains information extracted from Tier2, like calibrated energy and calibrated pulse shape parameters, and several event flags, like the QC flags. More details about the QC will be given in the following.

As the analysis becomes more and more refined, the information is stored in higher-level tiers. Tier4 contains the results of the high-level analysis, like the results of pulse shape discrimination (PSD) analysis, coincidence analysis, and LAr veto

analysis. More details about these aspects of the analysis will be given in the next chapter.

4.5.1 Quality cuts

A set of QC was established to identify and reject *non-physical* events.[3] Examples are events not related to any energy deposition (micro-discharges or cross talk) or signals with different characteristics than those for which the DSP algorithms were implemented (pile-up or signals that exceed the FADC dynamic range).

QC were applied event-based, meaning that all the HPGe detector waveforms (except for the detectors classified as OFF) needed to be evaluated to assess the quality of the event [23]. Every event with at least one waveform failing the QC would be rejected. First, all the waveforms must be correctly processed by the FADC and each module of the GELATIO chain. Additional criteria, based on the parameters extracted by the DSP algorithms, were used to classify the waveforms as baseline, physical, or saturated waveforms. Baseline waveforms contain no signal; hence they must be flat and featureless. Physical waveforms must contain one and only one pulse, the first half of the trace must be flat, and the trigger position must be found at the center of the trace. Signals sitting on the tail of a previous event (pre-trace pile-up) were identified through an exponential fit of the baseline, whereas multiple signals in the same waveform (in-trace pile-up) were identified through the number of triggering pulses. The pile-up probability during physics data taking was reduced to a negligible level because of the low event rate. Nevertheless, during calibration data taking, the event rate was much higher, and a significant fraction of pile-up was observed. Stronger criteria on the baseline slope of the calibration waveforms were applied to avoid biases in the energy calibration and pulse shape analysis. Waveforms that saturate the FADC dynamic range were tagged already by the FADC. Some of the GELATIO modules might fail, and the parameters extracted by the DSP algorithms might be unreliable.

Double-β signal events are characterized by one physical waveform and baseline waveforms in all the other channels. The efficiency of the QC for these events was estimated from TP and BL events to be $(99.941 \pm 0.001)\%$.

4.5.2 Energy calibration

As previously mentioned, between the end of a run and the beginning of the following, a calibration with ^{228}Th sources was performed to convert the ZAC estimator to physical energy (in keV). The pattern of γ lines observed in the calibration spectra was used to identify certain γ lines and calibrate the energy scale of a detector with their known energies. Additionally, the width of the γ lines indicates the detector

[3] More precisely, events for which the parameters computed by the DSP algorithms do not have a reliable physical meaning.

	FWHM at $Q_{\beta\beta}$ (keV)	
	pre-upgrade	post-upgrade
BEGe	2.9 ± 0.3	2.6 ± 0.2
Coax	3.6 ± 0.2	4.9 ± 1.4
IC	-	2.9 ± 0.1

TABLE 4.1: Energy resolution (FWHM) at $Q_{\beta\beta}$ for the different detector types, further split in pre- and post-upgrade for BEGe and Coax detectors.

energy resolution. Calibration data was also used to calibrate the parameters used for PSD exploiting the topologies of particular γ ray events in the calibration spectra.

After identifying the γ line peaks in the spectrum, fits were performed locally around each peak to determine their position and energy resolution. Calibration curves were obtained fitting the peak position versus the literature energy with a linear function.[4] On the other hand, the peak widths were fitted as a function of the energy using the semi-empirical formula:

$$\text{FWHM} = 2.355\sigma = 2.355\sqrt{a + b\,E}\,, \tag{4.1}$$

with E being the energy and a and b the fit parameters. This allowed obtaining the energy resolution at different energies, *e.g.* at $Q_{\beta\beta}$. The energy resolutions at $Q_{\beta\beta}$ are summarized in table 4.1 for different detector types and split in pre- and post-upgrade. The energy resolution was calculated by detector type and by partition. The concept of partition was introduced later during GERDA Phase II for the final results on the $0\nu\beta\beta$ decay search. Data from each detector were divided into periods in which all the parameters were stable, *i.e.* partitions. The partition approach improved the physics result by capturing the variations among the detectors and the variation over time. More details can be found in [24, 25]. Still, depending on the specific physics analysis, the energy resolution by detector type may be used.

4.6 Exposures, duty cycle, and data quality

The analysis exposures collected during the entire GERDA Phase II are summarized in table 4.2, for each detector type, split between before and after the upgrade. The total exposure used for the $0\nu\beta\beta$ decay search analysis, which will be presented in chapter 6, amounts to 103.7 kg yr. Data without proper PSD calibration cannot be used for the $0\nu\beta\beta$ analysis. Nevertheless, this can be used for several different analyses, where no PSD evaluation is required, such as the search for 0νECEC of ^{36}Ar, which will be presented in chapter 7. With this additional exposure, the total GERDA Phase II exposure amounts to 105.5 kg yr.

[4] After the upgrade, some detectors (mostly IC and one Coax detector) exhibited large residuals in the calibration curves. These effects could be accounted for by incorporating a quadratic correction to the calibration curve. More details can be found in [24, 25].

	Exposure (kg yr)		
	pre-upgrade	post-upgrade	combined
BEGe	31.5 (+1.3)	21.9 (+0.3)	53.3 (+1.6)
Coax	28.6	13.2	41.8
Natural	9.1	–	9.1
IC	–	8.6 (+0.2)	8.6 (+0.2)
Total	60.1 (+1.3)	43.6 (+0.5)	103.7 (+1.8)

TABLE 4.2: GERDA Phase II exposures in kg yr. The numbers in brackets correspond to additional exposure, where no PSD evaluation is available. This is not used for the $0\nu\beta\beta$ decay search analysis, but it can be used for different analyses. The total exposure is meant to be used for analysis and does not include the exposure accumulated with the natural detectors.

	duty cycle (%)	data quality (%)
pre-upgrade	93.0	80.7
post-upgrade	95.3	79.7
combined	87.7	80.3

TABLE 4.3: GERDA Phase II duty cycle and data quality. The combined duty cycle includes the additional time for upgrade works.

Before the upgrade, the duration of the data taking was 847.7 d, of which 788.6 d correspond to the data's lifetime. The duty cycle, *i.e.* the data's lifetime divided by the time required to collect them, is 93.0% for the pre-upgrade data. A slightly higher duty cycle was obtained after the upgrade. With a data-taking time of 481.5 d and a lifetime of 458.5 d, the duty cycle for the post-upgrade data is 95.3%. The combined Phase II duty cycle, including the additional time for upgrade works (93.3 d), is 87.7%.

The data quality was estimated by comparing the analysis exposures (listed in table 4.2) with the exposures before the data selection (described in section 4.4). The total exposure before any data selection criteria is 74.5 kg yr for the pre-upgrade data and 54.7 kg yr for the post-upgrade data. The resulting data quality is 80.7% and 79.7%, respectively, for the pre-upgrade and post-upgrade data. The data validation process removed about 20% of the collected data.

These numbers are summarized in table 4.3.

References

[1] Glenn F. Knoll. *Radiation Detection and Measurement*. 1999.

[2] B. Lehnert. "Search for $2\nu\beta\beta$ Excited State Transitions and HPGe Characterization for Surface Events in GERDA Phase II". PhD thesis. Technischen Universität Dresden, 2016. URL: https://www.mpi-hd.mpg.de/gerda/public/2016/phd2016_bjoernLehnert.pdf.

[3] GERDA Collaboration, M. Agostini, et al. "Results on Neutrinoless Double-β Decay of ^{76}Ge from Phase I of the GERDA Experiment". In: *Phys. Rev. Lett.* 111.12 (2013), p. 122503. DOI: 10.1103/PhysRevLett.111.122503. arXiv: 1307.4720.

[4] H. V. Klapdor-Kleingrothaus et al. "Search for neutrinoless double beta decay with enriched Ge-76 in Gran Sasso 1990-2003". In: *Phys. Lett. B* 586 (2004), pp. 198–212. DOI: 10.1016/j.physletb.2004.02.025. arXiv: hep-ph/0404088.

[5] IGEX Collaboration, C. E. Aalseth, et al. "IGEX ^{76}Ge neutrinoless double beta decay experiment: Prospects for next generation experiments". In: *Phys. Rev. D* 65 (2002), p. 092007. DOI: 10.1103/PhysRevD.65.092007. arXiv: hep-ex/0202026.

[6] P. S. Barbeau, J. I. Collar, and O. Tench. "Large-Mass Ultra-Low Noise Germanium Detectors: Performance and Applications in Neutrino and Astroparticle Physics". In: *JCAP* 09 (2007), p. 009. DOI: 10.1088/1475-7516/2007/09/009. arXiv: nucl-ex/0701012.

[7] D. Budjas et al. "Pulse shape discrimination studies with a Broad-Energy Germanium detector for signal identification and background suppression in the GERDA double beta decay experiment". In: *JINST* 4 (2009), P10007. DOI: 10.1088/1748-0221/4/10/P10007. arXiv: 0909.4044.

[8] R.J. Cooper et al. "A novel HPGe detector for gamma-ray tracking and imaging". In: *Nuclear Instruments and Methods in Physics Research Section A: Accelerators, Spectrometers, Detectors and Associated Equipment* 665 (2011). DOI: https://doi.org/10.1016/j.nima.2011.10.008.

[9] A. Domula et al. "Pulse shape discrimination performance of inverted coaxial Ge detectors". In: *Nucl. Instrum. Meth. A* 891 (2018), pp. 106–110. DOI: 10.1016/j.nima.2018.02.056. arXiv: 1711.01433.

[10] T. Comellato, M. Agostini, and S. Schönert. "Charge-carrier collective motion in germanium detectors for $\beta\beta$-decay searches". In: *Eur. Phys. J. C* 81.1 (2021), p. 76. DOI: 10.1140/epjc/s10052-021-08889-0. arXiv: 2007.12910.

[11] LEGEND Collaboration, N. Abgrall, et al. "The Large Enriched Germanium Experiment for Neutrinoless $\beta\beta$ Decay: LEGEND-1000 Preconceptual Design Report". 2021. arXiv: 2107.11462.

[12] K. Freund et al. "The Performance of the Muon Veto of the GERDA Experiment". In: *Eur. Phys. J. C* 76.5 (2016), p. 298. DOI: 10.1140/epjc/s10052-016-4140-7. arXiv: 1601.05935.

[13] K. T. Knöpfle and B. Schwingenheuer. "Design and performance of the GERDA low-background cryostat for operation in water". In: *JINST* 17.02 (2022), P02038. DOI: 10.1088/1748-0221/17/02/P02038. arXiv: 2202.03847.

[14] GERDA Collaboration, M. Agostini, et al. "Upgrade for Phase II of the GERDA experiment". In: *Eur. Phys. J. C* 78.5 (2018), p. 388. DOI: 10.1140/epjc/s10052-018-5812-2. arXiv: 1711.01452.

[15] A. Lubashevskiy et al. "Mitigation of ^{42}Ar/^{42}K background for the GERDA Phase II experiment". In: *Eur. Phys. J. C* 78.1 (2018), p. 15. DOI: 10.1140/epjc/s10052-017-5499-9. arXiv: 1708.00226.

[16] C. Wiesinger. "No neutrinos not found: First exploration of neutrinoless double beta decay half-lives beyond 10^{26} years". PhD thesis. Technische Universität München, 2020. URL: https://mediatum.ub.tum.de/doc/1575899/1575899.pdf.

[17] P. Krause. "The New Liquid Argon Veto of GERDA". Master thesis. Technische Universität München, 2019.

[18] R. Brun et al. *root-project/root: v6.18/02*. Version v6-18-02. 2019. DOI: 10.5281/zenodo.3895860.

[19] M. Agostini et al. "The MGDO software library for data analysis in Ge neutrinoless double-beta decay experiments". In: *J. Phys. Conf. Ser.* 375 (2012), p. 042027. DOI: 10.1088/1742-6596/375/1/042027. arXiv: 1111.7260.

[20] M. Agostini et al. "GELATIO: A General framework for modular digital analysis of high-purity Ge detector signals". In: *JINST* 6 (2011), P08013. DOI: 10.1088/1748-0221/6/08/P08013. arXiv: 1106.1780.

[21] M. Agostini, L. Pandola, and P. Zavarise. "Off-line data processing and analysis for the GERDA experiment". In: *J. Phys. Conf. Ser.* 368 (2012), p. 012047. DOI: 10.1088/1742-6596/368/1/012047. arXiv: 1111.3582.

[22] GERDA Collaboration, M. Agostini, et al. "Improvement of the energy resolution via an optimized digital signal processing in GERDA Phase I". In: *Eur. Phys. J. C* 75.6 (2015), p. 255. DOI: 10.1140/epjc/s10052-015-3409-6. arXiv: 1502.04392.

[23] A. Lazzaro. "Signal processing and event classification for a background free neutrinoless double beta decay search with the GERDA experiment". PhD thesis. Technische Universität München, 2019. URL: https://www.mpi-hd.mpg.de/gerda/public/2019/phd2019_AndreaLazzaro.pdf.

[24] C. Ransom. "Energy Calibration for the GERDA and LEGEND-200 Experiments". PhD thesis. University of Zurich, 2021. URL: https://www.mpi-hd.mpg.de/gerda/public/2021/phd2021_ChloeRansom_compressed.pdf.

[25] GERDA Collaboration, M. Agostini, et al. "Calibration of the GERDA experiment". In: *Eur. Phys. J. C* 81.8 (2021), p. 682. DOI: 10.1140/epjc/s10052-021-09403-2. arXiv: 2103.13777.

Chapter 5

Analysis techniques and background identification

Background discrimination can be achieved with HPGe detectors by analyzing the event topology. In GERDA Phase II, different observables based on event coincidences and pulse shape information were used to separate double-β decay events, *i.e.* single-site energy deposition in one HPGe detector, from different kind of backgrounds.

In preparation for the *unblinding*, which led to the final GERDA results on the search for $0\nu\beta\beta$ decay presented in the next chapter, several background studies were performed to characterize the analysis dataset. In this chapter, the results of the investigation of the intensity of known γ lines and the investigation of the background in the $0\nu\beta\beta$ decay analysis window, performed as part of this dissertation work, are reported.

5.1 The background in GERDA Phase II

Figure 5.1 shows the exposure-normalized background spectra obtained in GERDA Phase II with the BEGe, Coax, and IC detectors after QC, detector anti-coincidence cut, and muon veto cut, but before analysis cuts (LAr veto and PSD). The QC were introduced in section 4.5.1, whereas the other cuts will be introduced in the next section.

Here we focus on the background sources that contribute to the energy spectra. The main contributions are classified in the following.

Cosmic background Cosmic backgrounds are caused by the remaining muon flux reaching the experimental site. As anticipated in the previous chapter, muons can contribute to the energy spectrum through direct energy deposition or decay radiation of spallation products.

Internal $2\nu\beta\beta$ decay ^{76}Ge undergoes the SM $2\nu\beta\beta$ decay with a half-life of about 2×10^{21} yr (see chapter 9). These decays are uniformly distributed in the detector volume.

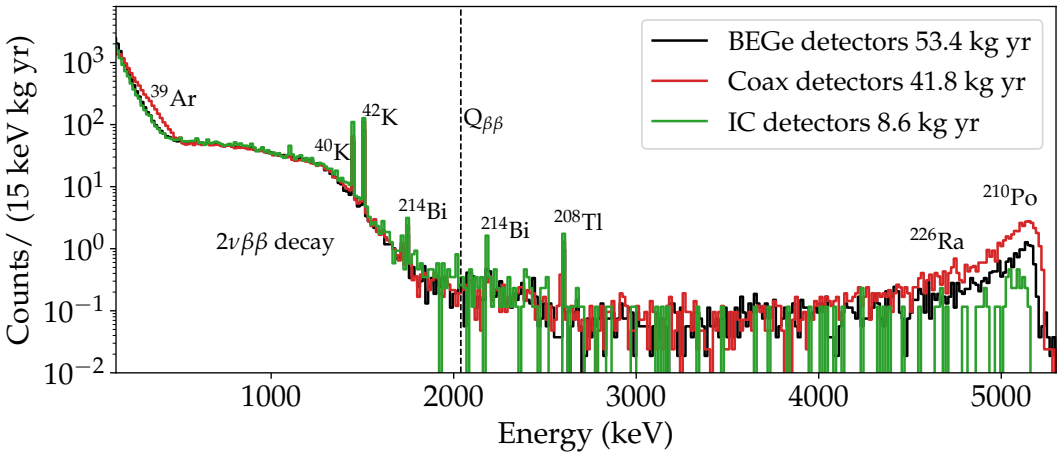

FIGURE 5.1: Exposure-normalized background spectra obtained in GERDA Phase II with the BEGe, Coax, and IC detectors after QC, detector anti-coincidence cut, and muon veto cut, but before analysis cuts. The most prominent features are indicated.

^{238}U and ^{232}Th decay chains An important background contribution to all rare event searches is the natural radioactivity from isotopes of the ^{238}U and ^{232}Th decay chains. These radioactive contaminations are present in all the structural components of the setup. The radio purity of all the materials has been investigated before their deployment through screening measurements [1, 2]. The decay products of the ^{238}U and ^{232}Th decay chains consist of γ, β, or α, and eventually coincidences among them. α particles originate from the ^{210}Po and ^{226}Rn decays. Since they can only penetrate the very thin p^+ contact, they must be emitted directly at the surface or in the very close LAr to be detected. Crossing the p^+ layer, only part of their initial energy is deposited in the active volume. Therefore, the α spectrum exhibits peaks with low-energy tails. γ and β particles are expected at different steps in the decay chains mentioned above, *e.g.* from ^{228}Ac, ^{212}Bi, ^{208}Tl, ^{214}Bi, and ^{214}Pb.

^{40}K ^{40}K is present in all the construction materials. In fact, they were not optimized for ultra-low ^{40}K contents because the Q-value of its decay is well below the $Q_{\beta\beta}$. The ^{40}K decay spectrum exhibits a prominent γ line at 1460.8 keV.

Comsogenic activation products ^{60}Co is produced by cosmogenic activation of copper, largely present in the GERDA setup. The ^{60}Co decay spectrum exhibits two coincident γ lines at 1333 keV and 1173 keV.

LAr contaminations Background contributions are expected from the LAr, which surrounds the detector array. ^{39}Ar is a cosmogenically produced isotope in LAr, which undergoes a β decay with an end-point at about 565 keV. ^{42}Ar is also cosmogenically produced in LAr. It decays to ^{42}K, which then decays to ^{42}Ca via β decay with a half-life of about 12 h and a Q-value of 3525 keV, well above $Q_{\beta\beta}$. For the β

particle to be detected, the decay must happen within a distance of a few centimeters to the detector surface. As the detectors are in direct contact with the LAr, the β component of ^{42}K potentially gives one of the most significant contributions to the background in the ROI. The ^{42}K decay spectrum also exhibits a prominent γ line at 1525 keV. The anthropogenic isotope ^{85}Kr is also present in LAr. It mostly undergoes β decay with a Q-value of 687 keV. In some cases, the decay proceeds through the meta-stable state of the daughter ^{85}Rb nucleus. This is followed by the emission of a 514 keV γ line.

Detector bulk contaminations Cosmogenically produced long-lived isotopes, *e.g.* ^{68}Ge, ^{60}Co, and ^{65}Zn, or bulk contaminations with ^{238}U and ^{232}Th, could also be found in germanium.

The three spectra in figure 5.1 agree well and exhibit the prominent features that were anticipated above: the β decay of ^{39}Ar below 500 keV, the broad continuum $2\nu\beta\beta$ decay between 600 keV and 2000 keV, individual γ lines from the various expected background contaminations up to the 2.6 MeV line from ^{208}Tl, and the α contribution above 3.5 MeV, up to the peak like structure emerging at 5.3 MeV, attributed to ^{210}Po.

The difference in the shape of the ^{39}Ar β decay in Coax detectors compared to BEGe and IC detectors is due to the different DL. Differences in the count rates of the γ lines between detector types were investigated and will be discussed in section 5.3.1. A more significant α contribution is observed in Coax detectors, likely due to the larger p^+ contact where the α contaminations are located. A detailed background model before analysis cuts was obtained with pre-upgrade BEGe and Coax data [3].

5.2 Background discrimination by event topology

Double-β decay events are single-site (SS) events occurring within the bulk of a single HPGe detector. The two electrons emitted in double-β decays produce a very localized energy deposition within $\sim 1\,\text{mm}^3$ in germanium. The SS event topology of double-β decays is sketched in the first drawing in figure 5.2. Internal α and β contaminations may have the same event topology. Potential bulk contaminations in the GERDA HPGe detectors were studied in GERDA Phase I and Phase II [4, 5]. Only upper limits were found, establishing an outstanding radio purity.

On the other hand, the external background contribution previously classified results in events with a larger spatial distribution. Background discrimination can be achieved by exploiting topological information. Observables based on event coincidences and pulse shape information were used in GERDA and are introduced in the following.

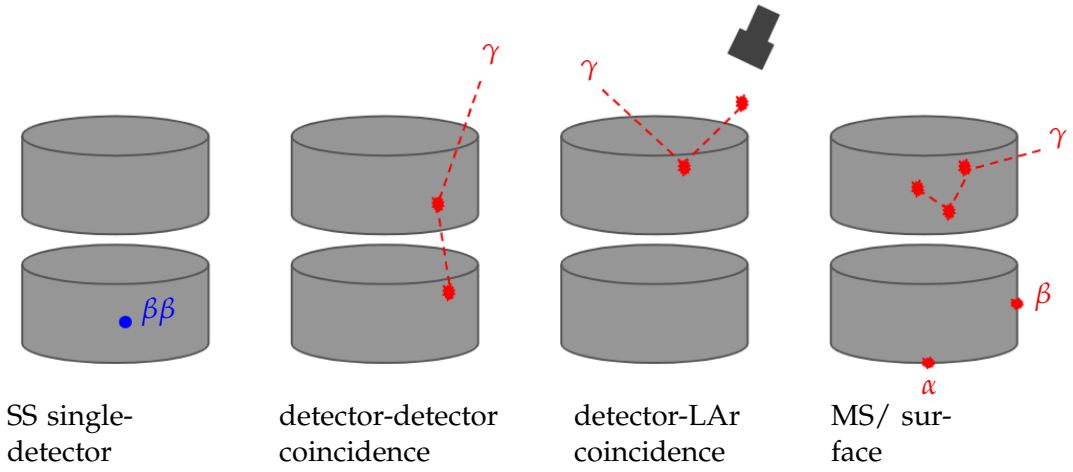

FIGURE 5.2: Signal and background identification by event topology. Double-β decays are SS energy depositions in one HPGe detector. Scattered γ background can be identified by detector-detector and detector-LAr coincidences. Pulse shape analysis allows identifying multi-site (MS) γ energy depositions, and surface β and α energy depositions.

5.2.1 Detector anti-coincidence

The granularity of the HPGe detector array allows for identifying energy depositions spread across multiple detectors.

Before their absorption, γ rays can scatter in the array producing simultaneous energy deposition in more than one HPGe detector. This event topology is sketched in the second drawing in figure 5.2. γ-γ or α / β-γ coincidences can also be identified by the same event topology.

A detector anti-coincidence cut was defined using the multiplicity of the event. The multiplicity of an event is the number of coincident signals in the HPGe detectors. Double-β decay signal events are selected by requiring multiplicity $= 1$.

5.2.2 Muon Veto

The muon veto system introduced in chapter 4 consisting of the water tank instrumented with PMTs and the scintillator panels allows for identifying muons passing through the experiment and correlating them to coincident energy depositions in the HPGe detectors due to muon-induced backgrounds.

A muon veto cut was defined using the muon veto flag provided by the independent DAQ system and the timestamp of the event. All events preceded by a muon trigger by less than 10 μs are rejected with negligible signal loss (<0.1%).

5.2.3 LAr anti-coincidence

The instrumentation with light detectors of the LAr volume in which the HPGe detectors were immersed allowed for the identification of simultaneous interactions

occurring outside the HPGe detectors.

γ background can produce events in which part of the energy is deposited in the HPGe detector and part in the LAr volume, generating scintillation light. This is sketched in the third drawing in figure 5.2. Energy depositions in the LAr are likely caused by γ cascades, where only one of the γ rays in the cascade deposits energy in the HPGe detectors. Also, γ rays undergoing only a single Compton-scattering in the HPGe detectors and being absorbed in the surroundings are likely to produce scintillation light in LAr.

A LAr veto cut was defined using the coincident energy detected by the PMT and SiPM detectors in an event. Events are vetoed if a scintillation signal with amplitude above the threshold is found in a narrow time window around the HPGe trigger. The threshold and time window were optimized channel-by-channel.

The acceptance of double-β decay events to the LAr veto cut was estimated using periodically injected TP and randomly triggered events. This is (97.7$\pm$0.1)% for the pre-upgrade configuration and (98.2$\pm$0.1)% for the post-upgrade design. The deadtime is predominately caused by random coincidences from the ^{39}Ar decays in LAr.

The performance of the LAr veto cut can also be studied on physics data by looking at specific features of the energy spectrum, namely the ^{40}K and ^{42}K full-energy peaks and the energy region dominated by $2\nu\beta\beta$ decays. The impact of the LAr veto cut in this energy region is shown in figure 5.3. The background due to the Compton scattering of the γ rays from ^{40}K and ^{42}K is clearly visible before the LAr veto cut. These events typically feature an energy deposition in the LAr; therefore, they are efficiently rejected by the LAr veto. After the LAr veto cut, the energy spectrum is an almost pure $2\nu\beta\beta$ decay continuum, which allows for precision measurement of the half-life of this process, as will be discussed in chapter 9. ^{42}K decays to ^{42}Ca through β^- transition: the γ ray event is likely to be accompanied by energy deposition in the LAr from the preceding β decay. The LAr veto cut efficiently suppresses these kinds of events. On the other hand, ^{40}K undergoes electron capture to ^{40}Ar, and no energy deposition is expected in the LAr. The suppression of the ^{40}K full-energy peak is (2.51$\pm$0.13) for the pre-upgrade data and (1.97$\pm$0.16)% for the post-upgrade data, in agreement with the deadtime due to ^{39}Ar random coincidences previously mentioned.

5.2.4 Pulse shape discrimination

Two types of background events can be distinguished from SS signal events using PSD: multiple energy deposition within one crystal, *i.e.* multi-site (MS) events, and surface events due to α or β decays on the detector surface. These event topologies are sketched in the last drawing of figure 5.2.

The n^+ electrode has a dead layer of about 1 mm, which stops the α particles. They can reach the active volume only through the much thinner dead layer of the p^+ electrode and the groove. Energy depositions near the p^+ electrode result in fast

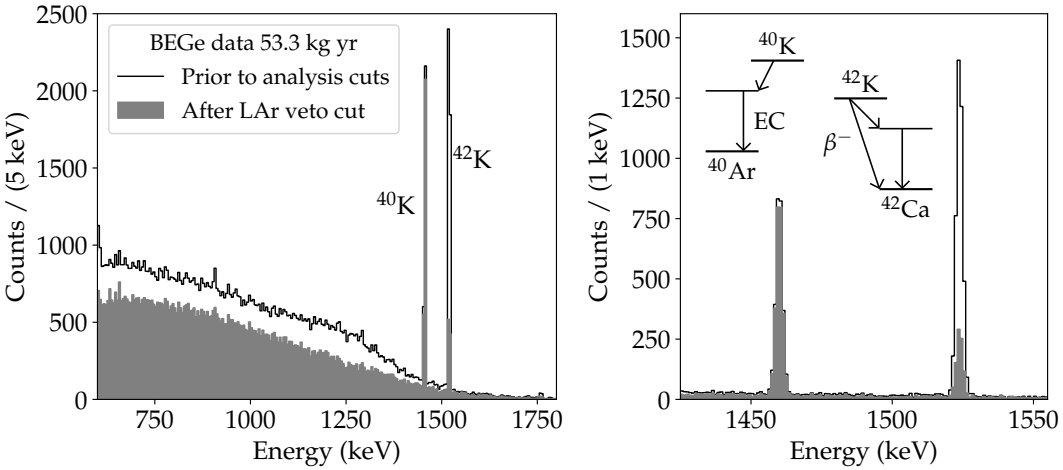

FIGURE 5.3: Performance of the LAr veto cut in physics data. (Left) Energy spectrum in the region dominated by $2\nu\beta\beta$ decay before analysis cuts and after applying the LAr veto cut. (Right) Zoom on the full-energy peaks of ^{40}K and ^{42}K. Their decay schemes are also sketched.

signals because of the stronger electric field in that part of the detector volume. On the other hand, β radiation may penetrate the n^+ dead layer and reach the active volume. Energy depositions near the n^+ electrode can create pulses with long rise time (RT) and incomplete charge collection due to the low electric field in this part of the detector.

The PSD techniques for rejecting MS and surface events depend on the detector geometry and noise condition. For the BEGe and IC detectors, one parameter, A/E, is used, where A is the maximum current amplitude and E is the energy, proportional to the area of the current pulse. Multi-site and n^+ surface events are characterized by wider current pulses, which translate into a low A/E value. On the other hand, p^+ surface events have a high A/E value. The performances of the A/E cut on physics data are shown in figure 5.4. The A/E classifier is shown as a function of the energy for the whole BEGe and IC data: events in the $2\nu\beta\beta$ decay region survive the cut with high probability. On the other hand, the ^{40}K and ^{42}K peaks, featuring MS topology, are significantly reduced, and α events above 3525 keV are all discarded by the A/E cut.

The different geometry and electric field configuration of Coax detectors do not allow using a single parameter for PSD. An artificial neural network (ANN) is used to discriminate between SS and MS events. In addition, a cut on the RT was applied to reject fast signals from p^+ surface events. The performances of the ANN and RT cuts on physics data are shown in figure 5.4. The ANN classifier is shown as a function of the energy for the whole Coax data. The RT is shown for the events surviving the ANN cut as a function of the energy. The ANN cut is particularly efficient in the region highly populated by MS events. On the other hand, the RT cut features a better rejection of α events at high energy.

An additional PSD cut was used for all three detector types to reject events from

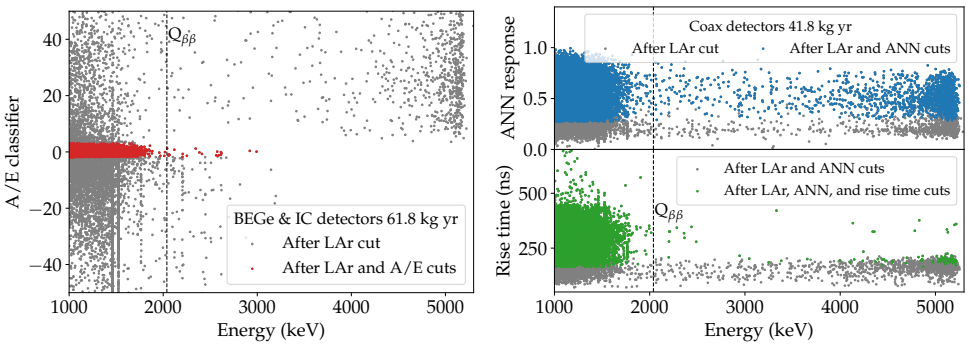

FIGURE 5.4: (Left) A/E classifier of physics events as a function of the energy for BEGe and IC data. (Right) ANN classifier and RT of physics events as a function of the energy for Coax data. The RT is shown only for events surviving the ANN cut.

	Efficiency (%)	
	pre-upgrade	post-upgrade
BEGe	88.2 ± 3.4	89.0 ± 4.1
Coax	69.1 ± 5.6	68.8 ± 4.1
IC	-	90.0 ± 1.8

TABLE 5.1: Combined PSD efficiency at $Q_{\beta\beta}$.

the n^+ contact or the groove featuring slow or incomplete charge collection. These events have an uncertainty on the energy reconstruction due to the short integration time of the ZAC filter [6], and they could survive the standard PSD methods, in particular for Coax detectors. A classifier (δE) was defined using the energy reconstructed with two pseudo-Gaussian filters with different integration times.

The acceptance of the $0\nu\beta\beta$ decay events to the PSD cut was estimated in various ways for the different PSD techniques. We refer to [7] for a complete treatment of the topic. Here, we simply report the combined PSD efficiency at $Q_{\beta\beta}$ for the different detector types, split between pre- and post-upgrade. The numbers are summarized in table 5.1 and were used in the search for $0\nu\beta\beta$ decay presented in chapter 6.

5.2.5 Complementarity of LAr veto and PSD cuts

The LAr veto cut and the PSD cut are highly complementary in the selection of $0\nu\beta\beta$ decay signal events and rejection of background events. To better understand this point, we consider two types of events in the calibration data: the double-escape peak (DEP) of ^{208}Tl and the full-energy peak (FEP) of ^{212}Bi. The energy spectrum around these two peaks is shown in figure 5.5.

The DEP is a SS event with external energy depositions. In the A/E classifier, this appears as a SS event and is therefore accepted as a signal. On the other hand, considerable energy is deposited in the LAr, and the event is vetoed by the LAr veto cut.

The FEP is a fully contained MS event. No energy deposition is expected in the LAr, and the event is accepted by the LAr veto cut. After LAr veto cut, a FEP appears prominently in the spectrum. On the other hand, the MS event is identified by the A/E classifier with a certain efficiency.

The different distributions of the LAr veto and A/E classifiers are shown in figure 5.5. The DEP events are distributed as signal events in the A/E classifier and as background events in the LAr veto classifier. The FEP events are distributed as signal events in the LAr veto classifier and as background in the A/E classifier. Unlike these two cases, a $0\nu\beta\beta$ decay event would be classified as a signal event in both observable parameters.

5.3 Background studies of the final GERDA dataset

5.3.1 Intensity of γ lines

Studies of the intensity of γ lines have been used in GERDA to extract information on the nature and location of the various background contaminations [1, 3].

In this work, we compared the intensity of the known γ lines in the whole spectrum between detector types and between pre-upgrade and post-upgrade data. We fit the different lines using the Bayesian Analysis Toolkit (BAT) software [8, 9] in an energy window of $\pm 15/20$ keV around the γ line energy. A Gaussian model with a strong prior on the peak position and energy resolution (FWHM) was used for the signal, while the background was modeled with a flat, linear, or quadratic function depending on the region of the spectrum. We fit all the lines in BEGe, Coax, and IC datasets, splitting the first two in pre- and post-upgrade. The spectra before analysis cuts were primarily used for extracting the count rates. In some cases, the LAr veto was used, both in anti-coincidence and coincidence, to enhance the sensitivity to specific lines. If no light is expected in coincidence with a FEP, this will appear more prominently after LAr veto cut. On the other hand, peaks belonging to a γ cascade are more likely to appear in coincidence with light in the LAr. The corresponding γ line may be more visible in the data rejected by the LAr veto cut.

All the results are summarized in appendix B. The count rates in BEGe and Coax detectors are mostly consistent for the pre- and post-upgrade datasets. The ^{40}K rate is the only exception. A smaller contamination is observed in the post-upgrade dataset for both BEGe and Coax detectors. The pre-upgrade rates are $49.3^{+1.2}_{-1.4}$ cts/kg yr and $59.5^{+1.4}_{-1.8}$ cts/kg yr, respectively for BEGe and Coax detectors. After the upgrade, these reduce to $44.5^{+1.4}_{-1.6}$ cts/kg yr and $50.0^{+2.5}_{-1.9}$ cts/kg yr. A reduction of about 10% is observed in both datasets. The count rates in the IC detectors are similar to those in the BEGe detectors, with the exception of the higher ^{40}K and ^{42}K rates in the IC detectors.

The two γ lines from ^{40}K and ^{42}K are the most prominent in the spectra and were also investigated detector by detector. Figure 5.6 shows the ^{40}K and ^{42}K count rates

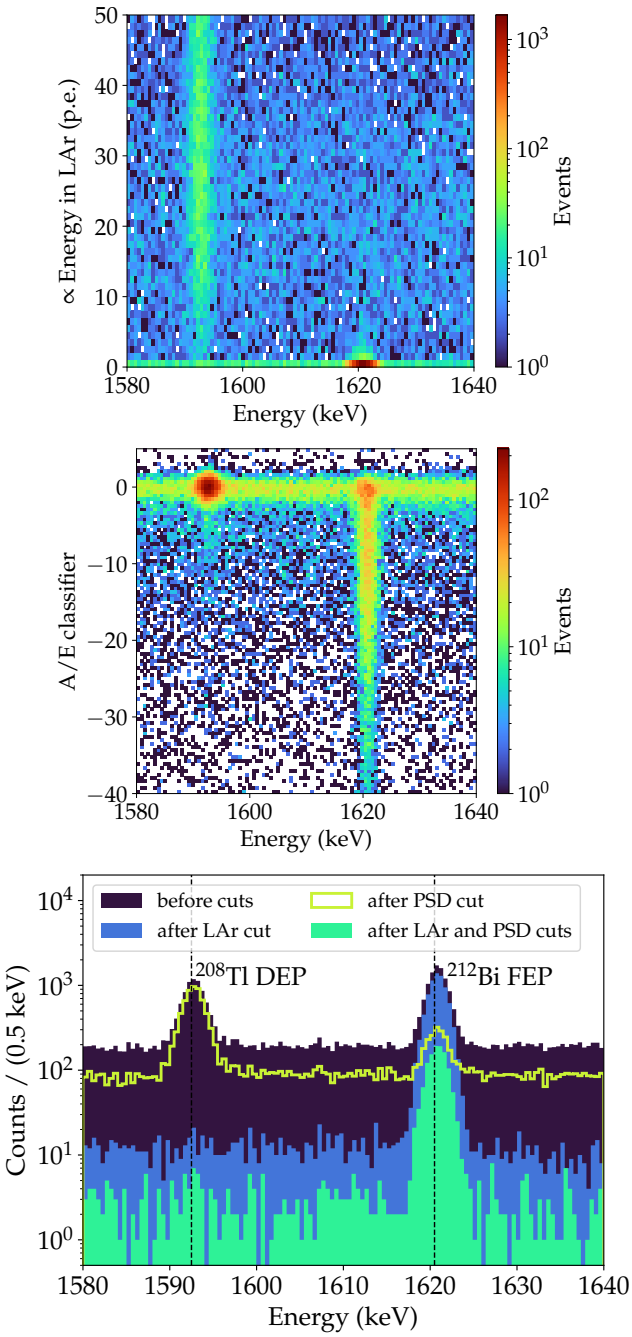

FIGURE 5.5: (Bottom) Energy spectrum of BEGe detectors zoomed on the ^{208}Tl double-escape peak (DEP) and the ^{212}Bi full-energy peak (FEP). Calibration data corresponding to the first photon calibration run was used. The effect of LAr veto cut, PSD cut, and the combination of the two on the peaks is shown. (Center) Distribution of the A/E classifier as a function of the energy. (Top) Distribution of the LAr veto classifier, proportional to the energy deposited in LAr, as a function of the energy. (See text for the interpretation of the figure.)

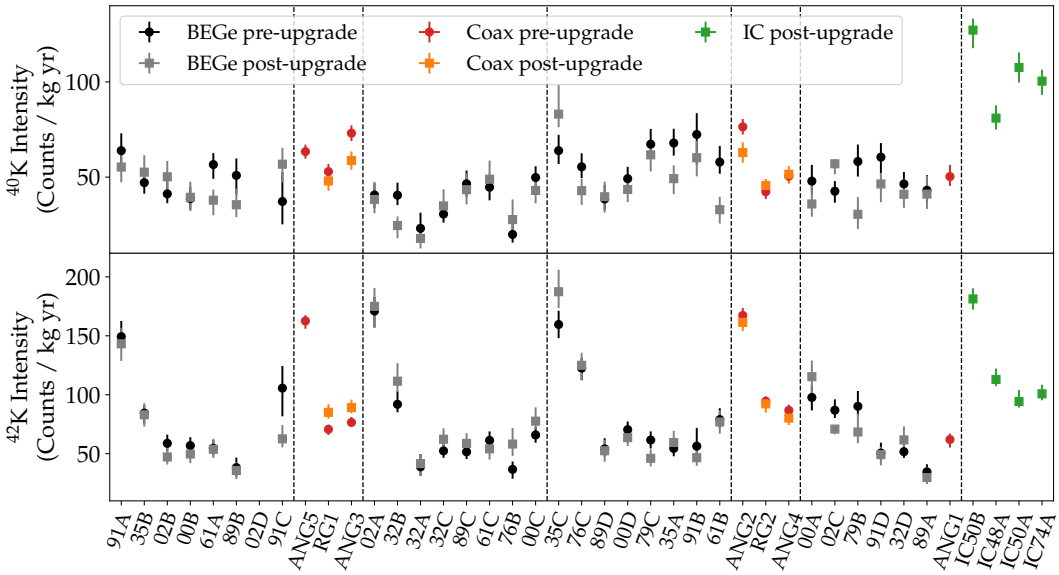

FIGURE 5.6: Intensity of the ^{40}K and ^{42}K γ lines at 1461 keV and 1525 keV, respectively, in each detector (the detector name is shown on the x-axis). The BEGe and Coax data are further split into pre- and post-upgrade. The vertical dashed lines divide the detectors according to the string to which they belong.

for each detector, split into pre- and post-upgrade for BEGe and Coax detectors. The intensity of the ^{40}K and ^{42}K lines in the IC detectors is generally higher, indicating higher contamination in the central part of the array, probably due to the presence of more structural materials. In addition, the ^{42}K rate in the first detector of each detector string is higher than the rate in the other detectors in the same string. These detectors are located at the top of the array. This is an indication of higher contamination of ^{42}K in this part of the array, which is closer to the cables and the electronics.

A "new" feature observed in the post-upgrade data is a γ line at 1125 keV. This is attributed to the γ line of ^{65}Zn at 1115.5 keV, which comes in coincidence with an X-ray, and is well visible only in the IC dataset. Evidence of the same line was already found in the natural detectors, while no indication was ever found in the BEGe and Coax detectors. As anticipated in section 5.1, ^{65}Zn might be produced by cosmogenic activation of the HPGe material. The surface exposure of the GERDA HPGe detectors was kept to a minimum to avoid contamination. The presence of this line in the IC detectors, but not in the BEGe and Coax detectors, could be explained by the longer time that the latter have been underground compared to the IC detectors introduced only after the upgrade.

5.3.2 Background in the $0\nu\beta\beta$ decay analysis window

The analysis window for the $0\nu\beta\beta$ decay search is defined as the union of the following energy windows in keV:

$$[1930, 2099] \vee [2109, 2114] \vee [2124, 2190] \, . \tag{5.1}$$

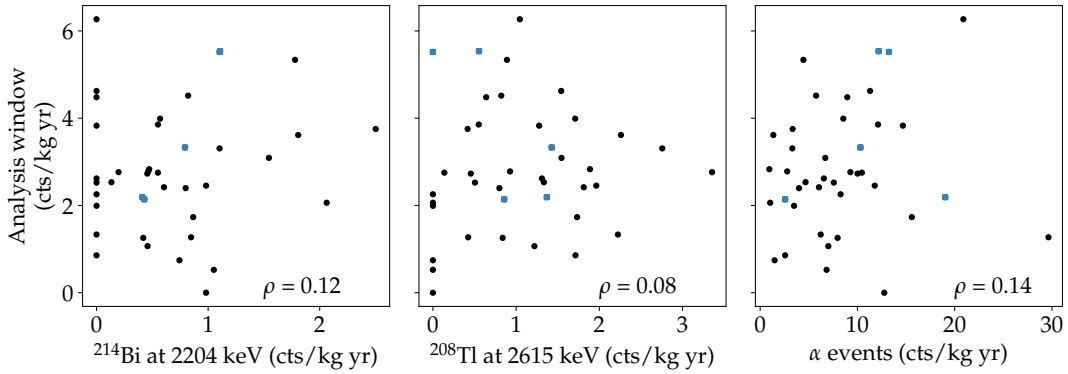

FIGURE 5.7: Correlation between the detector rate of events in the analysis window before analysis cuts and in different energy regions of the spectrum: ^{214}Bi γ line at 2204 keV, ^{208}Tl γ line at 2615 keV, and the αs between 3 and 4.5 MeV. In blue, the detectors with events left in the analysis window after analysis cuts are marked. The correlation coefficient ρ is indicated.

The excluded intervals (2104±5) and (2119±5) keV contain two known background peaks, the DEP from ^{208}Tl at 2104 keV and the FEP from ^{214}Bi at 2119 keV. The analysis window is limited on both sides by potential γ lines, from ^{42}K at 1921 keV and from ^{214}Bi at 2204 keV.

Data previous to the unblinding have been used to study the background's origin and uniformity in the $0\nu\beta\beta$ decay analysis window. The results are presented in the following.

Origin of the background According to the prediction of the background model before analysis cuts [3], the background in the analysis window can be attributed to ^{42}K, ^{232}Th and ^{238}U chains, and α particles with degraded energy, each contributing about equally.

We searched for correlations between the events in the analysis window and some features of the energy spectrum before analysis cuts. Two γ lines, ^{214}Bi at 2204 keV, ^{208}Tl at 2615 keV, and the α population were considered. The count rates were extracted for each detector individually. The rate of the two γ lines was calculated in an energy window of ±10 keV centered at the γ energy. The α's rate was calculated between 3 and 4.5 MeV.

The correlation plots between the count rate in the analysis window and each of the above energy windows are shown in figure 5.7. No indication of any correlation was found; the correlation coefficients are all below the 15%, as indicated in the figure. Special attention was paid to the detectors in which the 7 events were found in the analysis region after analysis cuts happened. These detectors are marked with blue squares in the plots in figure 5.7. No anomalous high count rates were observed for these detectors.

Uniformity of the background In all previous GERDA analyses, to search for $0\nu\beta\beta$ decay, data were divided into two data sets, according to the detector type, *i.e.* BEGe and Coax. The background index (BI) was assumed to be different for the two data sets. Nevertheless, in the last publication before this work [10], a very similar BI was measured for the two data sets: $5.7^{+4.1}_{-2.6} \times 10^{-4}$ counts/(keV kg yr) for the Coax data set and $5.6^{+3.4}_{-2.4} \times 10^{-4}$ counts/(keV kg yr) for the BEGe data set. In this work, the possibility of adopting a unique BI for all Phase II data was explored.

We searched for hints of non-uniformity of the background in the analysis window, depending on the detector, detector type, position within the array, or time. A maximum likelihood method is used to test the uniformity of the background in the analysis window. The model assumes that the counts in the i-th data set follow a Poisson distribution with mean given by $\lambda_i = \text{BI} \times \text{exposure}_i \times \text{energy window}$. The BI is assumed to be uniform among data sets. Given the number of events in each data set, the likelihood of the model writes:

$$\mathcal{L}(N_1, N_2, \dots | \lambda_1, \lambda_2, \dots) = \mathcal{P}(N_1|\lambda_1) \times \mathcal{P}(N_2|\lambda_2) \times \dots \ . \tag{5.2}$$

The test statistic is defined as:

$$t = \mathcal{L}(N_1, N_2, \dots | \lambda_1, \lambda_2, \dots) / \mathcal{L}(N_1, N_2, \dots | N_1, N_2, \dots) \ . \tag{5.3}$$

The probability distribution of the test statistic is evaluated with Monte Carlo (MC) methods, and the p-value of the data is computed. The p-value needs to be interpreted as the probability of obtaining data as extreme as those observed under the assumption of uniform background. The expected BI in the hypothesis of uniform background is 2.7 cts/(kg yr) before analysis cuts, 1.1 cts/(kg yr) after LAr veto cut only, 0.6 cts/(kg yr) after PSD cut only and 0.07 cts/(kg yr) after LAr and PSD cuts. The uniformity was tested for different choices of the data sets and for different combinations of cuts.

- We tested the uniformity of the background among detectors. The top plots of figure 5.8 show the count rates for each detector before analysis cuts, after LAr veto cut only, and after PSD cut only. These are compared to the expectation for a uniform background. The p-values obtained in the hypothesis tests are 0.02, 0.0001, and 0.40, respectively before analysis cuts, after LAr veto cut, and after PSD cut. The same test, performed after both LAr veto and PSD cuts, gives a p-value of 0.17. All the p-values are summarized in table 5.2. The low probabilities obtained before analysis cuts and after LAr veto cut only indicate a weak non-uniformity. This is also visible in the fluctuations of the count rates before analysis cuts and after LAr veto cut that are not fully compatible with the expected Poisson fluctuations. Nevertheless, this result was expected and can be explained by the α contribution to the data sets, which is non-uniform between detectors. The explanation above is supported by two additional tests.

Firstly, the distribution of the counts after high A/E cut is tested for BEGe and IC detectors. In fact, the effect of the high A/E cut is to remove the α contamination from the data sets. Secondly, the distribution of the counts rejected by the LAr veto cut was tested. In both cases, a good agreement with the hypothesis of uniformity between detectors was found. The p-value of the hypothesis test is 0.55 and 0.90, respectively.

- Detectors were grouped successively by the detector type, *i.e.* BEGe, Coax, IC. The bottom plots of figure 5.8 show the count rate per detector type before analysis cuts, after LAr veto cut, and after PSD cut. The background rate appears to be always very uniform between detector types. The p-values obtained in the hypothesis tests are 0.75, 0.95, and 0.09, respectively before analysis cuts, after LAr veto cut, and after PSD cut. The same test, performed after both LAr veto and PSD cuts, gives a p-value of 0.68.

- A test of the background uniformity in time was also performed. All the detectors were grouped together, and data were split into two datasets according to the time at which the events were recorded in relation to the upgrade, *i.e.* pre- or post-upgrade. The count rates of the two datasets are shown in appendix C, figure C.1. The hypothesis test gives p-values of 0.76, 0.64, and 0.03, respectively before analysis cuts, after LAr veto cut, and after PSD cut. The lower p-value after PSD cut could be due to the poor PSD performances of one Coax detector (ANG1) pre-upgrade. Removing this detector from the pre-upgrade dataset, the p-value after PSD improves to 0.18. Testing the uniformity after all analysis cuts gives a p-value of 0.28.

- Finally, detectors were grouped according to their position in the detector array. First, detectors in the same string were grouped together. The count rates per detector string are shown in appendix C, figure C.2. Then, detectors were grouped according to their position along the z-axis, *i.e.* top, middle, and bottom. The count rates for top, middle, and bottom detectors are shown in appendix C, figure C.3.

In conclusion, all the tests showed a very good agreement between the distribution of the counts and the hypothesis of uniformity. Few hints of non-uniformity observed before analysis cuts or after LAr veto cut were well understood and expected to disappear after all analysis cuts. The p-values obtained in the different hypothesis tests are summarized in table 5.2.

References

[1] GERDA Collaboration, K. H. Ackermann, et al. "The GERDA experiment for the search of $0\nu\beta\beta$ decay in ^{76}Ge". In: *Eur. Phys. J. C* 73.3 (2013), p. 2330. DOI: 10.1140/epjc/s10052-013-2330-0. arXiv: 1212.4067.

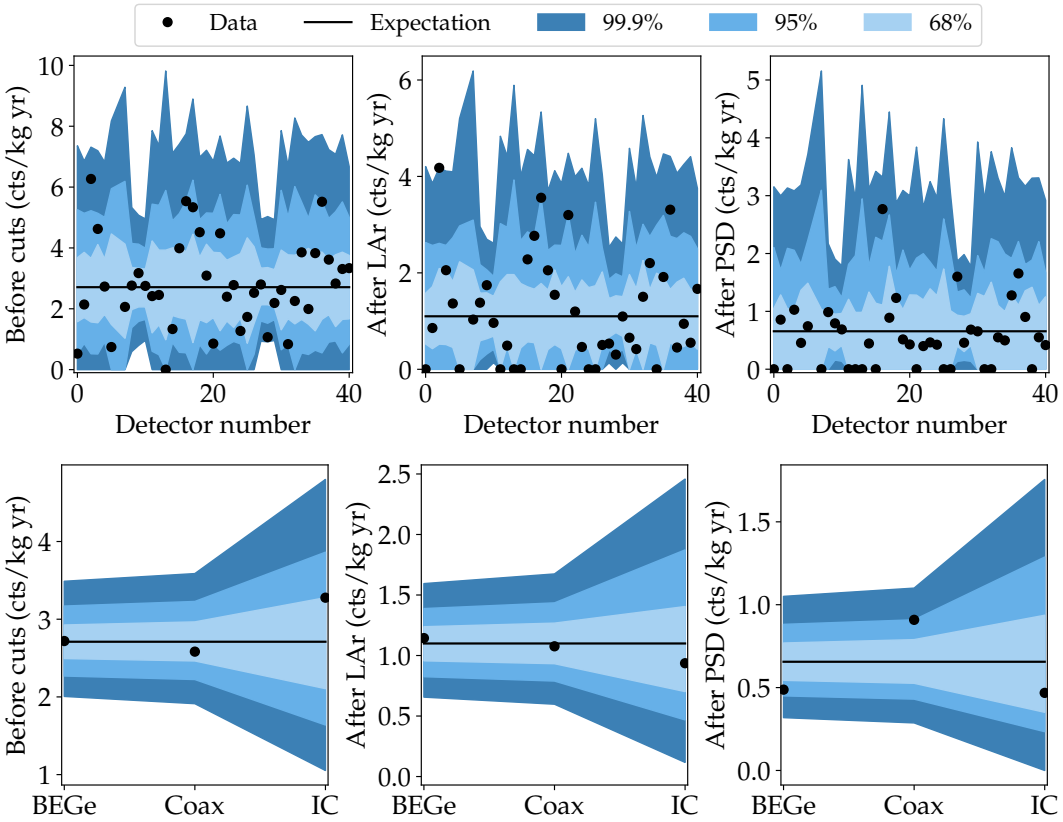

FIGURE 5.8: Count rates in the analysis window before analysis cuts (left), after LAr veto cut only (center), and after PSD cut only (right). The top plots show the rates per detector, the bottom plot per detector type. The expected rate for a uniform background is shown by the continuous line. The 68%, 95%, and 99.9% probability bands for Poisson fluctuations are also shown.

grouping	before cuts	after LAr	after PSD	after all cuts
detectors	0.02	0.0001	0.40	0.17
detector type	0.75	0.95	0.09	0.68
before/after upgrade	0.76	0.64	0.03	0.28
detector string	0.22	0.17	0.51	0.77
detector position	0.66	0.62	0.50	0.34

TABLE 5.2: Summary of p-values obtained testing the hypothesis of uniform background between detectors, detector type, time in reference to the upgrade, detector string, or position in the array.

[2] GERDA Collaboration, M. Agostini, et al. "Upgrade for Phase II of the GERDA experiment". In: *Eur. Phys. J. C* 78.5 (2018), p. 388. DOI: 10.1140/epjc/s10052-018-5812-2. arXiv: 1711.01452.

[3] GERDA Collaboration, M. Agostini, et al. "Modeling of GERDA Phase II data". In: *JHEP* 03 (2020), p. 139. DOI: 10.1007/JHEP03(2020)139. arXiv: 1909.02522.

[4] GERDA Collaboration, M. Agostini, et al. "Limits on uranium and thorium bulk content in GERDA Phase I detectors". In: *Astropart. Phys.* 91 (2017), pp. 15–21. DOI: 10.1016/j.astropartphys.2017.03.003. arXiv: 1611.06884.

[5] F. Novak. "The Search for Bulk Alpha-events in GERDA Phase II Data". Bachelor thesis. Technische Universität München, 2020.

[6] GERDA Collaboration, M. Agostini, et al. "Improvement of the energy resolution via an optimized digital signal processing in GERDA Phase I". In: *Eur. Phys. J. C* 75.6 (2015), p. 255. DOI: 10.1140/epjc/s10052-015-3409-6. arXiv: 1502.04392.

[7] GERDA Collaboration, M. Agostini, et al. "Pulse shape analysis in GERDA Phase II". In: *Eur. Phys. J. C* 82.4 (2022), p. 284. DOI: 10.1140/epjc/s10052-022-10163-w. arXiv: 2202.13355.

[8] A. Caldwell, D. Kollar, and K. Kröninger. "BAT: The Bayesian Analysis Toolkit". In: *Comput. Phys. Commun.* 180 (2009), pp. 2197–2209. DOI: 10.1016/j.cpc.2009.06.026. arXiv: 0808.2552.

[9] F. Beaujean et al. *BAT release, version 1.0.0*. Version 1.0.0. 2018. DOI: 10.5281/zenodo.1322675.

[10] GERDA Collaboration, M. Agostini, et al. "Probing Majorana neutrinos with double-β decay". In: *Science* 365 (2019), p. 1445. DOI: 10.1126/science.aav8613. arXiv: 1909.02726.

Chapter 6

Search for $0\nu\beta\beta$ decay of ^{76}Ge

At the end of GERDA Phase II, with a total exposure of 103.7 kg yr, the lowest BI on record of $5.2^{+1.6}_{-1.3} \times 10^{-4}$ counts/(keV kg yr) was measured in the ROI of the $0\nu\beta\beta$ decay. Combining Phase I and Phase II data, with a total exposure of 127.2 kg yr, the most stringent lower limit on the ^{76}Ge $0\nu\beta\beta$ decay half-life was set at 1.8×10^{26} yr at 90% C.L., coinciding with the median sensitivity for the null hypothesis.

The data validation and background studies of the final Phase II data set described in chapters 4 and 5 are examples of the contributions made, as part of this dissertation work, towards the final results of GERDA on the search for $0\nu\beta\beta$ decay, published in [1].

6.1 History of ^{76}Ge $0\nu\beta\beta$ decay searches

The first experiment reporting on the search for $0\nu\beta\beta$ decay of ^{76}Ge was performed in the 1960s by the University of Milan group, led by E. Fiorini [2]. With a BI of 1.06×10^{3} counts/(keV kg yr), which is very far from present-day levels, they established the half-life of this process to be $> 3.1 \times 10^{20}$ yr at 68% C.L.. Substantial improvement in detector technology and background reduction led over the next 25 years to an increased sensitivity by more than three orders of magnitude [3–6].

An important milestone was achieved in the 1990s, when the first germanium detector enriched in the isotope ^{76}Ge was used, by the ITEP-Yerevan experiment [7], followed by the IGEX [8] and Heidelberg-Moscow [9] experiments. The two latter also initiated the use of PSD, extending the limit on the half-life just above 10^{25} yr.

In 2001, a remarkable event in the history of $0\nu\beta\beta$ decay search happened. A subset of the Heidelberg-Moscow collaboration published a claim for direct observation of $0\nu\beta\beta$ decay of ^{76}Ge, with a half-life of $T^{0\nu}_{1/2} = (0.8 - 18.3) \times 10^{25}$ yr at 95% C.L. [10, 11]. This claim was largely criticized [12] and later excluded by the results of the GERDA experiment [13].

Modern experiments, *i.e.* the GERDA and MAJORANA DEMONSTRATOR experiments, introduced new detector technologies that optimize the capability of the PSD analysis. At the end of Phase II, the GERDA experiment measured a BI of $5.2^{+1.6}_{-1.3} \times 10^{-4}$ counts/(keV kg yr), with a total exposure of 103.7 kg yr [1]. This is the lowest BI of any $0\nu\beta\beta$ decay experiment. The MAJORANA DEMONSTRATOR has the

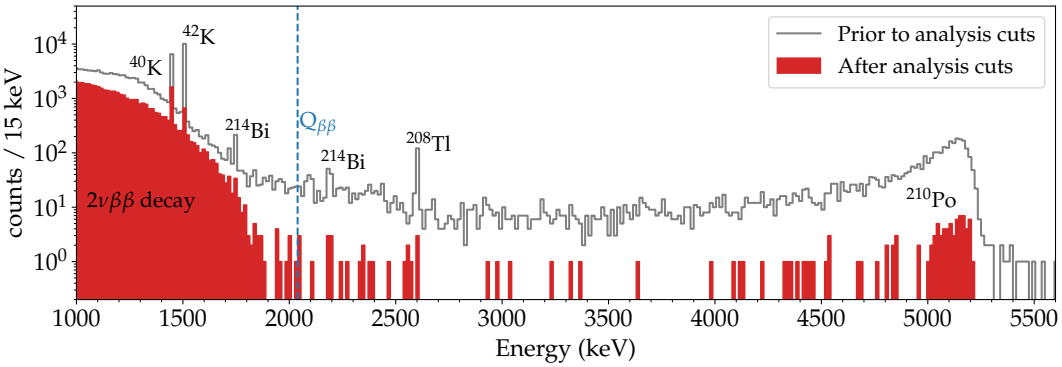

FIGURE 6.1: Energy distribution of the events corresponding to the 103.7 kg yr of GERDA Phase II data, before and after analysis cuts. The ^{76}Ge $2\nu\beta\beta$ decay dominates the energy region below 2 MeV. The most prominent γ lines and the α population around 5.2 MeV are also identified.

second lowest [14]. Despite the modest exposures compared to other technologies, the GERDA and MAJORANA DEMONSTRATOR experiments always had competitive or leading sensitivities that motivated the pursuit of a next-generation $0\nu\beta\beta$ decay experiment based on enriched HPGe detectors. The LEGEND Collaboration aims to develop a phased, ^{76}Ge double-β decay experimental program with discovery potential at a half-life beyond 10^{28} yr [15], building on the success of the GERDA and MAJORANA DEMONSTRATOR experiments.

6.2 Analysis data set

The analysis which led to the final GERDA results on the search for $0\nu\beta\beta$ decay was performed on the complete Phase II data combined with the Phase I data. The total exposure is 127.2 kg yr, of which 23.5 kg yr collected during Phase I and 103.7 kg yr during Phase II. In the following, we will concentrate on the Phase II data set. A detailed description of Phase I analysis methods can be found elsewhere [13].

The complete set of base cuts introduced in chapter 5 was applied to the data, *i.e.* quality cuts, muon veto, and detector anti-coincidence cuts. The LAr veto cut and PSD cut were also applied in the $0\nu\beta\beta$ decay analysis. We will refer to the latter as analysis cuts. Figure 6.1 shows the energy distribution of all events before and after applying the analysis cut.

6.3 Statistical analysis

The analysis window for the $0\nu\beta\beta$ decay search has been defined in the previous chapter, in section 5.3.2. The energy distribution of the events in the analysis window is fitted to search for a $0\nu\beta\beta$ decay signal. The signal is modeled with a Gaussian distribution, centered at $Q_{\beta\beta}$ and with the width given by the energy resolution. The background in the analysis window is modeled with a flat distribution.

For this analysis, the classical division of data in data sets according to the detector type used in previous GERDA publications was replaced by a division in partitions, *i.e.* periods in which all the parameters are stable. Each partition is characterized by its energy resolution, efficiency, and exposure. This construction allows a precise tracing of the performance of each detector at any given moment.

The statistical analysis is based on an unbinned extended maximum likelihood function and was performed in both frequentist and Bayesian frameworks. The likelihood function is given by the product of the partition likelihoods, weighted by the Poisson term:

$$\mathcal{L} = \prod_k \frac{(\mu_s^k + \mu_b^k)^{N_k}\, e^{-(\mu_s^k+\mu_b^k)}}{N_k!} \prod_{i=1}^{N_k} \frac{1}{\mu_s^k + \mu_b^k} \left(\frac{\mu_b^k}{\Delta E} + \frac{\mu_s^k}{\sqrt{2\pi}\sigma_k}\, e^{\frac{-(E_i - Q_{\beta\beta})^2}{2\sigma_k^2}} \right) , \tag{6.1}$$

where the first product runs over the partitions k, and the second over the events i, with energy E_i, in each partition. N_k is the number of events in the kth partition. The energy resolution σ_k is given in FWHM/2.35. Details about the energy resolution of each partition can be found in [16].

The expectation value of the number of signal events in each partition, which is proportional to the inverse of the half-life, is given by:

$$\mu_s^k = \frac{ln(2) N_A}{m_{76}}\, \epsilon_k\, \mathcal{E}_k\, \frac{1}{T_{1/2}^{0\nu}} , \tag{6.2}$$

where N_A is the Avogadro's constant, m_{76} the molar mass of ^{76}Ge, $\mathcal{E}_k$ the exposure, and ϵ_k the total detection efficiency. The different contributions to the total efficiency are the ^{76}Ge enrichment fraction, the detector AV fraction, the probability that the full $0\nu\beta\beta$ decay energy is contained within the AV, obtained by MC simulations, and all the efficiencies of the analysis cuts. A summary of the individual contributions and the combined efficiency, obtained by MC sampling of correlated and uncorrelated efficiencies, is provided in table 6.1.

The expectation value of the number of background events in the analysis window in each partition is given by:

$$\mu_b^k = \mathrm{BI} \times \Delta E \times \mathcal{E}_k , \tag{6.3}$$

with $\Delta E = 240$ keV being the size of the analysis window.

The free parameters of the fit are the signal strength $S = 1/T_{1/2}^{0\nu}$ and the BI, and they are common parameters to all partitions. The assumption of a common BI for all detectors is also a new feature of this analysis compared to previous ones, where independent parameters for each detector type were used. This was motivated by the lack of any statistically significant indication of non-uniformity of the background between detector type, time, or position within the array, as presented in the previous chapter, in section 5.3.2.

	pre-upgrade		post-upgrade		
	BEGe	Coax	BEGe	Coax	IC
Electrons containment	(89.7±0.5) %	(91.4±1.9) %	(89.3±0.6) %	(92.0±0.3) %	(91.8±0.5) %
^{76}Ge enrichment fraction	(88.0±1.3) %	(86.6±2.1) %	(88.0±1.3) %	(86.8±2.1) %	(87.8±0.4) %
AV fraction	(88.7±2.2) %	(86.1±5.8) %	(88.7±2.1) %	(87.1±5.8) %	(92.7±1.2) %
LAr veto cut	(97.7±0.1) %			(98.2±0.1) %	
PSD cut	(88.2±3.4) %	(69.1±5.6) %	(89.0±4.1) %	(68.8±4.1) %	(90.0±1.8) %
Total efficiency	(60.5±3.3) %	(46.2±5.2) %	(61.1±3.9) %	(47.2±5.1) %	(66.0±1.8) %

TABLE 6.1: Summary of the GERDA Phase II efficiencies for different detector types and before and after the upgrade. The contributions to the total detection efficiency for $0\nu\beta\beta$ decay are reported separately. The efficiency of the LAr veto cut is independent of the detector type and it is split only between pre- and post-upgrade. The efficiency of the muon veto and quality cuts are above 99.9% and are not shown.

Phase I data sets are included in the analysis as individual partitions with independent BIs.

6.4 Results

Before the unblinding, after applying the analysis cuts, 7 events remained in the analysis window. After unblinding, 6 more events were found. Details about these events are summarized in table 6.2.

No indication for a $0\nu\beta\beta$ decay signal was found in GERDA Phase II data. The best fit for the signal strength S lies at 0. The BI in Phase II extracted from the fit is:

$$\mathrm{BI} = 5.2^{+1.6}_{-1.3} \times 10^{-4}\,\mathrm{counts/(keV\,kg\,yr)}\,. \tag{6.4}$$

This is the lowest BI of any $0\nu\beta\beta$ decay experiment and met the design goal of GERDA of *background free* performance: the mean background expected in the signal region is 0.3 counts. The energy distribution of the 13 events found in the analysis window in Phase II is shown in figure 6.2, together with the best fit model.

A frequentist analysis, which uses a two-sided test statistic based on the profile likelihood, was performed to set a limit on the half-life of the process. The probability distributions of the test statistic are computed with MC techniques, as they are found to deviate from the χ^2 distributions significantly. A detailed description of the statistical method can be found in [17].

The lower limit obtained with Phase II data is $T^{0\nu}_{1/2} > 1.5 \times 10^{26}$ yr at 90% C.L.. The best fit of the combined Phase I and Phase II data for the signal strength S still lies at 0. The corresponding limit on the half-life is:

$$T^{0\nu}_{1/2} > 1.8 \times 10^{26}\,\mathrm{yr} \quad 90\%\,\mathrm{C.L.}\,, \tag{6.5}$$

channel	name	data set	date	energy (keV)
29	ANG4	pre-upgrade Coax	2016/02/10 13:04:08	1995.2
16	GD61C	pre-upgrade BEGe	2016/03/13 05:40:59	1958.7
36	ANG1	pre-upgrade Coax	2016/10/09 02:44:44	1950.9
1	GD35B	pre-upgrade BEGe	2016/11/27 23:47:40	2068.0
36	ANG1	pre-upgrade Coax	2017/11/01 01:02:13	1962.7
9	RG1	pre-upgrade Coax	2018/01/16 22:46:45	1957.5
16	GD61C	post-upgrade BEGe	2018/08/01 03:02:06	1970.1
1	GD35B	pre-upgrade BEGe	2016/08/30 01:57:02	2018.1
0	GD91A	pre-upgrade BEGe	2017/01/31 07:48:46	2056.4
20	GD76C	pre-upgrade BEGe	2017/08/24 12:48:05	2042.1
40	IC74A	post-upgrade IC	2018/10/09 01:09:14	2058.9
29	ANG4	post-upgrade Coax	2019/08/26 12:52:14	2015.9
34	GD32D	post-upgrade BEGe	2019/09/12 08:24:09	2012.1

TABLE 6.2: List of events in the analysis window, after applying analysis cuts. Before unblinding, 7 events (first group) were found, after unblinding 6 more events (second group) appeared. The channel number, detector name, data set, date and time, and the energy of the events are listed.

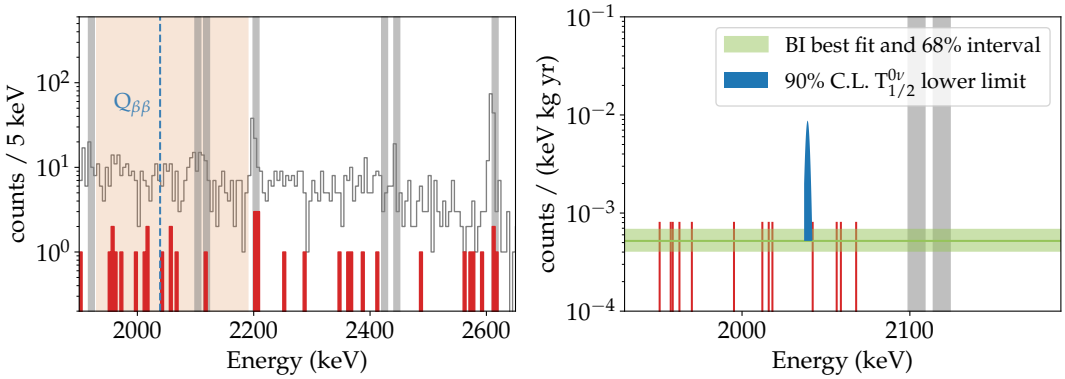

FIGURE 6.2: (Left) Zoomed view of the energy distribution of GERDA Phase II data between 1900 keV and 2650 keV, before and after analysis cuts. The analysis window around $Q_{\beta\beta}$ and the regions of expected γ lines are marked. (Right) Result of the fit to the unbinned data. The blue peak shows the expected $0\nu\beta\beta$ decay signal for $T^{0\nu}_{1/2}$ equal to the lower limit 1.8×10^{26} yr.

and coincides numerically with the sensitivity, defined as the median expectation under the no signal hypothesis.

The Bayesian analysis, performed using a uniform prior on the signal strength, gives a limit on the half-life from Phase I and Phase II together $T^{0\nu}_{1/2} > 1.4 \times 10^{26}$ yr at 90% C.I.. A stronger limit $T^{0\nu}_{1/2} > 2.3 \times 10^{26}$ yr at 90% C.I. is obtained using a uniform prior on $m_{\beta\beta}$ (as $S \propto m^2_{\beta\beta}$).

Three primary sources of systematic uncertainties were identified: uncertainties on the energy reconstruction and energy resolution affecting the shape of the Gaussian signal, and uncertainties on the efficiencies ϵ_k affecting the signal strength defined by equation 6.2. They are folded into the analysis through additional nuisance parameters, constrained by Gaussian pull terms. Their overall effect on the limit was estimated to be at the percent level.

Potential systematic uncertainties related to the fit model were also investigated. For instance, a more general linear distribution for the background in the analysis window was considered. This was found to only marginally impact the result, changing the limit by a few percent.

6.5 Effective Majorana neutrino mass

The lower limit on $T^{0\nu}_{1/2}$ can be converted into an upper limit on the $m_{\beta\beta}$ under the assumption that the decay is dominated by the exchange of light Majorana neutrinos. For a while now, $m_{\beta\beta}$ has been used to compare the reach of experiments using different double-β isotopes.

The GERDA limit on $m_{\beta\beta}$ is:

$$m_{\beta\beta} < [79, 180]\,\text{meV} \quad 90\%\,\text{C.L.}\,. \tag{6.6}$$

It has been obtained assuming a standard value of $g_A = 1.27$, the phase-space factor in [18] ($2.363 \times 10^{-15}\,\text{yr}^{-1}$), and the set of NMEs from [19–29], that are in the range (2.66 – 6.04) for ^{76}Ge.

A comparison of the $0\nu\beta\beta$ decay searches of the most relevant current experiments is shown in figure 6.3. The GERDA result is very competitive with the most stringent constraints from other isotopes. Only the KamLAND-Zen experiment recently set a limit on the half-life of $0\nu\beta\beta$ decay of ^{136}Xe at 2.3×10^{26} yr, resulting in the first exploration of the band of $m_{\beta\beta}$ values allowed in the IO scenario [30].

The comparison of the results in terms of $m_{\beta\beta}$ relies on the NME calculations and is affected by their uncertainty. This must be taken into account when comparing experiments using different isotopes. As noticed in a recent work [36], the comparison of the constraints from single isotopes may change for different NME models. For instance, even if KamLAND-Zen set the strongest limit on $m_{\beta\beta}$ for most of the NME calculations, there are some NME models for which the GERDA result is actually more stringent.

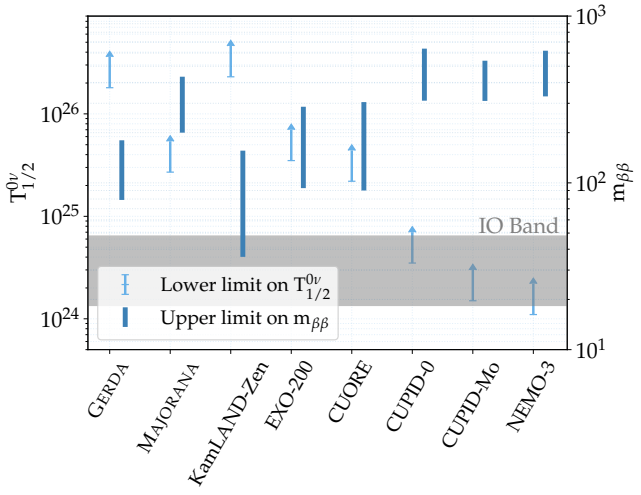

FIGURE 6.3: Results of current $0\nu\beta\beta$ decay searches [14, 30–35]. The lower limits on $T^{0\nu}_{1/2}$ is shown by the arrows on the left axis. The corresponding interval on $m_{\beta\beta}$ is also shown on the right axis. The band of values allowed for $m_{\beta\beta}$ in the IO scenario is marked.

References

[1] GERDA Collaboration, M. Agostini, et al. "Final Results of GERDA on the Search for Neutrinoless Double-β Decay". In: *Phys. Rev. Lett.* 125.25 (2020), p. 252502. DOI: 10.1103/PhysRevLett.125.252502. arXiv: 2009.06079.

[2] E. Fiorini et al. "A Search for Lepton Nonconservation in Double Beta Decay With a Germanium Detector". In: *Phys. Lett. B* 25 (1967), pp. 602–603. DOI: 10.1016/0370-2693(67)90127-X.

[3] F. T. Avignone et al. "Search for the Double Beta Decay of ^{76}Ge". In: *Phys. Rev. C* 34 (1986), pp. 666–677. DOI: 10.1103/PhysRevC.34.666.

[4] D. O. Caldwell et al. "Half-life limits on the zero-neutrino and two-neutrino double-β decay of ^{76}Ge". In: *Phys. Rev. D* 33 (1986), p. 2737. DOI: 10.1103/PhysRevD.33.2737.

[5] D. O. Caldwell. "Double beta decay: Present and future". In: *J. Phys. G* 17 (1991), S137–S144. DOI: 10.1088/0954-3899/17/S/014.

[6] D. Reusser et al. "Final report on the search for neutrinoless double-β decay of ^{76}Ge from the Gotthard underground experiment". In: *Phys. Rev. D* 45 (1992), pp. 2548–2551. DOI: 10.1103/PhysRevD.45.2548.

[7] A. A. Vasenko et al. "New Results in the ITEP / YePI Double Beta Decay Experiment With Enriched Germanium Detector". In: *Mod. Phys. Lett. A* 5 (1990), pp. 1299–1306. DOI: 10.1142/S0217732390001475.

[8] IGEX Collaboration, C. E. Aalseth, et al. "IGEX ^{76}Ge neutrinoless double beta decay experiment: Prospects for next generation experiments". In: *Phys. Rev. D* 65 (2002), p. 092007. DOI: 10.1103/PhysRevD.65.092007. arXiv: hep-ex/0202026.

[9] H. V. Klapdor-Kleingrothaus et al. "Latest results from the Heidelberg-Moscow double beta decay experiment". In: *Eur. Phys. J. A* 12 (2001), pp. 147–154. DOI: 10.1007/s100500170022. arXiv: hep-ph/0103062.

[10] H. V. Klapdor-Kleingrothaus et al. "Evidence for neutrinoless double beta decay". In: *Mod. Phys. Lett. A* 16 (2001), pp. 2409–2420. DOI: 10.1142/S0217732301005825. arXiv: hep-ph/0201231.

[11] H. V. Klapdor-Kleingrothaus, A. Dietz, and I. V. Krivosheina. "Neutrinoless double beta decay: Status of evidence". In: *Found. Phys.* 32 (2002). [Erratum: Found.Phys. 33, 679–684 (2003)], pp. 1181–1223. DOI: 10.1023/A:1019722802931. arXiv: hep-ph/0302248.

[12] C. E. Aalseth et al. "Comment on Evidence for neutrinoless double beta decay". In: *Mod. Phys. Lett. A* 17 (2002), pp. 1475–1478. DOI: 10.1142/S0217732302007715. arXiv: hep-ex/0202018.

[13] GERDA Collaboration, M. Agostini, et al. "Results on Neutrinoless Double-β Decay of ^{76}Ge from Phase I of the GERDA Experiment". In: *Phys. Rev. Lett.* 111.12 (2013), p. 122503. DOI: 10.1103/PhysRevLett.111.122503. arXiv: 1307.4720.

[14] Majorana Collaboration, S. I. Alvis, et al. "Search for neutrinoless double-β decay in ^{76}Ge with 26 kg yr of exposure from the Majorana Demonstrator". In: *Phys. Rev. C* 100.2 (2019), p. 025501. DOI: 10.1103/PhysRevC.100.025501. arXiv: 1902.02299.

[15] LEGEND Collaboration, N. Abgrall, et al. "The Large Enriched Germanium Experiment for Neutrinoless $\beta\beta$ Decay: LEGEND-1000 Preconceptual Design Report". 2021. arXiv: 2107.11462.

[16] C. Ransom. "Energy Calibration for the GERDA and LEGEND-200 Experiments". PhD thesis. University of Zurich, 2021. URL: https://www.mpi-hd.mpg.de/gerda/public/2021/phd2021_ChloeRansom_compressed.pdf.

[17] GERDA Collaboration, M. Agostini, et al. "Background-free search for neutrinoless double-β decay of ^{76}Ge with GERDA". In: *Nature* 544 (2017), p. 47. DOI: 10.1038/nature21717. arXiv: 1703.00570.

[18] J. Kotila and F. Iachello. "Phase space factors for double-β decay". In: *Phys. Rev. C* 85 (2012), p. 034316. DOI: 10.1103/PhysRevC.85.034316. arXiv: 1209.5722.

[19] T. R. Rodriguez and G. Martinez-Pinedo. "Energy density functional study of nuclear matrix elements for neutrinoless $\beta\beta$ decay". In: *Phys. Rev. Lett.* 105 (2010), p. 252503. DOI: 10.1103/PhysRevLett.105.252503. arXiv: 1008.5260.

[20] M. T. Mustonen and J. Engel. "Large-scale calculations of the double-β decay of ^{76}Ge, ^{130}Te, ^{136}Xe, and ^{150}Nd in the deformed self-consistent Skyrme quasiparticle random-phase approximation". In: *Phys. Rev. C* 87.6 (2013), p. 064302. DOI: 10.1103/PhysRevC.87.064302. arXiv: 1301.6997.

[21] N. López Vaquero, T. R. Rodríguez, and J. L. Egido. "Shape and pairing fluctuations effects on neutrinoless double beta decay nuclear matrix elements". In: *Phys. Rev. Lett.* 111.14 (2013), p. 142501. DOI: 10.1103/PhysRevLett.111.142501. arXiv: 1401.0650.

[22] M. Horoi and A. Neacsu. "Shell model predictions for ^{124}Sn double-β decay". In: *Phys. Rev. C* 93.2 (2016), p. 024308. DOI: 10.1103/PhysRevC.93.024308. arXiv: 1511.03711.

[23] J. Hyvärinen and J. T. Suhonen. "Nuclear matrix elements for $0\nu\beta\beta$ decays with light or heavy Majorana-neutrino exchange". In: *Phys. Rev. C* 91.2 (2015), p. 024613. DOI: 10.1103/PhysRevC.91.024613.

[24] J. Barea, J. Kotila, and F. Iachello. "$0\nu\beta\beta$ and $2\nu\beta\beta$ nuclear matrix elements in the interacting boson model with isospin restoration". In: *Phys. Rev. C* 91.3 (2015), p. 034304. DOI: 10.1103/PhysRevC.91.034304. arXiv: 1506.08530.

[25] J. Menéndez. "Neutrinoless $\beta\beta$ decay mediated by the exchange of light and heavy neutrinos: The role of nuclear structure correlations". In: *J. Phys. G* 45.1 (2018), p. 014003. DOI: 10.1088/1361-6471/aa9bd4. arXiv: 1804.02105.

[26] L. S. Song et al. "Nuclear matrix element of neutrinoless double-β decay: Relativity and short-range correlations". In: *Phys. Rev. C* 95.2 (2017), p. 024305. DOI: 10.1103/PhysRevC.95.024305. arXiv: 1702.02448.

[27] F. Šimkovic, A. Smetana, and P. Vogel. "$0\nu\beta\beta$ nuclear matrix elements, neutrino potentials and SU(4) symmetry". In: *Phys. Rev. C* 98.6 (2018), p. 064325. DOI: 10.1103/PhysRevC.98.064325. arXiv: 1808.05016.

[28] D. Fang, A. Faessler, and F. Šimkovic. "$0\nu\beta\beta$-decay nuclear matrix element for light and heavy neutrino mass mechanisms from deformed quasiparticle random-phase approximation calculations for ^{76}Ge, ^{82}Se, ^{130}Te, ^{136}Xe , and ^{150}Nd with isospin restoration". In: *Phys. Rev. C* 97.4 (2018), p. 045503. DOI: 10.1103/PhysRevC.97.045503. arXiv: 1803.09195.

[29] L. Coraggio et al. "Calculation of the neutrinoless double-β decay matrix element within the realistic shell model". In: *Phys. Rev. C* 101.4 (2020), p. 044315. DOI: 10.1103/PhysRevC.101.044315. arXiv: 2001.00890.

[30] KamLAND-Zen Collaboration, S. Abe, et al. "First Search for the Majorana Nature of Neutrinos in the Inverted Mass Ordering Region with KamLAND-Zen". 2022. arXiv: 2203.02139.

[31] NEMO-3 Collaboration, R. Arnold, et al. "Results of the search for neutrinoless double-β decay in ^{100}Mo with the NEMO-3 experiment". In: *Phys. Rev. D* 92.7 (2015), p. 072011. DOI: 10.1103/PhysRevD.92.072011. arXiv: 1506.05825.

[32] CUPID Collaboration, O. Azzolini, et al. "Final result of CUPID-0 phase-I in the search for the ^{82}Se Neutrinoless Double-β Decay". In: *Phys. Rev. Lett.* 123.3 (2019), p. 032501. DOI: 10.1103/PhysRevLett.123.032501. arXiv: 1906.05001.

[33] CUPID Collaboration, E. Armengaud, et al. "New Limit for Neutrinoless Double-Beta Decay of ^{100}Mo from the CUPID-Mo Experiment". In: *Phys. Rev. Lett.* 126.18 (2021), p. 181802. DOI: 10.1103/PhysRevLett.126.181802. arXiv: 2011.13243.

[34] CUORE Collaboration, D. Q. Adams, et al. "Search for Majorana neutrinos exploiting millikelvin cryogenics with CUORE". In: *Nature* 604.7904 (2022), pp. 53–58. DOI: 10.1038/s41586-022-04497-4. arXiv: 2104.06906.

[35] EXO-200 Collaboration, G. Anton, et al. "Search for Neutrinoless Double-β Decay with the Complete EXO-200 Dataset". In: *Phys. Rev. Lett.* 123.16 (2019), p. 161802. DOI: 10.1103/PhysRevLett.123.161802. arXiv: 1906.02723.

[36] E. Lisi and A. Marrone. "Majorana neutrino mass constraints in the landscape of nuclear matrix elements". In: *Phys. Rev. D* 106.1 (2022), p. 013009. DOI: 10.1103/PhysRevD.106.013009. arXiv: 2204.09569.

Chapter 7

Search for 0νECEC of ^{36}Ar

The LAr cryostat, which houses the GERDA detector array, contains ^{36}Ar, a candidate for ECEC and therefore for the lepton number violating 0νECEC. In this process, a monochromatic γ is emitted, with an energy of about 430 keV, which may be detected by the germanium detectors. The experimental signature, with monochromatic energy deposition in one germanium detector and no coincident energy in the LAr and the rest of the germanium detectors, makes GERDA well suited for the search of this process.

As part of this dissertation work, the search for 0νECEC of ^{36}Ar with GERDA Phase II data was performed in collaboration with the master student *M. Korošec*. This work resulted in the most stringent limit on the half-life of ^{36}Ar 0νECEC and will be published by the GERDA Collaboration.

7.1 Radiative 0νECEC of ^{36}Ar

^{36}Ar can undergo ECEC to the ground state of ^{36}S [1]. The corresponding lepton number violating process, 0νECEC, may occur via the radiative mode:[1]

$$^{36}Ar \rightarrow {}^{36}S + \gamma\ (429.88\,keV) + 2\text{ X-rays}\ (2.47\,keV + 0.23\,keV) \tag{7.1}$$

where the argon nucleus captures one electron each from its K- and L-shells and turns into ^{36}S. A γ and two low-energy X-rays are emitted to ensure energy and momentum conservation. The energy of the X-rays is $E_K = 2.47$ keV and $E_L = 0.23$ keV, known with a precision of 0.4 eV [3]. Given the available energy of the decay $Q_{ECEC} = 432.58 \pm 0.19$ keV [4], the corresponding energy for the γ is $E_\gamma = Q_{ECEC} - E_K - E_L = 429.88 \pm 0.19$ keV.

Resonance enhancement of the process is not possible for ^{36}Ar. In the light neutrino exchange scenario, and assuming a Majorana mass of the order of 0.1 eV, the half-life of ^{36}Ar 0νECEC is predicted in the order of 10^{40} yr, with calculations based on the Quasi-particle Random Phase Approximation (QRPA) [2].

[1] Given the available energy of the process, also the internal conversion mode would be allowed for ^{36}Ar. Nevertheless, the latter is strongly suppressed due to argon's low atomic number and the relatively high γ energy [2].

dataset	exposure [kg yr]	mass [kg]	live time [yr]
pre-upgrade BEGe	32.8	19.4	1.7
pre-upgrade Coax	28.6	15.6	1.8
post-upgrade BEGe	22.2	20.0	1.1
post-upgrade Coax	13.2	14.6	0.9
post-upgrade IC	8.7	9.6	0.9
Total	105.5	79.2	

TABLE 7.1: Exposures, masses, and live times of the individual datasets. The total mass and total exposure are also reported. The exposure used in this analysis is slightly larger than that used in the $0\nu\beta\beta$ decay analysis since no PSD cut was applied here.

Experimental searches for 0νECEC of ^{36}Ar have been performed since the very early stages of the GERDA experiment [5]. The most stringent limit to date on the ^{36}Ar 0νECEC half-life is $T_{1/2} > 3.6 \times 10^{21}$ yr, established in Phase I of the GERDA experiment [6]. More recently, the search for this process has been performed with the Dark matter Experiment using Argon Pulse-shape discrimination 3600 (DEAP-3600) detector [7], although with less sensitivity than GERDA Phase I.

7.2 Analysis datasets

The full GERDA Phase II data were used for the analysis. Due to the different detector properties, *e.g.* energy resolution and efficiency, and the changes in the detector configuration during the upgrade, data were split into 5 datasets, namely pre-upgrade BEGe, pre-upgrade Coax, post-upgrade BEGe, post-upgrade Coax, and post-upgrade IC. The natural coaxial detectors were excluded from the analysis since their performances were never thoroughly investigated for analysis purposes, and they made up a minimal amount of the exposure.

The base quality cuts and muon veto cut, introduced in chapters 4 and 5, were used in the analysis. The experimental signature used to search for ^{36}Ar 0νECEC in the GERDA data corresponds to the full energy deposition of the γ in one germanium detector. No coincident energy deposition is expected, neither in the other germanium detectors nor in the LAr. Consequently, the detector anti-coincidence cut and the LAr veto cut were also applied. A customized LAr veto cut was used for the post-upgrade data to accommodate the efficiency estimation, as explained in section 7.3. The PSD cut, successfully employed in the search for $0\nu\beta\beta$ decay, is not suited for this analysis and therefore not used. For this reason, part of the data excluded in the $0\nu\beta\beta$ decay analysis from BEGe and IC datasets because of the PSD cut was instead included here. This results in a slightly higher total exposure of 105.5 kg yr. The exposures, masses, and live times of the single datasets are summarized in table 7.1.

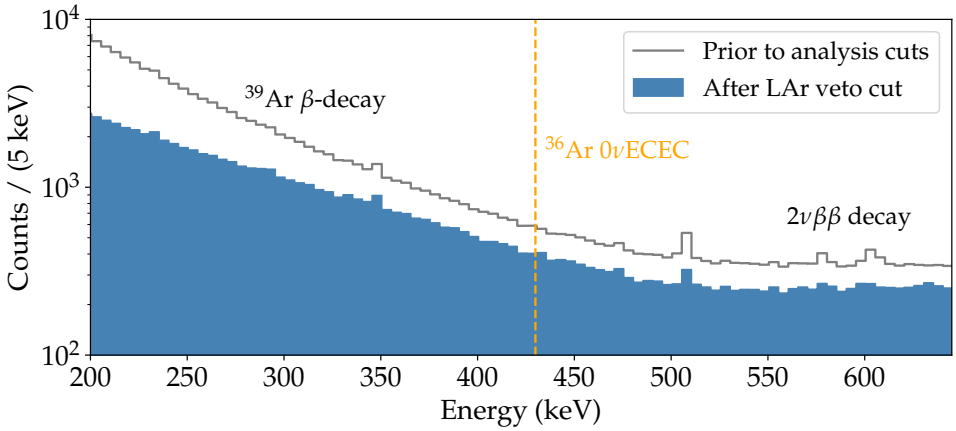

FIGURE 7.1: Energy distribution of the low energy events corresponding to 105.5 kg yr of GERDA Phase II data before analysis cuts and after LAr veto cut. The left part of the spectrum is dominated by the ^{39}Ar β decay with an endpoint at 565 keV. On the right side, the $2\nu\beta\beta$ decay dominates the spectrum.

Figure 7.1 shows the energy distribution of all GERDA Phase II data before analysis cuts and after applying the LAr veto cut at low energies. In ^{36}Ar 0νECEC, a γ with about 430 keV energy is emitted. In this low energy region of the spectrum, ^{39}Ar β decay dominates up to the endpoint at 565 keV, while $2\nu\beta\beta$ decay is the second dominant contribution.

7.3 Detection efficiency

The γ detection efficiency in the GERDA setup was determined via MC simulations with the GEANT4-based MaGe framework [8–11]. In total, 10^{10} γs with an energy of 429.88 keV were generated. The X-rays were neglected in the simulations. With their small energy, they cannot be detected in the germanium detectors. Nevertheless, they could still be seen by the LAr instrumentation and trigger the LAr veto. The impact of the X-rays on the efficiency was investigated and will be discussed in the following section. The γs were simulated in a cylindrical volume of LAr, with a radius of 1.5 m and a height of 2.5 m, around the detector array. Detector active volume and individual detector exposure are taken into account in the simulation, as detailed in [12].

The detection efficiency for each dataset is then obtained as the ratio between the number of events in the FEP in the specific dataset and the number of initially simulated events. The number of simulated events is high enough that the statistical uncertainties on these quantities are negligible.

The dominant systematic uncertainty on the detection efficiency comes from the large detector DL uncertainty. This is estimated by varying the detector DL by $\pm 1\sigma$, where σ is the DL uncertainty and evaluating the impact on the efficiency. The detection efficiencies for the individual datasets and their uncertainties are summarized

dataset	γ detection efficiency $[10^{-5}]$	combined efficiency $[10^{-5}]$
pre-upgrade BEGe	8.35 ± 0.25	8.11 ± 0.24
pre-upgrade Coax	7.36 ± 0.27	6.99 ± 0.26
post-upgrade BEGe	10.74 ± 0.30	10.21 ± 0.29
post-upgrade Coax	5.53 ± 0.24	5.25 ± 0.23
post-upgrade IC	3.60 ± 0.25	3.42 ± 0.24

TABLE 7.2: Efficiencies for the individual datasets. The second column indicates the γ detection efficiency as obtained from the MC simulations. This is multiplied by the X-ray's survival probability, giving the combined efficiency reported in the third column.

in table 7.2. Systematic uncertainties on the detector DL range from 3% to 7%.

7.4 X-rays survival probability

The energy of the two X-rays is low enough that, even if they reach the germanium detector surface, they cannot penetrate the DL and, therefore, not be detected by the germanium detectors. Nevertheless, since they deposit their energy in the LAr, they could be seen by the LAr instrumentation and trigger the LAr veto. The corresponding event would consequently escape the data selection.

The survival probability of the two X-rays to the LAr veto was evaluated and combined with the detection efficiency previously introduced. To do so, the LAr probability map developed for the GERDA experiment [13] was used. For each simulated event starting at the position (x, y, z) and corresponding to a full γ energy deposition, the probability $p(x, y, z)$ to detect the scintillation light can be evaluated. The number of photons n produced by the X-rays in one of these events is:

$$\begin{aligned} n &= E_{X-rays} \cdot 28.12 \, \frac{photons}{keV} \cdot p(x, y, z) \\ &= (2.4\, keV + 0.23\, keV) \cdot 28.12 \, \frac{photons}{keV} \cdot p(x, y, z) \end{aligned} \tag{7.2}$$

where 28.12 is the number of photons produced for an energy deposition of 1 keV in the GERDA LAr [13]. The probability P that the corresponding event survives the LAr veto cut is the Poisson probability $\mathcal{P}(0, n)$.

A mean survival probability was obtained, evaluating the survival probability for each simulated event and averaging the number of events corresponding to a full γ energy deposition in one germanium detector, $N_{\gamma_F EP}$:

$$\overline{P} = \frac{\sum_i \mathcal{P}(0, n_i)}{N_{\gamma_F EP}} \tag{7.3}$$

The resulting mean survival probability is $\overline{P} = 0.957$. Almost 5% of the events are discarded by the data selection due to the X-rays depositing their energy in LAr.

The total efficiency, which combines the γ detection efficiency and the X-rays survival probability, is summarized for the individual datasets in table 7.2.

The LAr probability map was developed assuming the pre-upgrade configuration of the LAr instrumentation [13]. The inner fiber-shroud, which was added only during the upgrade, is not included in the MC simulations used to obtain the LAr probability map. Therefore, to use the X-rays survival probability also for the post-upgrade datasets, a customized LAr veto cut was applied to the data. The SiPM channels corresponding to the inner fiber-shroud are not considered to build the LAr veto condition.

The calculation of the survival probability assumes that the two X-rays deposit all the energy at the exact point where the γ is emitted. A systematic uncertainty could be introduced if the X-rays traveled further before depositing their energy. Nevertheless, the assumption is justified by the X-rays having a very short attenuation length in LAr, calculated to be about 40 μm [14]. Since the binning of the LAr probability map is $3 \times 3 \times 3\,\mathrm{mm}^3$, the attenuation length of the X-rays can be neglected.

The systematic uncertainty introduced by the LAr probability map was also estimated. The methodology used to model the uncertainties on the LAr veto response is extensively discussed elsewhere [13]. The uncertainties on the LAr probability map introduce a systematic uncertainty on the survival probability of 0.5%. This is, however, negligible compared to the dominant DL systematic uncertainty.

7.5 Statistical analysis

The statistical analysis was performed in an energy window of ± 20 keV, centered around the γ energy of 429.88 keV, binned with 1 keV binning. In this energy region, the dominant backgrounds are the β decay of ^{39}Ar and the ^{76}Ge $2\nu\beta\beta$ decay. The sum of these contributions in the analysis window can be approximated by a linear distribution, as can be seen in figure 7.1. The signal is modeled with a gaussian peak, centered at the γ energy and with the width given by the energy resolution. The energy resolution of each dataset is derived from [15, 16].

A binned maximum likelihood fit was performed on the five datasets previously identified. Assuming that the number of events in each bin is Poisson distributed, the likelihood function is given by the product of Poisson probabilities for all bins and all datasets:

$$\mathcal{L}(\frac{1}{T_{1/2}}, \vec{\theta}_d) = \prod_d \prod_i \frac{\lambda_{i,d}^{n_{i,d}}}{n_{i,d}!} \cdot e^{-\lambda_{i,d}} \,, \tag{7.4}$$

where the products run over the number of bins i and the datasets d. The likelihood depends on the inverse of the half-life $1/T_{1/2}$ of ^{36}Ar 0νECEC, which is a common parameter among all the 5 datasets and the only parameter of interest, and on some nuisance parameters $\vec{\theta}_d$, that are dataset specific and include for instance the parameters that define the background distributions. Finally, $n_{i,d}$ denotes the number of

Parameters	pre-upgrade	post-upgrade
molar mass M_{Ar}	39.948 g/mol	
^{36}Ar abundance f_{36}	0.33 %	
LAr density	1385 kg/m^3	
LAr volume	17.66 m^3	
LAr mass m_{LAr}	23074 kg	
live time t	1.907 yr	1.174 yr
LAr veto cut efficiency ϵ_{LAr}	(97.7±0.1) %	(98.2±0.1) %

TABLE 7.3: Parameters used in the conversion of the number of signal events into half-life with equation 7.5. The first group of parameters is related to the LAr properties. Parameters used in the MC simulations from which the efficiency is calculated are given in the second group. Finally, the efficiency of the LAr veto cut is reported.

observed events in the bin i and dataset d, and $\lambda_{i,d}$ the expectation value for the same bin, given by the sum of signal and background in that bin $\lambda_{i,d} = s_{i,d} + b_{i,d}$.

The total number of signal events in a dataset is related to the inverse of the half-life through the relation:

$$S_d = ln(2) \cdot N_A \cdot \frac{m_{LAr}}{M_{Ar}} \cdot f_{36} \cdot t \cdot \epsilon_d \cdot \epsilon_{LAr} \cdot \frac{1}{T_{1/2}} , \tag{7.5}$$

where N_A is the Avogadro constant, M_{Ar} the molar mass of argon, f_{36} is the abundance of ^{36}Ar in ultra-pure natural argon, m_{LAr} is the mass of LAr in the simulation, which is used to calculate the efficiencies ϵ_d (table 7.2), t is the live time. This is the live time of the experiment, divided by the upgrade, and is different from the live times of the individual datasets given in table 7.1. In fact, the differences among individual detector live times are already included in the efficiency simulations. Finally, ϵ_{LAr} is the efficiency of the LAr veto cut and is the same as for the $0\nu\beta\beta$ decay analysis. All the above parameters are summarized in table 7.3.

7.6 Results

No indication of ^{36}Ar 0νECEC was found in GERDA Phase II data. The best fit for the number of signal events lies at 0. Data from the five datasets are shown in figure 7.2 together with the best fit model.

A modified frequentist approach, namely the CLs method, was used to set a lower limit on the half-life of the process. The CLs is defined as:

$$CLs = \frac{p_{s+b}}{1 - p_b} , \tag{7.6}$$

where p_{s+b} is the p-value calculated for the signal plus background hypothesis, and p_b the p-value of the alternative background-only hypothesis. The CLs method was

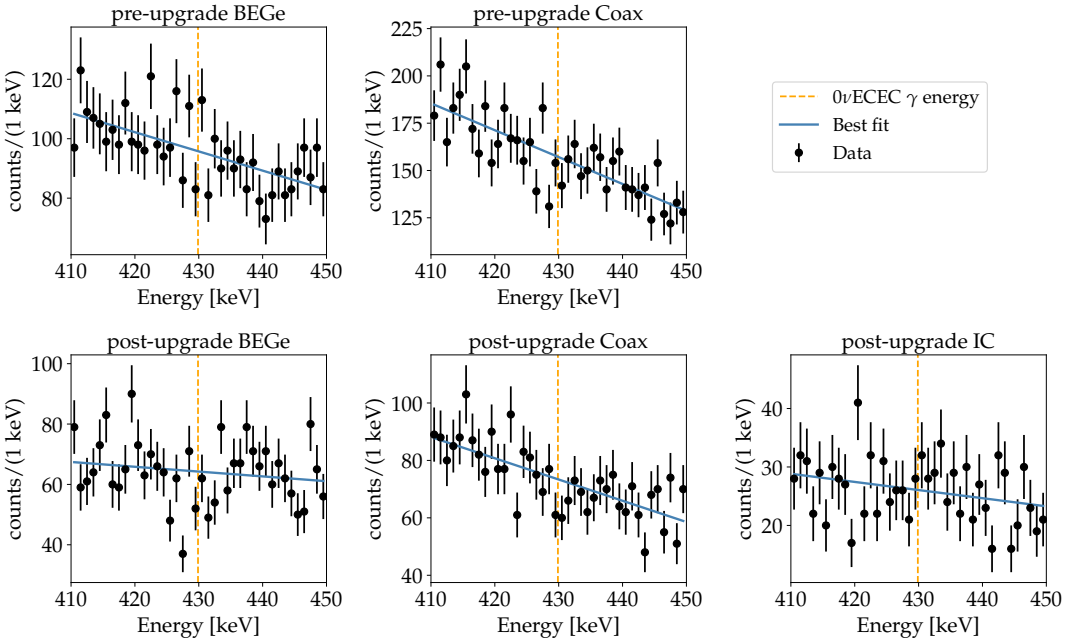

FIGURE 7.2: Phase II data for a total exposure of 105.5 kg yr, divided into the five analysis datasets. The combined best fit model, corresponding to 0 signal events is shown by the blue line. The dashed orange line indicates the γ energy, where a signal from ^{36}Ar 0νECEC would be expected.

found to be a more appropriate choice in the case of an experiment with low sensitivity, or, in different words, a background-dominated experiment [17]. Compared to a pure frequentist approach, the CLs exclusion region does not assure the correct coverage but often results in an over coverage.

The test statistic used for the p-value calculation is the profile likelihood ratio test statistic. Asymptotic distributions of the test statistic and the Asimov dataset are used, following the work of *G. Cowan et al.* [18]. The statistics in each bin is high enough for this assumption to be valid.

A scan of the observed CLs over different values of the inverse of the half-life is shown in figure 7.3. The median of the CLs distribution expected for the GERDA experiment in the absence of signal is also shown, together with the central 68% and 95% probability intervals.

The Phase II lower limit on the half-life is:

$$T_{1/2} > 1.14 \times 10^{22}\, yr \quad 90\%\,\text{C.L.}\,. \tag{7.7}$$

The sensitivity, *i.e.* the median expectation under the no signal hypothesis, is $T_{1/2} > 7.13 \times 10^{21}\, yr$ at 90% C.L..

Three main sources of systematic uncertainties were identified: uncertainties on the efficiencies ϵ_d affecting the number of signal events defined by equation 7.5, and uncertainties on the energy resolution and energy reconstruction affecting the shape

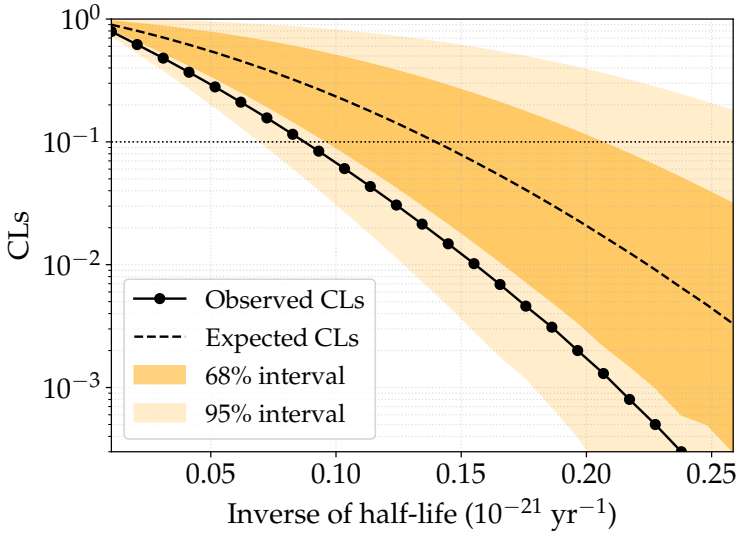

FIGURE 7.3: CLs as a function of the inverse of the half-life. The median of the CLs distribution for the GERDA experiment under the no signal hypothesis and the observed CLs for GERDA data are shown by the black continuous line and the dashed line, respectively. The spread of the CLs distribution, given by the central 68% and 95% probability intervals is also shown by the colored band. The 90% C.L. limit (sensitivity) on the number of events in the fit range is given by the intersection of the solid (dashed) black line with the dotted line, corresponding to a CLs of 0.1.

of the Gaussian signal. They are folded into the analysis through additional nuisance parameters, constrained by Gaussian pull terms. The efficiencies and their uncertainties are given in table 7.2, whereas the energy resolution and energy scale with the respective uncertainties are derived from [15, 16]. Their overall effect on the limit was estimated to be 5%.

Potential systematic uncertainties related to the fit model, in particular to the background distribution, were also investigated. First, the assumption of a linear distribution for the background was compared to a more general second-order polynomial distribution. This was found to have a negligible impact on the result.

The presence of additional structures in the background distribution was then investigated. In the analysis of Phase I data [6], a γ line from ^{108m}Ag, very close to the expected signal, was included in the background model. In this analysis, with the introduction of the LAr veto cut, no contribution from the above γ line is expected. Indeed, the decay of ^{108m}Ag proceeds through a cascade of three gammas at different energies, 433.9 keV, 614.3 keV, and 722.9 keV, with similar branching ratios. Therefore, the corresponding events are very likely to be discarded by the LAr veto cut. Additionally, no indication for any of the three lines was found in GERDA data, even before LAr veto cut [19]. A check of the validity of this assumption was done, introducing the 433.9 keV ^{108m}Ag line in the background model. This was found to have a negligible impact on the result.

An improvement of a factor $\sim$3 was obtained in this work with GERDA Phase II

data compared to the Phase I result. This can be attributed in part to the larger exposure and in part to the reduction of the background in the analysis region with the use of the LAr veto cut, as shown in figure 7.1.

A combination of the Phase I and Phase II limits was performed. The previous Phase I result was used as prior in Phase II analysis. A pull term constraining the inverse of the half-life was added to the likelihood. An exponential function is used for the pull term, peaked at zero, and normalized such that the 90% probability interval gives the Phase I limit on the half-life. The resulting Phase I and Phase II combined lower limit on the half-life is:

$$T_{1/2} > 1.64 \times 10^{22}\, yr \quad 90\%\,\text{C.L.}\,. \tag{7.8}$$

7.7 Conclusions and outlook

In this work, we searched for 0νECEC of ^{36}Ar using the whole exposure of GERDA Phase II. The experimental signature which we chose to search for ^{36}Ar 0νECEC is the full γ energy deposition in one HPGe detector and no coincident energy in the LAr or any other HPGe detector. We searched for this peak with a binned maximum likelihood fit performed simultaneously on 5 datasets, where we split the data among different detector types and pre- and post-upgrade.

We did not find any indication of a ^{36}Ar 0νECEC signal, and we set a limit on the half-life of this process using a test statistic based on the profile likelihood ratio and the CLs method. With Phase II only data, we obtained a lower limit on the half-life $T_{1/2} > 1.14 \times 10^{22}$ yr at 90% C.L.. A combined GERDA Phase I and Phase II limit was also obtained: $T_{1/2} > 1.64 \times 10^{22}$ yr at 90% C.L..

This result is the most stringent constraint on the half-life of 0νECEC of ^{36}Ar. The theoretical expectation in the light-neutrino exchange scenario and assuming a Majorana mass of ~ 0.1 eV is in the order of 10^{40} yr, many orders of magnitude beyond the GERDA experimental sensitivity. Nevertheless, new physics may be hiding in the most unexpected corner, so experimental searches of this process are still important.

To our knowledge, the GERDA experiment was, to date, the only experiment with the capability to search for the 0νECEC of ^{36}Ar with competitive sensitivities. The GERDA sensitivity is limited by the background in the energy region where the γ is expected, which is, for instance, orders of magnitude higher than the background in the ^{76}Ge $0\nu\beta\beta$ decay ROI. An additional limiting factor is the low detection efficiency since the γ is emitted in the LAr volume and must be detected in one of the HPGe detectors. Only γs emitted in the proximity of the detector array contribute to the total efficiency.

Among the planned future experiments, LEGEND will have the capability to search for the 0νECEC of ^{36}Ar. In the first phase of the project, LEGEND-200 will deploy about 200 kg of HPGe detectors. This is more than a factor of 4 compared to the GERDA detector mass and will imply a higher detection efficiency to 0νECEC

of ^{36}Ar. On the other hand, the background in the energy region where the γ is expected should be comparable to the GERDA background. Still, an improvement in the current sensitivity is foreseen. LEGEND-1000 will deploy about 1 ton of HPGe detectors, which will imply an even higher detection efficiency to 0νECEC of ^{36}Ar. In addition, underground Ar will be used instead of atmospheric Ar. This is depleted of ^{39}Ar, which is the main background contribution in this search. A big improvement in the sensitivity is therefore expected. To our knowledge, there is no other planned experiment with competitive sensitivity to GERDA and LEGEND in the search for 0νECEC of ^{36}Ar.

References

[1] V. Tretyak and Y. Zdesenko. "Tables of the results of double Beta decay research". In: *Atom. Data Nucl. Data Tabl.* 61 (1995), pp. 43–90. DOI: 10.1016/S0092-640X(95)90011-X.

[2] A. Merle. "The Mysteries of Leptons: New Physics and unexplained Phenomena". PhD thesis. Ruperto-Carola University of Heidelber, 2009. DOI: 10.11588/heidok.00010180.

[3] G.P. Williams et al. *X-RAY DATA BOOKLET*. Second edition. 2009. URL: https://cxro.lbl.gov/x-ray-data-booklet.

[4] M. Wang et al. "The AME 2020 atomic mass evaluation (II). Tables, graphs and references". In: *Chin. Phys. C* 45.3 (2021), p. 030003. DOI: 10.1088/1674-1137/abddaf.

[5] O. Chkvorets. "Search for double beta decay with HPGe detectors at the Gran Sasso underground laboratory". Master thesis. 2008. arXiv: 0812.1206.

[6] GERDA Collaboration, M. Agostini, et al. "Limit on the radiative neutrinoless double electron capture of ^{36}Ar from GERDA Phase I". In: *Eur. Phys. J. C* 76.12 (2016), p. 652. DOI: 10.1140/epjc/s10052-016-4454-5. arXiv: 1605.01756.

[7] M. G. Dunford. "A Search for the Neutrinoles Double Electron Capture of ^{36}Ar and a Measurement of the Specific Activity of ^{39}Ar in Atmospheric Argon with the DEAP-3600 Detector". PhD thesis. Carleton University, 2018. DOI: 10.22215/etd/2018-13483.

[8] GEANT4 Collaboration, S. Agostinelli, et al. "GEANT4–a simulation toolkit". In: *Nucl. Instrum. Meth. A* 506 (2003), pp. 250–303. DOI: 10.1016/S0168-9002(03)01368-8.

[9] J. Allison et al. "Geant4 developments and applications". In: *IEEE Trans. Nucl. Sci.* 53 (2006), p. 270. DOI: 10.1109/TNS.2006.869826.

[10] J. Allison et al. "Recent developments in Geant4". In: *Nucl. Instrum. Meth. A* 835 (2016), pp. 186–225. DOI: 10.1016/j.nima.2016.06.125.

[11] M. Boswell et al. "MaGe-a Geant4-based Monte Carlo Application Framework for Low-background Germanium Experiments". In: *IEEE Trans. Nucl. Sci.* 58 (2011), pp. 1212–1220. DOI: 10.1109/TNS.2011.2144619. arXiv: 1011.3827.

[12] GERDA Collaboration, M. Agostini, et al. "Modeling of GERDA Phase II data". In: *JHEP* 03 (2020), p. 139. DOI: 10.1007/JHEP03(2020)139. arXiv: 1909.02522.

[13] GERDA Collaboration, M. Agostini, et al. "Liquid argon light collection and veto modeling in GERDA Phase II". submitted to Eur. Phys. J. C. 2022. arXiv: 2212.02856.

[14] J.H. Hubbell and S.M. Seltzer. "X-Ray Mass Attenuation Coefficients | NIST". URL: https://www.nist.gov/pml/x-ray-mass-attenuation-coefficients.

[15] C. Ransom. "Energy Calibration for the GERDA and LEGEND-200 Experiments". PhD thesis. University of Zurich, 2021. URL: https://www.mpi-hd.mpg.de/gerda/public/2021/phd2021_ChloeRansom_compressed.pdf.

[16] GERDA Collaboration, M. Agostini, et al. "Calibration of the GERDA experiment". In: *Eur. Phys. J. C* 81.8 (2021), p. 682. DOI: 10.1140/epjc/s10052-021-09403-2. arXiv: 2103.13777.

[17] A. L. Read. "Presentation of search results: The CL(s) technique". In: *J. Phys. G* 28 (2002), pp. 2693–2704. DOI: 10.1088/0954-3899/28/10/313.

[18] G. Cowan et al. "Asymptotic formulae for likelihood-based tests of new physics". In: *Eur. Phys. J. C* 71 (2011). [Erratum: Eur.Phys.J.C 73, 2501 (2013)], p. 1554. DOI: 10.1140/epjc/s10052-011-1554-0. arXiv: 1007.1727.

[19] M. Korosec. "A New Limit on Radiative Neutrinoless Double Electron Capture of ^{36}Ar". Master thesis. Technische Universität München, 2021.

Chapter 8

Search for exotic double-β decay modes of ^{76}Ge

The existence of new particles in BSM theories can lead to exotic double-β decay modes with different final states from the SM $2\nu\beta\beta$ decay. Exotic double-β decay modes can also be considered, in which the final state is the same as in $2\nu\beta\beta$ decay, but the decay kinematics is affected by the BSM physics effect. In chapter 1, we have introduced some of these exotic double-β decay modes, and we have shown that the experimental quantity that allows distinguishing them from the SM $2\nu\beta\beta$ decay is the shape of the two-electron energy distributions.

As part of this dissertation work, a search for distortion of the two-electron energy spectrum compared to the SM $2\nu\beta\beta$ decay expectation has been performed on a selected dataset from GERDA Phase II data. We searched for double-β decays with Majoron emission, emission of light exotic fermions, and Lorentz violation. In figure 8.1, we recall the energy distribution predicted for the different exotic decay modes of ^{76}Ge in comparison to the SM $2\nu\beta\beta$ decay distribution.

Previously in GERDA, only the search for Majoron-involving double-β decays has been performed [1]. Improved results on these decays have been obtained here, and, for the first time with ^{76}Ge, a limit on Lorentz invariance violation has been set. We also obtained the first experimental limits on the search for light exotic fermions in double-β decays, discussed in chapter 3. This author was the leading author of the analysis and prepared a manuscript which will be published by the GERDA Collaboration [2].

8.1 Data selection and modeling

8.1.1 Data selection

The data set used in this analysis corresponds to data collected with the BEGe detectors in Phase II before the upgrade. The total exposure is 32.8 kg yr. [1] This dataset was selected among the total exposure to minimize the systematic uncertainties. The BEGe detectors are better understood and have been characterized more accurately

[1] The PSD cut is not used in this analysis. Therefore, the exposure includes the additional exposure where no PSD evaluation is available (see chapter 4).

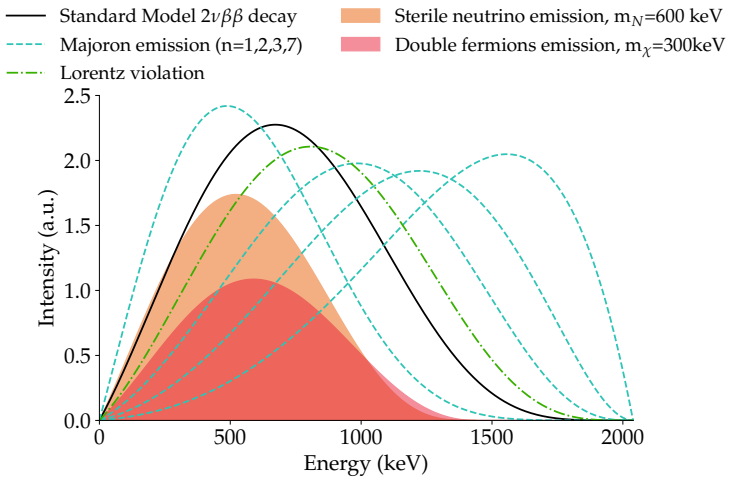

FIGURE 8.1: Energy distribution of the different exotic double-β decay modes shown in comparison to the SM $2\nu\beta\beta$ decay distribution for ^{76}Ge. The normalization is arbitrary and adjusted for better visualization.

than the Coax detectors, and the LAr instrumentation underwent significant changes during the upgrade that are not included in the modeling of the LAr veto system [3]. The information on the LAr veto system and its MC simulation are crucial elements of the analysis, as will be explained in the following.

The event topology of all the considered double-β decays is the same, and it is a localized energy deposition within one germanium detector. The total decay energy is shared among the two electrons and either the two anti-neutrinos or one or more exotic particles produced in the process. The electrons release all their energy within a few millimeters from the decay vertex in germanium. Both anti-neutrinos and the exotic particles escape the detector carrying away part of the decay energy. Thus, in all the considered decays, the reconstructed energy varies between zero and $Q_{\beta\beta}$, as shown in figure 8.1. If a massive exotic particle is produced in the process, the maximum energy is shifted to a lower value by the mass of the particle for a single production or twice the mass for pair production.

While an energy deposition of a double-β decay is fully contained in one germanium detector, background γ radiation, primarily interacting via Compton scattering, can undergo multiple separated energy depositions in more than one germanium detector. In addition, γ rays can deposit part of their energy in the LAr volume surrounding the detector array and trigger the LAr veto system. The detector anti-coincidence cut and the LAr veto cut were applied to reject background-like events. In addition, the base quality cuts and muon veto cut were applied. The acceptance of double-β decay events to the LAr veto cut is about 98%, estimated from the accidental coincidences of randomly triggered events (see chapter 5). The PSD cut, successfully employed in the search for $0\nu\beta\beta$ decay, was not used in this analysis. In fact, despite the possibility of discriminating between SS $2\nu\beta\beta$ decay events and MS background events, the efficiency of the PSD cut below 1 MeV is poorly

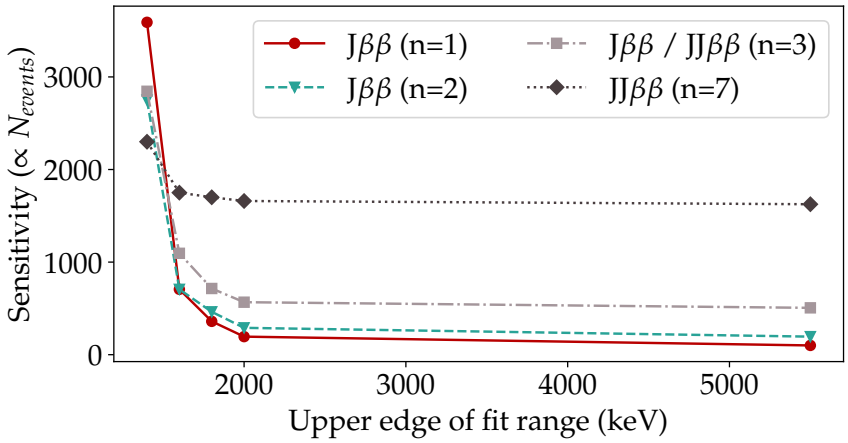

FIGURE 8.2: Sensitivity to the search for Majoron-involving double-β decay for different fit ranges.

understood [4], and its energy dependence would introduce additional systematic uncertainties in the analysis.

8.1.2 Fit model

Fit range The energy range for this analysis extends from 560 keV to 2 MeV. At low energy, the event rate in the GERDA experiment is dominated by the decay of ^{39}Ar. Above 2 MeV, the contribution due to $2\nu\beta\beta$ decay or any other exotic decay mode vanishes. A dedicated study was performed to define the upper limit of the fit range, which maximizes the sensitivity to new physics searches. Different fit ranges were studied, with the upper edge varying from 1400 keV to 5500 keV. The sensitivity to the search for Majoron-involving decays was computed for each fit range. The result is shown in figure 8.2. Better sensitivity is obtained by enlarging the fit range from 1400 keV to 2000 keV, but no significant improvement is observed extending further the fit range. As a result, 2 MeV was chosen as the upper edge of the fit range.

Fit components In the range chosen for this analysis, $2\nu\beta\beta$ decay is the dominant contribution to the energy spectrum. Several other background sources are expected to generate events in the same energy range. According to the results on the modeling of GERDA Phase II data before analysis cuts [5], above the Q-value of ^{39}Ar β decay at 565 keV, minor contributions due to ^{228}Ac, ^{228}Th, ^{214}Bi, ^{60}Co, and ^{40}K decays in the structural materials are expected. The decay of ^{42}K in the LAr volume is also expected to contribute to the background budget. Finally, a minor contribution is expected from α decays on the p^+ electrode of the detectors. In the background model before analysis cut, contributions for a given background source at different locations were treated independently. In this analysis, the LAr veto cut is applied, which leads to a strong reduction of the background. According to the background projection obtained by the modeling of the LAr veto, the γ background in the energy region dominated by $2\nu\beta\beta$ decay is reduced by a factor $\sim$ 10 by the LAr veto

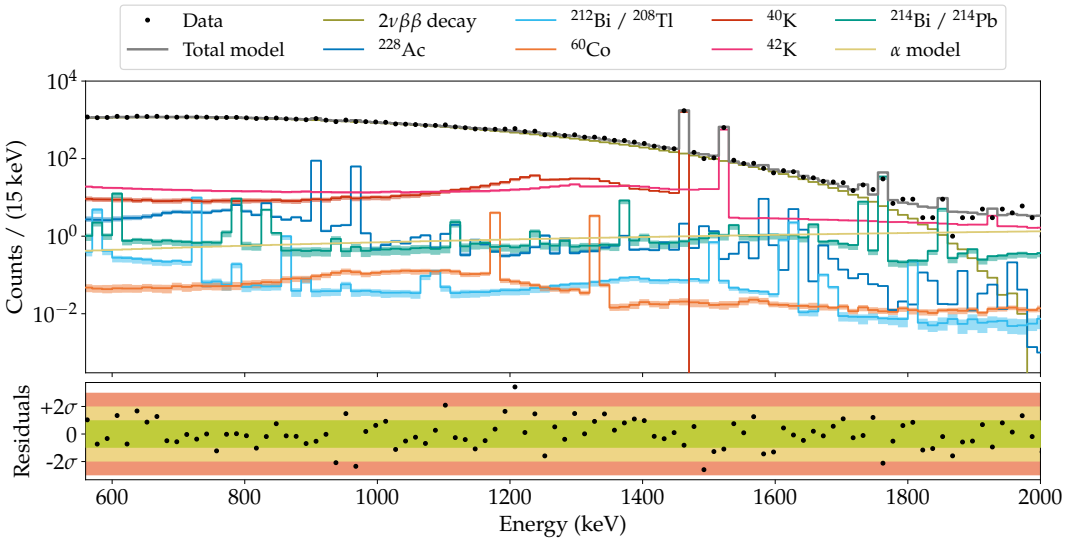

FIGURE 8.3: Background decomposition of the 32.8 kg yr of pre-upgrade BEGe data after the application of the LAr veto cut, as derived in [3]. The shaded bands represent the uncertainty of the LAr veto modeling. In the bottom panel, the difference between data and the total model normalized over the expected statistical fluctuation in each bin is shown.

cut [3]. Figure 8.3 shows the expected background model after LAr veto cut, as derived from the modeling of the LAr veto [3]. Consequently, in the fit model, only a subset of components was used. The signal and background components utilized in the fit are:

- SM $2\nu\beta\beta$ decay and exotic decays inside the detectors (each of them added independently);
- one component each for ^{228}Ac, ^{228}Th, ^{214}Bi, ^{60}Co, and ^{40}K decays close to the detector array (*e.g.* on holders, cables, mini-shroud, ...);
- two components for ^{42}K decay in LAr, to separate the contributions from the decays near and far from the surface of the detectors (*e.g.* inside/outside the mini-shroud);
- one component for the α decays on the p^+ electrode, which is well approximated by a linear function in the energy range of this analysis.[2]

Probability distribution functions The PDFs of signal and background events are obtained from MC simulations, performed using the GEANT4-based MaGe simulation framework [6–9], as detailed in [5]. Finite energy resolution, active volume, and exposure of the individual detectors are taken into account, including ON/OFF

[2] α decays are not expected to generate detectable scintillation light and no differences are expected from the background model before analysis cut. Nevertheless, the sophisticated α model developed in that work is unnecessary here, where the fit range extends only up to 2 MeV.

periods of the detectors during the whole data taking. Additional modeling of the detector response, *i.e.* the DL and TL model, and modeling of the LAr veto response were developed in support of this analysis and implemented in the simulation framework [3, 10–12]. The simulation of the LAr scintillation light production and detection chain was used to determine the effect of the LAr veto cut on the probability distribution functions, which was not included in previous works.

8.2 Statistical analysis and systematic uncertainties

A binned maximum-likelihood fit was performed in the energy window between 560 keV and 2000 keV, with a 10 keV binning. Given the BEGe energy resolution, a 10 keV binning does not remove physical features of the spectrum but is enough to avoid systematic uncertainties due to the energy scale. It has been verified that the binning does not affect the performance of the fit.

Assuming that the number of events in each bin is Poisson distributed, the likelihood function is given by the product of Poisson probabilities for all bins.

$$\mathcal{L}(S,\vec{\theta}) = \prod_i \frac{\lambda_i^{n_i}}{n_i!} \cdot e^{-\lambda_i} \,, \tag{8.1}$$

where the products run over the number of bins i. The likelihood depends on the exotic decay signal strength S, which is the only parameter of interest, and on some nuisance parameters $\vec{\theta}$, that include for instance the background contributions. Finally, n_i denotes the number of observed events in the bin i, and λ_i the expectation value for the same bin, given by the sum of signal and background in that bin $\lambda_i = s_i + b_i$.

The likelihood is then used to construct a frequentist test statistic based on the profile likelihood ratio [13]:

$$T_S = -2\,ln\frac{\mathcal{L}(S,\hat{\hat{\theta}})}{\mathcal{L}(\hat{S},\hat{\theta})} \,, \tag{8.2}$$

where $\hat{\hat{\theta}}$ in the numerator denotes the value of θ which maximizes the likelihood $\mathcal{L}$ for a specific value of S. The denominator is the maximized likelihood function. Thus, higher values of T_S correspond to increasing incompatibility between the data and the hypothesis S.

The probability distribution of the test statistic is evaluated with MC techniques for the background-only hypothesis, corresponding to the parameter of interest being equal to zero, and for a discrete set of non-zero values of the parameter of interest. The test statistic distributions are used to extract the p-value of the data:

$$p_S = \int_{T_{S,obs}}^{\infty} F(T_S|S)\; dT_S \,, \tag{8.3}$$

where $T_{S,obs}$ is the value of the test statistic T_S observed from the data, and $F(T_S|S)$ denotes the probability distribution of the test statistic under the assumption of the

signal strength S. The exclusion limit at a defined confidence level α is given by the value of S for which $p_S = 1 - \alpha$. In this work all the limits are given at 90% C.L., corresponding thus to a p-value of 0.1.

The parameter of interest S, on which the statistical inference is made, depends on the considered new physics process. In the search for double-β decays with the emission of Majorons or pairs of massive fermions, the parameter of interest is the strength of the exotic decay signal, proportional to the inverse of the decay half-life and expressed in number of events in the fit range. In the search for sterile neutrinos and Lorentz-violating effects, the parameter of interest is an internal parameter that defines the $2\nu\beta\beta$ decay distribution and is responsible for its distortion compared to the SM prediction. Additional parameters of the fits are the number of background and $2\nu\beta\beta$ decay events observed in the fit range. These are treated as nuisance parameters and left unconstrained, and their uncertainties are propagated by profiling [14].

8.2.1 Test statistic distribution

It is a known result due to Wilks' theorem that the probability distribution of the profile likelihood ratio test statistic follows, in the large sample limit, a χ^2 distribution with the number of degrees of freedom given by the number of parameter of interest [13]. The parameters of the fit corresponding to the number of observed events are naturally constrained to be positive. This has a consequence in the search for new physics, where the maximum likelihood estimator of the parameter of interest is close to the parameter's bound. In this case, the asymptotic distribution of the test statistic is a $\frac{1}{2}\chi^2$, *i.e.* a mixture of a delta function at zero and a χ^2 distribution with one degree of freedom, each term having weight 1/2 [13]. Nevertheless, in this analysis, not all the regularity conditions required by Wilks' theorem [13, 15] are satisfied, and deviations from the χ^2 distribution are expected.

The test statistic distribution was constructed with MC techniques: 10^4 pseudo-experiments were generated, fitted, and the test statistic was evaluated. The distribution of the test statistic is shown in figure 8.4a, for the J$\beta\beta$ decay ($n = 1$ mode). The pseudo-experiments were generated assuming the GERDA experiment without the J$\beta\beta$ decay. The test statistic for the 0 signal hypothesis (T_0) was evaluated for each pseudo-experiment, and the distribution $F(T_0|0)$ was obtained. This distribution is compared to the $\frac{1}{2}\chi^2$ distribution. A sensible deviation from the asymptotic distribution is observed.

Systematic uncertainties that affect the signal and background PDFs and, in turn, the result of the fit are folded into the analysis during the computation of the test statistic distribution. The different sources of systematic uncertainties will be discussed in the following. Here we limit the attention to the effect of systematic uncertainties on the test statistic distribution. The background model used in the MC generation of the pseudo-experiments is known only with limited precision. Each time a pseudo-experiment is generated, the model is sampled uniformly among the

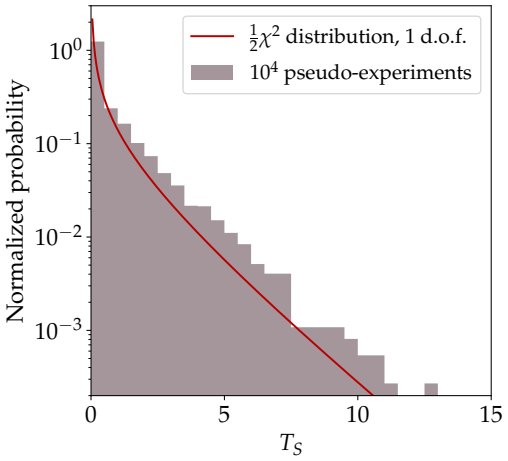

(A) Comparison of the test statistic distribution (without systematic uncertainties) with the $\frac{1}{2}\chi^2$ distribution.

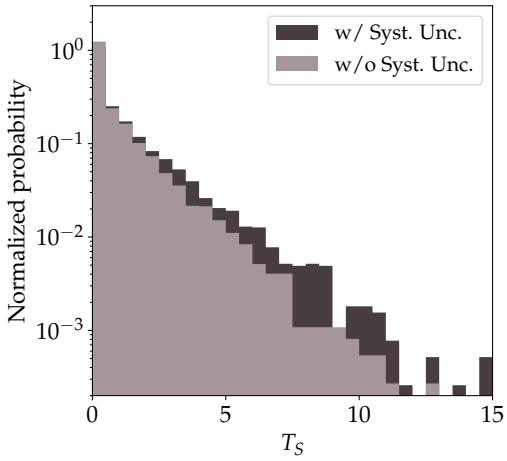

(B) Comparison of the test statistic distribution with and without the inclusion of systematic uncertainties.

FIGURE 8.4: Distribution of the test statistic $F(T_0|0)$ for the J$\beta\beta$ decay with $n = 1$. This was calculated with 10^4 pseudo-experiments assuming the GERDA experiment without the exotic decay.

interval defined by its uncertainties.[3] This can be formalized as a *hybrid Bayesian-frequentist* approach [14]. The test statistic distribution obtained with this procedure can be written as:

$$F(T_S) = \int F(T_S|S,\nu)\,\pi(\nu)\,d\nu\,, \tag{8.4}$$

where ν represents the set of model parameters that are a source of uncertainty, and $\pi(\nu)$ the prior distributions chosen for them. This procedure implies a broadening of the test statistic distribution that is used for statistical inference, and systematic uncertainties are naturally incorporated in the result [14]. The effect of the folding of the systematic uncertainties in the test statistic distribution is shown in figure 8.4b.

8.2.2 Experimental sensitivity

The experimental sensitivity is characterized by the median significance, assuming data generated in the $S = 0$ hypothesis, with which one rejects a non-zero value of S [13]. The median p-value assuming the hypothesis S can be written as:

$$\overline{p} = \int_{\overline{T}_S}^{\infty} F(T_S|S)\,dT_S\,, \tag{8.5}$$

where $\overline{T}_S$ is the test statistic value corresponding to the median of the distribution $F(T_S|0)$.

For each exotic signal hypothesis S, the distributions $F(T_S|0)$ and $F(T_S|S)$ are needed to compute the sensitivity. The first is obtained by evaluating the test statistic

[3] The sampling with uniform prior is a conservative choice. Any more complicated choice, like a Gaussian prior centered in the best model, would produce a lower impact on the final systematic uncertainty.

T_S on a set of pseudo-experiments generated without any exotic signal ($S = 0$), the second assuming an exotic signal equal to S. The sensitivity at a defined confidence level α is given by the value of S for which $\overline{p} = 1 - \alpha$. In this work all the sensitivities are given at 90% C.L., corresponding thus to a median p-value of 0.1.

8.2.3 Systematic uncertainties

Uncertainties on the shape of the signal and background distributions are generally related to the modeling of the background and the detector response. Given a γ decay in the vicinity of a detector, this can deposit the full energy in the detector, resulting in a peak in the energy spectrum, or undergo Compton scattering in the structural materials before depositing the rest of the energy in the detector, resulting in a continuous energy distribution up to the Compton edge. The ratio between the two classes of events is expected to change for γ decays very close to the detector or far from it.

Background source location Different locations of the background sources have been identified while modeling GERDA data before analysis cuts [5]. Still, this picture is changed by the LAr veto cut since the suppression efficiency is expected to be different for the different background components. On the other hand, without prior knowledge, the low background level does not allow to distinguish between different locations of a background source in the fit. As previously mentioned, only one component is used in the fit for each isotope, except for ^{42}K, for which two components are used. The systematic uncertainty introduced by this choice is accounted for in the MC generation of the pseudo-experiments, where the location of each background contribution is uniformly sampled among the complete set of locations defined in [5].

LAr veto modeling The modeling of the LAr veto response is affected by uncertainties in the optical parameters used in the MC simulations, such as the LAr attenuation length and the reflectivity of different materials in the detector array, among the others. A complete treatment of this topic can be found in [3, 12], where the methodology used to model systematic uncertainties of the LAr veto response is discussed. This model is used in the MC generation of the pseudo-experiments to account for the systematic uncertainty affecting the LAr veto response model.

Dead layer and Transition layer modeling The modeling of the germanium detector response can lead to additional systematic uncertainty. In the AV of the detector, where the CCE is maximal, the deposited energy is always well reconstructed. The CCE degrades in a 1 mm deep TL at the n^+ contact lithiated surface [16]. Energy deposition in this region is only partially reconstructed, depending on the efficiency profile and the size of the TL. In turn, both these parameters affect the energy distribution of different fit components, particularly the lower tail of intense γ peaks and

the low energy region of the $2\nu\beta\beta$ decay spectrum. The CCE is assumed to decrease linearly in the TL, which has an average size in the BEGe detectors of about 50% of the whole DL region [11]. In the PDFs, the TL size is assigned individually to each detector. In the MC generation of the pseudo-experiments, the TL size of each detector is varied in a conservative range of ± 5 standard deviations from the central value.

Theoretical calculations Finally, uncertainties in the theoretical calculations of the shape of $2\nu\beta\beta$ decay are considered. Different shapes of $2\nu\beta\beta$ decay are predicted if the calculations assume the Higher-State Dominance (HSD) or the Single-State Dominance (SSD) model. The HSD model is based on the assumption that all the intermediate states of the intermediate nucleus contribute to the decay rate [17]. This hypothesis has always been assumed in calculating the shape of the ^{76}Ge $2\nu\beta\beta$ decay. The SSD model, on the other hand, assumes that the $2\nu\beta\beta$ decay is governed by a virtual two-steps transition through the first 1^+ state of the intermediate nucleus [18]. This model has been observed to describe better the $2\nu\beta\beta$ decay of several nuclei [19–21]. In ^{76}Ge, the difference between the two models is maximal (about 10%) in the tail of the distribution, but only less than 0.5% around the peak of the distribution.[4] In both cases, the calculations have been performed using exact Dirac wave functions with finite nuclear size and electron screening as described in [17]. The $2\nu\beta\beta$ distribution is equally sampled from both models in the MC generation of the pseudo-experiments.

8.3 Results on the search for Majoron-involving decays

In chapter 1, we have introduced several double-β decays with the emission of one or two Majorons, J$\beta\beta$, and JJ$\beta\beta$ decays, respectively. In this work, we searched for 4 different decay modes corresponding to spectral index $n = 1$, 2, 3, and 7. The spectral index defines the energy distribution of the decay, as shown in figure 8.1.

The energy distribution of the Majoron-involving decay was added to the fit as an independent component that constitutes the signal. The parameter of interest is the number of signal events observed in the dataset, proportional to the inverse of the decay half-life.

No evidence of a positive signal was found for any of the considered Majoron models. In the analysis data set, 46430 $2\nu\beta\beta$ decay events are found, whereas 4610 events are associated with the other backgrounds. The best-fit value for the $n = 1$ and 7 lies at zero. A non-zero best-fit value is found in the case of $n = 2$ and 3, but the 68% C.L. interval includes zero. Therefore, a 90% C.L. limit has been set on the strength of each considered decay. The observed p-value has been evaluated for a discrete set of values of the parameter of interest, using the test statistic distribution computed with MC methods. The resulting p-value distributions are shown

[4] Private communication with *J. Kotila* and *F. Iachello*.

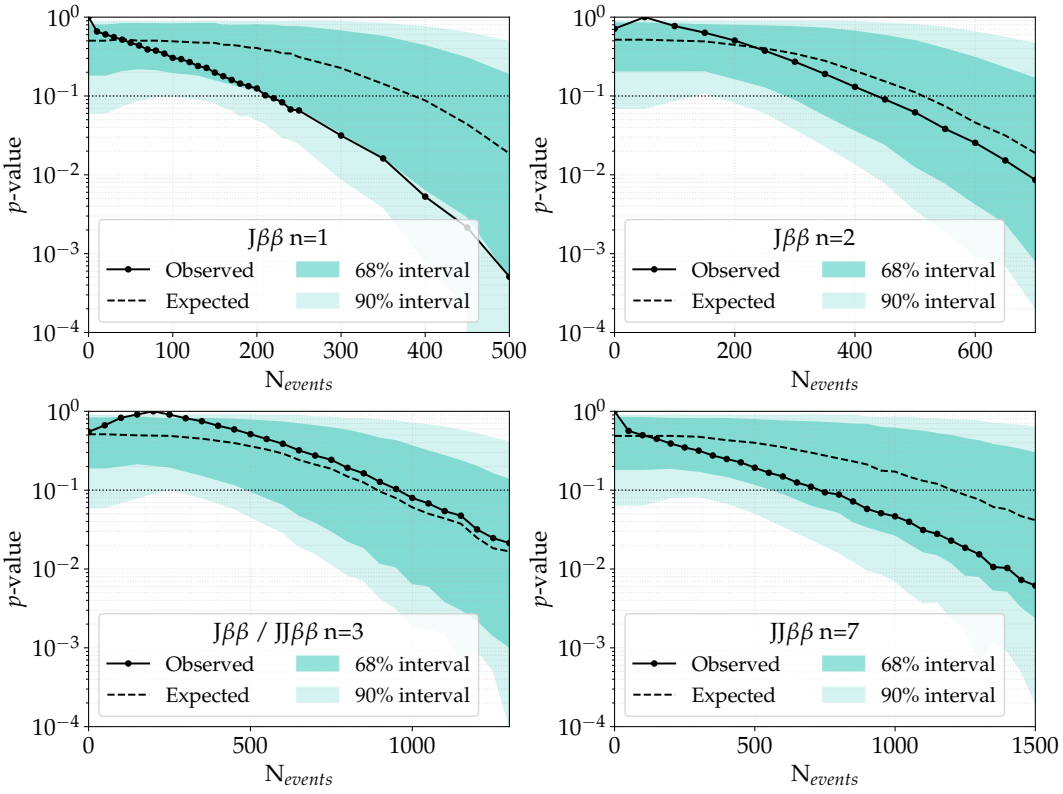

FIGURE 8.5: *p*-value as a function of the number of events in the fit range for the indicated Majoron decay modes. The dashed black line shows the median of the *p*-value distributions for several MC realizations of the GERDA experiment with no signal. The colored bands indicate the spread of the distributions, given by the central 68% and 90% probability intervals. The observed *p*-value for the GERDA data is represented by the solid black line. The 90% C.L. limit (sensitivity) on the number of events in the fit range is given by the intersection of the solid (dashed) black line with the dotted line, corresponding to a *p*-value of 0.1.

in figure 8.5, for all the considered Majoron-involving decays. The median of the *p*-value distribution, which gives the experimental sensitivity, and the 68% and 90% C.L. intervals are also shown in the same figure.

The impact of the systematic uncertainties has been studied by repeating the hypothesis test without including the systematic uncertainties in the distribution of the test statistic. In figure 8.6, the *p*-value distributions obtained without including the systematic uncertainties in the generation of the pseudo-experiments are shown, in comparison to the distributions shown in figure 8.5. A comparison of the 90% C.L. limits on the number of counts obtained with and without systematic uncertainties is presented in table 8.1. The contribution of the systematic uncertainties to the limits is about 12%, 15%, 14%, and 25%, respectively, for the Majoron decay modes with spectral index $n = 1$, 2, 3, and 7.

The one-sided intervals on the number of events are converted to lower limits on the half-life of the decays. The last can be related to the neutrino-Majoron coupling

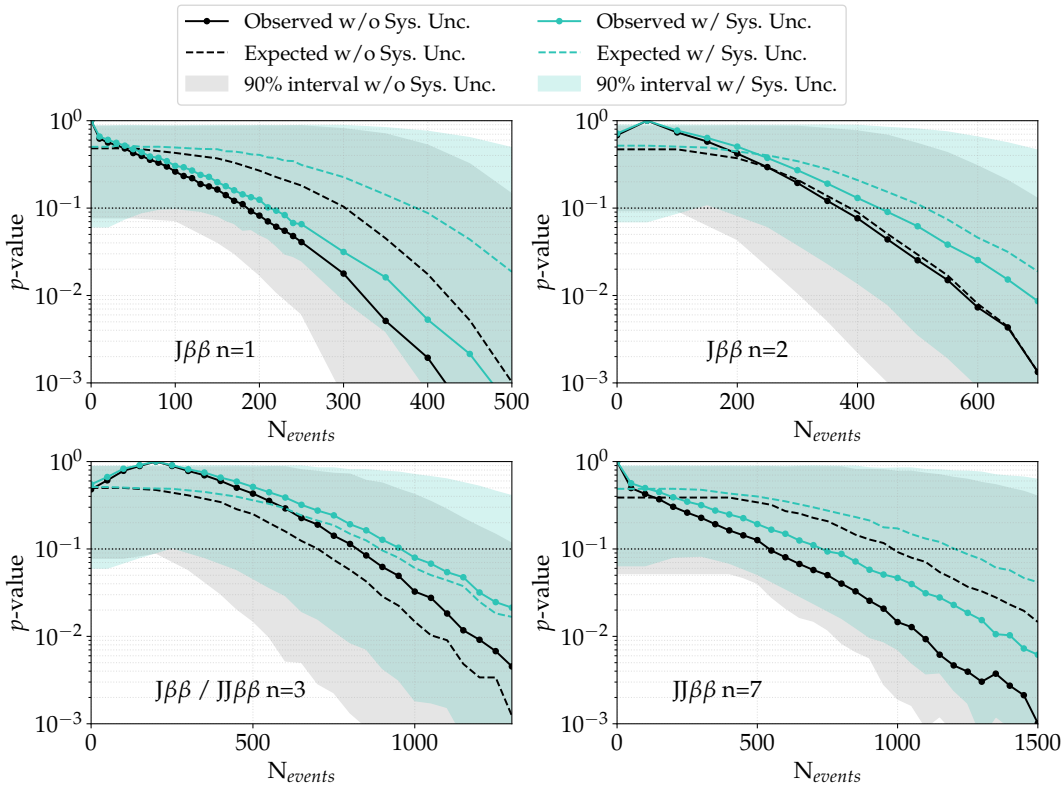

FIGURE 8.6: Comparison of p-value distributions with and without systematic uncertainties for the indicated Majoron decay modes. For details of the graphical representation see caption of figure 8.5.

Decay mode	90% C.L. limit on N_{events}		Impact (%)
	w/o Sys. Unc.	w/ Sys. Unc.	
$J\beta\beta$ ($n = 1$)	< 186	< 211	12
$J\beta\beta$ ($n = 2$)	< 371	< 436	15
$J\beta\beta$/ $JJ\beta\beta$ ($n = 3$)	< 824	< 956	14
$JJ\beta\beta$ ($n = 7$)	< 542	< 728	25

TABLE 8.1: Observed 90% C.L. limits on the number of events in the fit range obtained for the different Majoron-involving decays, with and without systematic uncertainties. The impact of the systematic uncertainties on each limit is also given in the last column.

Decay mode	$\mathcal{M}_\alpha$	G^α (10^{-18} yr^{-1})
J$\beta\beta$ ($n = 1$)	2.66 – 6.34	44.2
J$\beta\beta$ ($n = 2$)	–	–
J$\beta\beta$ ($n = 3$)	0.381	0.073
JJ$\beta\beta$ ($n = 3$)	0.0026	0.22
JJ$\beta\beta$ ($n = 7$)	0.0026	0.420

TABLE 8.2: Nuclear matrix elements and phase space factors for the decays with Majoron emission. Nuclear matrix element for the decay mode with $n = 1$ are taken from [22–32], for the decay modes with $n = 3$ and $n = 7$ from [33]. The phase space factors for all the decay modes are taken from [34]. No calculations are available for the decay mode with $n = 2$.

Decay mode	$T_{1/2}$ (yr)		Observed g_J
	Sensitivity	Observed limit	
J$\beta\beta$ ($n = 1$)	$3.5{\cdot}10^{23}$	$> 6.4{\cdot}10^{23}$	$< (1.8 - 4.4){\cdot}10^{-5}$
J$\beta\beta$ ($n = 2$)	$2.5{\cdot}10^{23}$	$> 2.9{\cdot}10^{23}$	–
J$\beta\beta$ ($n = 3$)	$1.3{\cdot}10^{23}$	$> 1.2{\cdot}10^{23}$	< 0.017
JJ$\beta\beta$ ($n = 3$)	$1.3{\cdot}10^{23}$	$> 1.2{\cdot}10^{23}$	< 1.2
JJ$\beta\beta$ ($n = 7$)	$5.8{\cdot}10^{22}$	$> 1.0{\cdot}10^{23}$	< 1.0

TABLE 8.3: Sensitivities and observed lower limits on the half-life, and upper limits on the coupling constant at 90% C.L. for the different Majoron-involving decays.

constant g_J through the relation:

$$[T_{1/2}]^{-1} = g_J^{2m} |g_A^2 \, \mathcal{M}_\alpha|^2 \, G^\alpha \, , \tag{8.6}$$

where $g_A = 1.27$ is the axial vector coupling constant, m is the number of emitted Majorons, $\mathcal{M}_\alpha$ is the nuclear matrix element, and G^α is the phase space of the decay. The latter two are summarized in table 8.2 for the different decay modes. The nuclear matrix elements for the decay mode with $n = 1$ are the same as for $0\nu\beta\beta$ decay. We used the full set of available calculations, which lie in the range 2.66 – 6.04 for ^{76}Ge [22–32]. The nuclear matrix elements for the decay modes with $n = 3$ and $n = 7$ have been calculated in [33] and the phase space factors for all the decay modes in [34]. For $n = 2$ there are no nuclear matrix elements and phase space calculations available, thus only the limit on the half-life is given. The lower limits and the sensitivities on the half-life of all the considered decays are summarized in table 8.3, together with the corresponding upper limit on the neutrino-Majoron coupling constant.

The obtained results represent an improvement of factor ~ 2 with respect to GERDA Phase I results [1] and are comparable with the limits obtained with other double-β decay isotopes [20, 35–38]. For $n = 7$ the limit on the half-life of the decay is a factor of 2 better than the current best limit [38], despite a factor of $\sim$7 lower

exposure used in this work. This result can be attributed to the particularly low background achieved in the energy region where the bulk of the $2\nu\beta\beta$ decay distribution lies and where the deformation introduced by the $n = 7$ model is expected. Nevertheless, the corresponding limits on the coupling constant are comparable since the phase space of the decay in ^{76}Ge is only $0.42{\cdot}10^{-18}\,\mathrm{yr}^{-1}$, compared to $12.5{\cdot}10^{-18}\,\mathrm{yr}^{-1}$ in ^{136}Xe [34]. A comparison of this result and the results obtained by different double-β decay experiments in the search for Majoron-involving decay was presented in chapter 1, table 1.4.

8.4 Results on the search for Lorentz and CPT violation

As introduced in chapter 1, the violation of Lorentz and CPT symmetries in the neutrino sector would affect the distribution of $2\nu\beta\beta$ decay. In particular, the isotropic component of the *counter-shaded* coefficient, $\mathring{a}^{(3)}_{\mathrm{of}}$, affects the kinematics of $2\nu\beta\beta$ decay. The effect can be described with a perturbation of the SM $2\nu\beta\beta$ decay, whose distribution is shown in figure 8.1.

Defining w as the ratio between the integral of the Lorentz violating perturbation's distribution and the integral of the SM $2\nu\beta\beta$ decay distribution, which is the measured quantity, this can be related to the coefficient $\mathring{a}^{(3)}_{\mathrm{of}}$ through the ratio between the phase space factors $G^{2\nu}$ and $dG_{LV}/\mathring{a}^{(3)}_{\mathrm{of}}$.

$$\mathring{a}^{(3)}_{\mathrm{of}} = w \cdot \frac{\mathring{a}^{(3)}_{\mathrm{of}} G^{2\nu}}{dG_{LV}} \,. \tag{8.7}$$

We used the calculations performed in [39] using exact electron wave functions to build the Fermi functions and with the inclusion of finite nuclear size and screening effects:

$$\frac{\mathring{a}^{(3)}_{\mathrm{of}} G^{2\nu}}{dG_{LV}} = 1.19 \cdot 10^{-4}\, GeV \,. \tag{8.8}$$

In the search for Lorentz violation, the parameter of interest is the parameter w defined above, which is directly proportional to the Lorentz violating coefficient $\mathring{a}^{(3)}_{\mathrm{of}}$.

No evidence of deviation from the SM $2\nu\beta\beta$ decay distribution has been observed. Therefore, a 90% C.L. limit has been set on $\mathring{a}^{(3)}_{\mathrm{of}}$. Since both positive and negative values of $\mathring{a}^{(3)}_{\mathrm{of}}$ are theoretically allowed, a two-sided interval is extracted for this parameter. The observed p-value has been evaluated for a set of values of $\mathring{a}^{(3)}_{\mathrm{of}}$, using the test statistic distribution computed with MC methods. The resulting p-value distribution is shown in figure 8.7. The median of the p-value distribution, which gives the experimental sensitivity, and the 68% and 90% C.L. intervals are also shown in the same figure.

We obtained a two-sided 90% C.L. interval of $(-2.7 < \mathring{a}^{(3)}_{\mathrm{of}} < 6.2)\cdot 10^{-6}$ GeV on the SME coefficient responsible for Lorentz violation in $2\nu\beta\beta$ decay. The expected sensitivity for the GERDA experiment under no signal hypothesis is $(-3.8 < \mathring{a}^{(3)}_{\mathrm{of}} < 4.9)\cdot 10^{-6}$ GeV. The impact of the systematic uncertainties on the limit was studied.

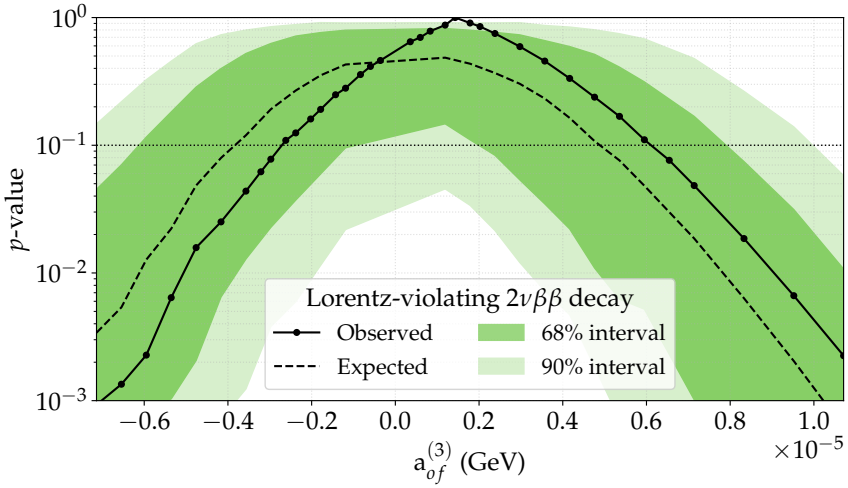

FIGURE 8.7: p-value as a function of the Lorentz-violating coefficient $\mathring{a}^{(3)}_{\mathrm{of}}$. For details of the graphical representation see caption of figure 8.5.

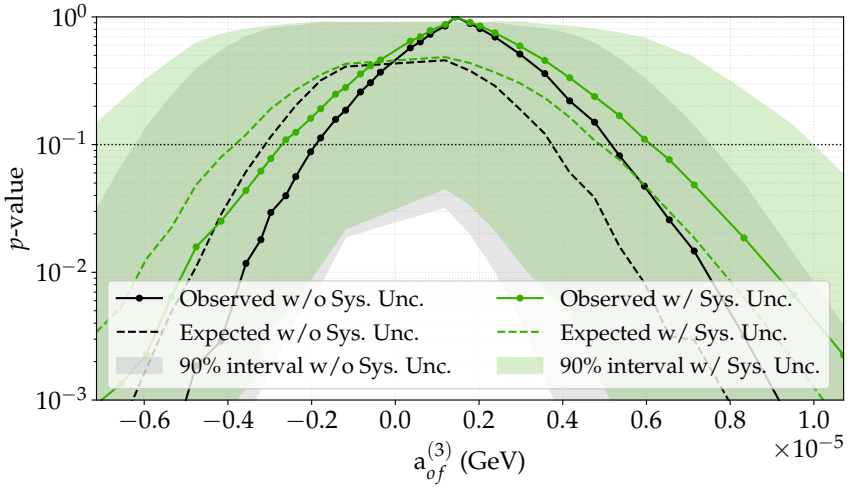

FIGURE 8.8: Comparison of p-value distributions with and without systematic uncertainties for the Lorentz violating parameter $\mathring{a}^{(3)}_{\mathrm{of}}$. For details of the graphical representation see caption of figure 8.5.

In figure 8.8, the p-value distribution obtained without systematic uncertainties is shown, in comparison to the distribution shown in figure 8.7. Without systematic uncertainties, we obtained a two-sided 90% C.L. interval of $(-1.9 < \mathring{a}^{(3)}_{\mathrm{of}} < 5.2) \cdot 10^{-6}$ GeV. The overall impact of the systematic uncertainties on the limit is about 34%.

The limit obtained in this work with ^{76}Ge $2\nu\beta\beta$ decay is competitive with the existing limits obtained with other isotopes [20, 37, 40, 41]. They have been summarized in chapter 1, table 1.5. The current best limit on $\mathring{a}^{(3)}_{\mathrm{of}}$, of the order of 10^{-7} GeV, was obtained with a very large statistic data set with the NEMO-3 experiment, with about $4.9 \cdot 10^5$ ^{100}Mo $2\nu\beta\beta$ decay events [20].

8.5 Results on the search for light exotic fermions

The emission of light exotic fermions in double-β decays was extensively discussed in chapter 3. In this work, we searched for sterile neutrinos and their Z_2-odd variant with masses of hundreds of keV.

The energy distribution of the decay with the emission of a sterile neutrino is shown in figure 8.1 for a mass of 600 keV. The endpoint of the distribution is shifted by the mass of the sterile neutrino compared to the SM $2\nu\beta\beta$ decay distribution. Given the $Q_{\beta\beta}$ of ^{76}Ge, a sterile neutrino with a mass up to 2 MeV could be emitted. Nevertheless, as the mass of the emitted sterile neutrino increases the energy distribution moves to the left, finally ending up below the energy threshold of the analysis so that no deformation of the shape is expected in the fit range. In fact, in this analysis, the emission of sterile neutrinos with masses between 100 and 900 keV was investigated.

To search for sterile neutrinos, the energy distribution of $2\nu\beta\beta$ decay is modified according to equation 3.3, using the calculations for $\Gamma^{N\nu}$ given in chapter 3. The parameter of interest is the mixing angle $\sin^2\theta$. The energy distribution also depends on the mass of the sterile neutrino, m_N. Different masses have been analyzed independently, fixing the value of the mass in the energy distribution.

No evidence of deviation from the SM $2\nu\beta\beta$ decay distribution has been observed. The best-fit value of $\sin^2\theta$ lies at zero for all the considered masses. Therefore, a 90% C.L. limit has been set on $\sin^2\theta$. The observed p-value has been evaluated for a set of values of $\sin^2\theta$, using the test statistic distribution computed with MC methods. The resulting p-value distribution is shown in figure 8.9 for all the considered sterile neutrino masses. The median of the distribution of the expected p-value, which gives the experimental sensitivity, and the 68% and 90% C.L. intervals are also shown in the same figure.

The most stringent limit was obtained for masses between 500 and 600 keV. For these masses, the 90% C.L. interval obtained on the mixing between sterile and active neutrinos is $\sin^2\theta < 0.013$. The expected sensitivity for the GERDA experiment under the no signal hypothesis is $\sin^2\theta < 0.026$ and $\sin^2\theta < 0.029$, respectively for $m_N = 500$ and 600 keV. Limits on the mixing $\sin^2\theta$ and the corresponding sensitivities for the different sterile neutrino masses considered are summarized in table 8.4. The limits obtained without systematic uncertainties are also reported in the same table, together with the impact of the systematic uncertainties on the limits, which varies between 17 – 40%, depending on the sterile neutrino mass. The p-value distributions obtained without systematic uncertainties are shown in figure 8.10.

As discussed in chapter 3, the production of two sterile neutrinos in double-β decay is allowed but strongly suppressed compared to the single production. On the other hand, the Z_2-odd fermion χ, introduced in chapter 3, can only be produced in pairs due to the additional symmetry. Consequently, β decay experiments, which set the most stringent bounds on sterile neutrinos in the keV – MeV mass range,

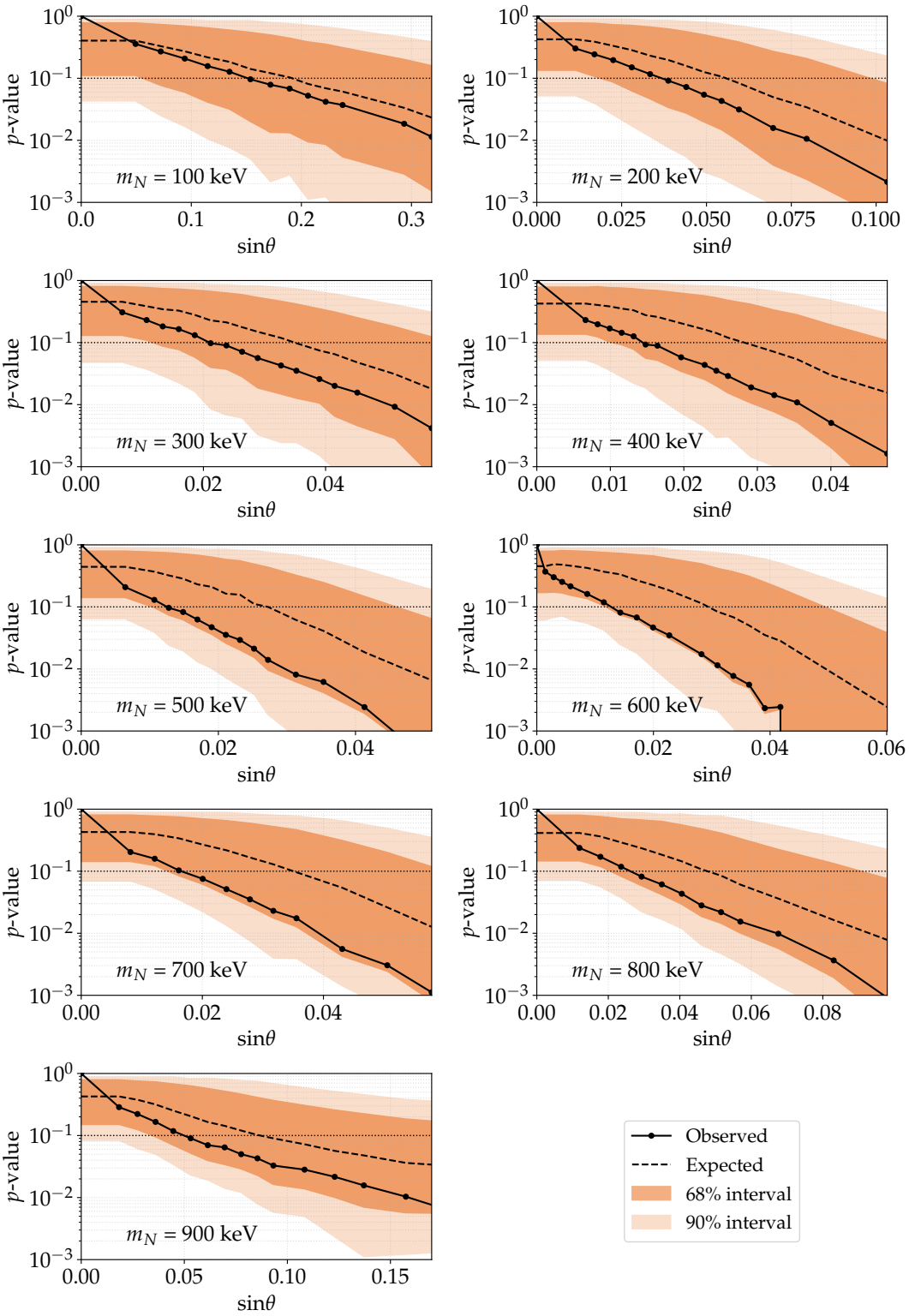

FIGURE 8.9: p-value as a function of the mixing $\sin^2\theta$ for the indicated sterile neutrino masses. For details of the graphical representation see caption of figure 8.5.

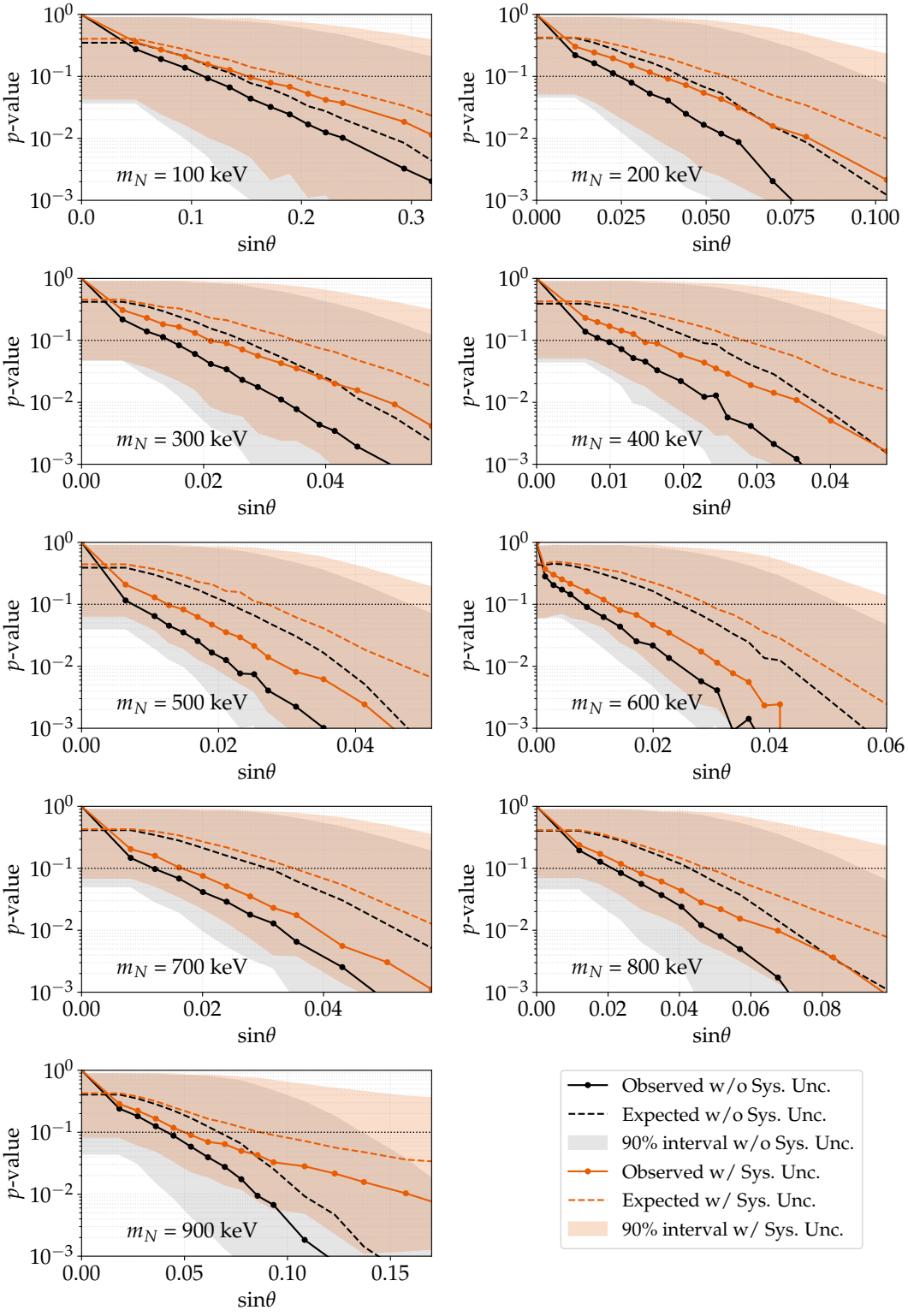

FIGURE 8.10: Comparison of p-value distributions with and without systematic uncertainties for the indicated sterile neutrino masses. For details of the graphical representation see caption of figure 8.5.

m_N (keV)	$\sin^2\theta$		Impact of
	Sensitivity	Observed limit	Sys. Unc. (%)
100	0.19	< 0.15 (0.11)	30
200	0.056	< 0.037 (0.024)	35
300	0.035	< 0.021 (0.014)	31
400	0.028	< 0.014 (0.0092)	36
500	0.026	< 0.013 (0.0069)	45
600	0.029	< 0.013 (0.081)	37
700	0.035	< 0.016 (0.012)	29
800	0.047	< 0.026 (0.021)	18
900	0.087	< 0.050 (0.041)	17

TABLE 8.4: Sensitivities and upper limits on the mixing angle $\sin^2\theta$ between active and sterile neutrinos, for different sterile neutrino masses m_N. The values in brackets of the observed limits were obtained without systematic uncertainties. The impact of the systematic uncertainties on the limit is also given in the last column.

cannot test these kinds of models, while double-β decays offer a unique opportunity to search for these exotic decays.

The energy distribution expected for double-β decay with the emission of two exotic fermions is analogous to the sterile neutrino case, with the difference that the endpoint of the distribution is shifted by twice the mass of the exotic fermion since two particles are emitted. This is shown for ^{76}Ge and a mass of 300 keV in figure 8.1. Given the $Q_{\beta\beta}$ of ^{76}Ge at around 2 MeV, only particles with mass below 1 MeV can be produced in pairs. Nevertheless, as for the emission of sterile neutrinos, for high masses, the energy distribution moves below the energy threshold of the fit, and no shape deformation is expected in the fit range. In fact, we searched for pair production of χ fermions with masses between 100 keV and 700 keV.

The energy distribution of the exotic decay is added to the fit as an independent component that constitutes the signal. The number of signal events observed in the fit range, which is proportional to the inverse of the decay half-life, is the parameter of interest in this analysis. The signal energy distribution also depends on the mass of the fermions, m_χ. Different masses have been analyzed independently, fixing the value of the mass in the energy distribution.

No evidence of a positive signal is found for any considered mass. The best fit for the number of exotic decay events always lies at zero. Therefore, a 90% C.L. limit has been set on the strength of each considered decay. The observed p-value has been evaluated for a discrete set of values of the parameter of interest, using the test statistic distribution computed with MC methods. The resulting p-value distribution is shown in figure 8.11, for all the considered exotic fermion masses. The median of the distribution of the expected p-value, which gives the experimental sensitivity, and the 68% and 90% C.L. intervals are also shown in the same figure.

The impact of the systematic uncertainties has been studied. In figure 8.12, the p-value distributions obtained without including the systematic uncertainties in the

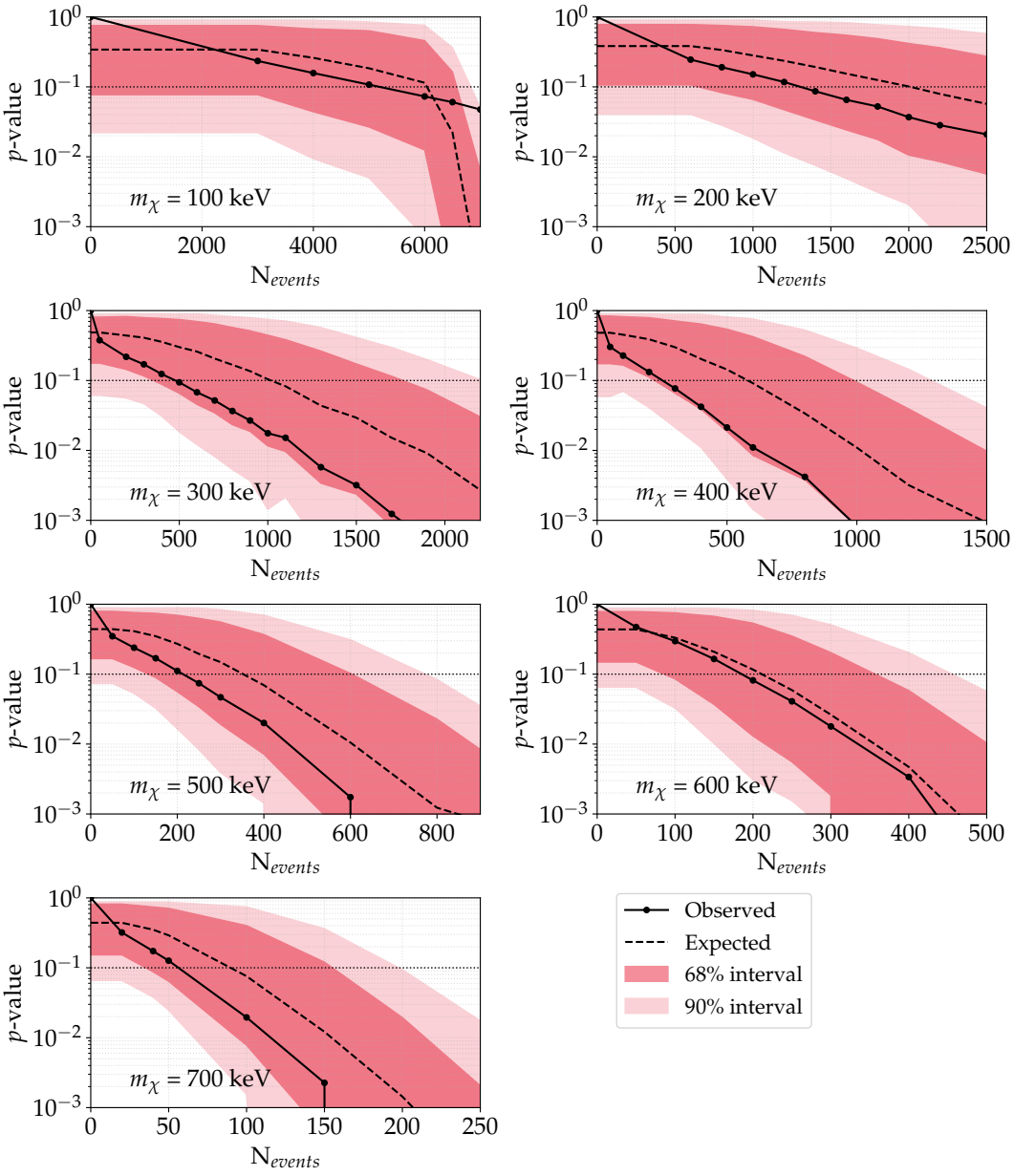

FIGURE 8.11: p-value as a function of the number of events in the fit range for the indicated masses of the exotic fermion χ. For details of the graphical representation see caption of figure 8.5.

Mass (keV)	90% C.L. limit on N_{events}		Impact (%)
	w/o Sys. Unc.	w/ Sys. Unc.	
100	< 3931	< 5185	24
200	< 861	< 1306	34
300	< 293	< 479	39
400	< 176	< 263	33
500	< 182	< 212	14
600	< 184	< 186	1
700	< 54	< 56	0.2

TABLE 8.5: Observed 90% C.L. limits on the number of events in the fit range obtained for different masses of the exotic fermion χ, with and without systematic uncertainties. The impact of the systematic uncertainties on each limit is also given in the last column.

distribution of the test statistic are compared to the distribution shown in figure 8.11. A comparison of the 90% C.L. limits on the number of counts obtained with and without systematic uncertainties is presented in table 8.5. The impact of the systematic uncertainties on the limits varies between 0.2 – 40%, depending on the mass of the exotic fermion.

The one-sided intervals on the number of events are converted to lower limits on the half-life of the decays. The last can be related to the coupling constant between the exotic fermions and neutrinos g_χ through the relation:

$$[T_{1/2}]^{-1} = g_\chi^2 \, C \, |g_A^2 \, \mathcal{M}_{0\nu}|^2 \, G^{\chi\chi} \, , \tag{8.9}$$

where $C = m_e^2/(8\pi^2 R^2)$ is a constant factor that contains the electron mass m_e and the nuclear radius $R = 1.2\,A^{1/3}$ fm, which in natural units (1/fm = 197.3 MeV) is $R = 0.026\,\text{MeV}^{-1}$ for ^{76}Ge, $\mathcal{M}_{0\nu}$ is the nuclear matrix element, that is the same as for $0\nu\beta\beta$ decay, and $G^{\chi\chi}$ the phase space for the emission of two massive fermions. For each fermion mass, we used all the available calculations of the nuclear matrix element of $0\nu\beta\beta$ decay, that are in the range 2.66 – 6.04 for ^{76}Ge [22–32] and compute the phase space factors according to the formula given in chapter 3, to convert the lower limit on the half-life in an upper limit on g_χ. The lower limits on the half-life, the expected sensitivity, and the upper limit on the coupling constant at 90% C.L. for the $\chi\chi\beta\beta$ decays and the different fermion masses considered are summarized in table 8.6. In the same table, also the computed phase space factors for the different masses are reported.

The limits on $\sin^2\theta$ and on the coupling g_χ are also shown as a function of the exotic fermion mass in figure 8.13. The best limit is obtained for a mass of 500–600 keV in the search for sterile neutrino, and for masses of 300 – 400 keV in the search for pair production of Z_2-odd fermions. The sensitivity to smaller masses is limited by the correlation between the SM $2\nu\beta\beta$ decay and the exotic decay. For low masses, the distribution of the decay into exotic fermions becomes indistinguishable from

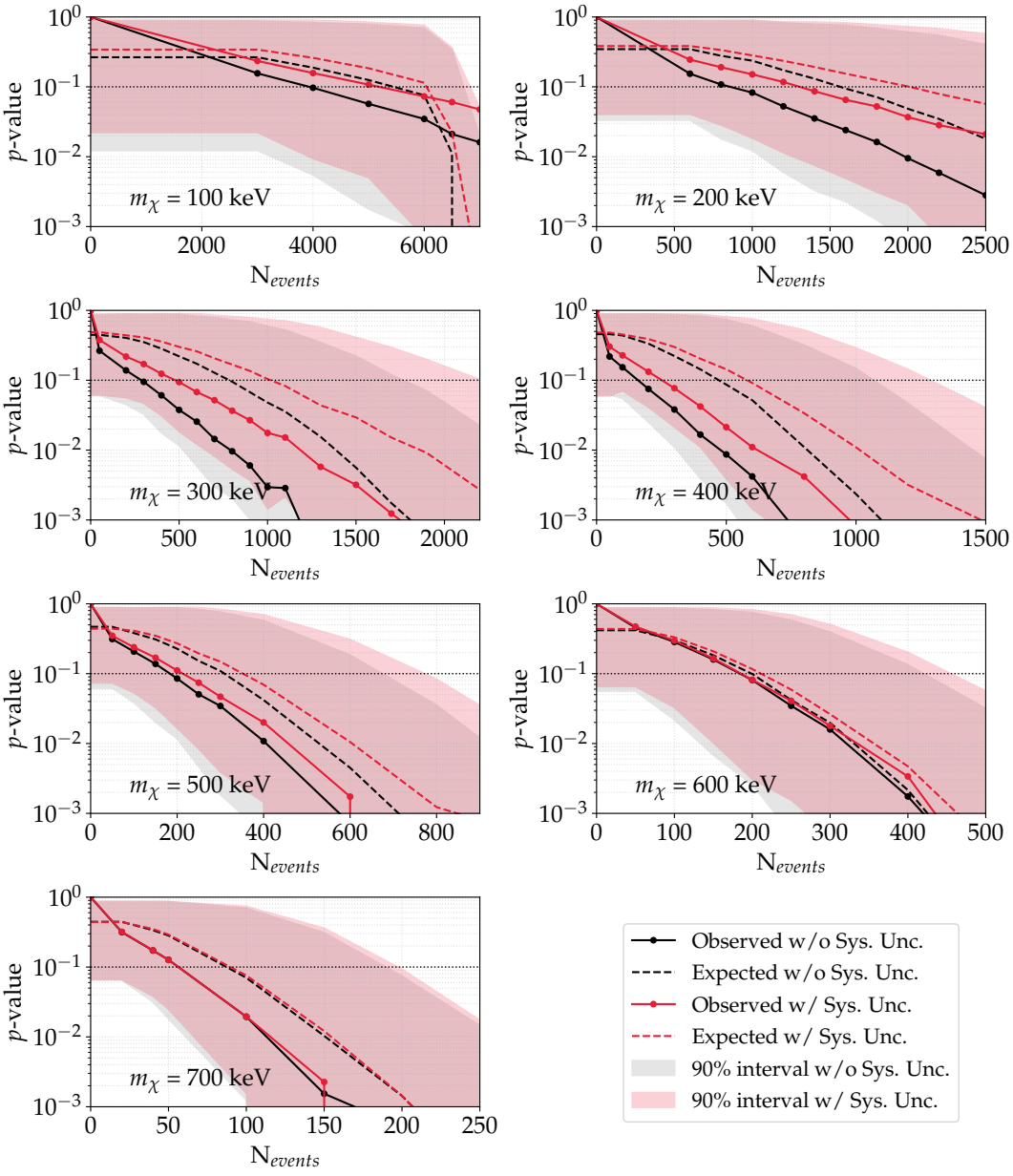

FIGURE 8.12: Comparison of p-value distributions with and without systematic uncertainties for the indicated masses of the exotic fermion. For details of the graphical representation see caption of figure 8.5.

m_χ (keV)	$G^{\chi\chi}$ (10^{-20} yr^{-1})	$T_{1/2}$ (10^{23} yr) Sensitivity	Observed limit	Observed g_χ (10^{-3} MeV^{-2})
100	4.2	0.15	> 0.18	< (1.4 – 3.2)
200	3.3	0.44	> 0.67	< (0.8 – 1.8)
300	2.3	0.77	> 1.6	< (0.6 – 1.4)
400	1.4	1.1	> 2.5	< (0.6 – 1.4)
500	0.75	1.2	> 2.1	< (0.9 – 2.2)
600	0.32	1.0	> 1.1	< (2.0 – 4.6)
700	0.10	0.16	> 0.25	< (7.4 – 17)

TABLE 8.6: Phase space factors $G^{\chi\chi}$, expected sensitivities and lower limits on the half-life $T_{1/2}$, and upper limits on the coupling constant g_χ at 90% C.L., for different fermion masses m_χ.

the SM $2\nu\beta\beta$ decay distribution, where two anti-neutrino are emitted. At higher masses, the sensitivity is weaker because of the limited space phase factor available for the exotic decay.

Existing bounds on the sterile neutrino mixing from β decay experiments [42–45] and solar neutrinos [46] are also shown in figure 8.13. The limits obtained in this work are not competitive. Still, they demonstrate the potential of double-β decay experiments to search for sterile neutrino, with larger exposure data sets and good control of the systematic uncertainties. There are no direct constraints on the pair production of Z_2-odd fermions. This work represents the first experimental search of such an exotic particle in double-β decays.

8.6 Conclusions and outlook

We presented the search for exotic double-β decay modes of ^{76}Ge, performed on a selected data set collected during Phase II of the GERDA experiment. No indication of deviations from the SM $2\nu\beta\beta$ decay distribution was found for any of the considered decay modes. Limits on the different models have been set with a frequentist hypothesis test based on the profile likelihood test statistic, whose probability distributions have been evaluated with MC methods.

In figure 8.14 the analyzed data set is shown, together with the best-fit model, corresponding to the absence of any new physics signal. The contributions from the SM $2\nu\beta\beta$ decay and other backgrounds are also shown separately. The limits at 90% C.L. on the different new physics contributions obtained from the individual analysis are shown. All the results presented in this work represent the most stringent limits obtained with ^{76}Ge.

The search for double-β decays with the emission of Majorons in ^{76}Ge was already performed in Phase I of the GERDA experiment [1]. The improvement of a factor of $\sim$ 2 obtained in this work, with only slightly higher exposure, can be attributed to the lower background and smaller impact of the systematic uncertainties. In this work, we searched for hints of violation of the Lorentz symmetry in $2\nu\beta\beta$

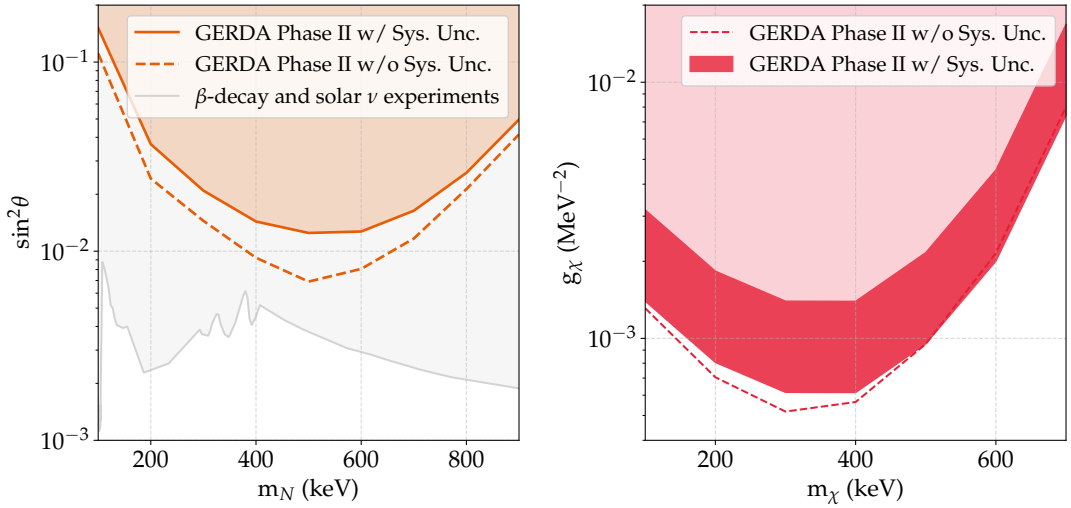

FIGURE 8.13: (Left) Limits at 90% C.L. on the mixing $\sin^2\theta$ as a function of the sterile neutrino mass. The excluded region is indicated by the orange shaded area. The limits that would be obtained with the GERDA experiment without systematic uncertainties are shown by the dashed line. Existing bounds from single-β decay experiments [42–45] and solar neutrinos [46] are also shown. (Right) Limits at 90% C.L. on the coupling g_χ as a function of the mass of the exotic fermion χ. The excluded region is indicated by the pink shaded area. The spread of the limit, indicated by the colored band, represents the NMEs uncertainty. The dashed line indicates the lower bound of the limit, which would be obtained with the GERDA experiment without systematic uncertainties.

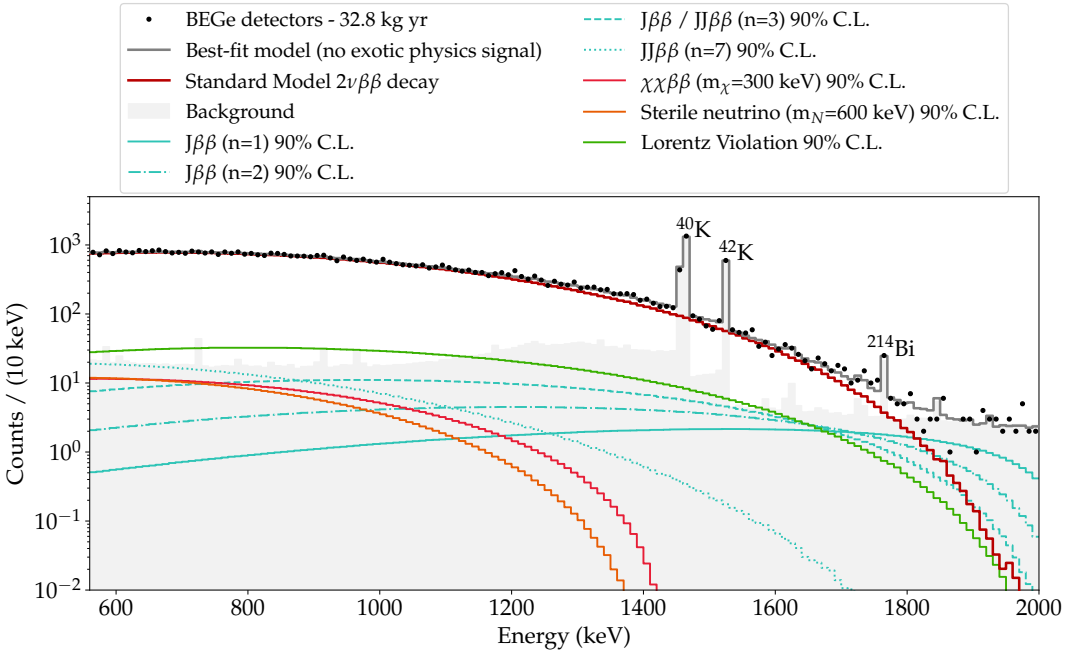

FIGURE 8.14: Data energy spectrum and best-fit model, corresponding to the absence of any new physics signal. The contributions from the SM $2\nu\beta\beta$ decay and other backgrounds are also shown separately by the solid red line and the shaded area, respectively. The most prominent γ-lines are labeled. The 90% C.L. limits on the different new physics contributions obtained in this work are also visualized with different colors.

decay for the first time with ^{76}Ge. We also performed the first experimental search for the emission of massive fermions, including sterile neutrinos, in $2\nu\beta\beta$ decay.

The LEGEND experiment [47], the future of double-β decay physics with ^{76}Ge, will provide in the next decade a large statistic data set of $2\nu\beta\beta$ decays. A substantial improvement of the sensitivity to BSM searches still requires a further reduction of the systematic uncertainties that will become dominant as the statistics increases. For instance, a better understanding of the background model after the LAr veto cut would be beneficial. The uncertainty of the background source location is one of the dominant contributions to the systematic uncertainty of the results presented in this work. With an increased statistic and reduction of the systematic uncertainties, LEGEND would have the possibility to test unexplored regions of the parameter space, for example, in the search for sterile neutrino with masses of hundreds of keV, as was shown in chapter 3.

References

[1] GERDA Collaboration, M. Agostini, et al. "Results on $\beta\beta$ decay with emission of two neutrinos or Majorons in ^{76}Ge from GERDA Phase I". In: *Eur. Phys. J. C* 75.9 (2015), p. 416. DOI: 10.1140/epjc/s10052-015-3627-y. arXiv: 1501.02345.

[2] GERDA Collaboration, M. Agostini, et al. "Search for exotic physics in double-β decays with GERDA Phase II". submitted to JCAP. 2022. arXiv: 2209.01671.

[3] GERDA Collaboration, M. Agostini, et al. "Liquid argon light collection and veto modeling in GERDA Phase II". submitted to Eur. Phys. J. C. 2022. arXiv: 2212.02856.

[4] GERDA Collaboration, M. Agostini, et al. "Pulse shape analysis in GERDA Phase II". In: *Eur. Phys. J. C* 82.4 (2022), p. 284. DOI: 10.1140/epjc/s10052-022-10163-w. arXiv: 2202.13355.

[5] GERDA Collaboration, M. Agostini, et al. "Modeling of GERDA Phase II data". In: *JHEP* 03 (2020), p. 139. DOI: 10.1007/JHEP03(2020)139. arXiv: 1909.02522.

[6] GEANT4 Collaboration, S. Agostinelli, et al. "GEANT4–a simulation toolkit". In: *Nucl. Instrum. Meth. A* 506 (2003), pp. 250–303. DOI: 10.1016/S0168-9002(03)01368-8.

[7] J. Allison et al. "Geant4 developments and applications". In: *IEEE Trans. Nucl. Sci.* 53 (2006), p. 270. DOI: 10.1109/TNS.2006.869826.

[8] J. Allison et al. "Recent developments in Geant4". In: *Nucl. Instrum. Meth. A* 835 (2016), pp. 186–225. DOI: 10.1016/j.nima.2016.06.125.

[9] M. Boswell et al. "MaGe-a Geant4-based Monte Carlo Application Framework for Low-background Germanium Experiments". In: *IEEE Trans. Nucl. Sci.* 58 (2011), pp. 1212–1220. DOI: 10.1109/TNS.2011.2144619. arXiv: 1011.3827.

[10] C. Wiesinger and L. Pertoldi. "GSTR-20-009: A LAr veto Monte Carlo model for GERDA Phase II". GERDA Scientific / Technical Report. 2020. URL: https://www.mpi-hd.mpg.de/gerda/internal/GSTR/GSTR-20-009-v1.pdf.

[11] K. von Sturm. "GSTR-20-008: Dead and transition layer optimization for the $2\nu\beta\beta$ fit". GERDA Scientific / Technical Report. 2020. URL: https://www.mpi-hd.mpg.de/gerda/internal/GSTR/GSTR-20-008-v1.pdf.

[12] C. Wiesinger. "No neutrinos not found: First exploration of neutrinoless double beta decay half-lives beyond 10^{26} years". PhD thesis. Technische Universität München, 2020. URL: https://mediatum.ub.tum.de/doc/1575899/1575899.pdf.

[13] G. Cowan et al. "Asymptotic formulae for likelihood-based tests of new physics". In: *Eur. Phys. J. C* 71 (2011). [Erratum: Eur.Phys.J.C 73, 2501 (2013)], p. 1554. DOI: 10.1140/epjc/s10052-011-1554-0. arXiv: 1007.1727.

[14] Particle Data Group, P. A. Zyla, et al. "Review of Particle Physics". In: *PTEP* 2020.8 (2020), p. 083C01. DOI: 10.1093/ptep/ptaa104.

[15] Sara Algeri et al. "Searching for new phenomena with profile likelihood ratio tests". In: *Nature Rev. Phys.* 2.5 (2020), pp. 245–252. DOI: 10.1038/s42254-020-0169-5. arXiv: 1911.10237.

[16] B. Lehnert. "Search for $2\nu\beta\beta$ Excited State Transitions and HPGe Characterization for Surface Events in GERDA Phase II". PhD thesis. Technischen Universität Dresden, 2016. URL: https://www.mpi-hd.mpg.de/gerda/public/2016/phd2016_bjoernLehnert.pdf.

[17] J. Kotila and F. Iachello. "Phase space factors for double-β decay". In: *Phys. Rev. C* 85 (2012), p. 034316. DOI: 10.1103/PhysRevC.85.034316. arXiv: 1209.5722.

[18] P. Domin et al. "Neutrino accompanied $\beta^{\pm}\beta^{\pm}$, β^{+}/EC and EC/EC processes within single state dominance hypothesis". In: *Nucl. Phys. A* 753 (2005), pp. 337–363. DOI: 10.1016/j.nuclphysa.2005.03.003. arXiv: nucl-th/0411002.

[19] O. Azzolini et al. "Evidence of Single State Dominance in the Two-Neutrino Double-β Decay of ^{82}Se with CUPID-0". In: *Phys. Rev. Lett.* 123.26 (2019), p. 262501. DOI: 10.1103/PhysRevLett.123.262501. arXiv: 1909.03397.

[20] NEMO-3 Collaboration, R. Arnold, et al. "Detailed studies of ^{100}Mo two-neutrino double beta decay in NEMO-3". In: *Eur. Phys. J. C* 79.5 (2019), p. 440. DOI: 10.1140/epjc/s10052-019-6948-4. arXiv: 1903.08084.

[21] E. Armengaud et al. "Precise measurement of $2\nu\beta\beta$ decay of ^{100}Mo with the CUPID-Mo detection technology". In: *Eur. Phys. J. C* 80.7 (2020), p. 674. DOI: 10.1140/epjc/s10052-020-8203-4. arXiv: 1912.07272.

[22] T. R. Rodriguez and G. Martinez-Pinedo. "Energy density functional study of nuclear matrix elements for neutrinoless $\beta\beta$ decay". In: *Phys. Rev. Lett.* 105 (2010), p. 252503. DOI: 10.1103/PhysRevLett.105.252503. arXiv: 1008.5260.

[23] M. T. Mustonen and J. Engel. "Large-scale calculations of the double-β decay of ^{76}Ge,^{130} Te,^{136} Xe, and ^{150}Nd in the deformed self-consistent Skyrme quasiparticle random-phase approximation". In: *Phys. Rev. C* 87.6 (2013), p. 064302. DOI: 10.1103/PhysRevC.87.064302. arXiv: 1301.6997.

[24] N. López Vaquero, T. R. Rodríguez, and J. L. Egido. "Shape and pairing fluctuations effects on neutrinoless double beta decay nuclear matrix elements". In: *Phys. Rev. Lett.* 111.14 (2013), p. 142501. DOI: 10.1103/PhysRevLett.111.142501. arXiv: 1401.0650.

[25] M. Horoi and A. Neacsu. "Shell model predictions for ^{124}Sn double-β decay". In: *Phys. Rev. C* 93.2 (2016), p. 024308. DOI: 10.1103/PhysRevC.93.024308. arXiv: 1511.03711.

[26] J. Hyvärinen and J. T. Suhonen. "Nuclear matrix elements for $0\nu\beta\beta$ decays with light or heavy Majorana-neutrino exchange". In: *Phys. Rev. C* 91.2 (2015), p. 024613. DOI: 10.1103/PhysRevC.91.024613.

[27] J. Barea, J. Kotila, and F. Iachello. "$0\nu\beta\beta$ and $2\nu\beta\beta$ nuclear matrix elements in the interacting boson model with isospin restoration". In: *Phys. Rev. C* 91.3 (2015), p. 034304. DOI: 10.1103/PhysRevC.91.034304. arXiv: 1506.08530.

[28] J. Menéndez. "Neutrinoless $\beta\beta$ decay mediated by the exchange of light and heavy neutrinos: The role of nuclear structure correlations". In: *J. Phys. G* 45.1 (2018), p. 014003. DOI: 10.1088/1361-6471/aa9bd4. arXiv: 1804.02105.

[29] L. S. Song et al. "Nuclear matrix element of neutrinoless double-β decay: Relativity and short-range correlations". In: *Phys. Rev. C* 95.2 (2017), p. 024305. DOI: 10.1103/PhysRevC.95.024305. arXiv: 1702.02448.

[30] F. Šimkovic, A. Smetana, and P. Vogel. "$0\nu\beta\beta$ nuclear matrix elements, neutrino potentials and SU(4) symmetry". In: *Phys. Rev. C* 98.6 (2018), p. 064325. DOI: 10.1103/PhysRevC.98.064325. arXiv: 1808.05016.

[31] D. Fang, A. Faessler, and F. Šimkovic. "$0\nu\beta\beta$-decay nuclear matrix element for light and heavy neutrino mass mechanisms from deformed quasiparticle random-phase approximation calculations for ^{76}Ge, ^{82}Se, ^{130}Te, ^{136}Xe , and ^{150}Nd with isospin restoration". In: *Phys. Rev. C* 97.4 (2018), p. 045503. DOI: 10.1103/PhysRevC.97.045503. arXiv: 1803.09195.

[32] L. Coraggio et al. "Calculation of the neutrinoless double-β decay matrix element within the realistic shell model". In: *Phys. Rev. C* 101.4 (2020), p. 044315. DOI: 10.1103/PhysRevC.101.044315. arXiv: 2001.00890.

[33] J. Kotila and F. Iachello. "Nuclear matrix elements for Majoron-emitting double-β decay". In: *Phys. Rev. C* 103.4 (2021), p. 044302. DOI: 10.1103/PhysRevC.103.044302. arXiv: 2104.02327.

[34] J. Kotila, J. Barea, and F. Iachello. "Phase-space factors and half-life predictions for Majoron-emitting decay". In: *Phys. Rev. C* 91.6 (2015). [Erratum: Phys.Rev.C 92, 029903 (2015)], p. 064310. DOI: 10.1103/PhysRevC.91.064310. arXiv: 1509.05154.

[35] KamLAND-Zen Collaboration, A. Gando, et al. "Limits on Majoron-emitting double-β decays of ^{136}Xe in the KamLAND-Zen experiment". In: *Phys. Rev. C* 86 (2012), p. 021601. DOI: 10.1103/PhysRevC.86.021601. arXiv: 1205.6372.

[36] NEMO-3 Collaboration, R. Arnold, et al. "Results of the search for neutrinoless double-β decay in ^{100}Mo with the NEMO-3 experiment". In: *Phys. Rev. D* 92.7 (2015), p. 072011. DOI: 10.1103/PhysRevD.92.072011. arXiv: 1506.05825.

[37] A. S. Barabash et al. "Final results of the Aurora experiment to study 2β decay of ^{116}Cd with enriched $^{116}CdWO_4$ crystal scintillators". In: *Phys. Rev. D* 98.9 (2018), p. 092007. DOI: 10.1103/PhysRevD.98.092007. arXiv: 1811.06398.

[38] EXO-200 Collaboration, S. Al Kharusi, et al. "Search for Majoron-emitting modes of ^{136}Xe double beta decay with the complete EXO-200 dataset". In: *Phys. Rev. D* 104.11 (2021), p. 112002. DOI: 10.1103/PhysRevD.104.112002. arXiv: 2109.01327.

[39] Ovidiu Nitescu, Stefan Ghinescu, and Sabin Stoica. "Lorentz violation effects in $2\nu\beta\beta$ decay". In: *J. Phys. G* 47.5 (2020), p. 055112. DOI: 10.1088/1361-6471/ab7e8c. arXiv: 2001.04859.

[40] EXO-200 Collaboration, J. B. Albert, et al. "First Search for Lorentz and CPT Violation in Double Beta Decay with EXO-200". In: *Phys. Rev. D* 93.7 (2016), p. 072001. DOI: 10.1103/PhysRevD.93.072001. arXiv: 1601.07266.

[41] CUPID Collaboration, O. Azzolini, et al. "First search for Lorentz violation in double beta decay with scintillating calorimeters". In: *Phys. Rev. D* 100.9 (2019), p. 092002. DOI: 10.1103/PhysRevD.100.092002. arXiv: 1911.02446.

[42] E. Holzschuh et al. "The β-spectrum of ^{35}S and search for the admixture of heavy neutrinos". In: *Phys. Lett. B* 482 (2000), pp. 1–9. DOI: 10.1016/S0370-2693(00)00476-7.

[43] K. Schreckenbach, G. Colvin, and F. Von Feilitzsch. "Search for mixing of heavy neutrinos in the β^+ and β^- spectra of the ^{64}Cu decay". In: *Phys. Lett. B* 129 (1983), pp. 265–268. DOI: 10.1016/0370-2693(83)90858-4.

[44] J. Deutsch, M. Lebrun, and R. Prieels. "Searches for admixture of massive neutrinos into the electron flavor". In: *Nucl. Phys. A* 518 (1990), pp. 149–155. DOI: 10.1016/0375-9474(90)90541-S.

[45] A. V. Derbin et al. "Search for a Neutrino with a Mass of 0.01 - 1.0 MeV in Beta Decays of ^{144}Ce and ^{144}Pr Nuclei". In: *JETP Lett.* 108.8 (2018), pp. 499–503. DOI: 10.1134/S0021364018200067.

[46] Borexino Collaboration, G. Bellini, et al. "New limits on heavy sterile neutrino mixing in ^{8}B decay obtained with the Borexino detector". In: *Phys. Rev. D* 88.7 (2013), p. 072010. DOI: 10.1103/PhysRevD.88.072010. arXiv: 1311.5347.

[47] LEGEND Collaboration, N. Abgrall, et al. "The Large Enriched Germanium Experiment for Neutrinoless $\beta\beta$ Decay: LEGEND-1000 Preconceptual Design Report". 2021. arXiv: 2107.11462.

Chapter 9

Precision measurement of the ^{76}Ge $2\nu\beta\beta$ decay half-life

With one of the longest half-life values among double-β decaying isotopes, a precision study of the ^{76}Ge $2\nu\beta\beta$ decay poses several challenges. Ultra-low background and an excellent understanding of the experiment's response are of utmost importance. In the Phase II of the GERDA experiment, both were achieved.

As part of this dissertation work, a precision determination of the half-life of ^{76}Ge $2\nu\beta\beta$ decay was obtained using pre-upgrade data after LAr veto cut from a subset of BEGe detectors re-characterized at the end of the experiment. This choice allowed for a drastic reduction of the systematic uncertainties compared to previous measurements and resulted in the most precise determination of ^{76}Ge $2\nu\beta\beta$ decay half-life, but also one of the most precise measurements of a double-β decay process. This author was the leading author of the analysis and prepared a manuscript which will be published by the GERDA Collaboration [1].

9.1 Past measurements of the ^{76}Ge $2\nu\beta\beta$ decay half-life

Pioneering measurements of the $2\nu\beta\beta$ decay rate of ^{76}Ge have been performed already in the nineties, with the first direct observation in 1990 by the ITEP-Yerevan [2] and the Battelle-Carolina [3] groups, followed by the International Germanium Experiments (IGEX) [4] and the Heidelberg-Moscow (HDM) experiment [5]. The latest result was reported by GERDA Phase I [6, 7], which measured a half-life of $T^{2\nu}_{1/2} = (1.926 \pm 0.095) \times 10^{21}$ yr. Figure 9.1 shows a collection of measurements performed over the years.

Past measurements were not always fully reciprocally compatible. The estimated $T^{2\nu}_{1/2}$ central value has been increasing over the years, and there is almost a factor 2 between the first and latest measurements. Conversely, the uncertainties did not significantly change, remaining at the 10% level for three decades. The increase in the $T^{2\nu}_{1/2}$ central value has been attributed to a systematic underestimation of the background, which decreases in time as experiments keep reducing their background level [8].

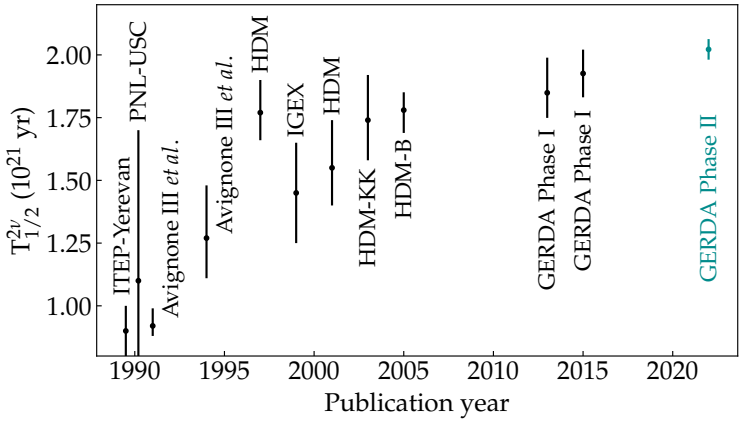

FIGURE 9.1: History of published ^{76}Ge $2\nu\beta\beta$ decay half-life measurements. Until 1994, results from the experiments ITEP-Yerevan [2], PNL-USC [3], and later joint efforts (Avignone II *et al.*) [9, 10] are included. Since 1997, results from the experiments HDM [5, 11], IGEX [4], and later re-analyses of HDM data by Klapdor-Kleingrothaus *et al.* (HDM-KK) [12] and by Bakalyarov *et al.* (HDM-B) [13] are available. From 2005 on, two measurements from GERDA Phase I are shown [6, 7], together with the Phase II measurement presented in this work.

The precision of previous GERDA measurements was limited by systematic uncertainties related to the Coax detector active mass and by the accuracy of the fit model as the signal-to-background ratio was at best 4:1 in the energy region from 600 to 1800 keV [7]. Both uncertainties have been drastically reduced in GERDA Phase II through the installation of the BEGe detectors, and the utmost reduction of the background through the LAr veto cut in the $2\nu\beta\beta$ decay-dominated energy region. Thanks to these improvements, in GERDA Phase II, a very low background measurement of the $2\nu\beta\beta$ decay rate became possible, with a signal-to-background ratio of 22:1 in the energy range between 560 and 2000 keV as will be presented in the following.

9.2 Active volume determination of BEGe detectors

For this analysis, only data collected with nine BEGe detectors was used. These detectors were chosen among the full BEGe dataset because they have been characterized before their deployment in the GERDA LAr cryostat and after the end of the GERDA data taking. Between the first characterization and the deployment, the BEGe detectors were stored for some time at room temperature. The DL thickness, the so-called full charge collection depth (FCCD), of HPGe detectors is expected to grow during storage at room temperature. Very little and mostly old literature is available on the topic, and there exists no reliable model. Some attempts to model the FCCD growth with a first principle diffusion model were also tried by GERDA collaborators but yet without a conclusive result. A linear growth of (0.10 ± 0.05) mm/yr was assumed in all GERDA analyses, *e.g.* in the search for

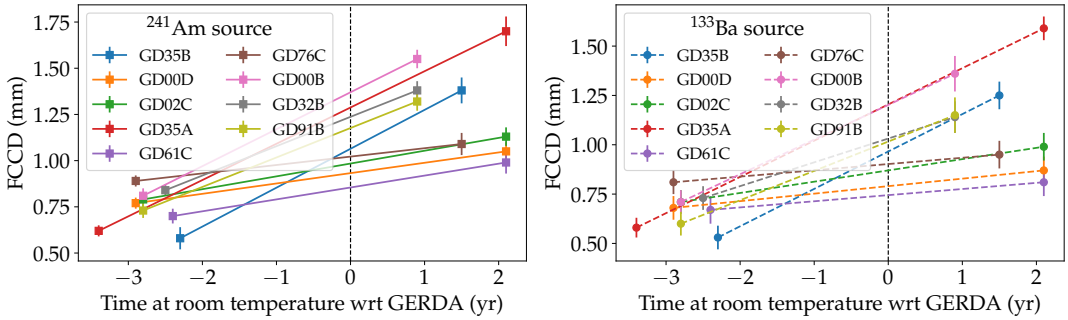

FIGURE 9.2: FCCD values as a function of the time detectors were stored at room temperature. The whole GERDA data taking is collapsed at 0 since no growth is expected when the detectors are operated in LAr. The FCCD was determined from two different measurements, conducted with an ^{241}Am and a ^{133}Ba source, shown on the left and on the right, respectively.

$0\nu\beta\beta$ decay [14]. Nevertheless, for the nine re-characterized BEGe detectors, different growths were observed, as shown in figure 9.2. The detector FCCD before the GERDA deployment was determined from two different measurements, conducted with an ^{241}Am and a ^{133}Ba source, as detailed in [15]. The same analysis procedures were used to determine the FCCD of the re-characterized detectors. The FCCD values of the re-characterized detectors obtained with the ^{241}Am and ^{133}Ba source are reported in appendix D.

The observed growths vary among detectors and are not fully compatible with the previous assumption of a linear growth of $(0.10 \pm 0.05)\,\mathrm{mm/yr}$. In absence of a reliable growth model, the FCCD of these nine detectors was determined with a linear interpolation between the two FCCD values measured before and after the GERDA data taking. In the reference frame chosen in figure 9.2, with the GERDA data taking at $t_0 = 0$, the interpolated FCCD x_0 can be obtained as the intercept of the line passing through the two points (t_1, x_1) and (t_2, x_2) defined by the two measurements at t_1 (time before the GERDA deployment) and t_2 (time of the re-measurement)

$$x_0 = x_1 - t_1 \cdot \frac{x_2 - x_1}{t_2 - t_1} \,. \tag{9.1}$$

The uncertainty on x_0 was propagated from the uncertainties on x_1 and x_2 as

$$\Delta(x_0) = \sqrt{\left(1 + \frac{t_1}{t_2 - t_1}\right)^2 \cdot \Delta(x_1)^2 + \left(\frac{t_1}{t_2 - t_1}\right)^2 \cdot \Delta(x_2)^2} \,. \tag{9.2}$$

The results of the linear interpolation obtained for the ^{241}Am and ^{133}Ba separately are shown in figure 9.3. The interpolated FCCD values are also reported in appendix D.

The FCCD of each detector is then determined as the mean of the two interpolated values extracted with equation 9.1 for the ^{241}Am and ^{133}Ba measurements

$$\overline{x}_0 = \frac{x_{0,\mathrm{Ba}} + x_{0,\mathrm{Am}}}{2} \,. \tag{9.3}$$

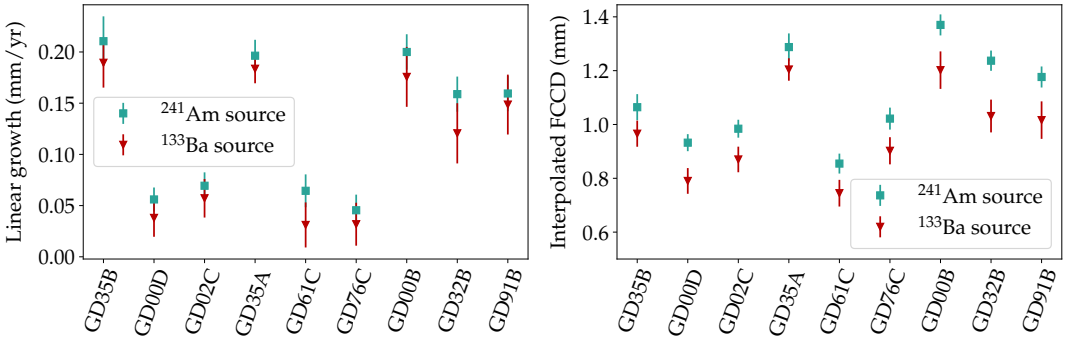

FIGURE 9.3: Results of the linear interpolation between the two FCCD values determined before and after the GERDA data taking. The linear growths are shown on the left, while the interpolated FCCD values at the time of GERDA data taking are shown on the right for the nine BEGe detectors indicated on the x-axis.

The uncertainty of the mean was estimated as a linear sum[1] of the uncertainties of the two values

$$\frac{\Delta(\overline{x})_{corr.}}{\overline{x}} = \frac{\Delta(x_{0,\mathrm{Ba}})}{x_{0,\mathrm{Ba}}} + \frac{\Delta(x_{0,\mathrm{Am}})}{x_{0,\mathrm{Am}}} \,. \tag{9.4}$$

In addition to this correlated uncertainty[2], a larger uncertainty is added, which reflects the uncertainty of the growth model. This uncertainty was chosen as the maximum interval defined by the FCCD determinations before and after GERDA (taken again as the mean between the ^{241}Am and ^{133}Ba measurements)

$$\Delta(\overline{x})_{uncorr.} = \overline{x}_2 - \overline{x}_1 \tag{9.5}$$

In this way, larger observed growths reflect in larger FCCD uncertainties, while detectors in which a smaller growth was observed will have smaller FCCD uncertainties. In the absence of a model description of the FCCD growth and given that the data do not indicate significant correlations between the growth in different detectors (figure 9.2), we treat this uncertainty as uncorrelated. The connection between the observed growth and the FCCD uncertainty is visible when comparing figure 9.4, where the FCCD values with their correlated and uncorrelated uncertainties are shown, and figure 9.2. The mean FCCD values with their correlated and uncorrelated uncertainties are also reported in table 9.1.

For each of the nine re-characterized detectors, this new FCCD value was used to determine the AV fraction f_{AV}, *i.e.* the fraction of the entire volume where an energy deposition is fully reconstructed. The f_{AV} was deduced by dividing the FCCD-subtracted volume by the crystal mass.[3] These are summarized in table 9.1. The f_{AV}

[1] A linear sum was chosen instead of a quadratic sum to have a more conservative uncertainty.

[2] The uncertainty of the mean was propagated from the uncertainties of the determined FCCD values, which are mostly correlated between detectors.

[3] Approximating each crystal as a cylinder with height h and diameter d, its total volume will be $V = \pi \cdot h \cdot (d/2)^2$. Given a FCCD thickness x, the active volume can be calculated as $V_a = \pi \cdot (h - 2x) \cdot (d/2 - x)^2$ and the f_{AV} as $f_{AV} = V_a/V$.

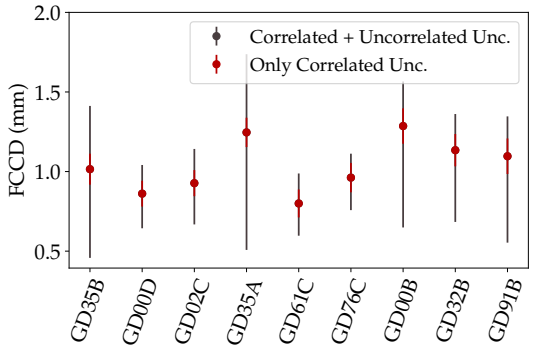

FIGURE 9.4: FCCD values at the time of GERDA data taking determined for the nine BEGe detectors indicated on the x-axis. Correlated uncertainties and the sum of correlated and uncorrelated uncertainties are shown separately.

Detector name	Exposure (kg yr)	FCCD ± corr. ± uncorr. (mm)	f_{AV} ± corr. ± uncorr.
GD35B	1.6	$1.02 \pm 0.10\,^{+0.30}_{-0.46}$	$0.888 \pm 0.010\,^{+0.032}_{-0.050}$
GD00D	1.5	$0.86 \pm 0.08\,^{+0.10}_{-0.14}$	$0.904 \pm 0.009\,^{+0.010}_{-0.015}$
GD02C	1.5	$0.93 \pm 0.08\,^{+0.13}_{-0.18}$	$0.897 \pm 0.009\,^{+0.014}_{-0.019}$
GD35A	1.5	$1.25 \pm 0.09\,^{+0.40}_{-0.65}$	$0.868 \pm 0.009\,^{+0.040}_{-0.067}$
GD61C	1.1	$0.80 \pm 0.09\,^{+0.10}_{-0.12}$	$0.900 \pm 0.010\,^{+0.013}_{-0.014}$
GD76C	1.6	$0.96 \pm 0.09\,^{+0.06}_{-0.11}$	$0.895 \pm 0.010\,^{+0.006}_{-0.012}$
GD00B	1.3	$1.29 \pm 0.11\,^{+0.17}_{-0.53}$	$0.850 \pm 0.013\,^{+0.018}_{-0.060}$
GD32B	1.4	$1.13 \pm 0.10\,^{+0.13}_{-0.35}$	$0.872 \pm 0.011\,^{+0.014}_{-0.038}$
GD91B	0.5	$1.10 \pm 0.11\,^{+0.14}_{-0.43}$	$0.871 \pm 0.013\,^{+0.016}_{-0.049}$

TABLE 9.1: Summary of the nine BEGe detectors used for the determination of the $2\nu\beta\beta$ decay half-life. The individual analysis exposures, the FCCD values, and the corresponding f_{AV} are reported. The uncertainties are divided into their correlated (first) and uncorrelated (second) contributions.

influences the $2\nu\beta\beta$ decay detection efficiency and, therefore, its uncertainty contributes to the uncertainty of the $2\nu\beta\beta$ decay half-life, as will be explained in the following.

9.3 Data selection, statistical analysis, and systematic uncertainties

The data set used in this analysis corresponds to data collected with the nine BEGe detectors mentioned above in GERDA Phase II before the upgrade. The nine BEGe detectors and their exposures are summarized in table 9.1; the total exposure is 11.8 kg yr. The choice of using only these nine detectors is justified by the negligible statistical uncertainty which was expected by using only 11.8 kg yr of exposure compared to the systematic uncertainty on the active volume, which, on the other

hand, can be very large given the results discussed in the previous section. Anticipating the results of this chapter, the systematic uncertainty on the half-life due to the uncertainty on f_{AV} is reduced compared to previous GERDA results due to the re-characterization of the detectors but still the dominant contribution to the total uncertainty. The reason for using only data before the upgrade is the same as in the search for exotic decays presented in chapter 8, namely that the MC modeling of the LAr veto system, which we use to estimate the effect of the LAr veto cut on the probability distribution functions of signal and background, assumes only the pre-upgrade LAr instrumentation [16].

The data selection criteria, the fit model, the statistical analysis, and the systematic uncertainties of the fit model are the same as in the search for exotic decays. We recall here, for convenience, the most relevant information, and refer to chapter 8, section 8.1.2 and 8.2, for more details.

A binned maximum-likelihood fit was performed in the energy window between 560 keV and 2000 keV, with a 10 keV binning. The likelihood function was used to construct a frequentist test statistic based on the profile likelihood ratio [17]

$$T_S = -2\,ln\frac{\mathcal{L}(S,\hat{\hat{\theta}})}{\mathcal{L}(S,\hat{\theta})}\,, \tag{9.6}$$

where S is the parameter of interest, which is the number of $2\nu\beta\beta$ decay events in the fit range, and θ is the set of nuisance parameters, that are the number of background events in the fit range. The probability distribution of the test statistic, evaluated with MC techniques, is shown in figure 9.5 left. This was obtained with 10^4 pseudo-experiments, generated assuming the GERDA experiment parameters. The effect of folding the systematic uncertainties in the test statistic distribution is also shown in the same figure. The distribution obtained without systematic uncertainties is well described by the asymptotic χ^2 limit [17]. The tail of the distribution is broadened by the introduction of systematic uncertainties.

From the test statistic distribution, the critical threshold of the test statistic corresponding to a 68% probability can be calculated. This is the test statistic value corresponding to a p-value of 0.68

$$\int_0^{T_{critical}} F(T_S) = 0.68\,. \tag{9.7}$$

This is illustrated in figure 9.5 right, where the cumulative distribution of the test statistic is shown. The critical threshold is given by the intersection of the cumulative distribution with the horizontal line indicating the 68% probability. The critical threshold obtained without systematic uncertainties is $T_{critical} = 1$, as expected in the asymptotic χ^2 limit [17]. The systematic uncertainties raise the critical threshold to $T_{critical} = 1.6$.

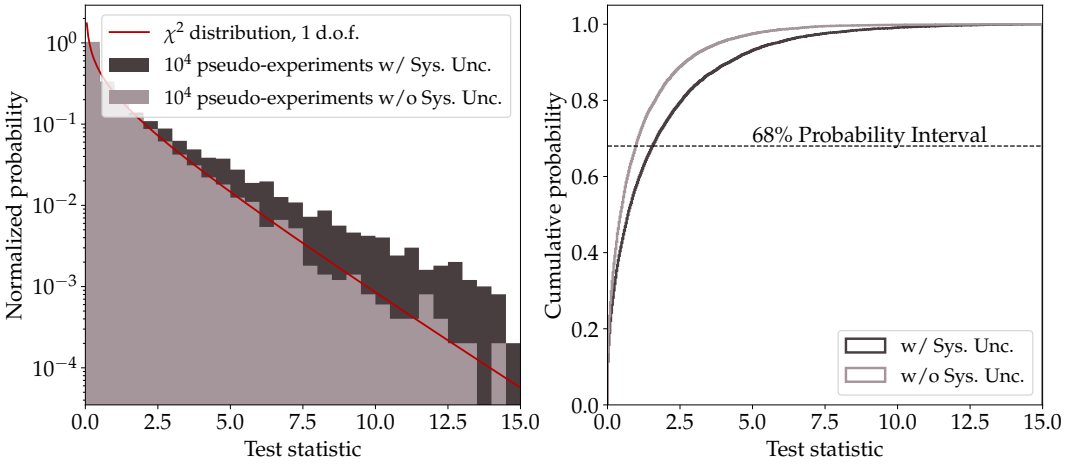

FIGURE 9.5: (Left) Test statistic distribution for the number of $2\nu\beta\beta$ decay events calculated with 10^4 pseudo-experiments. The distribution obtained without systematic uncertainties is well approximated by the asymptotic χ^2 distribution. A larger tail is obtained when all the systematic uncertainties are folded in the test statistic distribution. (Right) Cumulative distribution of the test statistic. The critical threshold is given by the intersection of the cumulative distribution with the horizontal line indicating the 68% probability.

9.4 Correlation studies with pseudo-experiments

We investigated the performance of the analysis and the correlations between the fit components by fitting 10^4 pseudo-experiments. First, we generated the pseudo-experiments assuming a fixed model and varying the number of events of each signal and background component according to statistical fluctuations. We then fit each pseudo-experiment with the same model.

The distribution of the reconstructed parameter, *i.e.* the number of events in the fit range, is shown in figure 9.6 for the $2\nu\beta\beta$ decay (top left) and each of the background components. A Gaussian function describes well the distribution of the $2\nu\beta\beta$ decay events. Given the very low background after the LAr veto cut, the distribution of the events for most of the background components is a Gaussian centered very close to 0. The distributions of the number of ^{42}K and α events (right bottom) deviate from the gaussian distribution because of the presence of correlations among these components.

The correlations between the different parameters are also shown in figure 9.6. The $2\nu\beta\beta$ decay component does not correlate with any background component (first column on the left). As anticipated, we observed correlations between the two ^{42}K components and the α component (highlighted in the right bottom corner). Two components were used in the fit for the ^{42}K background to cover the differences in the energy distribution which is predicted in case of a decay close to the detector surface (^{42}K-close) or further in the LAr volume (^{42}K-far). Still, the two energy distributions are similar, resulting in the above correlation. This correlation also creates the double-peak structure observed in the distribution of the ^{42}K-far component. The

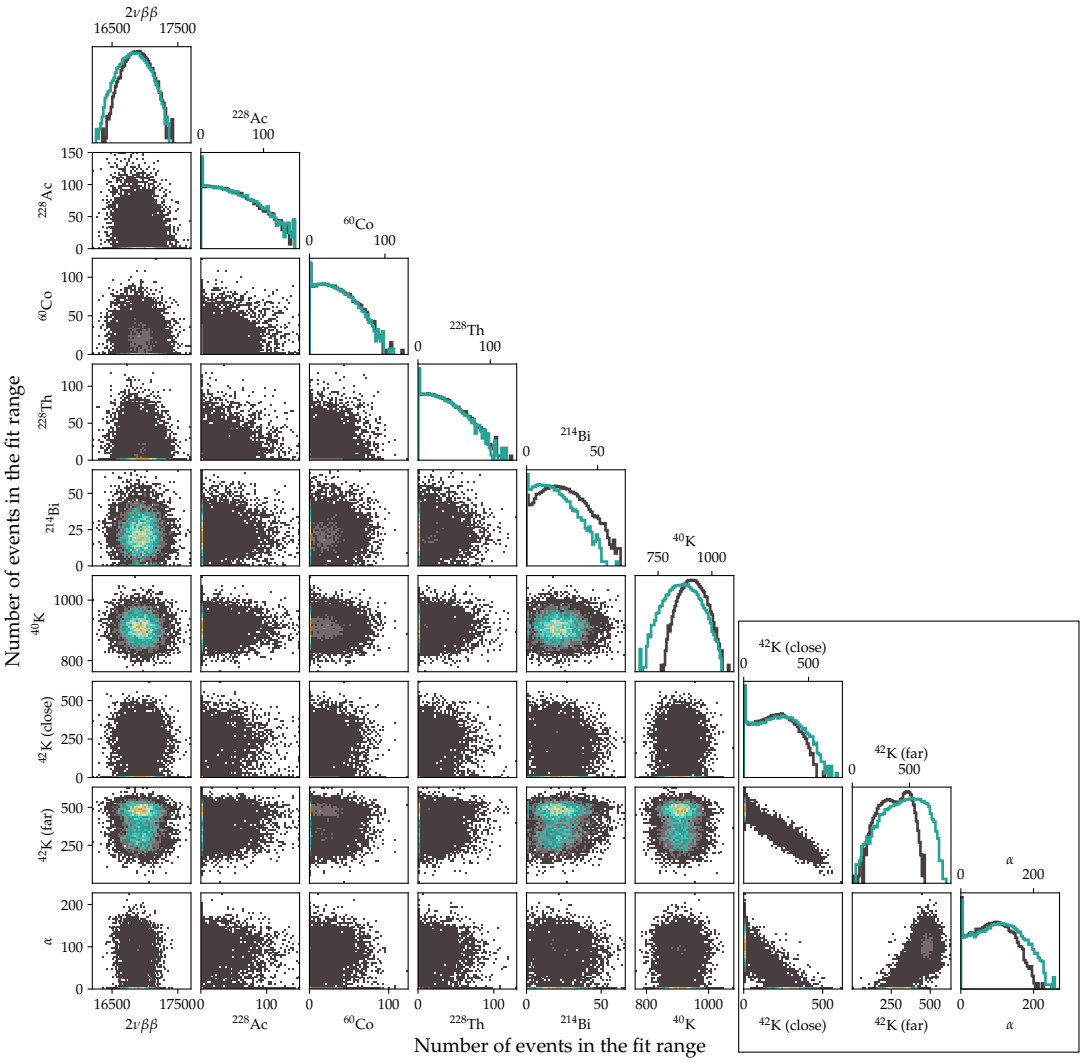

FIGURE 9.6: Result of the fit of 10^4 pseudo-experiments. The distributions of the number of events in the fit range are shown on the diagonal. The gray (green) distribution is obtained without (with) systematic uncertainties. Correlations between the different fit components are shown outside the diagonal. The black box highlights the only positive correlations observed between the ^{42}K and the α components.

correlation between the α component and the ^{42}K-close component is due to their similar energy distribution above 1800 keV, which is nearly flat. At these energies, the few counts observed in the spectrum, are expected to be shared by these two components, as can be seen in the expected background decomposition after LAr, shown in figure 8.3.

The generation of the pseudo-experiments was then repeated including the systematic uncertainties. In this case, not only the number of events of each signal and background component was varied according to statistical fluctuations, but also the model used to generate the experiments was varied at each repetition according to the systematic uncertainties discussed in section 8.2.3. For instance, the location of each background source is not fixed to the location of the fit model but varied among several possible locations. Each pseudo-experiment was then fit with the same fit model.

The distribution of the number of events in the fit range obtained in this case is shown in green in figure 9.6. A Gaussian function still describes well the distribution of the $2\nu\beta\beta$ decay events. Introducing the systematic uncertainties only affects the width of the distribution, while the median does not change. This result, together with the absence of correlations between the $2\nu\beta\beta$ decay component and the other background components, increase our confidence that systematic uncertainties related to the fit model, *e.g.* the background location, do not affect the estimation of the number of $2\nu\beta\beta$ decay events. Introducing the systematic uncertainties also enlarges the distribution of the number of background events. The effect is maximal in the ^{40}K and ^{42}K distributions because of the larger differences in the shape of the energy distribution expected for different background locations. The energy region between the Compton edge and the full energy peak, for instance, strongly depends on the location of the contamination in the array.

9.5 Results

Of the observed 18469 events in the analysis range, 16911 events are associated with the $2\nu\beta\beta$ decay. The observed test statistic on the data as a function of the number of $2\nu\beta\beta$ decay events is shown in figure 9.7. The critical threshold defining the 68% probability interval is also shown for the statistical and statistical plus systematics intervals. The 68% probability interval on the number of $2\nu\beta\beta$ decay events, extracted from the observed test statistic is $N_{2\nu} = (16911 \pm 147\,(\text{stat}) \pm 112\,(\text{sys}))$[4] counts in the fit range.

The number of $2\nu\beta\beta$ decay events is converted into the half-life through the relation:

$$T^{2\nu}_{1/2} = \frac{1}{N_{2\nu}} \cdot \frac{N_A\, log(2)}{M_{76}}\, f_{76}\, \epsilon_{QC}\, \epsilon_{LAr}\, M_{BEGe}\, T\, \mathcal{E}_{MC}\ , \tag{9.8}$$

[4] In fact, from the observed test statistic, the (stat+sys) interval is extracted from the corresponding critical threshold of the test statistic. The (sys) interval is then obtained by subtracting in quadrature the (stat) interval $\sigma_{(\text{sys})} = \sqrt{\sigma^2_{(\text{stat+sys})} - \sigma^2_{(\text{stat})}}$.

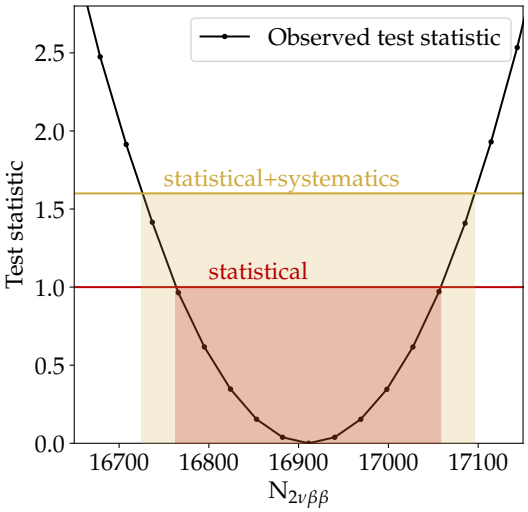

FIGURE 9.7: Observed test statistic distribution on the data as a function of the number of $2\nu\beta\beta$ decay events in the fit range. The critical threshold defining the 68% probability interval is shown in red and yellow for the statistical and statistical plus systematics intervals, respectively.

Convertion factors	
M_{76}	0.0759 kg
f_{76}	0.874 ± 0.003
ϵ_{QC}	0.99922 ± 0.00002
ϵ_{LAr}	0.977 ± 0.001
M_{BEGe}	20.024 kg
T	1.907 yr
$\mathcal{E}_{MC}$	0.1907 ± 0.0032

TABLE 9.2: Specific values of the quantities used in the conversion of the number of $2\nu\beta\beta$ decay events into half-life through equation 9.8. The total BEGe mass M_{BEGe} and the total Phase II live time T are used because the efficiency $\mathcal{E}_{MC}$ is calculated relative to them.

where N_A is the Avogadro's constant, M_{76} the molar mass of ^{76}Ge and f_{76} the fraction of enriched material, ϵ_{QC} is the efficiency of the quality cuts, and ϵ_{LAr} the efficiency of the LAr veto cut. M_{BEGe} is the total BEGe mass and T the total GERDA Phase II live time. The efficiency $\mathcal{E}_{MC}$ is the detection efficiency for $2\nu\beta\beta$ decay events in the nine BEGe detectors and the energy range of the analysis (560–2000 keV). The specific values of all these quantities are summarized in table 9.2. The efficiency $\mathcal{E}_{MC}$ is obtained through MC simulations and can be written as

$$\mathcal{E}_{MC} = \frac{\sum_i m_i^{tot}\, t_i\, f_i^{AV}\, \epsilon_{c,i}}{M_{BEGe}\, T} \tag{9.9}$$

The sum $\sum_i$ runs over the detectors included in the data set, labeled by the index i. All the detector specific parameters, like the detector mass m_i^{tot}, the AV fraction f_i^{AV}, the time of measurement t_i (which considers the detector status in each physics

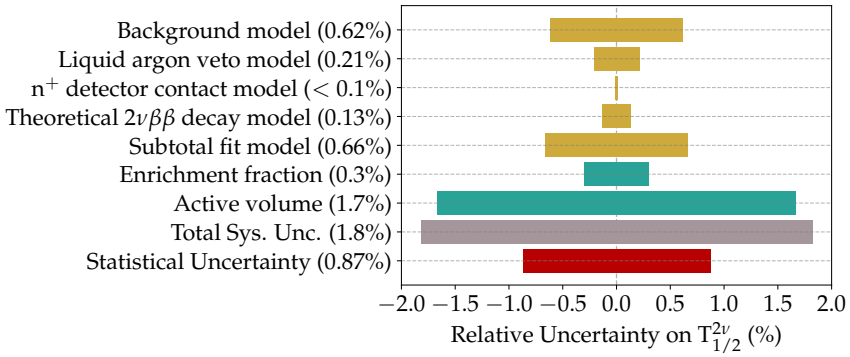

FIGURE 9.8: Breakdown of the uncertainties affecting the $2\nu\beta\beta$ decay half-life estimate. The statistical uncertainty is shown separately from the dominant total systematic uncertainty. Among the single contributions to the systematic uncertainty, a division is made between sources considered in the fit results (the subtotal of only these contributions is also shown) and sources that enter just the conversion between the observed number of events and half-life.

run), and the containment efficiency $\epsilon_{c,i}$, are taken into account separately for each detector. The containment efficiency $\epsilon_{c,i}$ corresponds to the probability that a $2\nu\beta\beta$ decay taking place in the AV of the detector deposits detectable energy in the analysis window (560–2000 keV). The efficiency is calculated relative to the total BEGe mass M_{BEGe} and the total GERDA Phase II live time T, which, in turn, need to be used in equation 9.8.

Uncertainties on the quantities that enter equation 9.8 contribute to the systematic uncertainty of the half-life. The uncertainties on the individual AV fractions f_i^{AV}, summarized in table 9.1, are propagated to the efficiency $\mathcal{E}_{MC}$ with a MC sampling, which includes both the correlated and uncorrelated uncertainties, as explained in appendix E. The uncertainties on the AV result in a 1.7% relative uncertainty on $\mathcal{E}_{MC}$, thus on the half-life. The ^{76}Ge enrichment fraction was estimated to be $(87.4 \pm 0.3\%)$ and contributes with a 0.3% relative uncertainty on the half-life.[5] The uncertainty on the other quantities appearing in the conversion, like the LAr veto and quality cuts efficiencies, are negligible. All the contributions to the statistical and systematic uncertainty budget are summarized in figure 9.8.

Converting the number of counts and summing in quadrature statistical and systematic uncertainties, the final $2\nu\beta\beta$ decay half-life estimate is obtained:

$$T_{1/2}^{2\nu} = (2.022 \pm 0.041) \times 10^{21}\, yr\ . \tag{9.10}$$

[5] This is smaller than what was quoted in previous GERDA publications. Three independent estimates of the BEGe enrichment fraction were available: ECP 0.8742(36), NAA 0.870(11) and 0.860(11), ICPMS 0.895(5) and 0.889(5) [18]. Being incompatible, they were combined as average plus standard deviation into 0.877(13). The two ICPMS measurements conducted at LNGS were corrected later using a calibration sample (private communications with S. Nisi). The corrected values are 0.877(9) and 0.871(9). With the correction, all three measurements are compatible within one sigma and can be combined using a weighted average into the final estimate of 0.874(3).

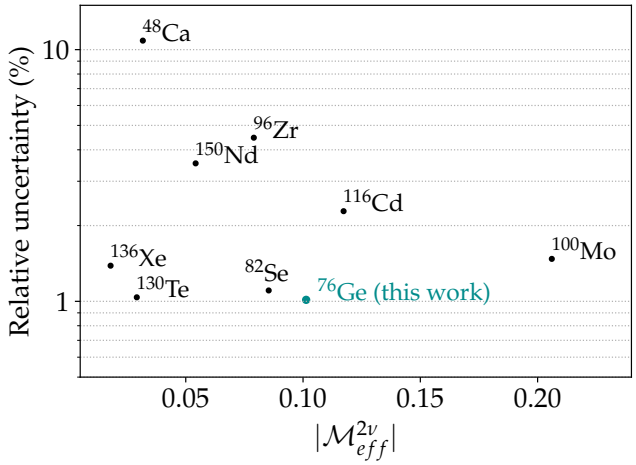

FIGURE 9.9: Experimental values of the effective NMEs $\mathcal{M}^{2\nu}_{\text{eff}}$ for various double-β emitters with the precision given on the vertical axis. The most precise determination of the half-life to date is used for each isotope [21–28], while the phase space factors are taken from [19].

The total 1σ uncertainty on $T^{2\nu}_{1/2}$ is 2.0%. This is dominated by the systematic uncertainty on the AV (1.7%). The total contribution to the systematic uncertainty from the fit model is only 0.7%, comparable to the statistical uncertainty (0.9%).

The $T^{2\nu}_{1/2}$ was converted into an experimental estimation of the effective NME, $\mathcal{M}^{2\nu}_{\text{eff}}$, through the relation:

$$[T^{2\nu}_{1/2}]^{-1} = \mathcal{G}^{2\nu} \, |\mathcal{M}^{2\nu}_{\text{eff}}|^2 \, . \tag{9.11}$$

The phase space factor for ^{76}Ge is $\mathcal{G}^{2\nu} = 48.17 \times 10^{21}\,\text{yr}^{-1}$ [19]. With the half-life obtained in this work (equation 9.10), the effective NME is $\mathcal{M}^{2\nu}_{\text{eff}} = (0.101 \pm 0.001)$. A comparison of the experimental determination of $\mathcal{M}^{2\nu}_{\text{eff}}$ obtained with different isotopes is shown in figure 9.9. The result obtained in this work for ^{76}Ge aligns with the high precision reached in the last years by several experiments. Experimental values of the NMEs are of utmost importance for the validation and improvement of nuclear-structure calculations [20] and can benefit the interpretation of a future $0\nu\beta\beta$ decay discovery.

9.6 Conclusions, discussion and outlook

Figure 9.10 shows the experimental data and the total best-fit model. The contributions of the $2\nu\beta\beta$ decay and the background to the total fit model are also shown separately. The $2\nu\beta\beta$ decay dominates this energy region. The background after the LAr cut is extremely low: the signal-to-background ratio, excluding the two prominent γ lines from ^{40}K and ^{42}K, is 22:1 in the whole energy range of the analysis (560 – 2000 keV), while it was only 2:1 in the same energy range according to the background model before analysis cuts [29]. Thus, the LAr cut reduces the background of more than a factor 10 in the energy region dominated by the $2\nu\beta\beta$ decay. A higher

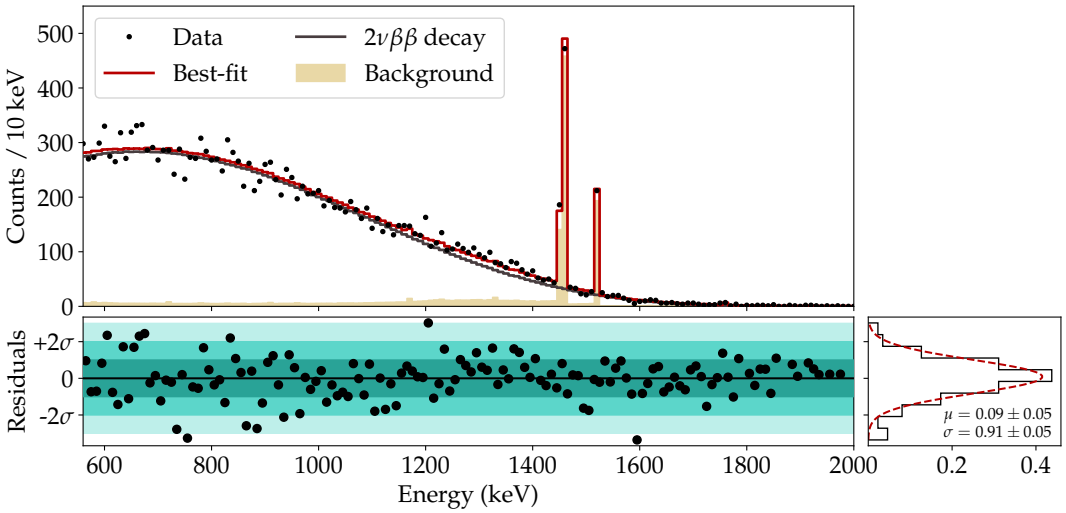

FIGURE 9.10: Best-fit signal and background decomposition of the nine BEGe energy spectrum after application of the LAr veto cut. In the bottom panel, the ratio between data and model in units of Poisson standard deviations is shown together with 68%, 95% and 99% probability intervals.

background is observed in the right part of the spectrum, above 1 MeV, compare to the energy region below. This is better visible on a logarithmic scale (see figure 9.11). A higher signal-to-background ratio of 44:1 is obtained when considering only this energy region (560 – 1000 keV).

The residuals, in number of standard deviations, are shown in the bottom panel of figure 9.10. Their distribution is also shown: this is compatible with a Gaussian distribution with mean zero and width equal to one. At energies of 1300 – 1400 keV, the residuals are systematically larger than 0. This is attributed to a non-optimal choice of the ^{42}K and ^{40}K location in the fit model. As mentioned above, the distribution of ^{42}K and ^{40}K, in particular the energy region between the Compton edge

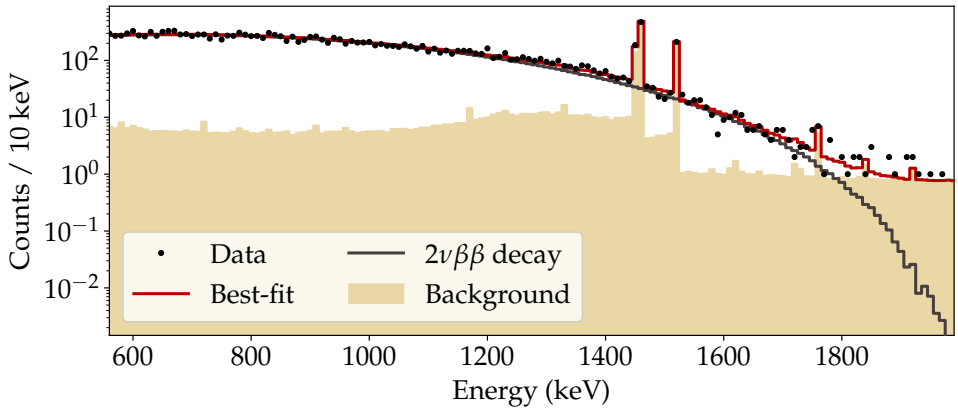

FIGURE 9.11: Best fit signal and background decomposition of the nine BEGe energy spectrum after LAr veto cut. The logarithmic scale is used to better visualize the background contribution.

and the full energy peak, strongly depends on the location of the respective contamination in the array. The effect is more visible after LAr veto cut since they are the dominant backgrounds, as shown in the background expectation after LAr in figure 8.3. Nevertheless, the systematic uncertainty related to the choice of the background location is included in the calculation of the test statistic, where all possible locations in the array are considered for ^{40}K and ^{42}K, and, in light of the correlation studies presented in section 9.4, we do not expect this to bias the estimation of the number of $2\nu\beta\beta$ decay events, thus the $2\nu\beta\beta$ decay half-life.

In conclusion, we determined the half-life of ^{76}Ge $2\nu\beta\beta$ decay to be $T^{2\nu}_{1/2} = (2.022 \pm 0.041) \times 10^{21}\, yr$. With a total uncertainty of 2.0%, this is the most precise determination of the ^{76}Ge $2\nu\beta\beta$ decay half-life and one of the most precise measurements of a $2\nu\beta\beta$ decay process, despite the longer half-life of ^{76}Ge compared to other isotopes (up to two orders of magnitude).

This result is compared to previous determinations of the ^{76}Ge $2\nu\beta\beta$ decay half-life in figure 9.1. This result is compatible with the uncertainties with the last GERDA Phase I measurement [7]. A small increase in the central value is observed between these two measurements, as it was systematically observed among the past measurements.

This tendency to increase the half-life estimation through the years is correlated to the signal-to-background ratio of the experiments. The best signal-to-background ratio achieved in past experiments before GERDA was approximately 1:1 (in 700 – 2040 keV), by the HDM experiment [11]. These experiments estimated the $2\nu\beta\beta$ decay half-life relying on the background subtraction. The expected background model was directly subtracted from the data, and the residual events were entirely attributed to $2\nu\beta\beta$ decay. The half-life estimation is strongly affected: an underestimation of the background would result in an overestimation of the $2\nu\beta\beta$ decay contributions, therefore in a shorter half-life.

Starting with GERDA Phase I, the half-life estimation was obtained from a spectral fit of the data, including both signal and background components. The statistical analysis using the full spectral information mitigates the effect of the background subtraction because the number of background events is also determined by fitting the data. Still, inaccuracies in the background model, *e.g.* a missing background component, might lead to an underestimation of the background. Finally, the relevance of the background modeling in estimating the $2\nu\beta\beta$ decay half-life depends on the signal-to-background ratio. In GERDA Phase I, a maximum signal-to-background ratio of 4:1 was obtained (in 600 – 1800 keV) [6, 7].

In this work, the highest signal-to-background ratio of any experiment with HPGe detectors was obtained, which is 22:1 in the energy range of the analysis (560 – 2000 keV). This superior signal-to-background ratio reduced the relevance of the background modeling in the estimation of the $2\nu\beta\beta$ decay half-life to a negligible level. The systematic uncertainty related to the background model ($< 0.6\%$) is strongly reduced compared to previous GERDA analyses (2 – 3% in [7]).

Further improvement of the precision of the ^{76}Ge $2\nu\beta\beta$ decay half-life estimate requires a precision determination of the AV of the HPGe detectors. This work showed that even with limited exposure (only 11.8 kg yr), the statistical uncertainty was subdominant. In contrast, the 1.6% systematic uncertainty related to the active volume fraction dominates the total uncertainty. The future LEGEND experiment will face the challenge of the AV determination for precision measurement of the $2\nu\beta\beta$ decay.

References

[1] GERDA Collaboration, M. Agostini, et al. "Precision measurement of the ^{76}Ge double-beta decay rate with GERDA Phase II". prepared for submission to Phys. Rev. Lett. 2022.

[2] A. A. Vasenko et al. "New Results in the ITEP / YePI Double Beta Decay Experiment With Enriched Germanium Detector". In: *Mod. Phys. Lett. A* 5 (1990), pp. 1299–1306. DOI: 10.1142/S0217732390001475.

[3] H. S. Miley et al. "Suggestive evidence for the two neutrino double beta decay of Ge-76". In: *Phys. Rev. Lett.* 65 (1990), pp. 3092–3095. DOI: 10.1103/PhysRevLett.65.3092.

[4] Angel Morales. "Review on double beta decay experiments and comparison with theory". In: *Nucl. Phys. B Proc. Suppl.* 77 (1999), pp. 335–345. DOI: 10.1016/S0920-5632(99)00440-5. arXiv: hep-ph/9809540.

[5] M. Gunther et al. "Heidelberg - Moscow beta-beta experiment with Ge-76: Full setup with five detectors". In: *Phys. Rev. D* 55 (1997), pp. 54–67. DOI: 10.1103/PhysRevD.55.54.

[6] GERDA Collaboration, M. Agostini, et al. "Measurement of the half-life of the two-neutrino double beta decay of ^{76}Ge with the GERDA experiment". In: *J. Phys. G* 40 (2013), p. 035110. DOI: 10.1088/0954-3899/40/3/035110. arXiv: 1212.3210.

[7] GERDA Collaboration, M. Agostini, et al. "Results on $\beta\beta$ decay with emission of two neutrinos or Majorons in ^{76}Ge from GERDA Phase I". In: *Eur. Phys. J. C* 75.9 (2015), p. 416. DOI: 10.1140/epjc/s10052-015-3627-y. arXiv: 1501.02345.

[8] F. T. Avignone and S. R. Elliott. "The Search for Double Beta Decay With Germanium Detectors: Past, Present, and Future". In: *Front. in Phys.* 7 (2019), p. 6. DOI: 10.3389/fphy.2019.00006. arXiv: 1901.02805.

[9] F. T. Avignone et al. "Confirmation of the observation of $2\nu\beta\beta$ decay of ^{76}Ge". In: *Phys. Lett. B* 256 (1991), pp. 559–561. DOI: 10.1016/0370-2693(91)91810-I.

[10] F. T. Avignone. "Double-beta decay: Some recent results and developments". In: *Prog. Part. Nucl. Phys.* 32 (1994), pp. 223–245. DOI: 10.1016/0146-6410(94)90022-1.

[11] H. V. Klapdor-Kleingrothaus et al. "Latest results from the Heidelberg-Moscow double beta decay experiment". In: *Eur. Phys. J. A* 12 (2001), pp. 147–154. DOI: 10.1007/s100500170022. arXiv: hep-ph/0103062.

[12] C. Dorr and H. V. Klapdor-Kleingrothaus. "New Monte-Carlo simulation of the HEIDELBERG-MOSCOW double beta decay experiment". In: *Nucl. Instrum. Meth. A* 513 (2003), pp. 596–621. DOI: 10.1016/j.nima.2003.07.018.

[13] A. M. Bakalyarov et al. "Results of the experiment on investigation of Germanium-76 double beta decay". In: *Phys. Part. Nucl. Lett.* 2 (2005), pp. 77–81. arXiv: hep-ex/0309016.

[14] GERDA Collaboration, M. Agostini, et al. "Characterization of 30 ^{76}Ge enriched Broad Energy Ge detectors for GERDA Phase II". In: *Eur. Phys. J. C* 79.11 (2019), p. 978. DOI: 10.1140/epjc/s10052-019-7353-8. arXiv: 1901.06590.

[15] B. Lehnert. "Search for $2\nu\beta\beta$ Excited State Transitions and HPGe Characterization for Surface Events in GERDA Phase II". PhD thesis. Technischen Universität Dresden, 2016. URL: https://www.mpi-hd.mpg.de/gerda/public/2016/phd2016_bjoernLehnert.pdf.

[16] GERDA Collaboration, M. Agostini, et al. "Liquid argon light collection and veto modeling in GERDA Phase II". submitted to Eur. Phys. J. C. 2022. arXiv: 2212.02856.

[17] G. Cowan et al. "Asymptotic formulae for likelihood-based tests of new physics". In: *Eur. Phys. J. C* 71 (2011). [Erratum: Eur.Phys.J.C 73, 2501 (2013)], p. 1554. DOI: 10.1140/epjc/s10052-011-1554-0. arXiv: 1007.1727.

[18] P. Grabmayar et al. "GSTR-13-009: Re-evaluation of enrichment fractions f_{Ge} and active volume fractions f_{av}". GERDA Scientific / Technical Report. 2013. URL: https://www.mpi-hd.mpg.de/gerda/internal/GSTR/GSTR-13-009.pdf.

[19] J. Kotila and F. Iachello. "Phase space factors for double-β decay". In: *Phys. Rev. C* 85 (2012), p. 034316. DOI: 10.1103/PhysRevC.85.034316. arXiv: 1209.5722.

[20] J. Engel and J. Menéndez. "Status and Future of Nuclear Matrix Elements for Neutrinoless Double-Beta Decay: A Review". In: *Rept. Prog. Phys.* 80.4 (2017), p. 046301. DOI: 10.1088/1361-6633/aa5bc5. arXiv: 1610.06548.

[21] CUORE Collaboration, D. Q. Adams, et al. "Measurement of the $2\nu\beta\beta$ Decay Half-Life of ^{130}Te with CUORE". In: *Phys. Rev. Lett.* 126.17 (2021), p. 171801. DOI: 10.1103/PhysRevLett.126.171801. arXiv: 2012.11749.

[22] EXO-200 Collaboration, J. B. Albert, et al. "Improved measurement of the $2\nu\beta\beta$ half-life of ^{136}Xe with the EXO-200 detector". In: *Phys. Rev. C* 89.1 (2014), p. 015502. DOI: 10.1103/PhysRevC.89.015502. arXiv: 1306.6106.

[23] O. Azzolini et al. "Evidence of Single State Dominance in the Two-Neutrino Double-β Decay of ^{82}Se with CUPID-0". In: *Phys. Rev. Lett.* 123.26 (2019), p. 262501. DOI: 10.1103/PhysRevLett.123.262501. arXiv: 1909.03397.

[24] E. Armengaud et al. "Precise measurement of $2\nu\beta\beta$ decay of ^{100}Mo with the CUPID-Mo detection technology". In: *Eur. Phys. J. C* 80.7 (2020), p. 674. DOI: 10.1140/epjc/s10052-020-8203-4. arXiv: 1912.07272.

[25] A. S. Barabash et al. "Final results of the Aurora experiment to study 2β decay of ^{116}Cd with enriched $^{116}CdWO_4$ crystal scintillators". In: *Phys. Rev. D* 98.9 (2018), p. 092007. DOI: 10.1103/PhysRevD.98.092007. arXiv: 1811.06398.

[26] NEMO-3 Collaboration, R. Arnold, et al. "Measurement of the double-beta decay half-life and search for the neutrinoless double-beta decay of ^{48}Ca with the NEMO-3 detector". In: *Phys. Rev. D* 93.11 (2016), p. 112008. DOI: 10.1103/PhysRevD.93.112008. arXiv: 1604.01710.

[27] NEMO-3 Collaboration, J. Argyriades, et al. "Measurement of the two neutrino double beta decay half-life of Zr-96 with the NEMO-3 detector". In: *Nucl. Phys. A* 847 (2010), pp. 168–179. DOI: 10.1016/j.nuclphysa.2010.07.009. arXiv: 0906.2694.

[28] NEMO-3 Collaboration, R. Arnold, et al. "Measurement of the $2\nu\beta\beta$ decay half-life of ^{150}Nd and a search for $0\nu\beta\beta$ decay processes with the full exposure from the NEMO-3 detector". In: *Phys. Rev. D* 94.7 (2016), p. 072003. DOI: 10.1103/PhysRevD.94.072003. arXiv: 1606.08494.

[29] GERDA Collaboration, M. Agostini, et al. "Modeling of GERDA Phase II data". In: *JHEP* 03 (2020), p. 139. DOI: 10.1007/JHEP03(2020)139. arXiv: 1909.02522.

Part III

Ordinary Muon Capture for $0\nu\beta\beta$ decay

Chapter 10

OMC as benchmark for nuclear-structure calculations

Future double-β decay experiments aim to fully explore the region $m_{\beta\beta} \gtrsim 10\,\text{meV}$, to conclusively test the parameter space allowed in the inverted mass ordering scenario while exploring a large part of that for the normal ordering scenario. Nuclear-structure calculations remain essential to connect $0\nu\beta\beta$ decay with the underlying new particle physics. At present, the calculated NMEs carry significant uncertainties, and the g_A puzzle remains unsolved.

Studies of Ordinary Muon Capture (OMC) can address both issues. The large energy and momentum transferred in OMC are analogous to that of $0\nu\beta\beta$ decay, making it a robust benchmark for related nuclear-structure calculations. For the same reason, OMC also benefits nuclear calculations connected to astrophysical neutrinos.

10.1 Motivation: the rate of $0\nu\beta\beta$ decay

$0\nu\beta\beta$ decay has been introduced in chapter 1. Here we recall the decay rate of $0\nu\beta\beta$ decay in the light neutrino exchange scenario

$$\Gamma^{0\nu} = \frac{1}{T^{0\nu}_{1/2}} = \mathcal{G}^{0\nu}(Q_{\beta\beta}, Z)\, g_A^4\, |\mathcal{M}^{0\nu}|^2\, \frac{m^2_{\beta\beta}}{m_e^2}\,. \tag{10.1}$$

Future experiments will reach sensitivities on the half-life $T^{0\nu}_{1/2}$ of the order of $10^{27} - 10^{28}$ yr, with the aforementioned implications on the Majorana nature of neutrinos. The feasibility of this ambitious goal strongly depends on the particle and nuclear physics aspects of $0\nu\beta\beta$ decay, *i.e.* on the phase space factor $\mathcal{G}^{0\nu}(Q_{\beta\beta}, Z)$ and nuclear matrix element $|\mathcal{M}^{0\nu}|$. While the phase space factors can be calculated with sufficient precision for all the double-β decaying isotopes of interest, large uncertainties are carried by the calculated NMEs.

NMEs contain all nuclear structure effects of $0\nu\beta\beta$ decay. Unfortunately, they cannot be directly measured and must be evaluated theoretically. For this purpose, different nuclear structure approaches are used, leading to NMEs that vary by a

factor of two or three, reflecting the approximate solution of the complicated many-body problem [1, 2].

In addition to the NME values, a possible uncertainty is related to the actual value of the g_A, factored out in equation 10.1. The value of g_A is commonly assumed to be $g_A \simeq 1.27$. Nevertheless, the theoretical predictions of the single-β and double-β decay rates seem to overestimate their measured values. This problem is usually cured by using an effective value of g_A. This phenomenological approach is referred to as the *quenching* of g_A. The consequences of the g_A quenching for $0\nu\beta\beta$ decay depend on the source of the problem, which is not yet understood [1].

Addressing the significant uncertainties of nuclear structure calculations and the g_A problem is one of the priorities of nuclear theory. The actual values of NMEs and g_A determine the possibility of future experiments reaching the desired sensitivity on $m_{\beta\beta}$. On the other hand, with the observation of $0\nu\beta\beta$ decay possibly being soon within reach, the precision of the theoretical inputs is of utmost importance for determining the new physics parameters, *e.g.* $m_{\beta\beta}$.

10.2 OMC and $0\nu\beta\beta$ decay

Measured half-life values of the single-β and double-β decays have traditionally been used to benchmark nuclear structure calculations in connection to the $0\nu\beta\beta$ decay NMEs. On the other hand, OMC can also be used for this purpose, with some advantages compared to the $2\nu\beta\beta$ and β decays [3]. OMC is based on the simple semi-leptonic reaction

$$\mu^- + p \rightarrow n + \nu_\mu \,, \tag{10.2}$$

which occurs via charged current weak interaction mediated by a W boson. It involves the capture of a negative muon by a proton in a target nucleus, resulting in the production of a neutron and a muon neutrino. The unique feature of OMC is the large energy and momentum transferred. While the exchanged momentum in $2\nu\beta\beta$ and β decays is of a few MeV, both OMC and $0\nu\beta\beta$ decay involve a high-momentum exchange of the order of 100 MeV.

The theoretical description of double-β decay processes assumes a virtual transition through the intermediate states of the intermediate nucleus. $0\nu\beta\beta$ decay proceeds via virtual transition through all the multipole states J^π of the intermediate odd-odd nucleus. In contrast, in $2\nu\beta\beta$ decay, only the 1^+ intermediate states are involved.

Experimental data on EC and β decay transitions can help describe the structure of these intermediate states. Still, they are limited to the energetically lowest J^+ states, usually the ground state of the intermediate nucleus. The OMC process is analogous to an EC transition, except that the mass of the captured muon is about

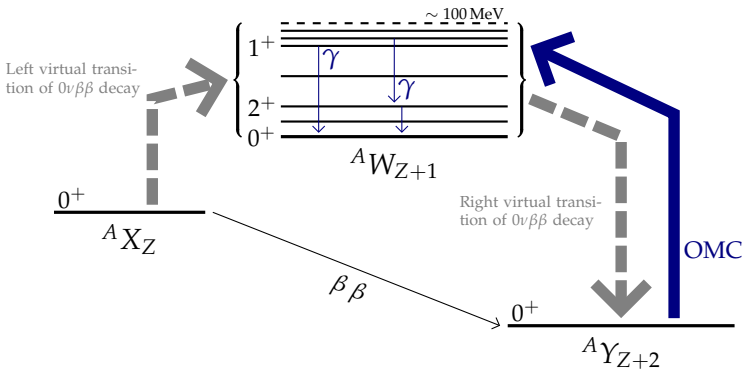

FIGURE 10.1: Schematic representation of double-β decay as a virtual transition through the intermediate states of the intermediate nucleus. In the $0\nu\beta\beta$ decay, high multipole states J^{π} of the intermediate nucleus are involved. OMC on a target consisting of the (A,Z+2) daughter nucleus can provide information about the right virtual transition, accessing the same intermediate states of the intermediate nucleus.

200 times the electron rest mass, allowing to probe intermediate states at high excitation energies. Thus, OMC can provide precious information on the structure of the intermediate states involved in the virtual transition of $0\nu\beta\beta$ decay [3, 4].

The connection between $0\nu\beta\beta$ decay and OMC is depicted in figure 10.1. Given a double-β decay isotope $^{A}X_{Z}$, its daughter nucleus $^{A}Y_{Z+2}$ would be the OMC target to access the intermediate states of the intermediate nucleus $^{A}W_{Z+1}$. The nucleus $^{A}Y_{Z+2}$ captures a muon and turns into an excited state of $^{A}W_{Z+1}$:

$$\begin{aligned} \mu^{-} + {}^{A}Y_{Z+2}(0^{+}) \rightarrow \nu_{\mu^{-}} + {}^{A}W_{Z+1}(J^{\pi}) \\ \rightarrow {}^{A}W_{Z+1}(0^{+}) + \gamma \, . \end{aligned} \tag{10.3}$$

The muon stops in the target forming a muonic atom. In most cases, it cascades down to the 1s level in a timescale of the order of 10^{-13} s [5]. Simultaneously with the muon stop, Auger electrons and muonic X-rays (μXs) are emitted [6]. When the muon reaches the 1s state of the muonic atom, it can be captured by the nucleus or decay into a high-energy electron (Michel electron) and two neutrinos (muon lifetime $\tau_{\mu} = 2.197\,\mu$s). Except for very light nuclei, the capture is far more likely than the decay [5]. OMC populates several excited states of the nucleus $^{A}W_{Z+1}$, up to the muon rest mass of 106 MeV.[1] The excited states decay to the ground state by emitting γ rays if they are particle-bound states or by emitting some neutrons or protons if they are particle-unbound states [5].

10.3 OMC and astrophysical neutrinos

OMC is also used to probe nuclear structure calculations in connection to astrophysical neutrinos, such as solar and supernova neutrinos [7, 8].

[1] In real nuclei, the excitation energy extends up to $\sim$ 70 MeV since excitations to higher states are suppressed by the small phase space and NME. [4]

Astrophysical neutrinos at low and medium energies interact with nuclei mainly through inverse β^- and β^+ decay:

$$\begin{aligned} {}^{A}_{Z}Y + \nu_e &\rightarrow {}^{A}_{Z+1}X + e^- \,, \\ {}^{A}_{Z+2}Y + \bar{\nu}_e &\rightarrow {}^{A}_{Z+1}X + e^+ \,. \end{aligned} \tag{10.4}$$

The rates of these processes depend on the NMEs $\mathcal{M}^{\nu(\bar{\nu})}$, which, in analogy to $0\nu\beta\beta$ decay NMEs, must be evaluated theoretically.

The pp, CNO, and ^{7}Be solar neutrinos are low-energy neutrinos. The $J_\pi = 1^+$ states mainly contribute to the NMEs. On the other hand, ^{8}B solar neutrino and supernova neutrino energy extends up to tens of MeV. Accordingly, the NMEs must include contributions from higher multipole states $J_\pi = 0^+, 1^\pm, 2^\pm, 3^\pm, \cdots$, depending on the neutrino energies [4].

Experiments with neutrino beams offer a direct way to study neutrino-nucleus interactions, but the tiny cross-section limits them. For the same arguments presented in the previous section about $0\nu\beta\beta$ decay, *i.e.* the large energy and momentum transferred, OMC is also advantageous compared to β decay and EC transitions to study the nuclear structure of the intermediate states of nuclei involved in interactions of astrophysical neutrinos.

References

[1] J. Engel and J. Menéndez. "Status and Future of Nuclear Matrix Elements for Neutrinoless Double-Beta Decay: A Review". In: *Rept. Prog. Phys.* 80.4 (2017), p. 046301. DOI: 10.1088/1361-6633/aa5bc5. arXiv: 1610.06548.

[2] M. Agostini et al. "Toward the discovery of matter creation with neutrinoless double-beta decay". 2022. arXiv: 2202.01787.

[3] M. Kortelainen and J. T. Suhonen. "Microscopic study of muon-capture transitions in nuclei involved in double-beta-decay processes". In: *Nucl. Phys. A* 713 (2003), pp. 501–521. DOI: 10.1016/S0375-9474(02)01303-9.

[4] H. Ejiri, J. T. Suhonen, and K. Zuber. "Neutrino-nuclear responses for astro-neutrinos, single beta decays and double beta decays". In: *Phys. Rept.* 797 (2019), pp. 1–102. DOI: 10.1016/j.physrep.2018.12.001.

[5] D. F. Measday. "The nuclear physics of muon capture". In: *Phys. Rept.* 354 (2001), pp. 243–409. DOI: 10.1016/S0370-1573(01)00012-6.

[6] D. Zinatulina et al. "Electronic catalogue of muonic X-rays". In: *EPJ Web Conf.* 177 (2018), p. 03006. DOI: 10.1051/epjconf/201817703006. arXiv: 1801.06969.

[7] G. Martínez-Pinedo, T. Fischer, and L. Huther. "Supernova neutrinos and nucleosynthesis". In: *J. Phys. G* 41 (2014), p. 044008. DOI: 10.1088/0954-3899/41/4/044008. arXiv: 1309.5477.

[8] K. G. Balasi, K. Langanke, and G. Martínez-Pinedo. "Neutrino-nucleus reactions and their role for supernova dynamics and nucleosynthesis". In: *Prog. Part. Nucl. Phys.* 85 (2015), pp. 33–81. DOI: 10.1016/j.ppnp.2015.08.001. arXiv: 1503.08095.

Chapter 11

The MONUMENT experiment

The large energy and momentum transfer occurring during OMC processes make them an ideal tool to experimentally address the many open questions concerning nuclear-structure calculations related to $0\nu\beta\beta$ decay and astrophysical neutrinos, as introduced in the previous chapter.

The MONUMENT experiment aims to carry out a series of measurements of OMC on several isotopes connected to $0\nu\beta\beta$ decay and astrophysical neutrinos. The OMC on ^{76}Se and ^{136}Ba, the targets of the first measurement campaign in October 2021, is of particular importance for the leading future $0\nu\beta\beta$ decay experiments using ^{76}Ge (LEGEND) and ^{136}Xe (nEXO, NEXT, KamLAND-Zen, ...), respectively.

A substantial contribution was made in the context of this dissertation work to the preparation and the performance of the first measurement, in particular to the design of the analysis strategy and to the analysis work itself. At the time of writing this work, the analysis of the data acquired during the first measurement is still a *work in progress*. Exciting results are expected soon.

11.1 The experiment

The use of OMC as a probe for the NMEs of $0\nu\beta\beta$ decay was originally proposed in 2002 by M. Kortelainen and J. Suhonen [1]. At the same time, the first experimental proposal, concerning the measurement of OMC rates in several double-β decay candidates, was submitted to the Paul Scherrer Institute (PSI) in Villigen, Switzerland [2]. Since then, pioneering measurements have been performed with several targets (^{48}Ti, ^{76}Se, ^{nat}Se, ^{106}Cd, ^{nat}Cd, ^{82}Kr, ^{nat}Kr, ^{150}Sm, ^{nat}Sm) [2–4]. Recent calculations for ^{76}Se agree with the experimental results obtained with the above measurements [5, 6]. In addition, as a by-product of these OMC measurements, a catalog of μXs has been generated [7], for nuclei with Z = 9 – 90, and will be updated as new measurements are performed. This is extremely useful for every experiment connected to muon physics.

The MONUMENT collaboration was formed in 2020 and is composed of 30 members from 13 different institutions around the globe. The goal of the project is to pursue explorative OMC measurements for double-β decay and astrophysical applications in three initial campaigns at PSI in the years 2021 to 2023.

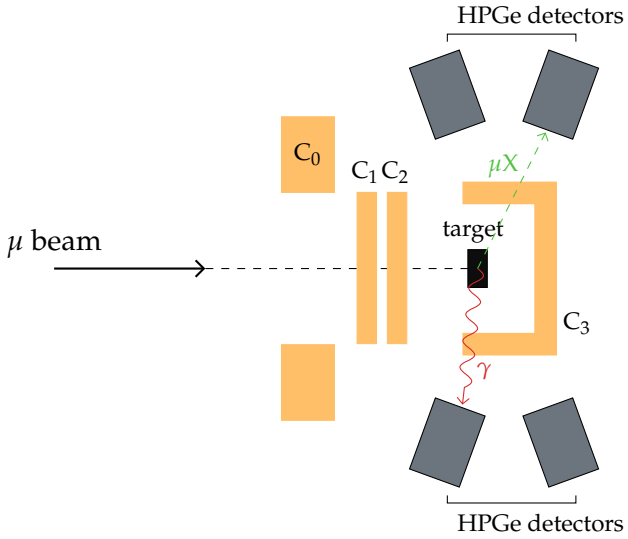

FIGURE 11.1: Schematic view of the measurement principle. A system consisting of four counters is used to select muons from the beam which are stopped in the target: a ring-shaped veto counter C_0 and two thin pass-through counters C_1 and C_2 are placed before the target, and a cup-like veto counter C_3 is surrounding the target. HPGe detectors placed around the target are used to detect the prompt μX and the delayed γ radiation.

The first beam time was successfully held in October 2021 [8]. Measurements with natural Se and Ba targets and isotopically enriched ^{76}Se and ^{136}Ba targets were performed. The analysis to extract the total and partial capture rates is currently ongoing. The result will benefit future $0\nu\beta\beta$ decay NME calculations of ^{76}Ge and ^{136}Xe, respectively.

The second beam time will commence in September 2022. Measurements with ^{100}Mo targets will be performed. OMC on ^{100}Mo can be related to nuclear reactions involving astrophysical neutrinos [9–11]. A third beam time is planned for 2023, where measurements with lighter nuclei, ^{40}Ca, ^{56}Fe, and ^{32}S, are foreseen. The goal of these measurements is to ultimately access the g_A quenching and the effective value of the pseudo-scalar coupling constant (g_P) in light and medium-heavy nuclei [11, 12].

11.2 Measurement principle

A precise measurement of the time and energy distributions of the γs following the muon capture is the goal of OMC experiments.

The measurement principle is sketched in figure 11.1. A target is exposed to a muon beam, whose momentum and position will be adjusted to maximize the probability of OMC. The target enclosure is preceded by a ring-shaped veto counter, C_0, and two thin pass-through counters, C_1 and C_2. An additional cup-like veto counter, C_3, surrounds the target enclosure. The four counters together allow us to

define the trigger for OMC:

$$\mu_{OMC} = \overline{C}_0 \wedge C_1 \wedge C_2 \wedge \overline{C}_3 \, . \tag{11.1}$$

The anti-coincidence of C_0 and the coincidence of C_1 and C_2 allow selecting only muons coming from the beam and which hit the target. The additional anti-coincidence of C_3 ensures that the muon was stopped in the target. The setup is completed with HPGe detectors, placed around the target unit at a distance of about 10 – 15 cm, and used to detect the prompt μXs and the delayed γ emissions following OMC.

After irradiation with the muon beam (online measurement), the target is placed for a longer time in a separate screening station to detect also the long-lived activity following OMC (offline measurement).

11.2.1 Correlated and Uncorrelated events

Two types of events are recorded during the online measurement: events correlated and uncorrelated in time with the muon stopped in the target.

If the signal in one of the HPGe detectors is not preceded by a muon stopped in the target[1] within a certain time window[2], the event is considered uncorrelated. The spectrum of uncorrelated events contains γ-lines from natural radioactivity, *e.g.* ^{40}K, U- and Th-chains, man-made backgrounds, *e.g.* ^{60}Co, ^{137}Cs, as well as beam-induced (n,γ)-reactions. The products of OMC are frequently unstable, emit γs as they decay, and contribute to the spectrum of uncorrelated events. The intensity of these lines can be used to extract the yield of the individual isotopes and isomers [4].

In correlated events, the signal in one of the HPGe detectors occurs within the defined time window after a muon stops in the target. The majority of these events are caused by the cascade of μXs, corresponding to the de-excitation of the muonic atom. Since the process happens within ps, the μXs can be considered prompt radiation. The capture of a muon is always accompanied by this μX emission. Therefore, the intensity of these lines shows the number of muons captured in the corresponding isotope [4].

In addition to prompt events, correlated events are also caused by the delayed γ radiation following OMC, whose energy and time distribution determination is the main subject of the experiment. The probability of OMC can be determined by measuring the exponential time evolution of these γ-lines [4]. On the other hand, the relative intensity of the γ-lines, compared to the μXs, can be used to extract the partial capture rates to the individual excited states.

[1] The definition of a muon stopped in the target is given by the trigger condition in equation 11.1.

[2] The size of the time window is of few μs depending on the expected muon lifetime in the given target.

Target	Measurement time (h)
^{136}Ba	208.86
natural Ba	45.5
^{76}Se	131.81
natural Se	15.72

TABLE 11.1: Rough estimate of the amount of data collected (with LLAMA DAQ) with each target during the first measurement campaign at PSI.

11.3 First measurement campaign at PSI

The first series of measurements at PSI was conducted for four weeks in October 2021. The first week was dedicated to the mounting of the setup and the tuning of the beam. Data-taking started in the second week and lasted for the remaining three weeks. After several calibration runs were performed with different calibration sources, measurements with 2 g of $^{136}BaCO_3$, 2 g of elemental ^{76}Se, and the same amount of natural isotopic-abundance Ba and Se were conducted. A rough estimate of the amount of data collected with each target is reported in table 11.1.

11.3.1 Experimental setup

The experiment was located at the πE1 beam line from PSI, which fulfills the experimental requirements in terms of muon energy and beam intensity. The beam consisted of negative muons, emitted in a backward direction from pions decaying in flight. The momentum of the muons was around 20 – 30 MeV/c, with a beam dispersion of about 2 %. The beam's intensity was of the order of 10^4 muons/s, corresponding to a rate of muons captured in the target of the same order of magnitude.

The experimental setup used during the beam time in October 2021 is shown in figure 11.2. It consists of nine HPGe detectors: eight of them placed around the target unit, while a ninth detector was placed under the setup to monitor the background during the full measurement time. The target unit consists of the target chamber and four scintillators connected to an equal number of PMTs. A schematic view of the target unit is shown in figure 11.3.

The eight detectors are mounted to an aluminum frame at about 10 cm from the target. A schematic view of the frame with the eight HPGe detectors is shown in figure 11.4.

The eight HPGe detectors are of three different types:

- Four large-volume n-type coaxial detectors (REGe detectors);
- Two large-volume p-type coaxial detectors (Coax detectors);
- Two p-type BEGe detectors.

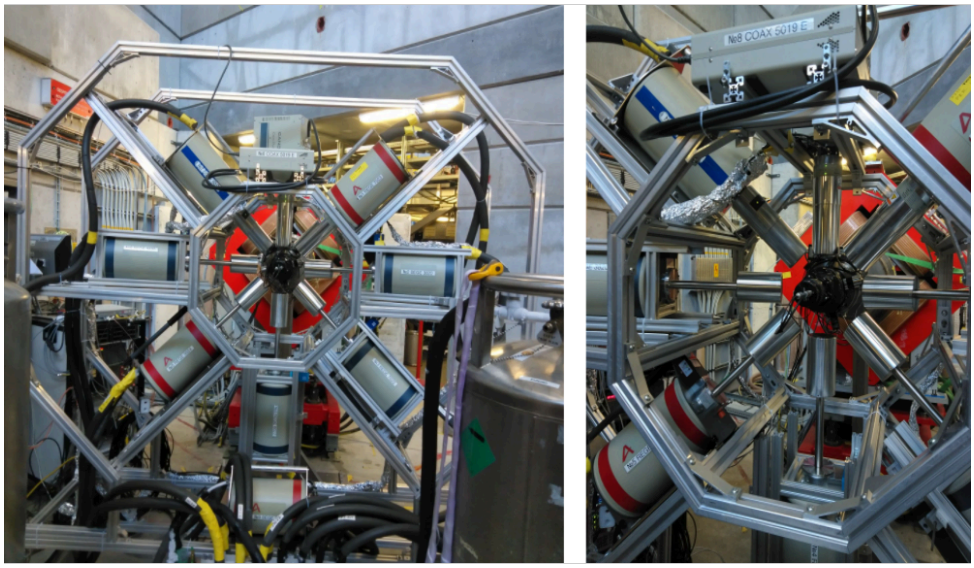

FIGURE 11.2: (Left) Aluminum frame with nine HPGe detectors mounted. (Right) Zoom on the eight detectors surrounding the target unit.

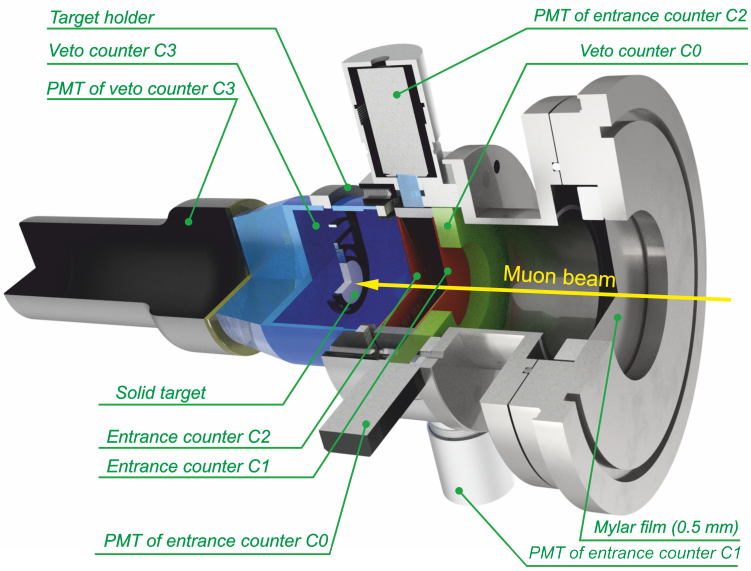

FIGURE 11.3: Schematic view of the target unit consisting of the target itself and the four scintillators connected to PMTs. The different components are highlighted. The direction of the incoming muon beam is also indicated. Picture from [8].

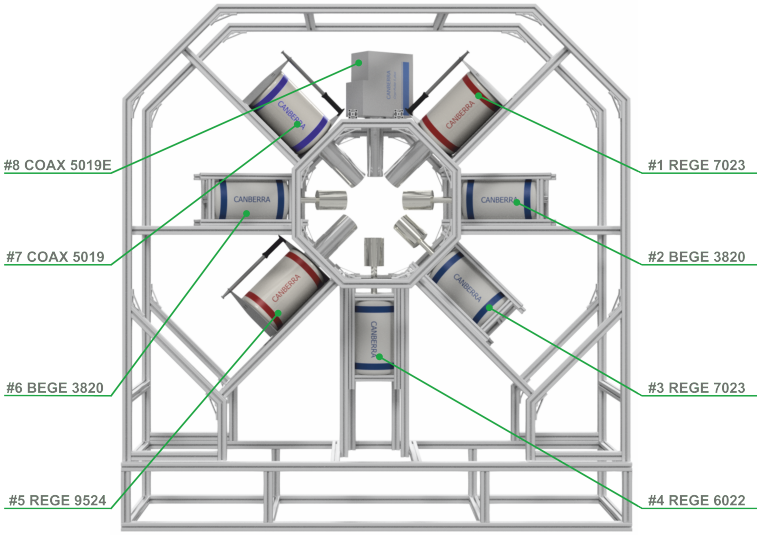

FIGURE 11.4: Schematic view of the aluminum frame with eight HPGe detectors mounted on it. Each detector is labeled by the detector number, the detector type, the relative efficiency, and the energy resolution (FWHM) at 1.3 MeV. For example, REGE 7023 means n-type coaxial detector with a relative efficiency of 70 % and FWHM of 2.3 keV. Picture from [8].

11.3.2 Data acquisition systems

Two parallel data acquisition (DAQ) systems were used, working entirely independently of each other. Each analog output of all HPGe detectors and PMTs was sent into a separate digital fan-in fan-out unit to provide two output signals per device, delivering input for both DAQ systems.

The first DAQ system, which we will refer to as MIDAS DAQ, is optimized to handle very high data rates without needing a fast storage server. The MIDAS DAQ was developed in the context of the muX experiment [13] and was already used in previous OMC measurements [4]. It utilizes a Struck SIS3316 digitizer module with 16 channels, 14-bit resolution, and a sampling frequency of 250 MHz. The MIDAS DAQ relies on the Digital Signal Processing (DSP) being performed online on the FADC. First, a trapezoidal filter is applied to the HPGe detector waveforms. The energy and the trigger time are then extracted and saved on disk. The trigger time and the pulse amplitude are calculated for the PMT waveforms and stored on the disk. In addition, a 1.4 μs waveform is saved for the HPGe detectors only to improve the time resolution in the offline analysis.

A second DAQ system was added to the experiment, used for the first time in the context of OMC measurements. We will refer to it as LLAMA[3] DAQ. The LLAMA DAQ utilizes a Struck SIS3316 digitizer with 16 channels, 16-bit resolution, and a 125 MHz sampling frequency. An Ethernet connection was established

[3]LLAMA stands for LEGEND Liquid Argon Monitoring Apparatus, which is a light detector integrating a VUV light source built into the LEGEND experiment to monitor optical properties of the LAr [14]. The DAQ program was initially developed in the framework of the LEGEND experiment and successively adapted for this experiment [15].

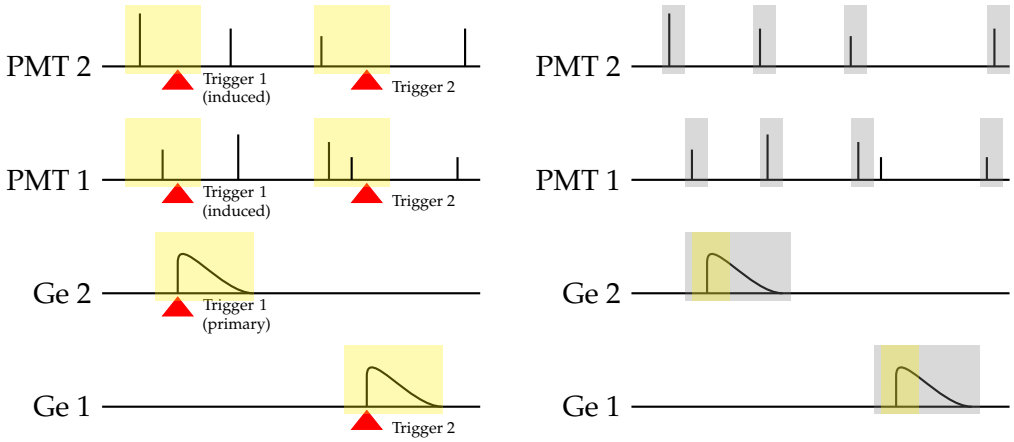

FIGURE 11.5: Comparison between the trigger scheme of LLAMA and MIDAS DAQ systems. Only two HPGe detectors and two PMTs are shown for simplicity. (Left) In LLAMA DAQ, a signal in one of the HPGe detectors triggers the acquisition of that detector and all the PMTs. The full trace, highlighted by the yellow area, is stored for offline analysis for both HPGe detectors and PMTs. (Right) In MIDAS DAQ, each HPGe detector and PMT is triggered independently (gray area). The trigger time and the energy of each signal are reconstructed online by the FADC, introducing a systematic dead time. Some relevant information could be lost in the process, as shown in PMT 1: the fourth signal, correlated with the signal in Ge 1, is not registered by the DAQ. Only a short trace and only for the HPGe detectors is stored for offline analysis (yellow area).

between the FADC and a dedicated readout server, providing a high-capacity and high-performance storage system with 160 TB of storage space and maximum data throughput of about 600 Mbit/s. Contrary to the MIDAS DAQ, the LLAMA DAQ does not utilize the online DSP features of the FADC, but all the waveforms from HPGe detectors and PMTs are streamed to the server, where they are stored for offline analysis. This approach allows for optimization of the DSP to achieve the best time and energy resolution. The absence of online processing also mitigates systematic dead times already observed in previous measurement campaigns using the MIDAS DAQ system.

Given the differences between the two DAQ systems, different trigger schemes were implemented, sketched in figure 11.5. In MIDAS DAQ, each detector (HPGe detectors and PMTs) is triggered independently. A dead time of about 1.5 μs follows. During this time, the online DSP is performed and the relevant information calculated. An event happening in the same detector in this time window is lost by MIDAS DAQ. In LLAMA DAQ, a signal in one of the HPGe detectors triggers the acquisition. The traces of that detector and all the PMTs are recorded, while other HPGe detectors are not read out (unless they trigger simultaneously).

In LLAMA DAQ, each waveform is recorded in high frequency (HF) and low frequency (LF) mode, with different trace lengths. For the HPGe detector signal waveforms, a long trace is necessary for offline energy reconstruction; on the other hand, a high sampling frequency is paramount for timing resolution. Given the possible

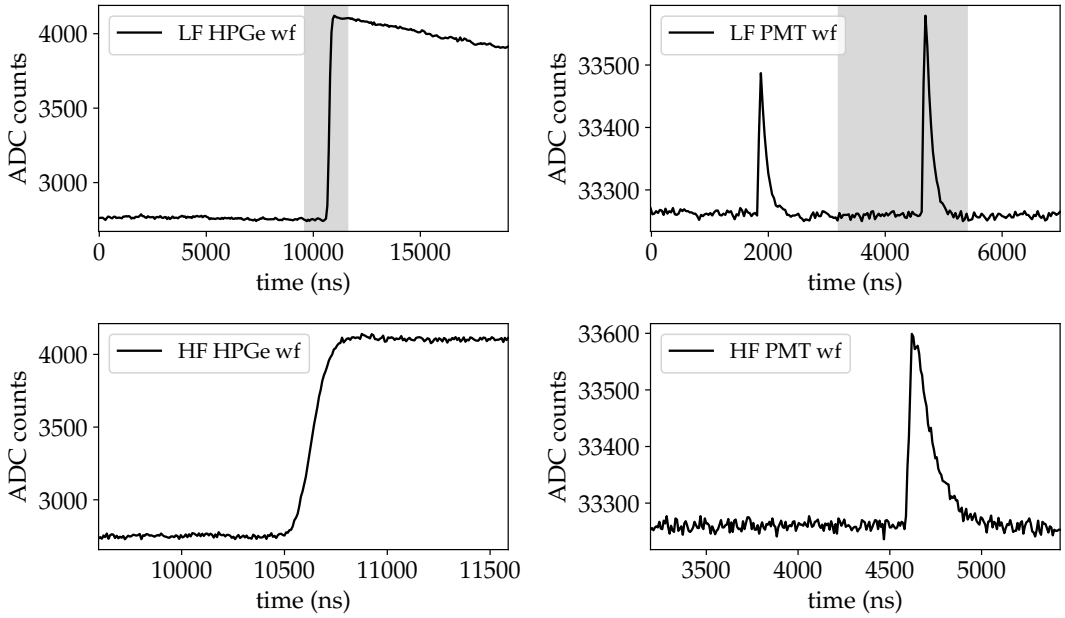

FIGURE 11.6: Example of waveforms (wfs) acquired with the LLAMA DAQ, for the HPGe detectors on the left and the PMTs on the right. The gray shaded area in the LF wfs indicates the time window for which the wf is also recorded in HF mode.

data throughput and the high event rate expected during the experiment, a compromise was found. A long trace of 20 μs was recorded at a low sampling frequency of 15 MHz. Preliminary studies before the beam time showed that a sampling frequency of 15 MHz still preserves the best energy resolution. A shorter trace of 2 μs, centered around the leading edge of the pulse, was also recorded with the maximum sampling frequency of 125 MHz to obtain the best time resolution. An example of the recorded HPGe waveforms is shown in figure 11.6.

The PMTs waveforms are recorded with 125 MHz sampling frequency for 2 μs before the trigger. This choice optimizes the resolution of the time difference between the muons in the PMTs and the signals in the HPGe detectors. The prompt μX and the delayed γ emissions are expected to happen within $\sim$ 1 μs from the muon capture. A longer trace of 7 μs (5.4 μs before the trigger and 1.6 μs after) is also recorded with a low sampling frequency of 30 MHz. The LF trace could provide additional information, *e.g.* concerning delayed coincidences. An example of the recorded PMT waveforms is shown in figure 11.6.

The following sections will focus on data acquired with the LLAMA DAQ, which was the focus of this dissertation work.

11.4 (Towards a) Multi-level data structure

One event in the LLAMA DAQ data consists of a waveform in one germanium detector (or more than one in the case of coincidences) and four PMT waveforms.

The event information at successive analysis steps is stored in a multi-tier hierarchical structure, following the data structure successfully implemented in GERDA and reported in chapter 4. The multi-level data structure is sketched in figure 11.7.

In the first step, raw data in the LLAMA DAQ format (Tier0) is converted into a standardized format based on ROOT [16] and the MGDO libraries [17], and split between HPGe detectors and PMTs. Between Tier0 and the successive level (Tier1), a data selection process is performed. Data are excluded from the analysis chain if a stable experimental configuration cannot be assured.[4]

The following level (Tier2) contains the result of the DSP, performed using the same software framework used in the GERDA experiment, namely GELATIO [18]. The output of the DSP is saved in the form of ROOT trees for further analysis. It contains general information about the event, like the timestamp and the ID of the HPGe detector where the signal was registered, and specific information on the waveforms relevant for the physics analysis, like the uncalibrated energy and the trigger position of the HPGe detector waveforms, as well as the amplitude and the position of all the pulses in the PMT waveforms. Additional information about the HPGe detector waveforms are available, like the baseline level and slope, the number of triggers in the trace, the position of the maximum and the minimum in the trace, and the RT of the pulse, for successive identification of pile-up or other non-physical events.

Until the Tier2 level, data from HPGe detectors and PMTs are analyzed in two separated chains. In the successive level (Tier3), the different streams are integrated into a unique ROOT tree. Tier3 contains a subset of the Tier2 parameters plus additional parameters calculated starting from the Tier2 parameters with auxiliary external inputs, like the calibrated energy and different event flags (aiming to classify different types of events). In addition, parameters combining the information from HPGe detectors and PMTs are present in the Tier3, like the multiplicity, *i.e.* the number of coincident HPGe detector signals, or the time difference between the signal in the PMTs and the signal in the HPGe detectors, reflecting the time difference between the muon entering the cell and the μXs or γs following its capture.

At present, Tier3 is the highest analysis level. In the future, higher tiers may be introduced containing the results of the high-level analysis.

11.4.1 Digital signal processing

The Digital Signal Processing (DSP) chain for HPGe detector waveforms starts with an evaluation of the baseline, *i.e.* the first 8 μs of the trace. Together with the mean value, the spread (RMS) and the exponential behavior of the baseline are evaluated.

The energy reconstruction is performed both with a pseudo-Gaussian filter and a trapezoidal filter. The Gaussian filter is approximated as a moving window deconvolution (MWD) followed by several moving window averages (MWAs). The energy is estimated as the amplitude of the resulting Gaussian pulse. The trapezoidal filter

[4] Reasons for data exclusion are, for instance, detector refilling, beam tuning, periods in which the beam was off or down for a while, or changes in the experimental setup.

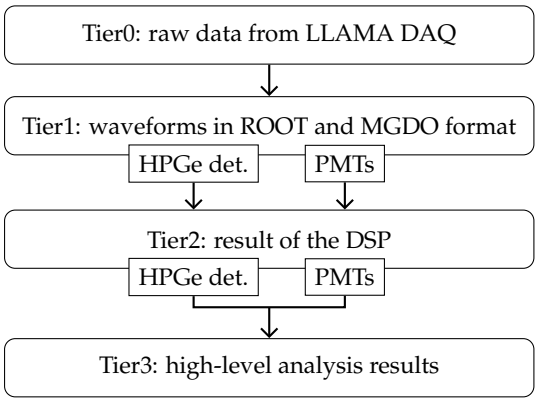

FIGURE 11.7: Multi-level structure of LLAMA DAQ data. Tier0 contains the raw data in the original format of the LLAMA DAQ. The waveforms are then converted in ROOT and MGDO format and stored in Tier1, separately for HPGe detectors and PMTs. The result of the DSP performed with the GELATIO software framework is stored in Tier2. Information from HPGe detectors and PMTs are then integrated and the result of the high-level analysis is stored in Tier3.

consists of a combination of a MWD and a MWA, whose sizes are related to the RT and the flat top (FT) of the resulting trapezoidal pulse, with MWA = RT and MWD = RT+FT [19]. The energy is estimated as the amplitude of the trapezoidal at a fixed position in the FT. The size of the MWD and the MWA was optimized for each detector to obtain the best energy resolution.

The optimization of the energy reconstruction with the trapezoidal filter was performed using data from a calibration run with ^{60}Co, applying trapezoidal filters with different combinations of MWA and MWD sizes and studying the energy resolution of the 1173 keV peak. A general preference for long shaping parameters was observed for all the detectors. As a result, a MWD size of 8 μs and a MWA size of 5 μs were chosen for all the HPGe detectors. The MWD size is limited by the length of the trace. For longer MWD sizes, the resulting trapezoidal pulse would move outside the trace. The optimized trapezoidal filter allows for obtaining a better energy resolution than the Gaussian filter. A better resolution is also obtained compared to the online trapezoidal filter of the MIDAS DAQ.[5] A comparison of the energy resolution is reported in table 11.2.

The trigger position is calculated with a simple leading-edge trigger algorithm applied both to the original waveform and after performing a fast trapezoidal filter (MWD = MWA $\sim$ 400 ns) to the waveform. The second method allows identifying multiple triggers in the same trace, *i.e.* pile-up events.

Additional parameters were evaluated to classify non-physical events, including the position of the minimum and the maximum in the trace and the RT of the pulse.

While most of the DSP algorithms are applied to the LF waveform, the trigger position and the RT are also evaluated on the HF waveform, which allows for obtaining

[5]The MIDAS energy resolutions were calculated using the MIDAS DAQ data corresponding to the same calibration run with ^{60}Co. The same analysis methods were used for a reliable comparison.

Detector number	Detector name	FWHM (keV) LLAMA	FWHM (keV) MIDAS
1	REGe 7023	3.64	4.48
2	BEGe 3820	1.83	1.81
3	REGe 7023	2.59	3.13
4	REGe 6022	2.49	3.16
5	REGe 9524	2.82	3.36
6	BEGe 3820	1.65	1.67
7	Coax 5019	2.55	3.05
8	Coax 5019E	2.55	2.53

TABLE 11.2: Comparison of the energy resolution (FWHM) calculated at the 1173 keV ^{60}Co peak, for LLAMA data with the optimized trapezoidal filter and MIDAS data with the online trapezoidal filter.

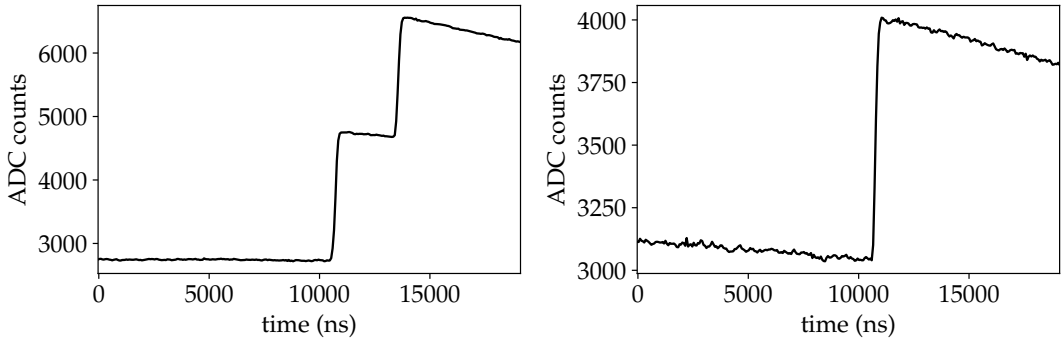

FIGURE 11.8: Example of in-trace pile-up event on the left and pre-trace pile-up event on the right.

a better time resolution.

The DSP of the PMT traces consists of a pulse finding algorithm, which calculates the baseline position and RMS recursively, excluding every time frame of the trace that exceeds four standard deviations of the previously determined mean value. The different pulses are then identified by a simple leading-edge trigger algorithm. The trigger positions and the corresponding pulse amplitudes are evaluated. Since the PMT pulses were found to be relatively slow, a very fast trapezoidal filter (MWD=90 ns and MWA=30 ns) is applied to the PMT traces before the pulse finding algorithm. This allows for an enhanced resolution of multiple pulses in the same trace in close proximity.

11.4.2 Pile-up events

One of the main challenges of the analysis was found to be the large fraction of pile-up events, which is due to the very high event rate typical for the experiment. We distinguish two types of pile-up events: the in-trace and the pre-trace pile-up. An example of the two is shown in figure 11.8.

The in-trace pile-up consists of a second event happening on the tail of the previous event, which triggered the DAQ. These events can be identified by the fast

trapezoidal trigger, which will result in a number of triggers > 1. The fraction of in-trace pile-up has been evaluated, using one of the first physics runs with ^{136}Ba, and it is $\sim 2\,\%$ in smaller detectors and $\sim 5\,\%$ in bigger detectors. The energy reconstruction of these events with the standard methods fails; therefore, they are discarded from the analysis.

When the event triggering the DAQ happens on the tail of a previous one, it will show an exponentially decaying baseline. This is what we call a pre-trace pile-up. These events can be identified by the slope of the baseline, which will be much larger than 0. The energy of pre-trace pile-up events is underestimated by the standard energy reconstruction methods, which rely on the baseline position. Consequently, γ peaks in the energy spectrum will show low energy tails.

Since the identification of many γ and μX lines and the calculation of their intensities is the experiment's goal, the underestimated energy of the pre-trace pile-up events may become a dominant systematic uncertainty. In addition, the estimation of the trigger position, which relies on the baseline level, is also biased in pre-trace pile-up events. This creates a bias in estimating the time difference between the incoming muon and the μXs and γs following the capture, which is also very important for the experiment. On the other hand, discarding all the pre-trace pile-up events would mean discarding a significant fraction of the statistics.

So far, any attempts to subtract the exponential decay from the baseline showed an increase in the noise and consequent degradation of the energy resolution. Different approaches are planned to find a suitable energy reconstruction method that would provide a correct energy estimation without compromising too much the energy resolution.

We should note that in the data collected with the MIDAS DAQ pre-trace pile-up events are not monitorable. While the in-trace pile-up events are tagged by the FADC, only a short waveform centered around the leading edge of the pulse is saved on disk, so the information about a non-flat baseline is not accessible. The possibility to access the whole waveform for each event, together with the possibility to adapt the DSP algorithms, is one of the advantages of the LLAMA DAQ.

11.4.3 Quality cuts

A set of quality cuts (QC) was established to identify non-physical signals and signals with different characteristics than those for which the DSP algorithms were implemented, like pile-up events or signals that exceed the FADC dynamic range.

QC are applied to each detector separately and include requirements on the baseline slope and RMS, the number of triggers, the position of the first trigger, and the position of the maximum in the trace.

Non-physical signals and signals that exceed the FADC dynamic range are discarded from the analysis. A different treatment is used for pile-up events depending on whether them being in-trace or pre-trace pile-up events. While in-trace pile-up events (number of triggers > 1) are always discarded, a different approach is used

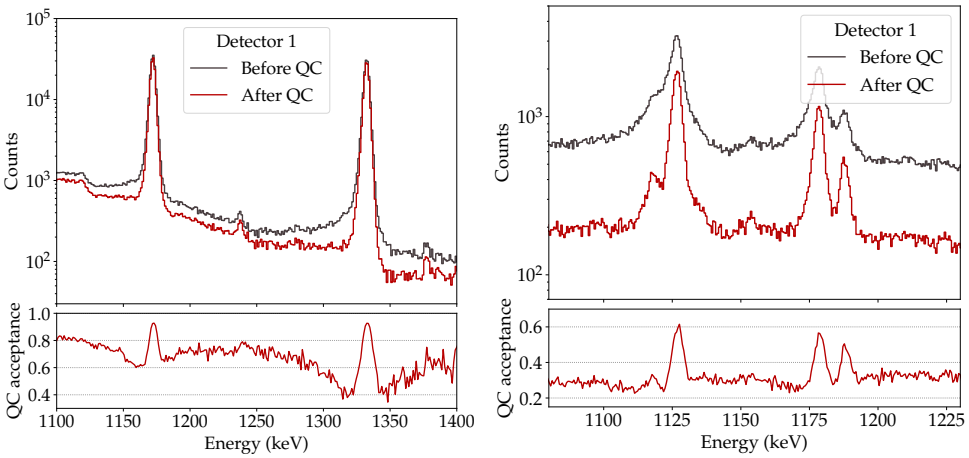

FIGURE 11.9: (Left) Energy spectrum obtained with detector 1 during a calibration run with ^{60}Co centered around the two ^{60}Co γ lines at 1173.2 keV and 1332.5 keV before and after QC. (Right) Energy spectrum obtained with detector 1 during about 3 hours of ^{136}Ba exposure zoomed on the two most prominent μXs (1227 keV and 1284 keV) belonging to the L(nd-2p) series before and after QC. The QC acceptance is shown in the bottom panel. See the text for the discussion of the figure.

for pre-trace pile-up events. Data are divided into two datasets: the *Golden* dataset and the *Silver* (or pile-up) dataset. In the Golden dataset, stringent requirements on the slope and the RMS of the baseline are applied to cut all the problematic pre-trace pile-up events and achieve the best performances in terms of energy and time resolution. The Silver dataset contains most of the pre-trace pile-up events that are excluded from the Golden dataset and will eventually be used in the analysis with some compromises on the energy and time resolution. A proper energy reconstruction method is still under investigation for the events in the Silver dataset.

Figure 11.9 shows the effect of the quality cuts on calibration (^{60}Co) and physics (^{136}Ba) data. The energy spectrum obtained with detector 1 during a ^{60}Co calibration run, centered around the two ^{60}Co γ lines (1173.2 keV and 1332.5 keV), is shown before and after the application of the QC. Events corresponding to the full energy deposition of the *gamma* in the HPGe detector, creating a peak in the energy spectrum, have very high acceptance ($> 90\%$). The effect of the quality cuts is maximal (resulting in small acceptance) on the peak tails, where the pile-up events are expected to lie. The events which survive QC belong to the Golden dataset, which will be used for further analysis. For the physics data, the energy spectrum obtained with detector 1 during about 3 hours of ^{136}Ba exposure is shown, zoomed on the two most prominent μXs (1227 keV and 1284 keV) belonging to the L(nd-2p) series, before and after the application of the QC. Still, higher acceptance of the events corresponding to the μXs peaks ($> 60\%$)[6] is observed compared to the events in the tails or background events (outside and in between the peaks).

[6]The acceptance in correspondence of the peaks in the physics data is reduced compared to calibration data because of the highest background.

The definition of the QC, which allows defining a clean set of data, *i.e.* the Golden dataset, is an extremely important step for any successive analysis. The comparison of the energy spectrum centered around two of the ^{136}Ba μXs before and after QC shows clearly the data quality improvement obtained by applying the QC. For instance, very close peaks in the energy spectrum are better resolved after QC.

11.5 Conclusions and outlook

The MONUMENT experiment aims to perform a series of explorative OMC measurements for double-β decay and astrophysical applications. The first measurement campaign was successfully held in October 2021 with a muon beam at PSI. Measurements with natural Se and Ba targets and isotopically enriched ^{76}Se and ^{136}Ba targets were performed. The identification of the μXs and γ lines in the spectrum of correlated events and the measurement of their energy and time distributions will allow us to calculate the total and partial capture rates of OMC on ^{136}Ba and ^{76}Se, which is the ultimate goal of the experiment.

Compared to previous OMC measurements, a new DAQ system was used during this measurement campaign, namely the LLAMA DAQ. This was introduced to cope with the systematic dead times previously observed with the MIDAS DAQ system. With substantial differences from the standard DAQ systems utilized in accelerator-based experiments, the LLAMA DAQ was proved successful for measuring the OMC products. The energy spectrum obtained with LLAMA DAQ with detector 1 during a ^{60}Co calibration run is compared to the same energy spectrum obtained with MIDAS DAQ in figure 11.10. The two spectra are comparable: the two ^{60}Co γ lines are visible at 1173.2 keV and 1332.5 keV, together with several other background peaks. The better energy resolution obtained with LLAMA DAQ, due to the offline optimization of the DSP and the definition of the QC, is visible in the inset of the figure, where the two ^{60}Co γ lines are shown.

Being newly introduced, the LLAMA DAQ also required a new analysis software to be developed. The step between the raw HPGe detector and PMT waveforms acquired with the LLAMA DAQ and the energy and time distribution of correlated events is not straightforward and requires several intermediate efforts. Substantial progress has already been made in some of them: the DSP algorithms were defined and optimized, "good" events were identified through QC, and the calibration of the HPGe detectors was performed with satisfactory results. Near future analysis plans include the efficiency calibration and identifying the different types of events (uncorrelated/correlated/prompt/delayed), both critical tasks to achieve the proposed physics results.

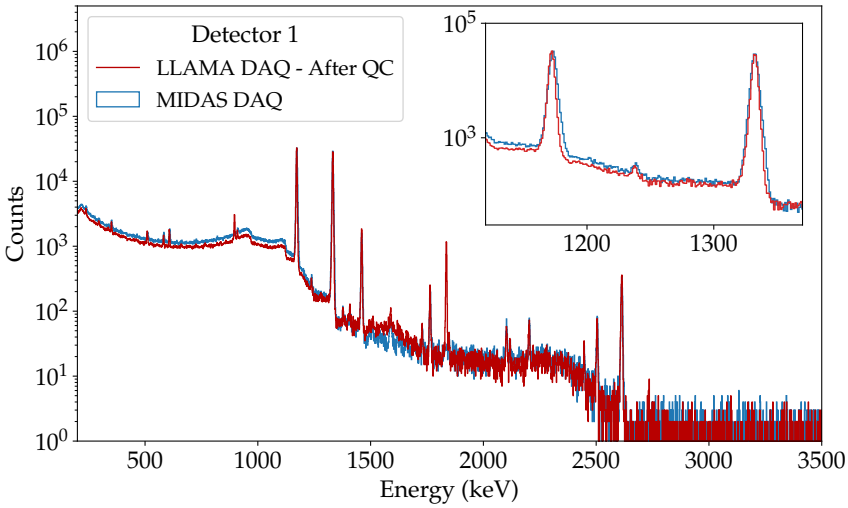

FIGURE 11.10: Comparison of the energy spectrum obtained with detector 1 with LLAMA and MIDAS DAQ during a calibration run with ^{60}Co.

References

[1] M. Kortelainen and J. T. Suhonen. "Ordinary muon capture as a probe of virtual transitions of $\beta\beta$ decay". In: *EPL* 58 (2002), pp. 666–672. DOI: 10.1209/epl/i2002-00401-5. arXiv: nucl-th/0201007.

[2] V. Egorov et al. "muCR42beta: Muon capture rates for double-beta decay". In: *Czech. J. Phys.* 56 (2006), pp. 453–457. DOI: 10.1007/s10582-006-0108-4.

[3] D. Zinatulina et al. "Ordinary muon capture (OMC) studies by means of γ-spectroscopy". In: *AIP Conf. Proc.* 1894.1 (2017), p. 020028. DOI: 10.1063/1.5007653.

[4] D. Zinatulina et al. "Ordinary muon capture studies for the matrix elements in $\beta\beta$ decay". In: *Phys. Rev. C* 99.2 (2019), p. 024327. DOI: 10.1103/PhysRevC.99.024327. arXiv: 1803.10960.

[5] L. Jokiniemi and J. T. Suhonen. "Muon-capture strength functions in intermediate nuclei of $0\nu\beta\beta$ decays". In: *Phys. Rev. C* 100.1 (2019), p. 014619. DOI: 10.1103/PhysRevC.100.014619.

[6] L. Jokiniemi and J. T. Suhonen. "Comparative analysis of muon-capture and $0\nu\beta\beta$-decay matrix elements". In: *Phys. Rev. C* 102.2 (2020), p. 024303. DOI: 10.1103/PhysRevC.102.024303.

[7] D. Zinatulina et al. "Electronic catalogue of muonic X-rays". In: *EPJ Web Conf.* 177 (2018), p. 03006. DOI: 10.1051/epjconf/201817703006. arXiv: 1801.06969.

[8] D. Bajpai et al. "OMC4DBD: ordinary muon capture as a probe of properties of double-beta decay processes". BVR 53: Progress Report R-20-01.1. 2022.

[9] H. Ejiri. "Nuclear spin isospin responses for low-energy neutrinos". In: *Phys. Rept.* 338 (2000), pp. 265–351. DOI: 10.1016/S0370-1573(00)00044-2.

[10] H. Ejiri, J. Engel, and N. Kudomi. "Supernova neutrino studies with ^{100}Mo". In: *Phys. Lett. B* 530 (2002), pp. 27–32. DOI: 10.1016/S0370-2693(02)01349-7. arXiv: astro-ph/0112379.

[11] L. Jokiniemi et al. "Pinning down the strength function for ordinary muon capture on ^{100}Mo". In: *Phys. Lett. B* 794 (2019), pp. 143–147. DOI: 10.1016/j.physletb.2019.05.037.

[12] J. T. Suhonen. "Value of the Axial-Vector Coupling Strength in β and $\beta\beta$ Decays: A Review". In: *Front. in Phys.* 5 (2017), p. 55. DOI: 10.3389/fphy.2017.00055. arXiv: 1712.01565.

[13] *muX | LTP | Paul Scherrer Institut (PSI)*. URL: https://www.psi.ch/en/ltp/mux.

[14] M. Schwarz et al. "Liquid Argon Instrumentation and Monitoring in LEGEND-200". In: *EPJ Web Conf.* 253 (2021), p. 11014. DOI: 10.1051/epjconf/202125311014.

[15] M. Schwarz. In preparation. PhD thesis. Technische Universität München.

[16] R. Brun et al. *root-project/root: v6.18/02*. Version v6-18-02. 2019. DOI: 10.5281/zenodo.3895860.

[17] M. Agostini et al. "The MGDO software library for data analysis in Ge neutrinoless double-beta decay experiments". In: *J. Phys. Conf. Ser.* 375 (2012), p. 042027. DOI: 10.1088/1742-6596/375/1/042027. arXiv: 1111.7260.

[18] M. Agostini et al. "GELATIO: A General framework for modular digital analysis of high-purity Ge detector signals". In: *JINST* 6 (2011), P08013. DOI: 10.1088/1748-0221/6/08/P08013. arXiv: 1106.1780.

[19] J. Stein et al. "X-ray detectors with digitized preamplifiers". In: *Nuclear Instruments and Methods in Physics Research Section B: Beam Interactions with Materials and Atoms* 113.1 (1996), pp. 141–145. DOI: https://doi.org/10.1016/0168-583X(95)01417-9.

Conclusions

Rare double-β decays might hold the key to unveiling physics BSM. The observation of $0\nu\beta\beta$ decay would unambiguously prove lepton number non-conservation and that neutrinos have a Majorana mass component, with important implications in particle physics and cosmology. The hunt for this rare decay gave rise, in the past, to a vast experimental program using different isotopes and diverse detection technologies, which converged today on a few future ton-scale experiments. These experiments also offer a unique opportunity to test other extensions of the SM, which predict the existence of new particles, violation of fundamental symmetries, or non-standard interactions and can lead to more exotic double-β decay modes.

This dissertation investigated the emission of light exotic fermions in double-β decays in two different scenarios. In the first, the existence of a massive sterile neutrino that mixes with the electron neutrino is assumed. The second scenario is characterized by the presence of an additional Z_2 symmetry that only allows the exotic fermion to be produced in pairs. This is a typical scenario for models adding new exotic fermions as dark matter candidates, which are charged under a Z_2 symmetry to make them stable. We estimated the sensitivity of current and future double-β decay experiments. We showed that the sensitivity of current double-β decay experiments on the active-sterile mixing angle $\sin^2\theta$ is weaker than the existing limits from single-β decay experiments and solar neutrinos. Still, future experiments with larger exposure will improve these limits, reaching

$$\sin^2\theta \sim 10^{-3} - 10^{-4}$$

for masses between a few hundred keV and a few MeV, and setting the most stringent constraints in this mass range. Double-β decay experiments also have the unique capability of probing models in which only the double production of light exotic fermions is allowed, leading to the first direct constraints on this kind of model. The effective coupling g_χ can be constrained at the level of

$$g_\chi \sim 10^{-2} - 10^{-3}\ \mathrm{MeV}^{-2}$$

by current experiments and can be improved by one order of magnitude in future experiments. This work on the search for exotic fermions in double-β decay has been published in [1]. This author estimated the sensitivity of current and future double-β decay experiments and contributed to the writing of the corresponding manuscript's sections.

Among the current generation of experiments, the GERDA experiment stands out for its ultra-low background and excellent performance. The main goal of the GERDA experiment was to search for $0\nu\beta\beta$ decay of ^{76}Ge with enriched HPGe detectors in an instrumented LAr volume at the LNGS in Italy. The Phase II of the experiment lasted from December 2015 to November 2019. Combining low-radioactive materials, passive shielding, germanium detectors with superior energy resolution, and active discrimination by event topology, the lowest BI of any double-β decay experiment has been measured at the end of Phase II in the $0\nu\beta\beta$ decay ROI

$$\mathrm{BI} = 5.2^{+1.6}_{-1.3} \times 10^{-4}\ \mathrm{counts/(keV\ kg\ yr)}\ ,$$

with a collected exposure of 103.7 kg yr. No $0\nu\beta\beta$ decay signal was found, and, combining Phase I and Phase II data, with a total exposure of 127.2 kg yr, the most stringent lower limit on the ^{76}Ge $0\nu\beta\beta$ decay half-life has been set

$$T^{0\nu}_{1/2} > 1.8 \times 10^{26}\ \mathrm{yr} \quad \text{at 90\% C.L.}\ ,$$

coinciding with the median sensitivity for the null hypothesis. This corresponds to a limit on the effective Majorana neutrino mass

$$m_{\beta\beta} < [79, 180]\ \mathrm{meV} \quad \text{at 90\% C.L.}\ ,$$

depending on the NMEs. The final results of the GERDA experiment on the search for $0\nu\beta\beta$ decay have been published in [2]. This author gave a substantial contribution to several aspects of the analysis, which led to this final result.

Depending on the relative number of protons and neutrons in the nucleus, double-β transitions may happen in the SM with the capture of two electrons and the emission of two neutrinos. The corresponding 0νECEC is an alternative probe for lepton number non-conservation and the Majorana nature of neutrinos. One of the 0νECEC candidates, ^{36}Ar, was naturally present in the LAr cryostat, which housed the GERDA detectors. This dissertation concerned the search for a γ peak with an energy of about 430 keV, which is the experimental signature of 0νECEC of ^{36}Ar. The whole GERDA Phase II exposure was used, and the LAr veto cut was applied to reduce the background in the region of interest. No indication of this line was found, and the most stringent lower limit on the half-life of this process was obtained

$$T_{1/2} > 1.64 \times 10^{22}\ \mathrm{yr} \quad \text{at 90\% C.L.}\ .$$

This analysis was performed by this author in collaboration with the master student *M. Korošec* as part of this dissertation work and will be published by the GERDA Collaboration.

Within this dissertation work, a comprehensive study of the ^{76}Ge $2\nu\beta\beta$ decay spectrum in GERDA Phase II data was performed. Precision determination of the half-life of this SM-allowed process provides essential inputs for nuclear-structure

calculations and ultimately benefits the interpretation of $0\nu\beta\beta$ decay results. On the other hand, the search for distortions of the two-electron spectrum compared to the SM prediction allows exploring new physics BSM.

The half-life of the ^{76}Ge $2\nu\beta\beta$ decay was determined with unprecedented precision using a subset of detectors (11.8 kg yr) characterized before their deployment in LAr and at the end of the experiment, allowing a precise determination of their active volume. We obtained

$$T_{1/2}^{2\nu} = (2.022 \pm 0.041) \times 10^{21} \text{ yr} .$$

With a total uncertainty of 2.0%, this is the most precise determination of ^{76}Ge $2\nu\beta\beta$ decay half-life and one of the most precise measurements of a double-β decay process. This result benefits from the high signal-to-background ratio achieved with the LAr veto cut. This is 22:1 in the energy region dominated by the $2\nu\beta\beta$ decay (this was at best 4:1 in previous experiments with Ge). Consequently, the systematic uncertainties related to the background modeling, which were significant in previous measurements, are strongly reduced to less than 1%. The dominant systematic uncertainty comes from the active volume determination, in particular from the growth of the DL when the detectors are stored at room temperature. This shows the importance of the AV determination for precision measurements in the future LEGEND experiment. This author was the leading author of the analysis of the ^{76}Ge $2\nu\beta\beta$ decay which led to the precision measurement of its half-life. A manuscript was prepared by this author, which will be published by the GERDA Collaboration [3].

A larger dataset (32.8 kg yr) was used to investigate exotic double-β decay modes of ^{76}Ge, searching for distortions of the $2\nu\beta\beta$ decay spectrum compared to the SM prediction. Improved limits on the decay involving Majorons have been obtained, compared to previous experiments with ^{76}Ge, with half-life values on the order of 10^{23} yr. The most stringent limit is obtained in the case of the J$\beta\beta$ decay corresponding to a spectral index $n = 1$. The half-life of this decay has been constrained to

$$T_{1/2} > 6.4 \times 10^{23} \text{ yr} \quad \text{at 90\% C.L.} ,$$

which corresponds to an upper limit on the neutrino-Majoron coupling constant

$$g_J < (1.8 - 4.4) \times 10^{-5} \quad \text{at 90\% C.L.} ,$$

depending on the NMEs.

For the first time with ^{76}Ge, limits on Lorentz invariance violation have been obtained. The isotropic coefficient $\mathring{a}_{\text{of}}^{(3)}$, which embeds Lorentz violation in double-β decay, has been constrained

$$(-2.7 < \mathring{a}_{\text{of}}^{(3)} < 6.2) \cdot 10^{-6} \text{ GeV} \quad \text{at 90\% C.L.} .$$

The first experimental constraints on light exotic fermions in double-β decay

have been obtained. The most stringent limit on the active-sterile mixing angle has been obtained for a sterile neutrino mass of 500 – 600 keV

$$\sin^2\theta < 0.013 \quad \text{at 90\% C.L.} .$$

The half-life of the decay into two Z_2-odd fermions has been constrained at the order of 10^{22-23} yr, depending on the fermion mass. The best limit is obtained for a mass of 400 keV

$$T_{1/2} > 2.5 \times 10^{23} \text{ yr} \quad \text{at 90\% C.L.} ,$$

which corresponds to an upper limit on the coupling constant

$$g_\chi < (0.6 - 1.4) \times 10^{-3} \text{ MeV}^{-2} \quad \text{at 90\% C.L.} ,$$

depending on the NMEs. This author was the leading author of the analysis which led to new limits on Majoron-involving decays, Lorentz violation, and emission of light exotic fermions in double-β decay with ^{76}Ge. A manuscript was prepared by this author, which will be published by the GERDA Collaboration [4].

The discovery of $0\nu\beta\beta$ decay with a half-life of the order of 10^{28} yr is within reach of the next generation of double-β decay experiments. The interpretation of the results in terms of particle physics parameter, *e.g.* the effective Majorana neutrino mass, relies on nuclear-structure calculations, which to date carry significant uncertainties. The large energy and momentum transferred in OMC processes are analogous to that of $0\nu\beta\beta$ decays. Thus, OMC is a robust benchmark for related nuclear-structure calculations.

The MONUMENT experiment aims to carry out a series of measurements of OMC on several isotopes connected to $0\nu\beta\beta$ decay. Within this dissertation, the first steps of the analysis of the data collected during the first measurement campaign with ^{76}Se and ^{136}Ba were compiled. These targets are particularly important for the leading future $0\nu\beta\beta$ decay experiment with ^{76}Ge (LEGEND) and ^{136}Xe (nEXO, NEXT, KamLAND-Zen), respectively. This author gave a substantial contribution to the preparation and performance of the first measurement, in particular to the design of the analysis and the ongoing analysis work itself.

References

[1] M. Agostini, E. Bossio, A. Ibarra, and X. Marcano. "Search for Light Exotic Fermions in Double-Beta Decays". In: *Phys. Lett. B* 815 (2021), p. 136127. DOI: 10.1016/j.physletb.2021.136127. arXiv: 2012.09281.

[2] GERDA Collaboration, M. Agostini, et al. "Final Results of GERDA on the Search for Neutrinoless Double-β Decay". In: *Phys. Rev. Lett.* 125.25 (2020), p. 252502. DOI: 10.1103/PhysRevLett.125.252502. arXiv: 2009.06079.

[3] GERDA Collaboration, M. Agostini, et al. "Precision measurement of the ^{76}Ge double-beta decay rate with GERDA Phase II". prepared for submission to Phys. Rev. Lett. 2022.

[4] GERDA Collaboration, M. Agostini, et al. "Search for exotic physics in double-β decays with GERDA Phase II". submitted to JCAP. 2022. arXiv: 2209.01671.

Appendices

Appendix A

Sensitivity to light exotic fermions

A rough estimation of the sensitivity to light exotic fermions can be obtained with a counting analysis and Poisson statistics. In this derivation, we neglect the systematic uncertainties. Their impact on the sensitivity has been shown in chapter 3 (see figure 3.2).

In the search for spectral distortions, the energy region of interest extends from the detector threshold to the $Q_{\beta\beta}$. In this window, most of the observed events are due to $2\nu\beta\beta$ decay, $N_{2\nu\beta\beta}$, with additional contributions due to different background processes, N_{others}.

The parameter of interest in the search for the Z_2-odd exotic fermion χ is the coupling constant g_χ, which is proportional to the number of events $N_{\chi\chi\beta\beta}$

$$g_\chi^2 \propto \mathcal{G}^{-1}\mathcal{M}^{-2}N_{\chi\chi\beta\beta}\ , \tag{A.1}$$

where $\mathcal{G}$ and $\mathcal{M}$ are the phase-space factor and the NME of the decay.

The precision with which a subdominant contribution can be constrained is proportional to the fluctuations of the background in the analysis window

$$\sigma_{N_{\chi\chi\beta\beta}} = \sqrt{N_{2\nu\beta\beta} + N_{others}}\ . \tag{A.2}$$

Expressing the number of events as a function of the decay rate (inverse of the half-life) throught the exposure $\mathcal{E}$

$$N_{\chi\chi\beta\beta} \propto \mathcal{E} \cdot R_{\chi\chi\beta\beta}\ . \tag{A.3}$$

equation A.2 becomes

$$\sigma_{R_{\chi\chi\beta\beta}} \propto \sqrt{(R_{2\nu\beta\beta} + R_{others})/\mathcal{E}}\ . \tag{A.4}$$

Putting everything together, we obtain an expression for the sensitivity on g_χ^2

$$\sigma_{g_\chi^2} \propto \mathcal{G}^{-1}\mathcal{M}^{-2}\sqrt{(R_{2\nu\beta\beta} + R_{others})/\mathcal{E}}\ . \tag{A.5}$$

The sensitivity scales with the square root of the exposure, but it is limited by the background, to which the $2\nu\beta\beta$ decay contributes. In addition, uncertainties in the

phase space and NMEs can limit the sensitivity.

The parameter of interest in the sterile neutrino search is the mixing angle $\sin^2\theta$, which is related to the ratio between the number of $\nu N\beta\beta$ decay events, $N_{\nu N\beta\beta}$, and the number of $2\nu\beta\beta$ decay events

$$\sin^2\theta \propto \mathcal{G}_{2\nu\beta\beta}/\mathcal{G}_{\nu N\beta\beta} \cdot N_{\nu N\beta\beta}/N_{2\nu\beta\beta}\ , \tag{A.6}$$

where $\mathcal{G}_{2\nu\beta\beta}$ and $\mathcal{G}_{\nu N\beta\beta}$ are the phase-space factor for the $2\nu\beta\beta$ and $\nu N\beta\beta$ decays, respectively. The statistical uncertainty on this quantity can be computed through standard error propagation

$$\sigma_{\sin^2\theta}/\sin^2\theta \propto \sqrt{(\frac{\sigma_{N_{\nu N\beta\beta}}}{N_{\nu N\beta\beta}})^2 + (\frac{\sigma_{N_{2\nu\beta\beta}}}{N_{2\nu\beta\beta}})^2 + 2\cdot(\frac{\sigma_{N_{\nu N\beta\beta}}\sigma_{N_{2\nu\beta\beta}}}{N_{\nu N\beta\beta}N_{2\nu\beta\beta}})\rho_{N_{\nu N\beta\beta},N_{2\nu\beta\beta}}}. \tag{A.7}$$

Because of the same arguments previously used to define the uncertainty on $N_{\chi\chi\beta\beta}$, the uncertainty on $N_{\nu N\beta\beta}$ will scale as

$$\sigma_{N_{\nu N\beta\beta}} \propto \sqrt{(R_{2\nu\beta\beta} + R_{others})\cdot\mathcal{E}}\ . \tag{A.8}$$

In addition, we can write the number of sterile neutrino events in terms of the number of $2\nu\beta\beta$ decays and the mixing angle. Also, the correlation coefficient $\rho_{N_{\nu N\beta\beta},N_{2\nu\beta\beta}}$ is proportional to the mixing angle, because of the relation A.6. Putting everything together, we can rewrite equation A.7 as:

$$\begin{aligned}
\sigma_{\sin^2\theta}/\sin^2\theta &\propto \sqrt{\frac{(R_{2\nu\beta\beta}+R_{others})\cdot\mathcal{E}}{R^2_{2\nu\beta\beta}\cdot\sin^4\theta\cdot\mathcal{E}^2} + \frac{1}{R_{2\nu\beta\beta}\cdot\mathcal{E}} + 2\cdot\frac{\sqrt{R_{2\nu\beta\beta}(R_{2\nu\beta\beta}+R_{others})\cdot\mathcal{E}}}{R^2_{2\nu\beta\beta}\cdot sin^2\theta\cdot\mathcal{E}^2}} \\
\sigma_{\sin^2\theta} &\propto \sqrt{\frac{(R_{2\nu\beta\beta}+R_{others})}{R^2_{2\nu\beta\beta}\cdot\mathcal{E}} + \frac{sin^4\theta}{R_{2\nu\beta\beta}\cdot\mathcal{E}} + \frac{2\cdot sin^2\theta\sqrt{R_{2\nu\beta\beta}(R_{2\nu\beta\beta}+R_{others})}}{R^2_{2\nu\beta\beta}\cdot\mathcal{E}}} \\
&\xrightarrow{sin^2\theta\sim 0} \mathcal{G}_{2\nu\beta\beta}/\mathcal{G}_{\nu N\beta\beta}\cdot\sqrt{\frac{(R_{2\nu\beta\beta}+R_{others})}{R^2_{2\nu\beta\beta}\cdot\mathcal{E}}}\ ,
\end{aligned} \tag{A.9}$$

where we reintroduced the dependence on the phase-space factors in the last expression. The sensitivity scales with the square root of the exposure, it is limited by the background, but in this case, a high $2\nu\beta\beta$ decay rate is advantageous due to the dependence $\sigma_{\sin^2\theta} \propto \sqrt{1/R_{2\nu\beta\beta}}$. The sensitivity also depends on the ratio between the phase space factors $\mathcal{G}_{2\nu\beta\beta}/\mathcal{G}_{\nu N\beta\beta}$.

Considering that the $2\nu\beta\beta$ decay rate is proportional to the inverse of the half-life, we expect the sensitivity of an experiment searching for $\chi\chi\beta\beta$ decay to scale with $\sqrt{1/(T^{2\nu}_{1/2}\cdot\mathcal{E})}$ while the relative sensitivity for the sterile neutrino mixing angle with $\sqrt{T^{2\nu}_{1/2}/\mathcal{E}}$. This means that experiments using an isotope with a long $2\nu\beta\beta$ decay half-life will be favored in the search for $\chi\chi\beta\beta$ decays as they will have a

lower background rate. However, they will be disfavored in the search for sterile neutrinos where the sensitivity on the $sin^2\theta$ is linearly proportional to the $2\nu\beta\beta$ half-life. Of course, the nuclear matrix element and phase space factor will also play a role when comparing different isotopes in the search for $\chi\chi\beta\beta$ decay.

This dependence of the sensitivity on the $2\nu\beta\beta$ decay half-life, obtained here with a simple counting analysis, was also observed in the results of the sensitivity projections presented in chapter 3, where a spectral fit and a full frequentist construction were implemented. In figure 3.3, we compared the sensitivity of different double-β decay experiments to light exotic fermions. In the search for sterile neutrino, the future CUPID experiment with ^{100}Mo ($T^{2\nu}_{1/2} \sim 7 \times 10^{18}$ yr) can set the most stringent constraints. On the other hand, in the search for Z_2-odd fermions, the short ^{100}Mo half-life limits the sensitivity of CUPID. In contrast, the nEXO experiment with ^{136}Xe ($T^{2\nu}_{1/2} \sim 2 \times 10^{21}$ yr) can set the most stringent constraints on the coupling g_χ.

Appendix B

Intensity of γ lines

The intensity of the most prominent γ lines in the GERDA Phase II spectrum was studied (see chapter 5, section 5.3.1 for details on the methodology). The intensities were compared between different detector types and between pre-upgrade and post-upgrade data.

The results obtained for the BEGe detectors are summarized in table B.1. The isotope is indicated in the first column, the energy of the line in the second column, and the branching ratio (BR) in the third column. The intensity of each line (in counts/kg yr) was extracted before analysis cut (Raw), after LAr veto cut (LAr AC), and in the spectrum of the events rejected by the LAr veto cut (LAr C). The results are reported respectively in the fourth, fifth, and last columns of table B.1, divided between pre-upgrade and post-upgrade data. The same results for the Coax detectors are summarized in table B.2 and for the IC detectors in table B.3.

Isotope	Energy (keV)	BR (%)	Raw (counts/kg yr)		LAr AC (counts/kg yr)		LAr C (counts/kg yr)	
			pre-upgrade	post-upgrade	pre-upgrade	post-upgrade	pre-upgrade	post-upgrade
^{42}K	1524.6	18.1	$76.6^{+1.6}_{-1.6}$	$75.5^{+2.2}_{-1.6}$	$16.1^{+0.7}_{-0.8}$	$14.7^{+0.9}_{-0.8}$	$60.3^{+1.7}_{-1.1}$	$61.1^{+1.6}_{-1.8}$
^{40}K	1460.8	10.7	$49.3^{+1.2}_{-1.4}$	$44.5^{+1.4}_{-1.6}$	$47.7^{+1.3}_{-1.2}$	$43.1^{+1.6}_{-1.3}$	$1.5^{+0.3}_{-0.3}$	$1.2^{+0.3}_{-0.3}$
^{60}Co	1332.5	100.0	$0.8^{+0.5}_{-0.4}$	$1.7^{+0.6}_{-0.5}$	< 0.6	$1.1^{+0.4}_{-0.4}$	$0.7^{+0.3}_{-0.3}$	$0.7^{+0.3}_{-0.4}$
	1173.2	99.9	$1.4^{+0.7}_{-0.5}$	$0.9^{+0.5}_{-0.6}$	$0.9^{+0.4}_{-0.5}$	< 0.5	$0.7^{+0.3}_{-0.3}$	$1.1^{+0.5}_{-0.4}$
^{228}Ac	911.2	25.8	$3.0^{+0.7}_{-0.7}$	$2.8^{+0.9}_{-0.7}$	$1.4^{+0.7}_{-0.5}$	$1.3^{+0.6}_{-0.6}$	$1.5^{+0.4}_{-0.4}$	$1.8^{+0.4}_{-0.6}$
	969.0	15.8	$1.7^{+0.6}_{-0.7}$	$0.6^{+0.7}_{-0.5}$	$0.9^{+0.6}_{-0.5}$	< 0.8	$0.7^{+0.4}_{-0.3}$	$1.1^{+0.5}_{-0.3}$
	964.8	5.0	< 0.6	$1.6^{+0.7}_{-0.7}$	< 0.3	$1.2^{+0.6}_{-0.5}$	$0.4^{+0.3}_{-0.3}$	$0.7^{+0.4}_{-0.3}$
	338.3	11.3	$2.2^{+1.2}_{-1.2}$	$2.9^{+1.3}_{-1.3}$	$1.0^{+0.6}_{-0.9}$	$2.7^{+1.2}_{-0.8}$	$1.3^{+0.7}_{-0.9}$	< 1.7
^{212}Bi	727.3	6.7	$1.5^{+0.7}_{-0.7}$	< 1.9	$1.0^{+0.6}_{-0.6}$	< 1.3	$0.5^{+0.4}_{-0.3}$	$0.6^{+0.4}_{-0.4}$
^{212}Pb	238.6	43.6	$13.2^{+2.1}_{-2.8}$	$10.4^{+2.7}_{-3.0}$	$10.5^{+1.5}_{-1.6}$	$5.1^{+1.7}_{-1.3}$	$2.8^{+1.5}_{-1.8}$	$3.3^{+1.5}_{-2.3}$
^{208}Tl	2614.5	99.8	$0.9^{+0.2}_{-0.1}$	$0.8^{+0.2}_{-0.2}$	< 0.1	< 0.1	$0.8^{+0.1}_{-0.2}$	$0.8^{+0.2}_{-0.2}$
	583.2	85.0	$2.8^{+1.0}_{-0.5}$	$1.0^{+0.6}_{-0.8}$	$0.7^{+0.4}_{-0.5}$	< 0.5	$2.4^{+0.5}_{-0.5}$	$1.5^{+0.5}_{-0.5}$
	860.6	12.5	$0.7^{+0.4}_{-0.6}$	< 1.0	< 1.0	< 0.5	$0.6^{+0.3}_{-0.4}$	$0.3^{+0.4}_{-0.2}$
^{214}Pb	295.2	18.4	$7.3^{+1.6}_{-1.6}$	$7.6^{+1.8}_{-1.9}$	$5.1^{+1.4}_{-0.9}$	$3.7^{+1.3}_{-1.1}$	$2.0^{+1.3}_{-1.1}$	$3.8^{+1.3}_{-1.3}$
	242.0	7.3	< 3.9	< 5.3	$2.4^{+1.2}_{-1.4}$	< 1.6	< 1.9	< 4.2
	351.9	35.6	$10.8^{+1.5}_{-1.2}$	$7.3^{+1.3}_{-1.3}$	$7.5^{+1.2}_{-0.8}$	$4.7^{+0.9}_{-0.9}$	$3.4^{+0.7}_{-0.9}$	$2.5^{+0.9}_{-0.8}$
^{214}Bi	609.3	45.5	$4.9^{+0.9}_{-0.7}$	$4.9^{+1.1}_{-0.8}$	< 1.2	$1.1^{+0.7}_{-0.6}$	$4.5^{+0.3}_{-0.7}$	$3.8^{+0.6}_{-0.6}$
	1764.5	15.3	$1.3^{+0.2}_{-0.3}$	$1.0^{+0.2}_{-0.2}$	$0.6^{+0.1}_{-0.2}$	$0.6^{+0.2}_{-0.2}$	$0.7^{+0.2}_{-0.2}$	$0.5^{+0.2}_{-0.2}$
	1238.1	5.8	$1.3^{+0.5}_{-0.5}$	$0.6^{+0.4}_{-0.5}$	$0.7^{+0.4}_{-0.4}$	< 0.6	$0.7^{+0.3}_{-0.4}$	< 0.9
	2204.1	4.9	$0.5^{+0.1}_{-0.1}$	$0.3^{+0.1}_{-0.1}$	$0.4^{+0.1}_{-0.1}$	$0.2^{+0.1}_{-0.1}$	$0.13^{+0.10}_{-0.06}$	$0.09^{+0.10}_{-0.06}$
	1377.7	4.0	< 0.6	$1.0^{+0.5}_{-0.4}$	< 0.4	$0.7^{+0.4}_{-0.3}$	< 0.5	$0.4^{+0.3}_{-0.2}$
	2447.9	1.5	$0.2^{+0.1}_{-0.1}$	$0.3^{+0.5}_{-0.4}$	$0.09^{+0.07}_{-0.05}$	$0.24^{+0.14}_{-0.08}$	$0.10^{+0.08}_{-0.05}$	$0.05^{+0.07}_{-0.05}$
	1120.3	14.9	$1.1^{+0.6}_{-0.5}$	$0.6^{+0.6}_{-0.5}$	< 0.9	< 0.7	$0.9^{+0.4}_{-0.3}$	$0.9^{+0.4}_{-0.4}$
e^+e^-	511.0		$2.6^{+0.8}_{-0.7}$	$3.1^{+0.8}_{-0.9}$	< 0.4	< 1.2	$3.7^{+0.6}_{-0.6}$	$3.1^{+0.5}_{-0.7}$
^{85}Kr	514.0	0.4	$5.7^{+0.9}_{-0.8}$	$4.9^{+1.0}_{-0.9}$	$3.6^{+0.6}_{-0.7}$	$2.1^{+0.6}_{-0.7}$	$2.0^{+0.6}_{-0.4}$	$3.0^{+0.6}_{-0.6}$
^{65}Zn	1125.0		< 0.6	$0.6^{+0.6}_{-0.4}$	< 0.4	$0.8^{+0.6}_{-0.4}$	< 0.5	< 0.5

TABLE B.1: γ lines count rates in the BEGe pre- and post-upgrade data sets.

Isotope	Energy (keV)	BR (%)	Raw (counts/kg yr)		LAr AC (counts/kg yr)		LAr C (counts/kg yr)	
			pre-upgrade	post-upgrade	pre-upgrade	post-upgrade	pre-upgrade	post-upgrade
^{42}K	1524.6	18.1	$109.7^{+1.7}_{-2.3}$	$96.4^{+2.8}_{-2.7}$	$23.5^{+0.9}_{-1.1}$	$16.3^{+1.4}_{-1.3}$	$85.4^{+2.2}_{-1.3}$	$78.5^{+2.9}_{-2.1}$
^{40}K	1460.8	10.7	$59.5^{+1.4}_{-1.8}$	$50.0^{+2.5}_{-1.9}$	$58.5^{+1.6}_{-1.5}$	$49.7^{+2.4}_{-1.8}$	$0.9^{+0.3}_{-0.3}$	$0.9^{+0.4}_{-0.4}$
^{60}Co	1332.5	100.0	$2.0^{+0.6}_{-0.6}$	$2.1^{+0.9}_{-0.8}$	$0.3^{+0.4}_{-0.2}$	$1.7^{+0.8}_{-1.2}$	$1.8^{+0.4}_{-0.4}$	$1.0^{+0.6}_{-0.5}$
	1173.2	99.9	$2.2^{+0.6}_{-0.8}$	< 2.1	< 1.1	< 1.6	$1.7^{+0.5}_{-0.4}$	< 1.3
^{228}Ac	911.2	25.8	$0.7^{+0.7}_{-0.5}$	$0.9^{+1.2}_{-0.7}$	< 1.0	< 2.0	$0.9^{+0.5}_{-0.3}$	$1.1^{+0.5}_{-0.6}$
	969.0	15.8	$1.1^{+0.6}_{-0.7}$	< 2.1	$0.4^{+0.5}_{-0.3}$	< 1.4	$0.5^{+0.4}_{-0.3}$	$0.9^{+0.4}_{-0.6}$
	964.8	5.0	$0.5^{+0.6}_{-0.5}$	< 1.8	$0.8^{+0.5}_{-0.6}$	< 1.2	< 0.5	$0.4^{+0.6}_{-0.3}$
	338.3	11.3	$2.2^{+1.2}_{-1.7}$	< 4.3	$1.7^{+1.5}_{-1.2}$	$2.0^{+2.0}_{-1.5}$	< 1.6	< 1.1
^{212}Bi	727.3	6.7	$0.8^{+0.7}_{-0.6}$	$2.7^{+1.3}_{-1.2}$	< 1.4	$1.7^{+0.8}_{-1.2}$	$0.5^{+0.4}_{-0.3}$	$1.1^{+0.6}_{-0.6}$
^{212}Pb	238.6	43.6	$3.8^{+2.4}_{-2.8}$	$4.3^{+2.9}_{-3.9}$	$2.3^{+2.1}_{-1.5}$	$4.9^{+3.0}_{-2.9}$	< 0.7	< 5.3
^{208}Tl	2614.5	99.8	$1.1^{+0.3}_{-0.2}$	$1.1^{+0.3}_{-0.3}$	< 0.2	< 0.3	$1.2^{+0.2}_{-0.2}$	$0.9^{+0.4}_{-0.2}$
	583.2	85.0	$2.2^{+1.0}_{-0.6}$	$4.3^{+1.5}_{-1.2}$	< 1.6	$0.9^{+1.0}_{-0.8}$	$1.7^{+0.5}_{-0.4}$	$3.6^{+0.9}_{-0.7}$
	860.6	12.5	< 1.4	< 1.4	< 1.0	< 1.1	$0.5^{+0.3}_{-0.4}$	< 1.0
^{214}Pb	295.2	18.4	$3.5^{+2.1}_{-2.3}$	$6.2^{+3.7}_{-2.8}$	$3.1^{+1.8}_{-1.8}$	$5.2^{+2.9}_{-2.2}$	< 2.5	< 4.1
	242.0	7.3	< 5.6	< 8.3	< 1.4	< 6.8	< 0.9	< 5.0
	351.9	35.6	$6.2^{+1.8}_{-1.7}$	$8.9^{+2.6}_{-2.8}$	$4.7^{+1.8}_{-1.1}$	$7.2^{+1.9}_{-2.6}$	$0.9^{+0.8}_{-0.7}$	$2.4^{+1.2}_{-1.4}$
^{214}Bi	609.3	45.5	$4.6^{+1.0}_{-0.9}$	$2.7^{+1.2}_{-1.2}$	$0.9^{+0.6}_{-0.6}$	< 0.9	$4.0^{+0.5}_{-0.7}$	$3.6^{+0.9}_{-0.6}$
	1764.5	15.3	$1.8^{+0.2}_{-0.3}$	$1.8^{+0.4}_{-0.4}$	$0.9^{+0.2}_{-0.2}$	$0.7^{+0.3}_{-0.3}$	$0.9^{+0.2}_{-0.2}$	$1.0^{+0.3}_{-0.3}$
	1238.1	5.8	< 1.2	< 1.5	< 0.6	< 1.5	$0.7^{+0.3}_{-0.5}$	< 0.6
	2204.1	4.9	$0.4^{+0.1}_{-0.1}$	$0.3^{+0.3}_{-0.1}$	$0.19^{+0.10}_{-0.09}$	$0.09^{+0.14}_{-0.07}$	$0.15^{+0.11}_{-0.07}$	$0.25^{+0.17}_{-0.14}$
	1377.7	4.0	< 0.8	< 0.9	< 0.3	< 1.0	$0.5^{+0.3}_{-0.3}$	< 0.5
	2447.9	1.5	$0.2^{+0.1}_{-0.1}$	< 0.2	$0.15^{+0.08}_{-0.07}$	< 0.1	< 0.1	< 0.2
	1120.3	14.9	$2.3^{+0.7}_{-0.6}$	$0.9^{+0.7}_{-0.9}$	$1.3^{+0.6}_{-0.5}$	< 0.8	$1.0^{+0.4}_{-0.4}$	$1.7^{+0.5}_{-0.7}$
e^+e^-	511.0		$5.2^{+1.1}_{-1.1}$	$4.3^{+1.3}_{-1.6}$	$0.8^{+0.7}_{-0.6}$	$0.9^{+0.8}_{-0.8}$	$4.8^{+0.6}_{-0.8}$	$3.0^{+1.1}_{-0.8}$
^{85}Kr	514.0	0.4	$5.7^{+0.8}_{-1.4}$	$4.4^{+1.6}_{-1.4}$	$4.4^{+0.9}_{-0.7}$	$2.2^{+1.3}_{-1.0}$	$0.4^{+0.5}_{-0.4}$	$2.2^{+1.0}_{-0.8}$
^{65}Zn	1125.0		$1.6^{+0.6}_{-0.7}$	< 1.4	$0.7^{+0.6}_{-0.4}$	< 1.0	$0.8^{+0.3}_{-0.4}$	< 1.1

TABLE B.2: γ lines count rates in the Coax pre- and post-upgrade data sets.

Isotope	Energy (keV)	BR (%)	Raw	LAr AC	LAr C
^{42}K	1524.6	18.1	$120.9^{+4.4}_{-3.3}$	$19.1^{+1.8}_{-1.3}$	$102.0^{+3.7}_{-3.2}$
^{40}K	1460.8	10.7	$99.9^{+4.3}_{-2.7}$	$97.9^{+3.7}_{-3.1}$	$2.6^{+0.8}_{-0.5}$
^{60}Co	1332.5	100.0	< 2.0	< 1.1	$0.7^{+0.6}_{-0.5}$
	1173.2	99.9	< 1.2	< 0.9	< 1.1
^{228}Ac	911.2	25.8	$2.9^{+1.1}_{-1.4}$	< 2.3	$1.9^{+0.7}_{-0.7}$
	969.0	15.8	$2.9^{+1.2}_{-1.2}$	$1.8^{+1.0}_{-1.0}$	$0.9^{+0.7}_{-0.4}$
	964.8	5.0	< 2.3	< 1.6	$0.9^{+0.6}_{-0.6}$
	338.3	11.3	$2.6^{+2.1}_{-1.7}$	$4.3^{+1.6}_{-1.6}$	< 1.5
^{212}Bi	727.3	6.7	$1.5^{+1.1}_{-1.1}$	$1.0^{+1.0}_{-0.8}$	$0.4^{+0.6}_{-0.4}$
^{212}Pb	238.6	43.6	$13.8^{+4.1}_{-3.6}$	$12.0^{+2.4}_{-2.7}$	$2.6^{+2.1}_{-2.3}$
^{208}Tl	2614.5	99.8	$1.8^{+0.5}_{-0.4}$	$0.1^{+0.1}_{-0.1}$	$1.7^{+0.5}_{-0.4}$
	583.2	85.0	$1.6^{+1.2}_{-1.1}$	< 1.9	$1.7^{+0.7}_{-0.8}$
	860.6	12.5	< 2.6	< 2.1	< 1.3
^{214}Pb	295.2	18.4	$5.4^{+3.5}_{-1.8}$	$5.8^{+2.2}_{-1.7}$	< 3.5
	242.0	7.3	$8.0^{+3.8}_{-4.0}$	< 3.9	$5.9^{+2.5}_{-2.1}$
	351.9	35.6	$8.7^{+2.3}_{-1.7}$	$6.9^{+1.7}_{-1.5}$	$2.2^{+1.4}_{-1.1}$
^{214}Bi	609.3	45.5	$4.9^{+1.5}_{-1.1}$	$1.4^{+1.0}_{-0.8}$	$3.7^{+1.2}_{-0.7}$
	1764.5	15.3	$2.5^{+0.5}_{-0.6}$	$0.8^{+0.4}_{-0.3}$	$1.5^{+0.5}_{-0.4}$
	1238.1	5.8	$0.9^{+0.7}_{-0.8}$	$0.9^{+0.7}_{-0.6}$	< 1.2
	2204.1	4.9	$1.2^{+0.5}_{-0.3}$	$0.3^{+0.2}_{-0.2}$	$1.0^{+0.3}_{-0.4}$
	1377.7	4.0	$1.2^{+0.8}_{-0.8}$	$0.6^{+0.6}_{-0.5}$	$0.5^{+0.5}_{-0.4}$
	2447.9	1.5	< 0.2	< 0.2	< 0.2
	1120.3	14.9	$3.8^{+1.4}_{-1.3}$	$1.9^{+1.1}_{-1.0}$	$1.9^{+0.8}_{-0.7}$
e^+e^-	511.0		$6.1^{+1.8}_{-1.5}$	$1.6^{+1.1}_{-1.0}$	$4.8^{+1.2}_{-1.0}$
^{85}Kr	514.0	0.4	$5.1^{+1.4}_{-1.5}$	$2.0^{+1.3}_{-0.9}$	$2.7^{+1.2}_{-0.7}$
^{65}Zn	1125.0		$10.5^{+1.6}_{-1.5}$	$9.9^{+1.3}_{-1.4}$	$0.7^{+0.7}_{-0.5}$

TABLE B.3: γ lines count rates in the IC pre-upgrade data set.

Appendix C

Background uniformity in the $0\nu\beta\beta$ decay analysis window

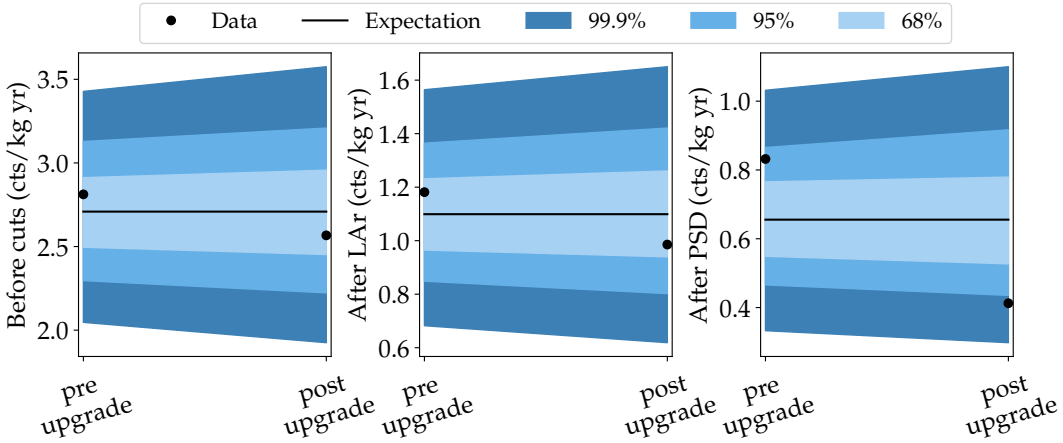

FIGURE C.1: Uniformity of the background in time, *i.e.* pre-upgrade and post-upgrade data. The count rates in the analysis window are compared with the hypothesis of uniform background before analysis cuts (left), after LAr veto cut only (center), and after PSD cut only (right). The expected rate for a uniform background is shown by the continuous line. The 68%, 95% and 99.9% probability bands for Poisson fluctuations are also shown.

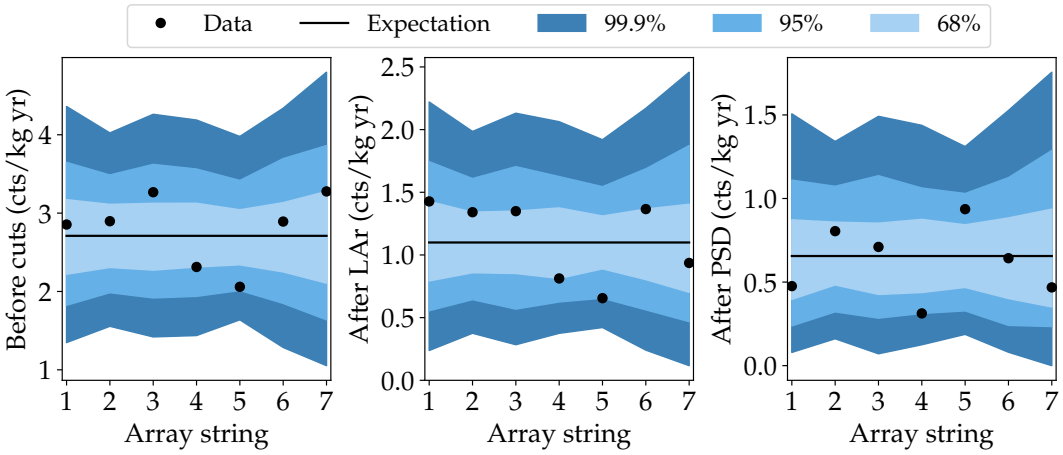

FIGURE C.2: Uniformity of the background tested grouping the detectors according to the string in which they are placed in the array. For details of the graphical representation see the caption of figure C.1.

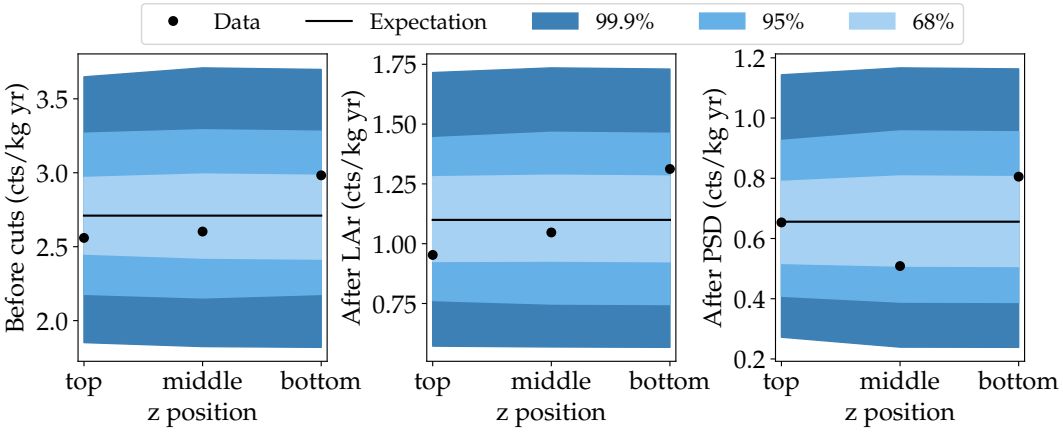

FIGURE C.3: Uniformity of the background tested grouping the detectors according to their position in the array along the z axis, *i.e.* top, middle, bottom. For details of the graphical representation see the caption of figure C.1.

Appendix D

Re-characterization of nine BEGe detectors

After the end of GERDA data taking, nine BEGe detectors were re-characterized and the FCCD of these detectors was determined using the standard GERDA procedure with ^{241}Am and ^{133}Ba sources. This work has been performed by GERDA collaborators [1, 2]. We report here the results, which have been used in this dissertation for a precision determination of the $2\nu\beta\beta$ decay half-life (see chapter 9).

Between the end of the data taking and the respective re-characterization, the detectors were stored at room temperature. Three detectors (GD00B, GD32B, and GD91B) were re-characterized shortly after the end of the data taking (0.9 yr), while the rest of the detectors were re-characterized about 2 yr after the end of the data taking. Among these 6 detectors, two (GD35B and GD76C) were used in LAr for some tests for a couple of months in between. The time for which each detector was stored at room temperature between the data taking and the re-characterization is reported in table D.1, together with the FCCD determined with the ^{241}Am and ^{133}Ba sources.

For completeness, we also report in table D.2 the FCCD values determined directly after the detector production [3] and the time for which the same detectors were stored at room temperature before their deployment in the GERDA LAr cryostat (from table 20 in [4]).

References

[1] A. Alexander and V. Biancacci. "New Dead Layer Characterization of BEGe detectors". GERDA Collaboration meeting. 2022. URL: https://www.mpi-hd.mpg.de/gerda/internal/LNGSJUN22/slides/22jun_DL-analysis-aa.pdf.

[2] S. Sailer. "BEGe re-characterization and HADES Status". GERDA Collaboration meeting. 2022. URL: https://www.mpi-hd.mpg.de/gerda/internal/LNGSJUN22/slides/22jun_hades_status_ssailer.pdf.

Detector name	t_1 (yr)	$FCCD_1$ (mm)		t_2 (yr)	$FCCD_2$ (mm)	
		^{241}Am source	^{133}Ba source		^{241}Am source	^{133}Ba source
GD35B	2.3	0.58 ± 0.09	0.53 ± 0.07	1.5	1.38 ± 0.07	1.25 ± 0.07
GD00D	2.9	0.77 ± 0.05	0.68 ± 0.07	2.1	1.05 ± 0.05	0.87 ± 0.07
GD02C	2.8	$0.79^{+0.07}_{-0.08}$	0.71 ± 0.07	2.1	1.13 ± 0.05	0.99 ± 0.07
GD35A	3.4	0.62 ± 0.04	$0.58^{+0.06}_{-0.05}$	2.1	1.70 ± 0.08	1.59 ± 0.06
GD61C	2.4	0.70 ± 0.07	$0.67^{+0.07}_{-0.08}$	2.1	0.99 ± 0.06	0.81 ± 0.07
GD76C	2.9	0.89 ± 0.06	0.81 ± 0.07	1.5	1.09 ± 0.06	0.95 ± 0.07
GD00B	2.8	$0.81^{+0.07}_{-0.08}$	0.71 ± 0.07	0.9	1.55 ± 0.05	1.36 ± 0.09
GD32B	2.5	0.84 ± 0.05	$0.73^{+0.06}_{-0.07}$	0.9	1.38 ± 0.05	1.14 ± 0.08
GD91B	2.8	$0.73^{+0.06}_{-0.07}$	0.60 ± 0.07	0.9	1.32 ± 0.05	1.15 ± 0.09

TABLE D.1: FCCD results of the nine re-characterized BEGe detectors. $FCCD_1$ was determined directly after the detector production. The detectors were then stored for a certain time t_1 at room temperature before their deployment in the GERDA LAr cryostat. $FCCD_2$ was determined during the re-characterization campaign of the nine BEGe detectors. Between the end of the data taking and the re-measurement, the detectors were stored for a certain time t_2 at room temperature.

Detector name	Linear growth (mm/yr)		Interpolated FCCD (mm)	
	^{241}Am source	^{133}Ba source	^{241}Am source	^{133}Ba source
GD35B	0.21 ± 0.02	0.19 ± 0.02	1.06 ± 0.05	0.97 ± 0.05
GD00D	0.06 ± 0.01	0.04 ± 0.02	0.93 ± 0.03	0.79 ± 0.05
GD02C	0.07 ± 0.01	0.06 ± 0.02	0.98 ± 0.03	0.87 ± 0.05
GD35A	0.20 ± 0.02	0.18 ± 0.01	1.29 ± 0.05	1.20 ± 0.04
GD61C	0.06 ± 0.02	0.03 ± 0.02	0.85 ± 0.04	0.74 ± 0.05
GD76C	0.05 ± 0.02	0.03 ± 0.02	1.02 ± 0.04	0.90 ± 0.05
GD00B	0.20 ± 0.02	0.18 ± 0.03	1.37 ± 0.04	1.20 ± 0.07
GD32B	0.16 ± 0.02	0.12 ± 0.03	1.24 ± 0.04	1.03 ± 0.06
GD91B	0.16 ± 0.02	0.15 ± 0.03	1.18 ± 0.04	1.02 ± 0.07

TABLE D.2: Observed linear growth and interpolated FCCD values at the time of GERDA data taking. (See chapter 9 for details on how these numbers are obtained.)

[3] GERDA Collaboration, M. Agostini, et al. "Characterization of 30 ^{76}Ge enriched Broad Energy Ge detectors for GERDA Phase II". In: *Eur. Phys. J. C* 79.11 (2019), p. 978. DOI: 10.1140/epjc/s10052-019-7353-8. arXiv: 1901.06590.

[4] E. Andreotti et al. "GSTR-16-002: Full Charge Collection Depth and Active Volume of GERDA Phase II BEGe detectors". GERDA Scientific / Technical Report. 2016. URL: https://www.mpi-hd.mpg.de/gerda/internal/GSTR/GSTR-16-002.pdf.

Appendix E

MC sampling with correlated and uncorrelated uncertainties

The detection efficiency is determined from MC simulations as the ratio between the number of detected events and the number of simulated events

$$\mathcal{E}_{MC} = \frac{N_{det}}{N_{sim}} \, . \tag{E.1}$$

The simulations consider all the detector-specific features, like the detector mass, the active volume fraction, and the live time (including the detector status in each physics run). While the detector mass and the live time can be considered to be known with negligible uncertainty, the active volume fraction introduced a non-negligible uncertainty in the efficiency calculation. The active volume fraction (f^{AV}) of each detector comes with a correlated and an uncorrelated uncertainty

$$f_i^{AV} \pm \sigma_{f_i^{AV},corr.} \pm \sigma_{f_i^{AV},uncorr.} \, , \tag{E.2}$$

which translates into a correlated and uncorrelated uncertainty of the individual detection efficiency

$$\mathcal{E}_i \pm \sigma_{\mathcal{E}_i,corr.} \pm \sigma_{\mathcal{E}_i,uncorr.} \, . \tag{E.3}$$

The total detection efficiency will be given by the sum, over all the detectors included in the analysis, of the individual detection efficiencies

$$\mathcal{E}_{MC} = \sum_i \mathcal{E}_i \, . \tag{E.4}$$

To propagate both the correlated and uncorrelated uncertainties of the individual $\mathcal{E}_i$ into $\mathcal{E}_{MC}$, a MC sampling of the efficiency was performed. The efficiency was sampled according to the sum of Gaussian distributions[1]

$$\sum_i \mathcal{G}(\mathcal{E}_i + g \cdot \sigma_{\mathcal{E}_i,corr.}, \sigma_{\mathcal{E}_i,uncorr.}) \, , \tag{E.5}$$

[1] We use the notation $\mathcal{G}(\mu, \sigma)$ to indicate the Gaussian distribution with mean μ and standard deviation σ.

where g is also randomly sampled (with a Gaussian distribution centered at 0 and with unitary width) but is common to all the terms in the sum to describe the correlation between the uncertainties. The efficiency $\mathcal{E}_{MC}$ is then determined as the mean of the resulting distribution and its uncertainty as the RMS of the same distribution.

List of abbreviations

Particle/nuclear physics

G_F Fermi constant

$m_{\beta\beta}$ effective Majorana neutrino mass

$2\nu\beta\beta$ two-neutrino double-beta

νSI neutrino self-interaction

$0\nu\beta\beta$ neutrinoless double-beta

0νECEC neutrinoless double-electron capture

A number of nucleons

BSM Beyond the Standard Model

CMB Cosmic Microwave Background

CP charge-conjugation parity

DM dark matter

ECEC double-electron capture

g_A axial-vector coupling constant

g_P pseudo-scalar coupling constant

HSD Higher-State Dominance

IO inverted ordering

NME nuclear matrix element

NO normal ordering

OMC Ordinary Muon Capture

PMNS Pontecorvo-Maki-Nakagawa-Sakata

QRPA Quasi-particle Random Phase Approximation

SM Standard Model

SME Standard Model Extension

SSD Single-State Dominance

Z atomic number

Experiments

GERDA Germanium Detector Array

AMoRE Advanced Molybdenum based Rare process Experiment

CUORE Cryogenic Underground Observatory for Rare Events

CUPID CUORE Upgrade with Particle Identification

DARWIN Dark matter Wimp search with liquid xenon

DEAP-3600 Dark matter Experiment using Argon Pulse-shape discrimination 3600

DONUT Direct Observation of the Nu Tau

EXO Enriched Xenon Observatory

HDM Heidelberg-Moscow

IGEX International Germanium Experiments

JUNO Jiangmen Underground Neutrino Observatory

KamLAND Kamioka Liquid scintillator Anti-Neutrino Detector

KamLAND-Zen KamLAND - Zero Neutrino double beta decay search

KATRIN Karlsruhe Tritium Neutrino (detector)

LEGEND Large Enriched Germanium Experiment for Neutrinoless $\beta\beta$ decay

LEP Large Electron-Positron (collider)

LHC Large Hadron Collider

MJD MAJORANA DEMONSTRATOR

NEMO-3 Neutrino Ettore Majorana Observatory 3

nEXO next-generation Enriched Xenon Observatory

NEXT Neutrino Experiment with a Xenon TPC

PandaX-III Particle and Astrophysical Xenon III

SNO Sudbury Neutrino Observatory

Laboratories

CJPL-II China Jin-Ping underground Laboratory II

LNGS Laboratori Nazionali del Gran Sasso

LSC Laboratorio Subterráneo de Canfranc

LSM Laboratoire Souterrain de Modane

PSI Paul Scherrer Institute

SURF Sanford Underground Research Facility

WIPP Waste Isolation Pilot Plant

Y2L Yangyang Underground Laboratory

Miscellaneous

μX muonic X-ray

C.I. confidence interval

C.L. confidence level

AC anti-coincidence

ANN artificial neural network

AV active volume

BAT Bayesian Analysis Toolkit

BEGe Broad Energy Germanium (detector)

BI background index

BL baseline

BR branching ratio

CCE charge collection efficiency

Coax coaxial (detector)

DAQ data acquisition

DEP double-escape peak

DL dead layer

DSP Digital Signal Processing

FCCD full charge collection depth

FEP full-energy peak

FT flat top

FWHM Full Width Half Maximum

HF high frequency (trace)

HPGe high-purity germanium

IC inverted coaxial (detector)

LAr liquid argon

LF low frequency (trace)

MC Monte Carlo

MS multi-site

MWA moving window average

MWD moving window deconvolution

PDF probability distribution function

PMT photomultiplier tubes

PSD pulse shape discrimination

QC quality cuts

ROI region of interest

RT rise time

SiPM silicon photomultipliers

SS single-site

TL transition layer

TP Test Pulse

TPC time projection chamber

WLS wavelength-shifting

ZAC Zero Area Cusp

Acknowledgements

I want to thank all those people who, in various ways, have contributed to this achievement.

First and foremost, I would like to thank my supervisor, Prof. Stefan Schönert, for allowing me to join his group and work in a vibrant and motivating surrounding. Your expertise and the passion with which you do your work are an immense source of inspiration.

Thanks to the whole review committee, Prof. Susanne Mertens for being the second corrector, and Prof. Andreas Weiler for chairing my defense.

I must thank Matteo for guiding me from the beginning of this journey with his experience and believing in me at difficult times more than I could. Thank you for being a mentor inside the university and a friend outside.

Special thanks to Christoph for his kindness and patience in sharing his expertise with me. Thanks for the incredible work we have done together and the many inspiring discussions.

And thanks to all my other colleagues, past and present, who, from day one, made me feel part of a team. Particular thanks to Christoph, Eli, Mario, Tommaso, and Patrick for everything we shared inside and outside the university.

Thanks to Prof. Alejandro Ibarra and Xavier M., for the collaborative work and the inspiring discussions.

Thanks to all the members of the GERDA collaboration, and in particular, Luigi and Katharina, for the continued collaborative work.

Thanks to all the MONUMENT people for all the work we have done and the lovely time we spent together over two beam-times.

Thanks to all my friends here in Munich and beyond for enriching my life outside the PhD. Particular thanks to Chiara, Sofia, Francesca, e Francesco. You are special to me.

Thanks to my family for the immense support and love.

And thank you, Nils, immense and indispensable support in the most challenging times. Thank you for the goodness and patience with which you look after me every day.